CRASHWORTHINESS OF TRAFFIC LIGHT STEEL POLES IN VEHICLE COLLISIONS

PRAVEEN KUMAR SIRIYA
Bachelor of Engineering, Delhi University, India.
Sept 1992

A thesis

presented to Ryerson University

in partial fulfillment of the

requirements for the degree of

Master of Applied Science

in the Program of Civil Engineering.

Toronto, Ontario, Canada, 2004

AUTHOR'S DECLERATION

I hereby declare that I am the sole author of this thesis.

I authorize Ryerson University to lend this thesis to other institutions or individuals for the purpose of scholarly research.

Praveen Siriya

I further authorize Ryerson University to reproduce this thesis by photocopying or by other means, in total or in part, at the request of other institutions or individuals for the purpose of scholarly research.

Praveen Siriya

BORROWER'S PAGE

Ryerson University requires the signatures of all persons using or photocopying this thesis. Please sign below and give address and date.

DATE	NAME	ADDRESS	SIGNATURE

ABSTRACT

Title: Crashworthiness of traffic light steel poles in vehicle collision.

Author: Praveen Siriya, M.A. Sc, Civil Engineering, Ryerson University, Canada. 2004

Vehicle crashworthiness focuses on the capability of a vehicle to protect its occupants in a collision. The Canadian Highway Bridge Design Code [2] does not provide design criteria for vehicle occupant safety except by field testing. The test-guided product development process is very costly and time-consuming. As an alternative, computer simulation tools are increasingly being used. The aim of this research is to contribute to the efficient design of traffic light poles by developing an experimentally calibrated, computer-based, finite-element model using LSDYNA [54], capable of predicting accurately their response when subjected to vehicle impact. The case of steel pole embedded directly in soil was proved to be strong enough to offer protection under service loading and vehicle impact. Side impact crashes proved to be more severe for the vehicle occupant as a result of the weak structural performance of the side doors of the vehicle. Based on this an innovative pole supported on hard rubber base is introduced to improve crashworthiness.

ACKNOWLEDGEMENTS

This research work is part of a multidisciplinary research project entitled "Crash Investigations: Outcome of Vehicle Design" sponsored by the Canadian Network of Centres of Excellence of the 21st Century Automobile, *NCE Auto 21* , and Transport Canada.

I would like to acknowledge the research assistantship received from Dr. Sennah's *NCE AUTO* 21 funding, Ryerson Post-Graduate Scholarship and the Teaching Assistantship from Civil Engineering Department of Ryerson University and all those faculty members who directly or indirectly helped me towards my thesis.

TABLE OF CONTENTS

LIST OF TABLES

LIST OF FIGURES

CHAPTER 1

INTRODUCTION

1.1 General

It is considered that in the field of vehicle safety and injury prevention, there should be a strong focus on the needs of families and children. To date, this area does not appear to have attracted the level of attention it deserves. A multi-disciplinary approach is advocated that links medical personnel in hospitals and rehabilitation centres to engineers and ergonomists who design and test vehicles. This approach is based on a belief that safety in automotive vehicles is fundamentally a function of both the design and function of vehicle safety systems, the design and function of highway hardware and the individuals who must make the decision to use them. As an outcome of vehicle design, vehicle occupants, involved in crash accidents with highway hardware, move out of position during or prior to vehicle collisions and, thus, suffer injuries which were not foreseen during the original design of the vehicle.

Older Traffic light poles are often made of wood. It was commonly known that these types of poles do not deform in crash accidents (see Figure 1.1). Hollow, round concrete poles reinforced with pre-stressed wires or strands have been used for long time in highways and traffic light stops and intersections. This type of concrete pole does not deform under light impact, however, it usually fails with less deformation (see Figure 1.2), compared to steel poles (see Figure 1.3). Steel poles are offered in lengths from 2.5 to 15 m, with round, octagon or dodecagon cross-sectional shapes.

1.2 Need for Research

Crashworthiness focuses on the capability of a vehicle to protect its occupants in a collision. The evaluation of vehicle crashworthiness has involved numerous full-scale crash tests of the vehicle and highway hardware to verify the compliance with regulatory requirements. This test-guided product development process is very costly and time-consuming. As an alternative, computer simulation tools are increasingly being used for the upfront assessment of crashworthiness without going through multiple-cycles of prototype testing and iterative design changes. In impact design, yielding of steel, as well as large deformation, is desirable for economic and safety reasons. As the structure is stressed in the plastic region, it continues to absorb the impact by balancing kinetic energy of the crash against its strain energy.

Finite element models of vehicles have been increasingly used in preliminary design analysis, component design, and vehicle crashworthiness evaluation, as well as roadside hardware design. Narrow road objects (poles, U-channel sign supports, barriers, etc) are a major cause of severe injury in highway crashes (see Table 1.1) [43].

The crash event is a severe and complicated phenomenon due to the complex interactions between structural and internal behaviour. Structures involved in crashes usually experience buckling deformation, high strain rate effects, fractures, and rapid structural unloading.

This leads to highly transient response arising from non-linear stiffness and viscous characteristics of the crushed materials. One of the most important engineering parameters that engineers employ in crashworthiness is the energy absorption. This energy is used as a quantified measure to assure that high impacts are sustained and absorbed by the structure. Therefore, the objective in crashworthiness is to build a structure on which material properties and geometrical shapes can absorb energy so that the safety regulations are achieved and, more importantly, the safety of the passengers is maintained. In the recent years, non-linear explicit finite element software has advanced significantly the computer modeling and simulation of automobile crashes. This capability allows the application of the software to model and analyze the performance of the roadside objects in crashes. Among the most advanced and widely used codes, finite-element simulation using explicit code such as LS-DYNA is widely used today for modeling crash problems.

A luminary pole is usually fabricated from hot rolled commercial quality carbon steel. The Canadian Highway Bridge Design Code (CHBDC-2000) [2] states that poles are to be designed to the minimum yield strength of the material with an adequate factor of safety and will withstand the dead loads of the structure as well as the specified wind loads. The base plate is usually fabricated from structural quality weld-able hot rolled carbon steel. Anchor bolts are fabricated from hot rolled carbon steel bars with high yield strength. The threaded end is galvanized to a minimum of 300 mm and each bolt is furnished with two flat washers and two hex nuts. The design of this type of luminary support is based on the concept of shear-away base, which is applicable for highways. However, in urban streets, shearing the pole base may cause the pole to fall over pedestrians and other cars present at the place of accidents. Crashworthiness is the performance of the available poles, designs and to investigate possible countermeasures and innovative methods to enhance the safety performance of these roadside structures, thus reducing the injuries and fatalities, when involved in vehicle crash accidents.

1.3 Objectives

The objectives of the present research are to evaluate the crash energy absorption and deformation characteristics of both the vehicle and the traffic light pole. Different pole support configurations are examined when subjected to frontal, offset and side impacts. The proper system of steel pole supports is expected to be strong enough to offer protection during minor impacts and remain flexible enough to avoid influencing the air bag deployment characteristics of the vehicle. Animations of the deformations of the vehicle structure, vehicle occupants and steel pole will be created for the different scenarios of pole supports. Specific objectives are listed as follows:

1. To develop a finite-element computer model, using commercially available explicit non-linear software LSDYNA to simulate crashes of a vehicle and a steel and aluminium pole in both side and frontal impact. In this model, a finite-element model for a mid-size sedan vehicle is used. The vehicle model is based on a 1991, 4-door, Ford Taurus.

2. To develop a new high energy absorption rubber-base for the traffic light pole that would enhance its safety performance when involved in crash accidents.

1.4 Contents and Arrangement of Thesis:

This thesis is divided into five chapters. In Chapter 1, the need for research and the objective of the research work are presented. Chapter 2 deals with the literature review pertaining to the current research work and the general evaluating criteria for research in vehicles involving road side hardware crash accidents. Chapter 3 discusses the finite element approach and tools required for computer-simulation of crashes and the validity of these tests with actual crash tests. Chapter 4 presents the results of the finite element modeling of vehicle impact with traffic light poles. Finally, based upon theoretical/simulation investigation, various conclusions and recommendations for the future research are presented in Chapter 5.

CHAPTER 2

LITERATURE REVIEW

2.1 General

Due to the increased complexity of today's vehicular fleet and the fact that full-scale crash tests do not provide sufficient information about loads, accelerations, stresses and strains, as such developing designs, based on the mechanical behaviour of highway accessories (barriers, poles, signs, guardrail terminals,... etc.) and analytical methods, have become a necessity. There needs to be more focus in utilizing computerized numerical methods for vehicle-crash simulation to improve highway roadside safety hardware and in assembling data required to develop, calibrate and validate these methods. This chapter presents a summary of the literature review on the analysis, design, testing and simulation of pole-type roadside hardware.

2.2 Design Specifications:

The 4th edition of AASHTO Standard Specifications Structural Supports for Highway Signs, Luminaries, and Traffic Signals of 2001 [3] covers the minimum design requirements for structural supports of these highway accessories in order to provide for public safety. It states that all structural supports shall be designed for the loads prescribed in these specifications using acceptable method of analysis.

Described in the specifications are specifications for steel, aluminium, fibre reinforced composites, wood, and pre-stressed concrete. Structural design is specified to meet serviceability, fatigue and ultimate limit state requirements. Standard details and specifications for steel and aluminium poles that meet the requirements of the AASHTO (2001) [4] were published in the Guide to Standard Highway Lighting Pole Hardware in 1980 [4]. The 2000 version of Canadian Highway and Bridge Design Code, CHBDC [2] follows these guidelines.

Figure 2.1 shows typical highway lighting pole consisting of pole shaft assembly, support arm assembly. Figure 2.2 shows different configurations of traffic signal support structures used in Canada.

2.2.1 Group Load Combinations:

The AASHTO Standard Specifications Structural Supports for Highway Signs, Luminaries, and Traffic Signals [3] details the procedure to derive dead load, live load, wind loads for structural design of steel, aluminium, pre-stressed concrete and wood luminary. The loads described in the specifications shall be combined into appropriate group load combinations as stipulated in Table 2.1. Each part of the structure shall be proportioned for the combination producing the maximum effect, using allowable stresses increased as indicated for the group load. The intent of the specifications is to provide an adequate margin of safety against failure (for example, minimum safety factors for bending for a steel tubular section is approximately 1.92 for group I loading and 1.45 for group II and group III loadings) to ensure the equity in safety factors among different materials covered by these specifications.

2.2.2 Dead Loads:

The dead load shall consist of the weight of the structural support, signs, luminaries, traffic signals, lowering devices, and any other appurtenances permanently attached to and supported by the structure. Temporary loads during maintenance shall also be considered as part of dead loads. Dead load should include all permanently attached fixtures, including hoisting devices and walkways provided for servicing of luminaries or signs. The points of application of the weights of the individual items shall be their respective centres of gravity.

2.2.3 Live Load

A live load consisting of a single load of 2200 N (500 lb) distributed over 0.6 m (2.0 ft) transversely to the member shall be used for designing members. The specified live load represents the weight of a man and equipment during servicing of the structure. The load need not be applied to the structural support. Any structural member designed for the group loadings shown in Table 2.1 will be adequately proportioned for this temporary live load application.

2.2.4 Ice Load

Ice load shall be a load of 145 Pa (3.0 psf) applied around the surfaces of the structural supports, traffic signals, horizontal supports, and luminaries; but it shall be considered only on one face of sign panels. More or less severe ice loads may be used provided historical ice accretion data is available for the region of interest. It is based on a 15 mm (0.60 in) radial thickness of ice, at a unit weight of 960 kg/m^3 (60 psf), applied uniformly over the exposed surface of the member.

2.2.5 Wind Loads

AASHTO Specifications [3] specify that wind load shall be the design pressure of the wind acting horizontally on the supports, signs, luminaries, traffic signals, and other attachments, P_z, be calculated by the following equation corresponding to the appropriate 50-year mean recurrence interval basic wind speed, and the appropriate importance factor selected from Table 2.2.

Wind Pressure Equation

The design wind pressure shall be computed using the following equation:

$$\left.\begin{array}{ll} P_z = 0.613 K_z G V^2 I_r C_d & \text{(Pa)} \\ P_z = 0.00256 K_z G V^2 I_r C_d & \text{(psf)} \end{array}\right\} \qquad 2.1$$

where: P_z is design wind pressure, K_z is height and exposure factor calculated as shown in table 2.3, G is gust effect factor, V is basic wind speed, I_r is importance factor which converts 50-year mean recurrence to other mean recurrence intervals as shown in Table 2.4, C_d is coefficient of drag. Values of G and C_d are presented elsewhere [4]. For hurricane recurrence intervals of 10 or 25 years, the design wind pressure for wind velocities greater than 45 m/s (100 mph) should not be less than the design wind pressure calculated for *V* equal to 45 m/s (100 mph) and the corresponding non-hurricane value I_r.

2.2.6 Structural Details of Pole Assemblies.

The Guide to Standardized Highway Lighting Pole Hardware [4] details structural aspect of aluminium and steel pole shaft assembly, support arm assembly, and pole anchoring assemblies. These poles come in heights ranging from 30′-50′. Three main shapes of pole are generally found (e.g. round, octagon, and dodecagon). Design wind speed is 130 km/h to 150 km/hr. Table 2.5 details sizes for steel and aluminium poles. Steel Pole shafts have structural capabilities equal or exceeding those intended by the 2001 AASHTO edition [3]. These pole shafts are welded, galvanized and/or painted in accordance of Standard Specifications [3]. An aluminium pole shaft is fabricated from alloy 6063 with T-6 temper after fabrication or alloy 6005 with T-5 temper after fabrication. Canadian Highway Bridge design code [2] follows AASHTO guidelines for design of poles. Figure 2.3 shows CHBDC pole support details anchor bolts with and without anchor bolt preload [2].

2.3 Breakaway structural performance

By definition, breakaway means a design feature that allows a sign, luminary, call box, or pole top mounted traffic signal support to yield, fracture, or separate near ground level upon impact. Breakaway supports shall be designed to yield, fracture, or separate when struck by a vehicle, thereby minimizing injury to the occupants of the vehicle and damage to the vehicle. This section addresses the structural, breakaway, and durability requirements for structures required to yield, fracture, or separate when struck by an errant vehicle. Structure types addressed include roadside sign, luminary, call box, and pole top mounted traffic signal supports. Breakaway devices shall meet the requirements herein and of NCHRP Report 350 [5] *(Recommended Procedures for the Safety Performance Evaluation of Highway Features).* Additional guidelines for breakaway devices may be found in the Roadside Design Guide [6].

2.3.1 Description of Breakaway Poles:

Breakaway poles consist of a lower connection (slip base), an upper connection (hinge mechanism), and structural support cables. The slip base and hinge mechanism activate on impact, reducing the effect of a semi-rigid pole on the errant vehicle while minimizing the effect on the utility service. The slip base is designed to withstand the overturning moments imposed by in-service wind loads as well as to yield appropriately to the forces of an automobile collision. The upper hinge mechanism is sized so as to adequately transmit service loads while hinging during a collision to allow the bottom segment of the pole to rotate up and out of the way. This upper connection reduces the effective inertia of the pole and minimizes the effect of any variation in hardware attached to the upper portion of the pole during a collision. The overhead guys (one above the upper connection and one below the neutral conductor) stabilize the upper portion of the pole during a collision to ensure the development of the bending moment necessary to activate the hinge. If enough utility conductors are present, the upper guys may possibly be eliminated. Approved breakaway designs consist of three basic modifications to existing (or new) timber poles. The modifications used are a slip base (lower connection), a plastic hinge (upper connection), and the overhead guys (structural support cables).

2.3.2 Design of Breakaway Supports:

Breakaway supports shall be designed to meet both the structural and the dynamic performance requirements of Sections 2.3.3 and 2.4 stated below. Design calculations or test data of production samples to support certification shall be provided, if requested by the owner. The data shall indicate a constant ability to produce a device that will meet both breakaway and structural requirements.

2.3.3 Structural Performance:

Breakaway supports shall be designed to carry the loads, using the appropriate allowable stresses for the material used. Where the structural adequacy of the breakaway support or components associated with the breakaway feature is in question, load tests shall be performed. The load tests shall be performed and evaluated based on the criteria that breakaway supports shall be tested to determine their ultimate strengths. The loading arrangement and structure configuration shall be selected to maximize the deflection and stresses in the critical regions of the structure or breakaway component. More than one test load arrangement shall be used; should a single arrangement not demonstrate the ultimate strength of the breakaway support. The breakaway support shall be tested in a manner that closely models field support conditions. The test load shall not be less than 1.5 times the loading for group II or III load combinations, whichever governs. Three samples for each test load arrangement shall be tested, to determine the ultimate load that the breakaway support assembly is capable of supporting in the weakest direction. If no individual ultimate load for the three samples differs by more than 10 percent from the mean, is divided, the mean value by 1.5 to determine the allowable load. If one of the ultimate loads differs from the mean by more than 10 percent, three additional samples shall be tested. Divide the average of the lowest three ultimate loads out of the six tests by 1.5 to determine the allowable load. The allowable load shall not be increased by 33 percent and shall be greater than or equal to the required loads for group II and III load combinations, as given in Section 2.2.

2.4 Breakaway Dynamic Performance

Breakaway supports shall meet the impact test evaluation criteria of Section 2.4.1 and/or Section 2.4.2. Additional provisions of Section 2.4.3 shall also be considered.

2.4.1 Impact Test Evaluation Criteria

Criteria for testing, documentation, and evaluation of breakaway supports shall be performed in accordance with the guidelines of NCHRP Report 350 [5]. Satisfactory dynamic performance for structural supports with breakaway devices shall include the following criteria: The standard vehicle shall be the 820C vehicle, which has a mass of 820 kg (1800 lb), or its equivalent. Structural supports shall meet the impact conditions of test level 3 in NCHRP Report 350 [5] for high-speed arterial highways. Test level 2 may be deemed acceptable for local and collector roads, provided approval is obtained. The specified impact conditions are noted in Table 2.6. The breakaway component of the support shall readily activate in a predictable manner by breaking away, fracturing, or yielding, when struck head-on by the test vehicle. Detached elements, fragments, or other debris from the structural support shall not penetrate or show potential for penetrating the occupant compartment, or present an undue hazard to other traffic, pedestrians, or personnel in a work zone. Deformation of, or intrusions into, the occupant compartment that could cause serious injuries shall not be permitted.

The vehicle shall remain upright during and after collision, although moderate rolling, pitching, and yawing are acceptable Figure 2.4. The longitudinal component of occupant velocity at impact with the interior surface of the passenger compartment, due to a vehicle striking a breakaway support, shall not exceed 5 m/s (16.4 fps), and preferably should not exceed 3 m/s (9.84 fps), at vehicle impact speeds of 35 to 100 km/h (21.7 to 62.1 mph) for test level 3 and from 35 to 70 km/h (21.7 to 43.5 mph) for test level 2. The longitudinal and lateral component of occupant ride-down acceleration shall be limited to a maximum of 20 g's with 15 g's preferred. After collision, the vehicle's trajectory should not excessively intrude into adjacent traffic lanes. Vehicle trajectory behind the support structure is acceptable. For breakaway or frangible supports that may house electrical components or breakaway wiring devices, dynamic performance shall be established with a mock-up of the components or devices in place.

2.4.2 Analytical Evaluation of Impact Tests

Standard Specifications Structural Supports for Highway Signs, Luminaries, and Traffic Signals [3] state that analytical evaluation of impact tests may be allowed in lieu of physical testing provided that an analytical model has been proven to accurately and conservatively predict the dynamic performance of the structural breakaway support, and deformation of, or intrusion into the passenger compartment is not likely. Verification of the analytical model shall be supported by an adequate number of full-scale impact tests.

2.4.3 Additional requirements

Standard Specifications Structural Supports for Highway Signs, Luminaries, and Traffic Signals [3] specifies the following provisions are to ensure predictable and safe displacement of the breakaway support: Substantial remains of breakaway supports shall not project more than 100 mm (4 in) above a line between the straddling wheels of a vehicle on 1500mm (60 in) centres (see Figure 2.5). The line connects any point on the ground surface on one side of the support to a point on the ground surface on the other side, and it is aligned radially or perpendicular to the centreline of the roadway, breakaway support mechanisms are designed to function properly when loaded primarily in shear, most mechanisms are designed to be impacted at bumper height, typically 450 to 500 mm (18 to 20 in) above the ground. If impacted at a significantly higher point, the bending moment in the breakaway base may be sufficient to bind the mechanism, resulting in non-activation of the breakaway device. For this reason, it is critical that breakaway supports not be located near ditches or on steep slopes or at similar locations where a vehicle is likely to be partially airborne at the time of impact. The type of soil may also affect the activation mechanisms of some breakaway supports. Additional guidance on typical breakaway supports may be found in Roadside Design Guide [6].

Breakaway supports, including those placed on roadside slopes, must not allow impacting vehicles to snag on either the foundation or any substantial remains of the support. Surrounding terrain may be required to be graded in order to permit vehicles to pass over any non-breakaway portion of the installation that remains in the ground or rigidly attached to the foundation. The specified limit on the maximum stub height lessens the possibility of snagging the undercarriage of a vehicle after a support has broken away from its base, and minimizes vehicle instability if a wheel hits the stub. The necessity of this requirement is based on field observations. The maximum mass of combined luminary support and fixtures attached to breakaway supports shall be limited to 450 kg (992 lb). Any increases in these limits are to be based on full-scale crash testing and an investigation of the range of vehicle roof crush characteristics that go beyond the recommended testing procedures of NCHRP Report 350 [5]. Efforts shall be made in all breakaway supports housing electrical components to effectively reduce fire and electrical hazards posed after structure impact by an errant vehicle. Upon knockdown, the support / structure shall electrically disconnect as close to the concrete foundation (pole base) as possible.

For multi-post breakaway roadside sign supports, the following shall be required to meet satisfactory breakaway performance: The hinge shall be at least 2100 mm (84 in) above the ground so that no portion of the sign or upper section of the support is likely to penetrate the windshield of an impacting car or medium size truck. A single post, spaced with a clear distance of 2100 mm (84 in) or more from another post, shall have a mass no greater than 65 kg/m (44 lb/ft). The total mass below the hinge, but above the shear plate of the breakaway base, shall not exceed 270 kg (600 lb). For two posts spaced with less than 2100 mm (84 in) clearance, each post shall have a mass less than 25 kg/m (17 lb/ft). No supplementary signs shall be attached below the hinges if such placement is likely to interfere with the breakaway action of the support post or if the supplemental sign is likely to penetrate the windshield of an impacting vehicle. All breakaway supports in multiple support sign structures are considered as acting together to cause the occupant velocity at impact, unless the following items are met: each support is designed to independently release from the sign panel, the sign panel has sufficient torsion strength to ensure this release, and the clear distance between supports is greater than 2100 mm (84 in). For multi-post breakaway roadside sign supports, there shall be sufficient strength in the connections between the post and the sign to allow the hinge system to function on impact. For multi-post breakaway roadside sign supports, the posts shall have enough rigidity to properly activate the breakaway device. The slip base breakaway device shall be oriented in the direction that ensures acceptable dynamic performance.

2.5 Experimental and Analytical Studies on Structural Performance of Pole Structures:

2.5.1 Fatigue, Design, Testing and Modeling:

Gilani and Whittaker [7, 8] developed finite element model for as-built post used for CMS (Changeable Message Sign), to assess the causes of its failure due to fatigue. Analysis of field data shows mechanical damping to be approximately 0.5% of critical in the first two modes and that galloping[1] instability was probably the cause of failure of CMS structures. Four types of loading were considered in this study e.g. natural wind gusts, truck induced wind gusts, vortex shedding[2], and galloping. They found that galloping instability was a potential cause of failure of the CMS structure.

---

[1]*Galloping*

Galloping is an unstable phenomenon caused by aerodynamic forces generated on certain cross-sectional shapes resulting in displacements transverse to the wind. For horizontal structures subjected to wind, the resulting motion occurs in the vertical plane. Galloping is most likely the primary cause of excessive vibrations in these types of structures. Hamilton et al. [9] hypothesize that due to the overall interaction of the entire mast arm structure, galloping may also initiate horizontal motion.

[2]*Vortex Shedding:*

As a steady uniform airflow travels over the face of a body, it reaches points of separation on each side where thin sheets of tiny vortices are generated. As the vortex sheets detach, they interact with one another and roll up into discrete vortices that are shed alternately from the sides of the object. The asymmetric pressure distribution created by the vortices around the cross section results in a sinusoidal forcing function transverse to the air flow's direction (in the case of horizontal mast arms, this results in vertical motion). When the vortex shedding frequency approaches the natural frequency of a structure, it results in an increase in vortex strength and a tendency for the vortex shedding frequency to couple with the frequency of the structure.

The finite element analysis of the gusset-retrofitted post confirmed that the addition of gussets served to substantially reduce the maximum stress in the weldment of the post to the base plate. The fatigue life of all the specimens studied also exceeded the AASHTO (American Association of State Highway and Transport Officials) design fatigue life of 400,000 cycles for a stress range of 69 MPa. Results also showed that there were high stress concentrations around the conduit holes, and conduit geometry appears to play a very small role in the value of maximum stress. The substantial out-of-flatness of the annular flange plates led to the development of high local strains in the walls of the mast arms upon tightening of the flange bolts. The concrete jacket retrofit increased the stiffness and mechanical damping of the post structure. In addition concrete jacket substantially reduced the stresses in the post and increased the fatigue life of the post.

Over a span of six years more than a dozen traffic signal mast arms in Missouri fractured at the arm-post weld connection. Almost all the failures are associated with propagation of defects or cracks. It is, therefore, imperative to evaluate existing mast arms using a simple yet accurate procedure. Genda et al. [10] proposed a statistical methodology to predict the fatigue life of signal mast arm structures on the basis of field-measured strain data. They found that both wind speed and the ratio between stress and the square of the wind speed follow a logarithmic normal distribution. The stress concentration depends on the length of weld leg along the mast arm well. They also found that signal structures in normal service condition will not crack under natural wind gusts during their service life.

Cook et al. [11] suggested installation of damping device to reduce and perhaps eliminate the fatigue failures due to wind induced vibrations for traffic signs and signals. The results from initial testing indicated that a tapered impact damper provides the best overall potential for both vertical and horizontal damping. The evaluation of wind-induced response of light and slender structures is strictly bound to damping modeling. Pagnini and Solari (2001) [12] investigated four structures: 30 m high Geo tower, 10 m high Conical lighting column, 12 m high Tapered column, and 14 m high Urban light column with top diameter of 280 mm and bottom diameter of 80 mm, providing for each of them, the logarithmic damping decrement as a function of motion amplitude. The urban light column was instrumented with strain gauges at the base section and was excited to vibrate in the first mode, providing the decaying oscillations of the response by switching the vibrodyne. The possibility of establishing an increase of the damping coefficient on increasing the vibration amplitude is very important in the structural design and the production cost. In the light of experiments performed they concluded that damping measurements related to large amplitudes are almost impossible.

A method of frequency domain analysis in a laboratory was studied by

Harrison and Roschke [13] for simulating wind vibration affecting roadside transportation structures. The approach was intended to be complementary to or in lieu of a test in a large-scale wind tunnel. A full-size two-pole roadside sign was erected in a laboratory and attached to an electromechanical actuator. The dynamic response of the structure to an impact load from the actuator was converted into the frequency domain to determine a harmonic transfer function. Records of velocities from several actual strong wind events recorded in free-field conditions were combined with drag coefficients to predict the variation of pressure on the structure. Time histories of force that are to be imposed by the actuator on the signposts were developed using frequency response functions and converting them into the frequency domain by Fast Fourier Transform (FFT). Results showed that nearly identical structural response of a roadside sign to simulated wind events can be obtained by using an actuator in a laboratory environment. Of course, limitations of the approach included neglect of localized effects, vortex shedding, and unsymmetrical boundary conditions. It was also noted that correct reproduction of the response at one point on the sign blank does not guarantee that effects of loading on other components of the sign are properly matched with field responses.

2.5.2 Breakaway Support:

Large directional signs are necessary on highways for efficient guidance of traffic. However, they require fixed supports, which constitute a hazard to the occupants of an errant vehicle. In order to reduce the hazard, breakaway connections are currently used on high-speed highways to support the roadside signs. These connections will slip under impact, therefore, preventing injuries to the occupants of an impacting vehicle. The breakaway connection works as long as the tension of the bolts is maintained within an allowable range. A method to ensure that the bolts are tensioned to the proper value was studied by Pinelli et al. [14]. It is based on the use of Belleville spring washers. Laboratory and field tests were performed to verify the adequacy of the new method. The variations of tension in bolts installed with flat washers and with spring washers were monitored over a period of 1 year for selected signs. The measurements showed that, at the time of installation, the new method was significantly more effective in ensuring the proper tension in the bolts. Similarly, over the long term, the bolts installed with spring washers maintained the tension on the bolt more effectively and without any loosening. They concluded that over the long term bolts installed with spring washers appear to maintain the tension in the bolt. No instances of consistent bolt loosening below the allowable range of tensions were observed. On the contrary, several bolts installed with flat washers could not maintain the tension in the allowable range. Differential expansion and contraction of the sign structures under the action of temperature variations induce changes in the tension of the bolt. These cycles, which are both daily and seasonal, could contribute to the loosening of bolts equipped with flat washers. Regardless of the installation method, it is also critical to ensure an effective maintenance of the road signs.

Alberson and Ivey [15] introduced improved breakaway utility pole AD-IV Figure 2.5 and subjected it to three pendulum tests. Use of AD-IV upper connection does not result in any significant performance differences during automobile collisions. The advantages of AD-IV are two fold. First, the costly machining of wind straps for Hawkins Breakaway System (HBS) has been eliminated. Second, if the AD-IV upper connection allows the upper part of the pole to lean during high winds or excessive ice, the pole can easily be straightened by simply loosening the large through bolts that clamp the wind straps, tightening or loosening the wind bolts to change the slope of the upper pole segment, and then retightening the through bolts. Use of the AD-IV lower connection should result in a slight reduction of energy absorbed in activating the slip base Ivey D. [16], owing to three factors: (a) the weight of the square plate is reduced, (b) the friction to be overcome using four bolts is approximately two-thirds the friction associated with the six-bolt HBS (Hawkins Breakaway System) connection, and (c) the orientation of the slots in the comers of the AD-IV base is optimum for release if it is impacted from the primary traffic direction. In the case of HBS, the two bolts with slots located 90 degrees out of phase with the traffic direction must be moved laterally to allow the slip base to activate. A 1980 Honda Civic was used for the full scale crash test. The inertial mass of the test vehicle was 1,800 lb (816 kg), and its gross static mass was 2,130 lb (966 kg). The vehicle was directed into the utility pole by the cable reverse tow and guidance system and was released to be freewheeling and unrestrained just before impact. The vehicle impacted the pole at a speed of 59.6 mph (95.9 km/hr), and the angle of impact was 15.0 degrees relative to the strung wires. The results met the test criteria of NCHRP Report 230 [17].

Use of direct embedded pre-stressed concrete poles for the support of substation equipment and electrical bus conductors is a very cost-attractive alternative to steel substation structures supported on cast-in-place foundations. Substation structures are subjected to electromagnetic forces and structural response to electromagnetic forces due to short circuits (shock loads) especially, for the case of rigid bus support structures. Nunez et al. [18] in their study compared the dynamic response of pre-stressed concrete pole (115kV 3-phase) substation structure to the response of more traditional steel substation structures. A dynamic factor was suggested to consider the impact effect on these structures. A proposed testing method to verify the theoretical results by applying a shock load to the substation structure was also presented. From the results of his analysis, he concluded that the maximum bending response of the structure is essentially equivalent for pre-stressed concrete poles and steel poles. The relative maximum deflection response expressed as the dynamic factor for deflections is also very similar between the two types of structures. However, the absolute maximum response in terms of deflections shows values more than two times greater for steel poles in comparison to pre-stressed concrete poles. This fact, in conjunction with the higher damping exhibited by pre-stressed concrete poles, constitutes a serviceability advantage of pre-stressed concrete poles. It was also be concluded that the duration of the impulse loading affects the number of oscillations of the structure but it has no apparent effect in the overall maximum response.

2.5.3 Design and Testing of Poles and components.

End plates and base plates are routinely used in cantilevered structures supporting traffic signs, signals, and lights. Despite this fact, a standard procedure for the design of these plates has never been established. Elsafi [19] developed a new procedure for the design of end plates and base plates of these structures. He proposed a procedure based on beam-and-plate bending and torsion theories, and intended to use for designing plates of square configurations. They also compared the thickness and stresses obtained using their new procedure with those estimated using finite-element analysis, and supported earlier conclusions reached through physical testing. Full-scale testing of these poles indicated structural inadequacy of the base plates and anchor bolts. Finite-element models were then developed and calibrated using the test data to evaluate a representative sample of poles from the poles then used in New York State. That evaluation, based on the structural adequacy of the base plates and bolts of these poles, confirmed a deficiency of the manufacturers' methods in designing adequate base plates and bolts to carry anticipated design loads. This proposed method could only be applied to square plates.

Kocer and Arora [20] proposed design of steel transmission poles as an optimization problem by identifying design variables, a cost function, and constraints. Non-linearity in structural response calculations due to large deflections was included in the formulation. They concluded that the optimal design process can lead to less expensive and safer designs compared to the conventional design process. All constraints of the problem are satisfied in the optimal design process, whereas, it is difficult to satisfy them with the conventional design process. Also, once the problem formulation is installed into an optimizer, solutions for additional cases can be obtained quite easily. As a result, variations in the problem conditions can be studied in a shorter time, leading to, perhaps, a better final design.

Kocer and Arora [21] observed that an important consideration in structural engineering is the expense of construction. This can be minimized by optimizing designs while satisfying all the requirements, such as safety, aesthetics, and serviceability. They designed a prestressed concrete transmission pole as an optimization problem by identifying design variables, a cost function, and constraints.

They used idealized stress-strain curve for sake of simplicity and divided loads applied to poles into two categories: weather related loads and other loads such as accidental loads, construction and maintenance loads as discussed in Precast / Prestressed Concrete Institute Guidelines [22], Krauthemmer et al. [23], and ASCE Guidelines for transmission line structural loadings [24]. They found that the selection of the cost function to have a profound effect on the optimum design. They only minimized the material cost and other costs such as manufacturing, transportation, installation were left for future studies.

Sicking et al. [25] discussed the design and development of steel breakaway posts as compared to wood posts. They noted that wood is readily available and inexpensive, but the quality of the wood and the associated breaking forces vary widely. The strength of a wooden post is affected by many factors: post size, ring density, knot location and size, cracks and checks, species, moisture content, etc. Broken wood posts are also considered to be an environmental hazard because of the chemical preservatives used to control decay and a significant problem with the proper disposal of accident debris. They stressed upon the need of certain design concepts to be included in design (e.g. post strength in both the weak and the strong axis). The post must break away in a predictable manner with a predictable force if impacted along the weak axis, such as a head-on impact with the terminal. On the other hand, the post must be sufficiently resistant in the strong axis for impacts with the side of the terminal to contain and redirect the vehicle. The post must be shipped as a single piece to avoid field assembly and be drivable to maintain ease of installation in the field and ease of maintenance (i.e. the post must be virtually maintenance free). The post should be competitively priced in comparison to wooden posts. They, therefore, designed and tested a breakaway steel post system for use in tangential terminal and found that the post exhibited consistent strength for redirection impacts and failed at very low loads in head-on impacts.

Nunez and Fouad [26] analyzed, the second order effects induced by the interaction of vertical gravitational and transverse loads acting on pole type structures used on highways, to determine the accuracy of the simplified second order effects by using amplification factors for second-order effects. They considered two grades of steel with yield strength of 345 MPa (50 ksi) and 450 MPa (65 ksi). The load parameters considered included vertical top and wind load. The geometrical variables included pole length (15.24 m, 30.48 m, and 45.72 m), with cross-sectional shapes such as round; hexagonal; and dodecagonal, wall thickness 6.35 mm; 9.53 mm; and 12.7 mm respectively. Their analysis found that the 1994 Standard Specifications for Structural Supports for Highway Signs, Luminaries and Traffic Signals [27] clearly overestimated the second order effects for pole-type structures.

Yang and DeWolf [28] developed a procedure to conduct a systems reliability analysis for highway truss sign supports subject to random wind loading and corrosion. The procedure provided a method for updating the resistance strength as the structure deteriorates. The study demonstrated that the most effective way to improve the system reliability is to increase the restraint of the connection at the top of the truss where it supports the sign and to increase the column stiffness. There are three kinds of uncertainties: involving the material strength, the member dimensions, and the live loads. In their study, physically measured dimensions for springs, column, diagonal length, and cross-section dimensions were considered as deterministic quantities. It was first shown that the out-of-plane stability is critical and that it was necessary to modify the original structural design to provide adequate design strength. For in-plane behaviour, it was further shown that the columns govern the safety. It was shown in the reliability analysis that reinforcing the columns will be most beneficial to the in-plane structure reliability. The diagonal's reliabilities are generally higher than that of the columns and, thus, they are not critical to the overall structure reliability. Thus, changing their size will not significantly increase the reliability of the structure.

Reid and Paulsen [29] evaluated the sign system, which is designed to support the wind loads on the sign as well as to allow the sign support to release on impact, and swing up and out of the way, when impacted by an errant vehicle. Two alternative designs for improving the wind load capacity of large dual-support signs were analyzed; thicker fuse plate design and a balanced hinge design. The safety performance of the sign systems was evaluated using non-linear, large deformation finite-element analysis (FEA). They commented that very large signs pose a difficult challenge for the roadside safety design engineer. Making the large sign strong enough to withstand high wind loads and "weak" enough to fail as desired during impact is much more complicated than for the relatively small sign. Crash simulation indicated that both designs have the potential for meeting the safety recommendations set forth by NCHRP 350 [5]. If the improvement of wind load capacities on large signs is to be considered further, it is recommended that the models be re-evaluated with an improved slip base model. The re-evaluation should also include varying the parameters on each design, investigating the possibility of combining the two designs, and testing intermediate sign sizes.

2.5.4 Finite Element Analysis:

The slip-base design mechanism is used to support signs and luminaries in highways are designed to break away in crashes with vehicles. This mechanism is intended to minimize occupant injuries by providing reduced resistance to the impacting vehicles. Conventional design and evaluation of safety performance of these systems by trial and error and crash testing is inefficient, as well as cost prohibitive. Therefore, finite element (FE) models that can accurately simulate the performance of the slip-base system in various crash scenarios are desirable. Azim et al. [30] conducted finite element crash simulations of Bogie *(bogie vehicle is used in lieu of actual vehicles for crash testing to save costs)* with flexible honeycomb nose; impacting the slip-base sign support and validated using the corresponding instrumented crash tests. They arrived at a validated DYNA3D model of the slip-base design that can be used initially as a predictor for the full crash tests and subsequently, as a tool for design parametric studies to optimize the performance of this class of mechanisms in reducing the crash pulse intensity in highway collisions. Simulations of frontal impacts at 32, 64, and 96 km/h and oblique impact at 20° and 96 km/h were completed successfully. Their investigation also demonstrated that the simpler modeling approaches for the slip-base mechanism, where flanges are tied together by a threshold force, could not predict occurrences of critical events. The FE approach and this validated model can be exercised in numerous crash scenarios for design optimization of other variations of slip-base systems in size, orientation, etc., or for performance evaluation of impacts with various vehicles.

2.5.5 Composite Structures and Fibre Reinforced Composites (FRC) Poles:

Considerable research interest has been directed towards the use of composite materials for crashworthiness applications because they can be designed to provide impact energy absorption capabilities which are superior to those of metals when compared on a weight basis. The sectional composite pole is a classic example of matching and placing materials in the most effective way. The strength of composite pole is that it maximizes the strengths and minimizes the weakness of each material it consists of. A sectional composite pole is a multi-section tapered column structure that has different materials from section to section along its length. The first sectional composite application was the result of an effort to extend the height of some existing spun concrete poles at Austin Energy in 1995 [31].

Mamalis et al. [32] reviewed information from a variety of sources to compare the findings of researchers in this field of energy absorption. They underlined the need of understanding of the bending crush behaviour of thin walled composite shell. The findings of extensive research work which has been carried out pertaining to the axial collapse and bending of thin-walled structural components have demonstrated that there are several variables which may control the energy absorption capability of composite materials. The principal ones are: (i) Materials (e.g. fibre and matrix materials, laminate design, temperature), (ii) Structural geometry (e.g. circular tubes, square/rectangular tubes, conical shells), (iii) Loading (e.g. axial, combined bending). In a head on collision the various structural components do not collapse in a simple, ideal form but in a non-axial manner meaning components are subjected to combined bending and axial loads. They concluded that Carbon-epoxy shells generally absorb more energy than glass-epoxy or aramid epoxy specimens. Specific energy tends to vary with ply orientation. An angle of 45° seems to be a critical ply orientation in the construction of a laminate as far as the energy absorbing capability is concerned. In general, specific energy absorption of various composite materials decreases with increasing temperature above approximately 0°C. Specimen geometry has a strong effect on the energy absorbing capability of composite shells; corners have a negative influence on it. In general, circular tubes and conical shells with small semi-apical angles appear to show better crashworthiness than the other types. The energy absorbed by tulip triggered specimens show significantly higher crashworthiness behaviour than the bevel triggered ones of the same geometry and materials. The crushing speed affects the energy absorption capability of axially loaded shells but the increase or the decrease of the specific energy depends on the material properties. Even though the modelling of real structures made of composite materials and subjected to combined loading is extremely difficult, the techniques like failure analysis and numerical simulation for the estimation of the energy absorption capability of axially loaded and bent shells with simple cross-sectioned geometries provide crashworthiness researchers with valuable tools of design.

Nelson [33] reviewed the proposals submitted to the NSEC (National

Electricity Safety Council of America) to introduce specific strength and load factors for FRC poles. Some of his conclusions are FRC poles are not expected to replace wood poles on a wholesale basis largely due to the current costs. FRC poles are more expensive. The FRC strength factors are currently the same as wood. Benefits of FRC poles include that they are lightweight; apparently woodpecker proof and can be manufactured in various colours and shapes. They require special attaching steps for climbing. FRC poles are manufactured with UV (ultraviolet) inhibitors and urethane coatings combining to provide excellent service life in utility pole applications.

Foedinger et. al. [34] developed of an energy absorbing fiber-reinforced composite (FRC) utility pole design that meets structural performance requirements for environmental loading. This is in accordance with the National Electrical Safety Code (NESC) for Class 4 poles and safety performance criteria in compliance with NCHRP Report 350 [5] Test Level 2 conditions for utility poles (see Figure 2.6). Developmental testing and analyses were performed to support development of a prototype design for demonstration testing. Full-scale crash testing has demonstrated the ability of the composite pole to absorb vehicle impact energy by progressive crushing and fracture propagation as the vehicle is brought to a controlled stop. In addition to offering improved safety performance, the energy absorbing FRC pole provides significant functional advantages such as reduced weight, improved strength-to-weight ratio, increased longevity, ease of installation, low maintenance, and resistance to environmental degradation.

Foedinger [34] found that relatively little attention has been devoted to the development of safer utility poles beyond breakaway timber pole designs and recognized the serious hazard presented by unforgiving timber utility poles installed. They stressed upon the need to bring about a new generation of utility pole designs employing energy absorbing composite materials offering a solution to developing and implementing safer utility poles that have a cost advantage over breakaway timber poles. Also they can be tailored to achieve the desired functional performance and energy absorption characteristics inherently without the need for additional strength members or add-on energy absorption devices. Their research resulted in the development of an energy absorbing fiberglass-reinforced composite (FRC) utility pole design that meets structural performance requirements for environmental loading in accordance with the National Electrical Safety Code (NESC) for Class 4 poles and safety performance criteria in compliance with NCHRP Report 350 [5] Test Level 2 conditions for utility poles. Developmental testing and analyses were performed to support development of a prototype design for demonstration testing (see Figure 2.7). Full-scale crash testing demonstrated the ability of the composite pole to absorb vehicle impact energy by progressive crushing and fracture propagation as the vehicle is brought to a controlled stop. In addition to offering improved safety performance, the energy absorbing FRC pole provides significant functional advantages such as reduced weight, improved strength-to-weight ratio, increased longevity, ease of installation, low maintenance, and resistance to environmental degradation.

2.6 Vehicle Collision Characteristics:

2.6.1 Impact locations:

An investigation of the Fatal Accident Reporting System (FARS) and National Accident Sampling System (NASS) showed that narrow objects, like the luminary support, utility poles and signs, accounted for 60% of the side-impact fixed roadside objects accidents and 80% of the fatal side-impact accidents [35]. On the other hand, accident data indicate that side impacts are not hazardous when the object struck is broad and, thus, are not likely to cause serious injury. Each year, about 225,000 people are involved in side-impact collisions with roadside objects, such as trees, utility poles, and guardrail terminals. It has been estimated that the societal cost of side-impact collisions with fixed roadside objects exceeds $3 billion annually. One in 3 vehicle occupants involved in side impacts with roadside objects is injured, and 1 in 100 is fatally injured. Side impacts with roadside objects are a significant cause of human trauma, and improved roadside hardware design can help to alleviate that suffering.

Developing roadside hardware with better side-impact performance is an emerging factor for improving roadside safety in the next decade. The purpose of side-impact crash tests is to assess the risk of injury to vehicle occupants in the event of a side-impact collision and to develop techniques for minimizing this risk. Narrow objects like trees, utility poles, and guardrail terminals subject the side of a vehicle to highly concentrated loadings that are difficult to resist without extensive vehicle deformation. An investigation of the Fatal Accident Reporting System and National Accident Sampling System showed that narrow objects, like the luminary support, accounted for 60 % of the side-impact fixed roadside object accidents and 80 % of the fatal side-impact accidents. Although 60 % of all side impacts involve vehicles striking each other, nearly 40 % involve single vehicles striking fixed objects, such as trees, utility poles, light poles, and guardrail terminals. Buth et al [59] performed the first side-impact crash tests of roadside features, for the Federal Highway Administration at the Texas Transportation Institute in the mid-1970s.

Crash test impact conditions should be relevant to the types of collisions that occur in the field. There are two basic approaches to selecting field-relevant test conditions: the practical worst case approach and the most probable condition approach. Although NHTSA has generally adopted test conditions for the most probable (i.e., the mean) impact conditions, the roadside safety community has traditionally used a practical worst-case philosophy. With this approach, the test conditions selected are more demanding than the typical impact though not necessarily the most severe. For example, 90 % of fixed roadside object side impacts occur at a lateral velocity of 50 km/h or less, and nearly all such accidents occur at velocities of less than 60 km/h [34]. An impact velocity of 50 km/h represents the 90th percentile impact velocity, and 60 km/h represents essentially the 99th percentile of side-impact fixed roadside object impact velocities. Of equal importance is the expected harm in side-impact collisions. Roughly half of severe occupant injuries [e.g., Abbreviated Injury Score• (AIS)>3] occur when the total change in velocity is less than 50 km/h, and almost two-thirds of moderate and severe injuries (e.g., AIS>2) occur at velocities below 50km/h [35]. The basic 50-km/h impact velocity represents a reasonable worst-case test condition with respect to expected impact speeds, as well as expected harm that is relevant to the way such collisions occur in the field. Accident data indicate that side impacts are not hazardous when the object struck is broad. Impacts in which a vehicle slides sideways into the middle of a guardrail, median barrier, or bridge rail do not to cause serious injury. Narrow objects, on the other hand, account for 60 % of the collisions and 80 % of the side impact fatalities.

---

[1] *The Abbreviated Injury Scale (AIS) is an anatomical scoring system first introduced in 1969. Since this time it has been revised and updated against survival so that it now provides a reasonably accurate was of ranking the severity of injury. The latest incarnation of the AIS*

score is the 1990 revision. The AIS is monitored by a scaling committee of the Association for the Advancement of Automotive Medicine.

Injuries are ranked on a scale of 1 to 6, with 1 being minor, 5 severe and 6 an un-survivable injury. This represents the 'threat to life' associated with an injury and is not meant to represent a comprehensive measure of severity. The AIS is not an injury scale, in that the difference between AIS1 and AIS2 is not the same as that between AIS4 and AIS5. AIS scores are: 1-Minor, 2-Moderate, 3-Serious, 4-Severe, 5-Critical, and 6-Unsurvivable.

Unlike the more typical roadside feature crash tests in which intrusion into the passenger compartment is excluded, side impact collisions with roadside objects such as poles, trees, and guardrail terminals are characterized by large intrusions into the occupant compartment. However, in side impact collisions with roadside objects, the occupant interacts directly with the vehicle's door. The intrusion of the door is so extensive and so rapid that the struck door acts nearly independently of the vehicle's centre of gravity. Finite element simulations have demonstrated that the occupant is unaffected by the rigid body motion of the vehicle in a side impact; the occupant interacts exclusively with the interior door of the vehicle and the struck object. The intrusion of the door into passenger compartment is one of the most hazardous characteristics of side impact accidents. The occupant strikes the intruding door structure in typically every accident. Any significant penetration or deformation of the passenger compartment is disallowed in all other types of full scale crash tests. The severity of side impact collisions, however, makes it an unreasonable and unobtainable restriction. Figure 2.7 shows a typical representation of an intrusion measuring system using a displacement transducer.

2.6.2 Analytical procedure for vehicle impact with Luminaries supports

NCHRP 318 [36] details procedure for analyzing impacts with breakaway base luminary supports (see Figure 2.8). A procedure was developed to determine appropriate design parameters for these systems for impacts with small automobiles. The procedure was broken into three phases of impact. During the first phase, the impacting vehicle crushed into the luminary support until the force on the pole reaches a level sufficient to activate the breakaway mechanism. Energy was dissipated only through crushing of the vehicle. It was assumed that the crush force was proportional to the crush distance. Using the law of conservation of energy, the velocity at the end of this phase was calculated from the vehicle's stiffness and slip-base activation force as shown in:

$$V_a = \sqrt{V_i^2 m_s F_s^2 /(k_v m_v)} \qquad 2.2$$

Where: V_i = initial impact velocity; V_a = velocity at activation of slip-base mechanism;

F_s = slip-base or fracture mechanism activation force; k_v = ratio of crush force to crush distance; and m_v = mass of impacting vehicle, m_s = mass of impacting vehicle.

From Equation 2.2, it was noted that as a vehicle's stiffness is reduced, its velocity at the activation of the slip-base mechanism is reduced. This effect arises from an increase in vehicle crush and the accompanying energy dissipation associated with the reduction in vehicle stiffness. After the lateral force on the luminary support reaches the activation force of the slip-base or fracture mechanism, energy is assumed to be dissipated because of two events: (1) the mechanism slips and/or fractures and (2) momentum is transferred to the support. The question is which of the two events occurs first or do they occur simultaneously? The velocity change arising from momentum transfer is proportional to the vehicle's velocity at the start of momentum transfer. Conversely, the velocity change arising from energy dissipation by the breakaway mechanism increases as the vehicle's velocity at the start of energy dissipation decreases. Because the sequence of these two events is not well known, it was conservatively assumed that momentum is transferred prior to energy dissipation associated with the breakaway mechanism. As such, the predicted velocity change after both events will be higher than if the two events occurred simultaneously or in reverse order. Consequently, the second phase of impact was assumed to involve only momentum transfer from the vehicle to the support as the base of the support was accelerated. The laws of conservation of linear and angular momentum were used to determine the velocity change of an impacting vehicle due to momentum transfer to the support. The relations of this formulation are shown in Equation 2.3. This equation gives the predicted vehicular velocity at the end of phase two.

$$V_b = V_a \frac{d^2 + r^2 - er^2 m_s / m_v}{d^2 + r^2 + er^2 m_s / m_v} \quad \text{.......... 2.3}$$

where V_a = vehicle velocity at beginning of phase two; V_b = vehicle velocity after momentum transfer to support; d = distance from vehicle bumper (or contact point) to centre of gravity of luminary support; r = radius of gyration of support; m_v = mass of vehicle; m_s = mass of support; and e = coefficient of restitution for the vehicle.

The third phase of impact was then assumed to involve only energy dissipation as the slip-base or fracture mechanism released. The law of conservation of energy was used to determine the velocity of the vehicle after losing contact with the pole. To simplify the analysis, the force-deflection relationship associated with the breakaway mechanism was assumed to vary linearly. The energy associated with failure of the breakaway mechanism can then be calculated if the travel distance during fracture can be estimated. Equation 2.4 gives vehicle velocity at the end of the impact event.

$$V_c = \sqrt{V_b^2 - F_s \delta_s / m_v} \quad \text{.......... 2.4}$$

where: V_c =vehicle's velocity at end of impact, δ_s = distance traveled by base of support during slippage or fracture of breakaway mechanism.

Equations 2.2 to 2.4 were incorporated into design criteria for slip-base installations that can safely accommodate small cars.

Coefficient of Restitution

Although it is known that restitution occurs for vehicles striking breakaway installations, little data are available for quantifying this value for such impacts. A coefficient of restitution of 0.5 was found to give good correlation for four full-scale crash tests simulated by the program.

Effective Vehicle Bumper Height

The base plates of most slip-base installations are typically mounted 3″ to 4″ above grade. This distance must be considered when locating the vehicle's point of impact along the pole. A vehicle's effective bumper height is defined as the distance from the slip plane to the point of action of the imparted vehicle force (see Figure 2.9). Simply stated, it is the height of the base plate subtracted from the vehicle's bumper height measured from the midpoint of the bumper.

Base Activation Force

The base activation force is defined as the force required to activate the slip-base mechanism or to fracture a frangible base. This activation force, or slip force, is dependent on a wide variety of factors. These factors include bolt diameter, bolt torque, surface treatment and finish, friction coefficient between the sliding surfaces (including bolts against notches), and notch geometry. The slip force is also dependent on the height at which the vehicle contacts the pole above the slip plane.

Slip Distance

As previously described, the change in vehicular velocity for the third phase of impact is dependent on the travel distance of the slip base or fracture mechanism. Based on static tests of slip-base mechanisms, slip distances in the range of 1 to 3 in. are common.

Validation

The analysis was validated using a computer program by comparing predicted velocity changes with results of a number of pendulum tests and full-scale bogie tests. The initial phase of the validation effort involved the pendulum tests. The model simulated the bogie crash tests with reasonably good accuracy. The predicted velocity changes were within ± 0.6 m/sec (2 ft/sec) of the average measured values.

2.6.3 Analytical procedure for vehicle impact with sign supports

A procedure similar to that developed for the luminary supports was developed [36] for analyzing impacts with breakaway sign supports, directed toward determining appropriate design parameters for impacts with mini-cars. The breakaway sign installation is characterized by the presence of a hinge at the level of the sign blank created by cutting the flange and web of the sign post. A fuse plate is spliced over the weakened post to transfer wind loads to the base. On impact, the sign post rotates about the hinge, allowing the vehicle to pass beneath the sign. During the first phase of impact, the vehicle crushes into the sign support until the force on the sign post reaches a level sufficient to activate the breakaway features. Energy is dissipated only through the crushing of the vehicle. In contrast to the luminary support, both slip-base and fuse plate forces must be overcome during this phase. Figure 2.10 shows a free body diagram for the sign support. Using equilibrium considerations, the vehicle force was equated to an equivalent slip force as shown in Equation 2.5

$$F_v = \frac{F_F D_b + F_s h}{d} = F_{se} \quad \text{.....................................2.5}$$

where: F_v = vehicle force; F_F = force required to activate fuse plate; F_s = slip-base activation force; D_b = depth of sign post; h = distance from slip base to hinge; d = distance from vehicle bumper to hinge; and F_{se} = effective slip-base activation force. Using conservation of energy, the velocity at the end of this phase was then formulated in terms of the effective slip force as shown in Equation 2.6

$$V_a = \sqrt{V_i^2 - F_{se}^2 /(k_v m_v)} \quad \text{.......................................2.6}$$

where: V_i = initial impact velocity; V_a = velocity at activation of breakaway mechanism; F_{se} = effective slip-base activation force; k_v = frontal stiffness of impacting vehicle; and m_v = mass of impacting vehicle. Conservation of angular momentum was used to determine the velocity change of the impacting vehicle due to momentum transfer to the support. Equation 2.7 gives the predicted vehicular velocity at the end of the second phase.

$$V_b = V_a \frac{m_v d^2 - eI_s}{m_v d^2 + I_s} \quad \text{.......................................2.7}$$

where: V_a = vehicle velocity at beginning of phase two; V_b = vehicle velocity after momentum transfer to support; d = distance from vehicle bumper to hinge; I_s = mass moment of inertia of sign support; m_v = mass of vehicle; and e = coefficient of restitution for vehicle. The third phase of impact was assumed to involve only energy dissipation as the fuse plate and slip-base mechanisms released. To simplify the analysis, the force-deflection relationships associated with the slip base and fuse plate were assumed to vary linearly. The Law of Conservation of energy was used to determine the velocity of the vehicle at the end of the impact event. The energy associated with failure of the breakaway articles was formulated in terms of the slip distance of the base. For impacts in which the hinge is activated, the effective slip-base activation force is calculated using Equation 2.5. The slip force F_s (lb) and fuse plate force F_F *(lb)* are then determined using an appropriate effective coefficient of friction. The post height is taken to be the distance from the slip base to the hinge, and the post weight is calculated based on this length.

Effective Friction Coefficient

The majority of breakaway sign supports are mounted on rectangular or unidirectional slip bases. Because of the basic differences in base geometry, bolt orientation, and notch geometry, the rectangular slip base has an effective friction coefficient different from the triangular or multidirectional base.

Validation

The preceding analysis technique was validated by comparing redirected velocity changes with results of four full-scale crash tests from [38, 39].

2.6.4 Analytical procedure for vehicle impact with base-bending sign supports

Small Sign Supports

Because only one test of a small sign installation was conducted in the study [36], it was desirable that an estimate be made of the impact performance of other vehicles under 1,800-lb with other sign supports. The procedure presented was only an approximation to a very complex problem. Impacts with base-bending sign supports involve highly non-linear behaviour of the support, the soil, and the vehicle.

For many widely used small sign supports the critical velocity change of an impacting vehicle occurs at low rather than high impact speeds. High carbon, high strength steels exhibit this behaviour. Supports with breakaway features such as the slip base or the lap-splice at ground level also exhibit this behaviour. Further, the mass of most small sign installations is relatively small in comparison to the impacting vehicle. The vehicular velocity change is due in large part to an energy loss (distortions in sign posts, soil displacements and damping, and vehicular crush) as opposed to a momentum transfer, especially for low-speed impacts. For purposes of estimating velocity change, it was assumed that energy loss is independent of vehicle mass. Based on this assumption, the velocity change of a given vehicle is estimated from that measured in a test of another vehicle as follows:

$$(\Delta KE)_T = \tfrac{1}{2} M_T \left(V^2_{IT} - V^2_{FT} \right) \quad \text{..........} 2.8$$

Where: $(\Delta KE)_T$ = change in kinetic energy of test vehicle during contact with support; M_T = mass of test vehicle; V_{IT} = impact velocity of test vehicle; and V_{FT} = final velocity of test vehicle after loss of contact with support. Then, for a different size vehicle with mass M_V impacting at V_{IT}:

$$(\Delta KE)_T = \tfrac{1}{2} M_V \left(V^2_{IT} - V^2_{FT} \right) \quad \text{..........} 2.9$$

The change in velocity, ΔV is then calculated as follows:

$$\Delta V = V_{IT} - V_{FV} \qquad 2.10$$

It is noted that for sign impacts, the occupant impact velocity will, in most cases, approximately equal the velocity change of the vehicle during impact. This is borne out by results of various tests.

2.7 Vehicle Impact Simulation

Zaouk et al. [37] presented a developed and validated a finite element model of a 1994, C-1500, Chevrolet pickup truck model for multiple impact applications at National Crash Analysis Centre (NCAC), Highway Administration (FHWA) and the National Highway Traffic Safety Administration (NHTSA). The Chevrolet C-1500 truck is a multi-purpose pickup tuck. The vehicle obtained by the NCAC was a Regular Cab, Fleet side Long-Box C-1500 with a total length of 5.4 meters (212.6 in.) and a wheelbase of 3.34 meters (131.5 in.). The engine is a 4.3-liter Vortec V6 with Electronic Fuel Injection coupled to a manual transmission with a rear wheel drive configuration. However, several other models exist, such as higher engine capacity, automatic transmission and four wheel drive configuration, with no change in the general geometry. The truck was first disassembled and grouped into seven main groups: the frame, front inner, front outer, cabin, doors, bed and miscellaneous. The three dimensional geometric data of each component was then obtained by using a passive digitizing arm connected to a desktop computer. Since this model was to be used for multi-purpose crash applications, considerable detail was included in the rail frame, and front structures including bumper, radiator, radiator assembly, suspension, engine, side door and cabin of the vehicle. These parts were digitized as detailed as possible, minimizing any loss in the geometry, which may affect the deformation and buckling behaviour of the part. As an example, the chassis or main frame, one of the most important structural parts in the truck, was digitized and meshed using two different methods. The first did not include any of the buckling holes while the second included all these holes. In the first case, the model behaved poorly when compared to the test. However the second case behaved as expected. In including these holes, the running time increased. This was caused by the increase in element numbers and the decrease in the element size on the rails. However, there was a significant gain in the model's behaviour. Another aspect of increasing the model's accuracy is material testing. Several coupons from parts such as the engine cradle, fender, hood, bumper, rails, door and doorframe were tested to obtain their properties. These parts were tested for tension and shear and tests were conducted at three different rates: slow static, low rate dynamic and high rate dynamic. The results from these tests were incorporated in the model. The model consists of 61,776 nodes, 52,541 shell elements, 109 beam elements and 1716 hexahedron elements. The PATRAN file consists of 211 groups, corresponding to the number of element properties, as well as the number of all components. Specifically, the properties of each component are defined by a set of material cards with 5 types of materials being used in the model. Each of the 211 components is subdivided into either shell elements, beam elements or hexahedron element. There are two types of shell elements used in the calculation, viz. quadrilateral shell and triangular shell. The formulations of both types of shell elements used for this paper are based on Belytschko-Tsay theory [41]. Initially, degenerate quadrilateral elements were utilized for the triangular shell elements, this caused some inaccurate behaviour. To solve this problem, the Co triangular elements are used. Only one type of beam and one type of hexahedron elements are used in the model. The formulations of the beam elements are based on Hughes-Liu theory, while the hexahedron elements use one point integration constant stress formulation.

Five LS-DYNA material models are used in the truck model. The elastic material model was used in components such as the engine, transmission, rear axle and rear suspension. The Blatz-Ko material model was used in several mounts such as between the cabin and nails, engine and rails, etc. For large deformations the rate-dependent tabular isotropic elastic-plastic material model, is the most commonly used material type for this paper. Two types of nodal constraints, nodal rigid body constraints and spot welds, were used. The spot weld option was used to model the spot-welds between the sheet metal. The nodal rigid body constraint was used to model the bolts. Two types of joints, spherical and revolute, were used to connect the front suspension of the truck model. LS-DYNA sliding interface Type-13 in LS-DYNA is used to model the contact between the different components of the truck.

The simulations were performed on a SMP (Symmetric Multi-Processing) computer consisting of 16 processors. The SMP version of the LS-DYNA, version 936, was used. The simulation for the frontal impact was run from 0 to 150 milliseconds time interval. The CPU time for the run was 49 hrs. For the case of comer impact, the simulation was conducted for 400 msec of impact with a CPU time of 152 hrs using 4 processors. In both simulation cases, a fixed time step of 1 μsec was used. The acceleration records for selected nodal points were outputted every 50 μsec. These nodal points were chosen based on the sensor locations of the test vehicles. For frontal impact with rigid wall, these positions include: engine, dashboard, and cabin rail while in the 1.07 m (42 in.) vertical wall the centre of gravity (CG) was added. An SAE-60 filter was used to reduce numerical noise effects in the simulation for nodal acceleration records, as well as for the test data.

The simulation results demonstrated a prediction mode for highway barrier impacts based on a model validation with a full frontal barrier impact and a comer impact into a vertical wall. These results are preliminary and show a first attempt at such prediction. The results from these simulations are encouraging and show some reasonable correlation with the full scale tests. The validation of the pickup truck model is by far not complete. Further analysis is being performed to reduce the differences between the full scale tests and the simulations for the two cases presented here. The model will also be validated against other full scale tests of different impact configurations including side impact with the moving deformable barrier (MDB), offset head-on and angle impact with another vehicle, and impact into roadside narrow objects and barriers such as the vertical wall and guardrail.

2.8 Crashworthiness Evaluation Procedure for Roadside Hardware

Side-impact collisions with roadside objects such as trees, luminary signs, and guardrails, represents a serious type of accident, have not been adequately addressed by the roadside hardware testing community due to the difficulties of performing and evaluating such crash tests. During the past decade, the National Highway Traffic Safety Administration has developed procedures and criteria for performing side-impact vehicle-to-vehicle crash tests. This is to incorporate the latest side-impact research from the vehicle crashworthiness community and to integrate it with the procedures and evaluation criteria used in designing roadside hardware. A 50 km/h full broadside impact at the centre of the driver-side door of a small two-door 820-kg passenger car is recommended for evaluating side-impact performance with roadside objects.

2.8.1 Protocols for impact testing of pole car crash

First side impact crash test of a roadside hardware was performed in the UK in 1969 [38] when a small car was directed laterally across a wetted pavement towards a pole. Side-impact crash tests are significantly more difficult to perform than typical safety appurtenance crash tests. Accelerating the vehicle laterally requires test facilities that are not commonly found in the roadside research community. Table 4 illustrates the increasing severity of injury with increasing total velocity change. More than 60% of all minor injuries occurred in accidents where the lateral change in velocity was less than 10 km/h. In contrast, 75% of the severe and fatal injuries occurred in accidents where the lateral change in velocity was greater than 31 km/h. Clearly, the severity of injury experienced by the vehicle occupants is related to the amount of energy dissipated. It has been suggested that injury can be defined as exposure to energy Injury [39]; more energy should be correlated with a higher proportion of severe injuries. The proportion of severely and moderately injured occupants increases as the lateral change in velocity increases. Severe life-threatening injuries [abbreviated injury score (A1S) >3] can be observed across the range of impact speeds, but 75% occur at velocities greater than 30 km/h. The mean velocity for occupants who received AIS >3 injuries was approximately 40 km/h. Impacts occurring in the 30-60 km/h range resulted in more than 1 chance in 5 of sustaining an AIS ≥4.

The impact point for side-impact crash tests of roadside structures should be at the centre of the driver's side door on a small passenger vehicle. This location is near the longitudinal centre of gravity of the vehicle and about 250 mm in front of the dummy's shoulder. Since the door is weakest at the centre, the maximum amount of intrusion should be observed when the impact is located at this point. Nearly 60% of the side impacts in the study sample occurred between the A and B pillar, (Troxel et al. (1991) [40]). Impacts that occur between the A and B pillars are located on the front door, very close to the front-seat occupant

2.8.2 Euro-NCAP Test Protocols

As per Euro-NCAP [41] the rigid pole is a vertical metal structure beginning no more than 102 mm above the lowest point of the tires on the striking side of the test vehicle when the vehicle is loaded as specified in Section 1 and extending at least 100 mm above the highest point of the roof of the test vehicle. The pole is 254 ±3 mm in diameter and set off from any mounting surface, such as a barrier or other structure, so that the vehicle will not contact such a mount or support at any time within 100 ms of the initiation of the vehicle to pole contact. Mark a line along the vertical centre-line of the pole which may be used to check the alignment of the test vehicle on the carrier. During the acceleration phase of the test, the accelerations of the carrier should not exceed 1.5 m/s^2. Measure the speed of the vehicle as near as possible to the point of impact, using an infrared beam intercepting two markers at a measured distance apart. The actual test speed in the test details target speed = 29±0.5 km/h. The impact angle should be 90°±3°. Align the vehicle on the carrier so that the angle between the vehicle's longitudinal and the direction of movement of the carrier is 90°.

2.8.3 NCHRP 350 Test Protocols

The vehicle shall strike the test object at a lateral velocity of 50 km/hr ± 4 km/hr. The impact velocity shall be measured using a high-speed camera. The lateral velocity shall be measured after the tow mechanism is completely separated from the vehicle but just before first contact between the vehicle and test device. The yaw rate of the vehicle shall be less than 5 degrees/sec just prior to the time of impact as measured by an overhead high-speed camera positioned over the impact point. The longitudinal component of velocity just prior to the impact must be less than ± 4 km/hr. Investigation of the NASS and FARS data has indicated that 90 % of side impact collisions with fixed roadside objects occur at a lateral velocity of 50 km/hr or less [42]. The velocity measurement must reflect the actual impact velocity to the extent possible. For this reason it is necessary that the vehicle be sliding freely when the measurement is taken. Generally vehicles come to rest still in contact with the test article in side impact collisions so braking will not usually be necessary.

The vehicle shall be oriented such that the forward direction of the vehicle is perpendicular to the longitudinal direction of a hypothetical roadway and the front of the vehicle shall face the hypothetical roadway. At the time of impact the side slip distance, S, shall be less than 300 mm as measured by the overhead high-speed camera located over the impact point. S is measured from the rear-most impact-side corner of the vehicle to the front-most corner on the impact side parallel to the hypothetical roadway. The impact angle in side impacts with roadside features can be crudely measured in the NASS accident data using the direction of force variable. Severe injuries (e.g., AIS>3) are most often associated with directions of force between 45 and 105 degrees from the front of the vehicle and 60 % of all side impact collisions have angles in this range. Figure 2.11 shows directions of force in side impact collisions involving passenger compartment. While the mean direction of force was approximately 60 degrees, the most frequently observed direction of force was 90 degrees. A full-broadside collision is specified because it represents a very hazardous condition for vehicle occupants that are commonly observed in the field. A full broadside collision is, therefore, a practical worst-case impact scenario.

The purpose of measuring the side slip distance S is to ensure that the vehicle is essentially perpendicular to the hypothetical roadway. The typical 820C vehicle is 3700 mm ± 200 mm long. If the distance S, measured parallel to the hypothetical roadway, is less than 300 mm the yaw angle at impact will be less than 5 degrees. The impact point shall be located on the driver-side door at the hip-point location of the centre of the door is considered to be the weakest point on the door since the bending moment is maximized at this location. In most small passenger vehicles, the centre of the door will be located near a point on the driver between the knee and the hip. Occupants are at higher risk when the impact occurs on the door since the amount of vehicle intrusion will be maximized [42]. The location corresponding to the peak risk is at the location where the occupant's head and hip would be in a typical small two-door passenger car [43]. The impact point is easily determined by inserting the ATD adjustment wrench into the hip adjustment bolt when the driver side door is open and the ATD has been positioned in the seat. A string and plum-bob can be attached to the end of the wrench and a reference point marked on the sill of the vehicle. The impact point is then defined as a vertical line passing through this reference point.

2.8.4 Criteria for Risk Evaluation

Side impact collisions are particularly serious impacts, but no evaluation guidelines exist; (Hiranmayee et al. [43]). However, evaluating the results of side impact collisions have been difficult because no widely recognized evaluation criteria exist that relate observable roadside object crash test results to the risk of injury to a hypothetical occupant. Three primary injury mechanisms are involved in side impact collisions with roadside objects (i) Injuries to the Head, (ii) Injuries to Thorax, and (iii) Injuries to Pelvis.

NHTSA has developed specific Anthropometrical Test Devices (ATD) measured injury criteria for each of these body regions—Head Injury Criteria (HIC), Thoracic Trauma Index (TTI), and Pelvic Acceleration (P_y). Although relating ATD responses to the risk of human injury is complex and controversial, biomechanics researchers have attempted to assess the relationship among the HIC, TTI, and Py and the probability of sustaining a life-threatening injury. In general, an HIC of 1000, a TTI of 90 g, and pelvic accelerations of 130 *g* represent approximately a 20 % probability of sustaining a life-threatening injury under similar conditions in a real-world collision. Figure 2.12 shows biomechanical and protection limits.

Unlike the more typical roadside feature crash tests in which intrusion into the passenger compartment is excluded, side impact collisions with roadside objects such as poles, trees, and guardrail terminals are characterized by large intrusions into the occupant compartment. If relatively little occupant compartment intrusion occurs, the vehicle can often be treated as an essentially rigid body and the occupant as another rigid body translating within the boundaries of the occupant compartment. This is the basis of the flail space technique and the occupant risk criteria first proposed by Michie in 1981 [44, 45]. In side impact collisions with roadside objects, however, the occupant interacts directly with the vehicle's door. The intrusion of the door is so extensive and so rapid that the rigid body assumption is not valid. In effect, the struck door acts nearly independently of the vehicle's centre of gravity. Finite element simulations have demonstrated that the occupant is unaffected by the rigid body motion of the vehicle in a side impact; the occupant interacts exclusively with the interior door of the vehicle and the struck object [45].

HEAD INJURY

Although head injuries are not specifically addressed in NHTSA side impact crash test evaluation procedures [Federal Motor Vehicle Safety Standard (FMVSS) 214], they are an important injury mechanism in impacts with tall roadside objects such as poles and trees [46, 47]. The HIC have been commonly used in frontal impact evaluation for decades to assess the level of head injury risk in frontal collisions. An HIC of 1000 is conventionally considered to represent the threshold at which linear skull fractures will begin to appear [48]. Some precedent exists for using the HIC in lateral impacts, although, strictly speaking, the HIC has never been validated for measuring lateral head trauma (Fan et. al.) [49].

The HIC is also appropriate only when the head and the vehicle interior come into contact. If a roadside object does not extend above the bottom of the side-door window, the HIC does not need to be calculated because no contact would be possible with the struck object and no head injury would be likely.

The HIC is given by the following expression *(II)*:

$$HIC = \left(\left(\frac{1}{t_2 - t_1}\right)\int_{t_1}^{t_2} a.dt\right)^{2.5} (t_2 - t_1) \quad \text{..............} 2.11$$

Where

t_1 = beginning of the evaluation interval (s),

t_2 = end of the evaluation interval (s), and

a = instantaneous resultant acceleration of the head in *g's*.

The time interval, (t_2-t_1) must be chosen such that the difference is less than 36 ms and the HIC value is maximized.

Head injury is considered to relate to the magnitude and length of acceleration. The head can sustain high accelerations if the loading is relatively short and lower accelerations if the time is relatively long, as illustrated by the Wayne State tolerance curve Fan [50]. If (t_2 – t_1) is replaced by the value Δt, the following expression is obtained:

$$HIC \bullet g = \Delta t\left(\frac{1}{\Delta t}\int_{t}^{t+\Delta t} a \cdot g \cdot dt\right)^{2.5} \quad \text{..............} 2.12$$

If both sides are multiplied by the acceleration due to gravity (g), the integral of the acceleration is simply the change in velocity that occurs during the period Δt, so the integral can be replaced by the symbol ΔV, yielding

$$HIC = \Delta t \left(\frac{\Delta V}{g \Delta t} \right)^{2.5} \qquad \text{.......... 2.13}$$

In graphical terms, the quantity $\Delta V/\Delta t$ can be represented by the slope of a curve on a velocity-time history. Larger slopes will result in larger HIC values. In calculating the HIC, Δt must be less than 36 ms as specified by NHTSA calculation procedures [51]. Although no lower limit is specified in FMVSS 208 for Δt, the practical lower limit would be the data acquisition rate. The smallest Δt possible for measurements using vehicle-based data collected is 10 ms [52]. Although ATD data are collected and filtered at 1650 Hz (SAE J211 Class 1000) [53], vehicle data are usually collected and filtered at 300 Hz (SAE J211 Class 180). If an ATD is not in the test vehicle, the acceleration data based on vehicle and barrier accelerations would be collected at 300 Hz. Further, for plotting purposes, acceleration data are often filtered with a cut-off frequency of 100 Hz (SAE Class 60). Sampling and filtering to SAE Class 60 would result in a data point each 10 ms. Early tests that were the basis for developing the HIC involved head-form drop tests onto flat, rigid surfaces. The interaction time (i.e., the time the head form and the rigid surface were in contact) in most of these tests was 12 ms. A practical lower bound time interval of 10 ms, thus, appears to have both experimental and physical significance.

If Δt is assumed to be 10 ms, the critical HIC as 1000, and the acceleration due to gravity as about 10 m/s^2, the previous expression can be rewritten as

$$\left[\frac{\Delta V}{\Delta t}\right]_{max} \leq 10 \sqrt[2.5]{\frac{1000}{0.01}} = 1000 m/s^2 \ldots\ldots\ldots\ldots 2.14$$

Thus, the maximum slope of the velocity-time history of the hypothetical occupant's head during any 10-ms interval must be less than 1000 m/s^2 (approximately 100 *g*). If the maximum slope is less than 1000 m/s^2, the HIC measured by an ATD should be less than the critical HIC value of 1000.

THORACIC INJURY

The TTI is given by the following expression:

$$TTI(d) = \frac{1}{2}[T_{12} + \max(LURY, LLRY)] \ldots\ldots\ldots\ldots 2.15$$

Where:

TTI (d) = Thoracic Trauma Index,

T_{12} = peak lateral acceleration of the T_{12} spinal segment (g),

LURY = peak left-upper rib Y acceleration (g), and

LLRY = peak left-lower rib Y acceleration (g).

TTI (d) is an average peak acceleration of the ATD thorax. If the average peak acceleration of the thorax can be estimated from either full scale crash test data or finite element simulations, it should correlate well with the TTI (d) because they are both measures of the same physical phenomena. The overall average acceleration of the thorax can be estimated using elementary kinematics as follows:

$$V_f = V_i + a \cdot \Delta t \qquad 2.16$$

where : V_f = final velocity of the thorax, V_i = initial velocity of the thorax, a = average acceleration of the thorax during the time period, and Δt = interaction time of the ATD with the intruding object.

Assuming the average peak acceleration of the ATD is approximately equal to the TTI while the ATD is in contact with the door (i.e., TTI x $g = a$) yields the following equation:

$$TTI \bullet g = \frac{V_f - V_i}{\Delta t} = \frac{\Delta V}{\Delta t} < 90g \qquad 2.17$$

The thorax criteria can be applied in the same way as the HIC. The largest difference between the vehicle impact velocity and the velocity of the struck object is calculated after 10 ms from impact. The difference in velocity must be less than 9 m/s for the TTI to be less than 90 g. In most scenarios, the maximum difference will be found very early in the impact, usually just after the 10-ms limit.

PELVIC INJURY

Pelvic injury is included as an evaluation criterion in the NHTSA FMVSS 214 side impact standard and, thus, is included in this study for consistency [52]. The peak lateral acceleration of the pelvis must be less than 130 *g* for acceptable performance. The peak lateral acceleration can be approximated by the largest slope on a velocity-time history, and the pelvic injury criterion can be written as

$$(P_y \bullet g)_{\max} = \left\{ \left[\frac{\Delta V}{\Delta t} \right]_{\max} \right\} \le 130.0g = 1300m/s^2 \quad \text{.........................2.18}$$

If the minimum possible Δt is estimated as 10 ms, then the maximum allowable change in velocity is

$$\Delta V_{\max} \le 130 \cdot 10 \cdot (0.01) = 1300\text{m/s}^2 \quad \text{..............................2.19}$$

The pelvic injury criterion can thus be stated as the maximum difference between the vehicle impact velocity and the velocity of the impacted face of the struck object should not be greater than 13 m/s at every point on the velocity-time history of the struck object 10 ms after first contact between the vehicle and roadside object.

In short, the three criteria can be related to the velocity-time history of the intruding object:

$${}_{t>0.010}\Delta V_{\max} \le 10.0 \text{ m/s (head injury)}$$

$^{t>0.010}\Delta V_{max} \leq 9.0$ m/s (thoracic injury) 2.20

$^{t>0.010}\Delta V_{max} \leq 13.0$ m/s (Pelvis injury)

2.8.5 Vehicle Deformation Criteria

One of the NCHRP Report 350 [5] test evaluation criteria that is notably missing from the recommendations in Table 2.8 is limits on the magnitude of passenger compartment intrusion. Since side impacts often result in large passenger compartment penetrations, it might be expected that passenger compartment deformation would play a major role in evaluating side- impact collisions. Hinch et al. [53] examined the relationship between HIC, TTI, and vehicle crush in a series of eight side-impact crash tests with luminaries. They found that the correlation between HIC and vehicle crush was both negative and very weak (R^2 = 0.013), and the correlation between TTI and crush was also very poor (R^2 = 0.095) (where R is coefficient of regression). These results indicate that crush is a poor predictor of ATD response and, therefore, is also a poor predictor of occupant risk. The amount of vehicle crush is really just a measure of the amount of energy dissipated by the vehicle during the entire impact. Predicting the potential for injury requires addressing not only the amount of energy dissipated but also the rate at which it is dissipated. This is another area that requires a great deal more research to determine the relationship between intrusion and intrusion rate and occupant injury. Table 2.9 compares impact conditions for side impact crash tests.

CHAPTER 3

FINITE ELEMENT ANALYSIS

3.1 General

The main advantages of the finite element method are flexibility in terms of discretization geometry and in the application of different types of boundary conditions. To simulate front / side impact crash LS-DYNA [54] explicit finite element software is used. In finite element modeling results could be obtained for each element, node, material, etc. and could be refined by using close meshing (discretization) at the particular area, part etc. as opposed to multi-body dynamic approach. Also post-buckling loads of complex structures and contact problems with changing contact regimes involving friction can be dealt within LS-DYNA.

3.2 LS-DYNA SOFTWARE

LS-DYNA is a general purpose finite element code for analyzing the deformation dynamic response of structures including structures coupled to fluids. The main solution methodology is based on explicit time integration. An implicit solver is currently available with somewhat limited capabilities including structural analysis and heat transfer. A contact-impact algorithm allows difficult contact problems to be easily treated with heat transfer included across the contact interfaces.

By a specialization of this algorithm, such interfaces can be rigidly tied to admit variable zoning without the need of mesh transition regions. Other specializations, allow draw beads in metal stamping applications to be easily modeled simply by defining a line of nodes along the draw bead. Spatial discretization is achieved by the use of four node tetrahedron and eight node solid elements, two node beam elements, three and four node shell elements, eight node solid shell elements, truss elements, membrane elements, discrete elements, and rigid bodies. A variety of element formulations are available for each element type. Specialized capabilities for airbags, sensors, and seatbelts have tailored LS-DYNA for applications in the automotive industry. LS-DYNA currently contains approximately one-hundred constitutive models and ten equations-of-state to cover a wide range of material behaviour.

3.3 Explicit Finite Element Approach

Explicit method solves for the equilibrium at time t by direct time integration using the central difference method:

$$m \bullet \ddot{x}_t + c \bullet \dot{x}_t = F_t - (F_S)_t \qquad \text{3.1}$$

$$\dot{x}_t = \frac{x_{t+\Delta t} - x_{t-\Delta t}}{2\Delta t} \qquad \text{3.2}$$

$$\Delta t < 2[\sqrt{1+\zeta^2} - \zeta] / \varpi_{\max} \qquad \text{3.3}$$

where $\ddot{x}_t$ is the acceleration, and $\dot{x}_t$ is the velocity vectors. m and c are the diagonal mass and damping matrices, respectively. Δt is the time step for the time integration,

ω_{max} is the maximum eigen frequency of the system. ζ is the fraction of critical damping of the highest mode. This explicit integration procedure is conditionally stable, where the time step Δt is subjected to a limitation via Equation 3.3. Since a longer calculation time is necessary for the problems where the natural time is quite large, one has to reduce the natural time of a process by, for example, artificially increasing the punch speed. Artificially increasing the mass density allows one to use larger time step which makes it possible to complete the finite element analysis problem in fewer incremental steps. However, such attempts at improving the analysis efficiency result in an increase of inertia effects which affect the accuracy of the solution.

The calculation cost of the explicit solution procedure is directly proportional to the size of the finite element model. This is its major advantage compared to the implicit method, where the calculation cost is proportional to the square of the matrix bandwidth of the mesh for very large models. The diagonalized mass matrix allows the explicit method to use a very fine mesh at any location without taking the increase of wave front into consideration. Another advantage of explicit method is the use of simpler algorithms to treat the contact constraints due to small time increment.

Implicit method solves for equilibrium at the time $t+\Delta t$:

$$K^T(u^{i-1})\,\delta u^i = F - R(u^{i-1}) \quad \text{........ 3.4}$$

$$\Delta u^i = \Delta u^{i-1} + \delta u^i \quad \text{........ 3.5}$$

where, $K^T(u^{i-1})$ is the tangent stiffness matrix of deformation system, δu, F and R are the incremental displacement, applied external load and the internal load vectors, respectively. Due to the nonlinear nature of problems, an iteration procedure is used to ensure equilibrium. Depending upon the procedure chosen, each iteration requires the formation and solution of the linear system of equations (see Equation 3.4). With the increase of the size of problems (e.g. 3D solids), this system of equation can become very large and the computational cost of solving this system may dominate the total CPU time. Due to the iterative nature of the solution procedure, a successful solution requires the satisfaction of convergence criterion at each incremental step. Generally, the convergence speed is quite problem dependent and failure to converge results in premature termination of the analysis.

3.4 Constraints and restraints in LSDYNA

Hourglass Control

Hourglass modes are nonphysical, zero-energy modes of deformation that produce zero strain and no stress. Hourglass modes occur only in under-integrated (single integration point) solid, shell, and thick shell elements. LS-DYNA has various algorithms for inhibiting hourglass modes. The default algorithm (Type 1), while being the cheapest (in terms of processing time), is generally not the most effective algorithm. Generally set HGEN to 2 in *control_energy to compute hourglass energy and use *database_glstat and *database_matsum to report the hourglass energy for the system and for each part, respectively. That way, we have a way to confirm that hourglass energy is small relative to peak internal energy for each part (<10% as a rule-of-thumb).

Stiffness-based hourglass control (Types 4 and 5) is generally more effective than viscous hourglass control for structural parts. Usually, when stiffness-based hourglass control is invoked, it is preferable to reduce the hourglass coefficient, usually in the range of .03 to .05, so as to minimize nonphysical stiffening of the response and at the same time effectively inhibiting hourglass modes. For high velocity impacts, viscosity-based hourglass control (Types 1, 2, and 3) is recommended even for solid/structural parts. Type 6 hourglass control invokes an assumed-strain co-rotational formulation for Type 1 solid elements and under-integrated 2D solids (shell Types 13 and 15). With the hourglass type set to 6 and the hourglass coefficient set to 1.0, an elastic part need only be modeled with a single Type 1 solid through its thickness to achieve the exact bending stiffness. Type 6 hourglass control should always be used for Type 1 solids in implicit simulations.

A way to entirely eliminate hourglass concerns is to switch to element formulations with fully-integrated or selectively reduced (S/R) integration. There can be a downside to this approach. For example, Type 2 solids are much more expensive than the single point default solid. Secondly, they are much more unstable in large deformation applications (negative volumes much more likely). Third, Type 2 solids have some tendency to 'shear-lock' and thus behave too stiffly in applications where the element shape is poor. Triangular shells and tetrahedral solid elements do not have hourglass modes but have drawbacks with regard to overly stiff behavior in many applications. A good way to reduce hour-glassing is to refine the finite element mesh.

3.5 Contacts in LSDYNA

Most contact types do not check for edge-to-edge penetrations as the search entails only nodal penetration through a segment. This may be adequate in many cases; however, in some unique shell contact conditions, the treatment of edge-to-edge contact becomes very important. There are several ways to handle edge-to-edge contact; the merits/demerits of each one of these methods are discussed below.

CONTACT_AUTOMATIC_GENERAL_EXTERIOR

By default, *CONTACT_AUTOMATIC_GENERAL considers only exterior edges in its edge-to-edge treatment. An exterior edge is defined as belonging to only a single element or segment whereas interior edges are shared by two or more elements or segments. The entire length of each exterior edge, as opposed to only the nodes along the edge, is checked for contact. As with other penalty-based contact types, SOFT=1 can be activated to effectively treat contact of dissimilar materials.

**CONTACT_AUTOMATIC_GENERAL_INTERIOR*

Edge-to-edge contact which includes consideration of interior edges may be invoked in one of two ways. One method takes advantage of the beam-to-beam contact capability of *CONTACT_AUTOMATIC_GENERAL. This labour-intensive approach involves creating null beam elements (*ELEMENT_BEAM, *MAT_NULL) approximately 1 mm in diameter along every interior edge wished to be considered for edge-to-edge contact and including these null beams in a separate AUTOMATIC_GENERAL contact. The elastic constants in *MAT_NULL are used in determining the contact stiffness so reasonable values should be given. Null beams do not provide any structural stiffness. A preferred alternative to the null beam approach, available in version 960, is to invoke the interior edge option by using *CONTACT_ AUTOMATIC_ GENERAL_ INTERIOR. A certain cost penalty is associated with this option.

**CONTACT_SINGLE_EDGE*

This contact type treats edge-to-edge contact but, unlike the other options above, it treats only edge – to – edge contact. This contact type is defined via a part ID, part set ID, or a node set on the slave side. The master side is omitted.

Rigid Body Contact

Components for which deformation is negligible and stress is unimportant may be modeled as rigid bodies using *MAT_RIGID or *CONSTRAINED_ NODAL_ RIG1D_ BODY. The elastic constants defined in *MAT_RIGID are used for contact stiffness calculations. Thus, the constants should be reasonable (properties of steel are often used).

Though there are several contact types in LS-DYNA which are applicable specifically to rigid bodies (RIGID appears in the contact name), these types are seldom used. Any of the penalty-based contacts applicable to deformable bodies may also be used with rigid bodies, and in fact, are generally preferred over the RIGID contact types. Rigid bodies and deformable materials may be included in the same penalty-based contact definition. Constraints and constraint-based contacts may not be used for rigid bodies. Rigid bodies should have a reasonably fine mesh so as to capture the true geometry of the rigid part. An overly coarse mesh may result in contact instability. Another meshing guideline is that the node spacing on the contact surface of a rigid body should be no coarser than the mesh of any deformable part which comes into contact with the rigid body. This promotes proper distribution of contact forces. As there are no stress or strain calculations for a rigid body, mesh refinement of a rigid body has little effect on CPU requirements.

3.6 Elements in LS DYNA

Shell elements used in this study are Belytschko-Lin-Tsay [55] elements. The midsurface of the quadrilateral shell element, or reference surface, is defined by the location of the element's four comer nodes (see Figure 3.1). An embedded element coordinate system that deforms with the element is defined in terms of these nodal coordinates. Then the procedure for constructing the co-rotational coordinate system begins by calculating a unit vector normal to the main diagonal of the element:

$$\hat{e}_3 = \frac{s_3}{\|s_3\|} \quad \text{......} 3.6$$

$$\|s_3\| = \sqrt{s_{31}^2 + s_{32}^2 + s_{33}^2} \quad \text{......} 3.7$$

$$s_3 = r_{31} \times r_{42} \quad \text{......} 3.8$$

where the superscript caret is used to indicate the local (element) coordinate system. It is desired to establish the local x axis $\hat{x}$ approximately along the element edge between nodes 1 and 2. This definition is convenient for interpreting the element stresses which are defined in the local $\hat{x}-\hat{y}$ coordinate system. The procedure for constructing this unit vector is to define a vector s_1 that is nearly parallel to the vector r_{21}, as shown below:

$$s_1 = r_{21} - (r_{21} \cdot \hat{e}_3)\,\hat{e}_3 \quad \text{3.9a}$$

$$\hat{e}_1 = \frac{s_1}{\|s_1\|} \quad \text{3.9b}$$

The remaining unit vector is obtained from the vector cross product

$$\hat{e}_2 = \hat{e}_3 \times \hat{e}_1 \quad \text{3.10}$$

If the four nodes of the element are coplanar, then the unit vectors $\hat{e}_1$ and $\hat{e}_2$ are tangent to the midplane of the shell and $\hat{e}_3$ is in the fibre direction. As the element deforms, an angle may develop between the actual fibre direction and the unit normal $\hat{e}_3$. The magnitude of this angle may be characterized as

$$|\hat{e}_3 \bullet f - 1| < \delta \quad \text{3.11}$$

where, f is the unit vector in the fibre direction and the magnitude of δ depends on the magnitude of the strains. For most engineering applications, acceptable values of δ are on the order of 10^{-2} and if the condition presented in Equation 3.11 is met, then the difference between the rotation of the co-rotational coordinates $\hat{e}$ and the material rotation should be small. The global combination of this co-rotational triad defines a transformation matrix between the global and local element coordinate systems. This transformation operates on vectors with global components $A = (A_x, A_y, A_z)$ and element coordinates components $\hat{A} = (\hat{A}_x, \hat{A}_y, \hat{A}_z)$ and is defined as;

$$\{A\}=\begin{Bmatrix}A_x\\A_y\\A_z\end{Bmatrix}=\begin{bmatrix}e_{1x}&e_{2x}&e_{3x}\\e_{1y}&e_{2y}&e_{3y}\\e_{1z}&e_{2z}&e_{3z}\end{bmatrix}\begin{Bmatrix}\hat{A}_x\\\hat{A}_y\\\hat{A}_z\end{Bmatrix}=[\mu]\{\hat{A}\}=[q]^T\{\hat{A}\} \quad \text{3.12a}$$

where e_{ix}, e_{iy}, e_{iz} are the global components of the element coordinate unit vectors. Transformation from local coordinate system to global coordinate system is defined by the inverse matrix, i.e.;

$$\{\hat{A}\}=[\mu]^{-1}\{A\} \quad \text{3.12b}$$

3.7 Non Linear Dynamics in LS-DYNA

Material Nonlinearity

The next higher level of complexity involves the use of nonlinear relations between stress and strain components. Even when computing displacement gradients to first order, only the higher order material relationship introduces higher order effects in the differential equation. Material nonlinearity might easily be coupled with geometric nonlinearity and drawing a clear boundary between them might be hard in many cases. This kind of nonlinearity introduces new parameters into the differential equation, namely new material constants (i.e., higher order elastic parameters). In many practical cases, we might not have knowledge of these parameters or they might be hard to estimate. Negligence of the second and higher order cross terms ensures that a wave equation is linear. If these terms are neglected in the Taylor expansion of δu, we are still confined to examine only a small neighbourhood around a reference point. Assuming that products of the displacement gradients are small, assures that the principle of superposition is valid. The validity of this principle can be proved by applying two deformations consecutively. The order of application of the deformations has no effect on the final observed deformation. The principle of superposition is a fundamental property of the linear theory of elasticity.

3.8 Energy Absorption Criteria

It is important to analyze the energy absorption by the different components in the vehicle. This can be obtained in the simulation by computing the material internal energies in the model.

The total kinetic energy initially in the model would be given as:

$$E = \frac{1}{2} m \bullet v^2 \qquad \text{..3.13}$$

where:

$m =$ mass of vehicle, $v =$ initial velocity of the vehicle.

Applying equation 3.13 for the study vehicle with m = 1357 kg and velocity v = 13.88 m/s (50 km/hr) results in:

E = 130.7 K Joules

The internal energy of the materials is the sum of Plastic strain energy and the elastic strain energy as shown in Figure 3.2.

3.9 Finite Element Modelling of Traffic Light Pole

Steel poles come in various sizes, shapes and serve different purposes. This study involves two types of luminary poles, (1) Pole Supported on concrete foundation, using base plate, and anchor bolts; (2) Pole embedded in soil. The steel pole considered in this study is modeled using Belytschko-Lin-Tsay shell element with five through-the-thickness integration points. The Belytschko-Lin-Tsay shell elements requires 725 mathematical operations compared to 4066 operations for the under integrated Hughes-Liu element. The selectively reduced integration formulation of the Hughes-Liu element requires 35,367 mathematical operations. Because of its computational efficiency, the Belytschko-Lin-Tsay shell element has been used in this study. The finite element model of the pole consists of 944 quadratic shell elements, 8 laterally and 118 longitudinally property type Belytschko-Lin-Tsay default element in LSDYNA.

Steel and Aluminium Pole Materials are considered in this study with following material properties [56];

1. Aluminium Grade 6063-T5

$\rho = 27$ kN/m^3, E= 69 GPa, $\nu = 0.33$, $\sigma_y = 145$ MPa, elongation at break (plastic strain) is 12%. See idealized stress-strain curve Figure 3.3 (a)

2. Steel

ϱ=78.2 kN/m^3, E= 207 GPa, ν= 0.28, σ_y = 270 MPa, elongation at break (plastic strain) 40%.) See idealized stress-strain curve Figure 3.3 (b)

where: ϱ is mass density, E is modulus of elasticity, ν is Poisson's ratio, σ_y is Yield Stress.

3.10 Finite Element Modelling of Pole Support

Five different configurations of pole supports were analyzed as shown in Figures 3.4 and 3.5. The first support configuration was made of steel plate fixed to concrete foundation using anchor bolts. The second support configuration was same as the first one but with springs installed between the nuts and bolts over and under the steel plate. Third support configuration was same as the second one but with rubber dampers instead of springs. The fourth support configuration was made by embedding the pole into the soil to a certain depth. The fifth configuration (see Figure 3.5) was made of hollow cylindrical or conical rubber base fixed to the pole and the concrete foundation using four anchor bolts. Rubber was modelled using a Blatz-ko rubber element in LS-DYNA. Properties for this rubber material are taken as ϱ=10.63 kN/m^3, E= 2.46 GPa, ν= 0.323, σ_y = 24.7 MPa, elongation at break (plastic strain) 5E08. These values of rubber are same as for car tire properties in car model obtained from (http://www.ncac.gwu.edu/archives/model/index.html). Steel plates were modelled using shell elements while the anchor bolts and nuts were modelled using solid elements.

3.11 Soil - Pole Interaction Modeling

The following subsections explain the methodology used to model the soil pole interaction [57]. In this case shell elements were used to model the embedded part of the pole. Springs were identified at each node in the vertical and horizontal direction of the embedded part as shown in Figure 3.6. Since pole separation is possible under the lateral loads (as shown in Figure 3.7), spring elements were identified to carry compressive forces only.

3.11.1 Lateral Bearing Capacity for Clay.

For static lateral loads the ultimate unit lateral bearing capacity of soft clay P_u has been found to vary between 8c and 12c where c is undrained shear strength of undisturbed clay soil samples [57]. In the absence of more definitive criteria for cyclic loading the following expression is recommended. The value of P_u increases from 3c to 9c as X increases from 0 to X_R according to:

$$P_u = 3c + \Upsilon' X + J c X / D \qquad 3\text{-}14$$

and

$$P_u = 9\,c \text{ for } X \geq X_R \qquad 3\text{-}15$$

where:

P_u is the ultimate resistance, in force/unit length, c is the undrained shear strength of undisturbed clay soil samples, in stress units, D is the pole diameter, γ' is the buoyant unit weight of soil, in weight density units, J dimensionless empirical constant with values ranging from 0.25 to 0.5, determined by field testing. For this study it has been taken as 0.5, X is depth below soil surface; X_R is depth below soil surface to bottom of reduced resistance zone.

For a condition of constant strength with depth, Equations 3-14 and 3-15 are solved simultaneously to give:

$$X_R = 6D / ((\gamma' D / c) + J) \qquad \textbf{3-16}$$

Where the strength varies with depth, Equations 3-14 and 3-15 may be solved by plotting the two equations, i.e., P_u vs. depth. The point of first intersection of two equations is taken to be X_R. These empirical relationships may not apply where strength variations are erratic. In general, minimum values of X_R should be about 2.5 pole diameters. Lateral soil resistance-deflection relationships for poles in soft clay are generally nonlinear.

Lateral resistance P can be obtained from the equation:

$$P = 0.5\, P_u\, (y/y_c)^{1/3} \qquad \textbf{3.17}$$

where:

P is the actual lateral resistance of soil, in force / unit length, y is the actual lateral deflection, y_c equals 2.5 ε_c D, ε_c is the strain which occurs at one-half the maximum stress on laboratory undrained compression tests of undisturbed soil samples [57] (see table 3.2) and D is the pole diameter. For static lateral loads, the ultimate bearing capacity, P_u, of stiff clay (c > 96 kPa) varies between 8c and 12c. Due to rapid deterioration under cyclic loadings, the ultimate static resistance should be reduced for cyclic design considerations. While stiff clays also have nonlinear stress-strain relationships, they are generally more brittle than soft clays. In developing the stress-strain curves and subsequent p-y curves for cyclic loads, consideration should be given to the possible rapid deterioration of load capacity at large deflections for stiff clays.

3.11.2 Lateral Bearing Capacity for Sand

The ultimate lateral bearing capacity for sand has been found to vary from a value at shallow depths determined by Equation 3-18 to a value at deep depths determined by Equation 3-19. At a given depth the equation giving the smallest value of P_u should be used as the ultimate bearing capacity.

$$P_{us} = (C_1X + C_2D)\,\gamma' X \qquad \text{3-18}$$

$$P_{ud} = C_3\,D\,\gamma'\,X \qquad \text{3-19}$$

Where P_u is the ultimate resistance (force/unit length), (s=shallow, d=deep), γ' is the buoyant soil weight, in weight density units, X is depth, C_i Coefficient determined from Figure 3-8 as a function of Φ', Φ' is angle of internal friction, and D is the average pole diameter from ground level to the bottom of the pole.

The lateral soil resistance-deflection (p-y) relationship for sand is also nonlinear and in the absence of more definitive information for cyclic loading. The following expression can be used for lateral resistance at a depth X:-

$$P = 0.9\ Pu\ \tanh\left[(k\ X\ y)/\ (A\ P_u)\right] \qquad 3\text{-}20$$

Where P_u is the ultimate bearing capacity at depth X in units of force per unit length, k is the initial modulus of subgrade reaction in force per volume units determined from Figure 3.9 as a function of the angle of internal friction (Φ'), y is the lateral deflection, and X is the depth below ground level.

Figures 3.10 to 3.13 show horizontal spring constants used in this study. Vertical subgrade reaction is taken as 10% of above values.

3.12 Car and Analysis Selection

NCHRP- 820C [5] test criteria recommends use of a small car around 820 kg weight in crash testing. If this car can pass the lateral impact with the pole then the larger would also pass by virtue of its stronger structure. In this study the finite element model of Ford Taurus 1991 Car has been used as obtained from (http://www.ncac.gwu. edu/archives/model/index.html), and this model has been validated for pole impact testing by field test done at EASi Engineering [59]. This model consists of 30357 elements (140 beam elements, 23997 shell Elements, 4750 triangular elements, 1107 hexagonal elements, 10 wedge elements, and 2 spring elements, 91 rigid bodies). View of the finite element model of the car is shown in Figure 3.14.

3.13 Car Model and Fidelity of the EASi Ford Taurus Model:

A finite element simulation of the Ford Taurus impacting a rigid pole with the Side Impact Dummy (SID) model in the driver-side seat was performed to assess performance and validity of the models by EASi [58]. The simulation was compared to two tests that were conducted at the Federal Outdoor Impact Laboratory (FOIL) and sponsored by the National Highway Traffic Safety Administration (NHTSA). The test conditions are listed below in Table 3.3. The impact location, 1,150-mm rearward of the front axle, corresponds to point on the door midway between the steering wheel and the SID chest. Since results from other tests on vehicle impact with traffic poles are yet unavailable, the finite element used in this study has not been verified except for convergence in output.

3.14 Parametric Study:

Two types of round poles, made of Steel and Aluminium, with bottom diameter of 280 mm, top diameter of 130 mm, and height of 10.52 m (above ground level) were crash simulated using LSDYNA 3D. The thicknesses of the pole walls were 3.05 mm and 3.9 mm for steel and aluminium pole, respectively. These poles were simulated for Front and Side Impact crashes. Four different soil conditions were considered in this study (i.e. stiff clay, soft clay, loose sand, and dense sand). Figures 3.10 and 3.11 show the lateral spring coefficient as a function of the lateral deflection for dense sand and loose sand, respectively, at certain depths of the embedded length of the pole. Figures 3.12 and 3.13 show similar relationships for soft clay and stiff clay, respectively. Pole embedded in such soils was simulated for four embedment depths viz. 900 mm, 1100 mm, 1300 mm, and 1500 mm for both front and side impact scenarios. Nine different rubber bases were simulated for front and side impact crash scenarios as shown in Table 3.1.

CHAPTER 4

RESULTS

4.1 General

Vehicle crash with traffic light poles was performed for the first 100 ms of impact using the nonlinear finite-element code LS-DYNA. The vehicle model was given initial velocity of 50 km/hr for frontal impact and a 90° side impact, except as otherwise noted in the following sections. The pre-processor used was LSDYNA FEMB v 27 (reference). The average CPU time varied from 24 hrs to 32 hrs for each run. The post processor used was LS-POST v 2.0 release 2. The following sub-sections show a summary of the results in terms of accelerations, displacements and energy absorption by different structural elements. The effects of key parameters on these straining actions were reported for both frontal and side impact. There parameters included the types of support configuration, depth of pole embedded in soil, pole material type, frontal and side impact conditions, and soil condition.

4.2 Frontal Impact

4.2.1 Effect of Pole Support Configurations

To study the effect of the types of support configurations shown in Figure 3.4, the vehicle model was given an initial velocity of 60 km/hr to impact the pole from the front side. Figure 4.1 shows deformations of both the vehicle and the pole at different time increments for pole support fixed to the concrete foundation. While the shapes of the steel pole embedded in soil before and after the crash are shown in Figure 4.2. Figure 4.3 shows energy absorbed by the pole material for different support configurations, shown in Figure 3.4, when impacted under the same conditions. It should be noted that the embedment length of the pole into soil was taken 1.5 m and the soil properties were of those for loose sand. At 7 ms, it was observed the anchor bolts utilized in the first support type (Figure 3.4.a) fractured at the ground level, shearing the steel base plate away from the ground in the same direction of vehicle motion. Then, the pole was laid on the vehicle at a higher time increment. It should be noted that this support type is specified by the Canadian Bridge Design Code [2] for Canadian highways. In the second support type, where the springs were utilized between the bolts over and under the steel base plate (Figure 3.4.b), the base plate also fractured and sheared away from the ground. Similar behavior was observed in case of the third support type where rubber pads were considered (Figure 3.4.c). However, in the fourth support type, where the steel pole was embedded in the soil (Figure 3.4.d), the steel pole was observed to be highly deformed and did not fall down.

Figure 4.3 shows the time-history of the change of the absorbed energy by the pole for all the support types considered in this study. It can be observed that the pole embedded in soil absorbed 68 kJ while the pole with fixed supports absorbed about 20 kJ (about 3.5 times higher that the former). Other support configurations with springs and dampers shown in Figure 3.4 did not show any considerable change in energy absorption characteristics of pole when compared to the pole with fixed supports. This may be attributed to the high deformation occurred in the pole as a result of the impact.

4.2.2. Effect of Soil Types

Figure 4.4 shows a comparison of energy absorbed by steel pole in a frontal impact at a speed of 50 km/hr, for first 100ms of the impact for different types of soils considered in this study (e.g. dense sand, loose sand, stiff clay, and soft clay). It can be observed the energy absorbed by pole embedded in soft clay was the highest among other soil types, followed by that for loose sand. It can also be observed that irrespective of soil dynamic properties, the pole embedded in soil provides significant energy characteristics in frontal impact when compared to the case of pole fixed to concrete foundation. For example, at 100 ms, the energy absorbed by the pole embedded in soft clay, loose sand, stiff clay and dense sand were 100%, 50 %, 50%, and 25% more that for pole fixed to the concrete foundation, respectively.

Figure 4.5 compares relative distance between a point on the steering wheel and the corresponding point on the driver's seat in frontal impact scenario. It can be observed that the maximum relative displacement between these two locations in case of pole with fixed support and poles embedded in soft clay, Stiff clay, dense sand, and loose sand after 100 ms of impact were 225 mm, 300 mm, 300 mm, 320 mm, and 320 mm, respectively. Values were noted to be higher in case of sandy soil than in case of clayey soil. However the pole with fixed support to the concrete foundation showed the least movement since the bolts were sheared at early stage of impact. Figure 4.6 compares the acceleration at a point on the driver's seat for the case of pole with fixed support and pole embedded in sandy and clayey soils. It can be observed that peak values of accelerations were 50 g, 30 g, 35 g, 32 g (where g is acceleration due to gravity = 9.81 m/s^2) for pole with fixed support and poles embedded in soft clay, dense sand, and loose sand respectively. It is observed that acceleration values in case of soil embedded poles are within the acceptable value by different protocols (50g). However, the acceleration values in case of fixed support are close to limit.

4.3 Side Impact

The finite-element simulation was performed using the non-linear FE code LS-DYNA to impact the pole with a vehicle at an initial velocity of 50 km/hr to in side impact scenarios. Figure 4.7 shows deformations of both the vehicle and the pole, with fixed support to the concrete foundation, at different time increments during impact. It is observed that at 25 ms, anchor bolts started to yield. At 50 ms, the front passenger side tire had lifted above the ground and vehicle began to yaw. At 75 ms, the roof beam bent, the vehicle yaw was considerable, the anchor bolts were about to fracture and the pole intruded the passenger compartment. Figure 4.8 shows deformations of both the vehicle and the pole embedded in soil at different time increments during impact. It should be noted that the impact point in case of side impact simulations was 1150 mm rearward of front axle.

Figure 4.9 compares energy absorbed, during the first 100 ms of impact, by steel pole supported on anchor bolts, embedded 1500 mm in dense sand, loose sand, stiff clay, and soft clay. It can be observed that the maximum values of the absorbed energy were 5 kJ, 11 kJ, 16 kJ, 14 kJ, and 17 kJ for pole fixed to concrete foundation and poles embedded in dense sand, loose sand, Stiff clay and soft clay, respectively. Pole embedded in soft clay is found to be absorbing energy about 3.5 times more than the pole fixed to concrete foundation. This may be attributed to the high deformation occurred in the pole embedded in soil as a result of the impact. Figure 4.10 compares distance between a point on the driver's door and the corresponding point on the driver's seat (intrusion). It can be observed that the maximum relative displacement between these two points (the intrusions) were recorded as 350 mm, 325 mm, 310 mm, 290 mm, and 260 mm for pole with fixed support to concrete foundation and poles embedded in Stiff clay, dense sand, soft clay and loose sand respectively. A general trend of relative displacement history was observed for all types of support configuration. However, the relative displacement in case of pole fixed to the concrete foundation is the highest among others due to the lesser outward deformation occurred in the pole compared to poles embedded in soil. This entails more inward deformation in the side door when impacted by pole fixed to concrete foundation, and less inward deformation in the side door when impacted by the poles embedded in soil.

Figure 4.11 compares acceleration at a point in the driver's seat for different soil parameters, indicating a likely change in acceleration endured by the occupant. It can be observed that the maximum values of accelerations observed were 200 g, 200 g, 160 g, 100 g, and 200 g for the cases of pole embedded in dense sand, stiff clay, loose sand, and soft clay, respectively. It can be observed that the acceleration values in all the cases are more than the acceptable value. This may ob attributed to the fact that the vehicle doors are weak when impacted normal to their plane. It is also interesting to note that acceleration achieves a sudden peak in time window of 25ms to 45ms, and then immediately dies when time progresses. This is the time period when energy absorption begins to increase after an initial flat curve (see Figure 4.9). Figure 4.12.a compares decay of kinetic energy of the system in frontal and side impact conditions. While Figure 4.12.b shows difference in kinetic energy dissipated by the system for frontal and side impacts. It can be observed that approximately up to the 35 ms from the initial impact, both systems loose kinetic energy at the same rate. While from about 35 ms to 80 ms the system in front impact condition lost energy more than that in case of side impact conditions, after which the system performed with almost similar rate of energy dissipation.

In conclusion, it is observed that for both side and frontal impact conditions, the pole embedded in the soft clayey soil absorbed much more energy than the pole fixed to concrete foundation using anchor bolts. Also, it can be observed that the energy absorbed by the steel pole in case of frontal impact was generally higher than that in case of side impact. This may be due to the fact that vehicle door deformed considerably, absorbing more energy to the extent that the steel pole is not affected as in the case of frontal impact. Simulation showed that nodes on driver car seat exhibited resultant accelerations more that 100 g, when car impacted pole sideways.

4.4 Effect of Embedment Depth

4.4.1 Side Impact

Figure 4.13.a compares energy absorbed by the steel pole embedded in soft clay for various embedment depths during side impact. It was observed that energies absorbed by the pole for embedment depths of 700 mm, 900 mm, 1100 mm, 1300 mm,

and 1500 mm were recorded as 11 kJ, 13 kJ, 15 kJ, 16 kJ, and 17 kJ respectively. Figure 4.13.b compares energy absorbed by the steel pole embedded in Stiff clay for various embedment depths during side impact. It was noted that energies absorbed by the pole for embedment depths of 700 mm, 900 mm, 1100 mm, 1300 mm, and 1500 mm were found to be 8 kJ, 11 kJ, 11 kJ, 13 kJ, and 16 kJ respectively. Figure 4.13.c compares energy absorbed by the steel pole embedded in loose sand for various embedment depths during side impact. Energies absorbed by the pole of embedment depths of 700 mm, 900 mm, 1100 mm, 1300 mm, and 1500 mm were recorded as 8 kJ, 10 kJ, 11 kJ, 14 kJ, and 14 kJ respectively. Figure 4.13.d compares energy absorbed by steel pole embedded in dense sand for various embedment depths during side impact. It was observed that energies absorbed by the pole of embedment depths of 700 mm, 900 mm, 1100 mm, 1300 mm, and 1500 mm were found to be 3 kJ, 4 kJ, 11 kJ, 11 kJ, and 11 kJ respectively. From the above-mentioned observations, it was found that the pole with embedment depth of 1500 mm absorbed more energy than other poles of less embedment depths. Also the pole with embedment depth of 700 mm was the least effective in contributing to energy absorption.

Figure 4.14 (a) compares the intrusion of passenger compartment for varied types of soil, for pole with embedment depth of 900 mm in side impact. The maximum values of intrusion obtained for dense sand, loose sand, stiff clay, soft clay, and for pole with fixed support to the concrete foundation were recorded as 750 mm, 600mm, 650 mm, 590 mm, and 725 mm respectively. Figure 4.14.b shows similar results but for 1100 mm embedment depth. The maximum values of intrusion obtained for dense sand, loose sand, stiff clay, soft clay, and pole with fixed support to the concrete foundation were observed to be 700 mm, 625 mm, 690 mm, 550 mm, and 700 mm respectively. Figure 4.14.c compares the intrusion of passenger compartment for varied types of soil, for pole depth of 1300 mm. The maximum values of intrusion obtained for dense sand, loose sand, stiff clay, soft clay, and for pole with fixed support to the concrete foundations were found to be 725 mm, 650mm, 700 mm, 590 mm, and 725 mm respectively. Figure 4.14.d shows similar results but for embedment depth of 1500 mm. The maximum values of intrusion obtained for dense sand, loose sand, stiff clay, soft clay, and pole with fixed support to the concrete foundation were obtained as 725 mm, 400mm, 600 mm, 600 mm, and 725 mm respectively. From the above-mentioned observations, it can be noted that soft clayey soil is generally found to be the most effective in containing intrusion of passenger compartment to relatively lower levels. Also, it can be observed that the intrusion decreases with the decrease on the embedment depth. This may be attributed to the fact that the smaller the embedment length, the larger the lateral deformation of the pole.

Figure 4.15 shows the locations of nodes number 523, 1317, 19589, 708, and 1122 at the driver's door for which accelerations are compared for different pole-soil-depth combinations. Figures 4.16.a compares acceleration at node number 523 for the steel poles of different embedment depths in dense sand. Absolute peak acceleration values were observed as 1500 g, 4242 g, 853 g, and 995 g for embedment depths of 1500 mm, 1300 mm, 1100 mm, and 900 mm, respectively. Figure 4.16.b shows similar results at node number 1317. Absolute peak acceleration values were found to be 554 g, 759 g, 650 g, and 538 g for embedment depths in dense sand of 1500 mm, 1300 mm, 1100 mm, and 900 mm, respectively. Figure 4.16.c compares acceleration-time history at node number 19589 for steel pole embedded in dense sand. Absolute peak acceleration values were recorded as 263 g, 681 g, 2698 g, and 2167 g for embedment depths in dense sand of 1500 mm, 1300 mm, 1100 mm, and 900 mm, respectively. Figure 4.16.d compares acceleration sat node number 708 for the steel pole embedded in dense sand. Absolute peak acceleration values were recorded as 576 g, 510 g, 555 g, and 1188 g embedment depths in dense sand of 1500 mm, 1300 mm, 1100 mm, and 900 mm, respectively. Figure 4.16.e shows similar results at node number 1122. Absolute peak acceleration values were observed to be 646 g, 2629 g, 809 g, and 765 g embedment depths in dense sand of 1500 mm, 1300 mm, 1100 mm, and 900 mm, respectively. Figures 4.17, 4.18, and 4.19 show acceleration-time histories at the driver's door for the steel pole embedded 1500 mm, 1300 mm, 1100 mm, and 900 mm, in loose sand, stiff clay and soft clay, respectively. It is generally noted that the acceleration values at node number 19589, a nodal point directly on the impact surface, were very high in the first 10 to 20 ms, and then died out immediately to very low values for the rest of the 100 ms, whereas other nodes exhibit a fair distribution of acceleration values. Also, it can be noted that peak acceleration values are more than the norm of 50 g's associated with crash testing.

4.4.2 Frontal Impact

4.5 Effect of Pole Material Type

Results in previous section showed that steel pole embedded 1500 mm in soil absorbed most energy as compared to other shallower embedment depths. An aluminium pole identical to steel pole in geometry was crash simulated for 100 ms. Results from vehicle impact with steel and aluminium poles embedded in soil were then compared. Figure 4.20 shows comparison of the energy absorbed by aluminium pole embedded 1500 mm in soft clayey soil to that absorbed by the steel pole. It can be observed that the absorbed energy values after 100 ms of the impact were 17 kJ and 40 kJ for the steel and aluminium poles, respectively; an increase of 2.5 times for aluminium pole. Figure 4.21 show a comparison of the energy absorbed by the aluminium pole embedded 1500 mm in stiff clayey soil to that absorbed by the steel pole of similar geometry. The peak absorbed energy values were obtained as 15 kJ and 30 kJ for steel and aluminium poles, respectively; an increase of 2 times for aluminium pole. Similar behaviour was observed as shown in Figures 4.22, and 4.23 for loose sand and dense sand, respectively.

Results were also investigated to examine nodal accelerations and intrusion of passenger compartment in side impact of steel and aluminium poles. Figure 4.24.a presents comparison between the acceleration at the roof beam level experienced by the vehicle when impacted at 90° angle to the driver's door for a pole embedded 1500 mm in dense sand. Results show that the side impact with the steel pole induced peak acceleration of about 250 g while it was about 25 g in case of aluminium pole. Figure 4.24.b compares acceleration-time history at the roof beam level experienced by the car when impacted normal to the driver's door in case of poles embedded 1500 mm in loose sand. Results show that impact with steel pole induces accelerations of about 120 g, while aluminium pole produced a peak acceleration of about 70 g. Figure 4.25 compares acceleration at a node on the B pillar, for steel and aluminium pole impacted sideways by a car. Results show that accelerations levels were around 240 g and 170 g for steel and aluminium poles, respectively. These results indicate that aluminium pole is as twice effective in energy and acceleration aspects of crash as the steel pole.

A comparative study was conducted to investigate the effect of embedment depth on intrusion of passenger compartment, the accelerations and absorbed energy when the aluminium pole was side impacted by a car. Figure 4.26.a compares the effects of embedment depth on energy absorbed by the aluminium pole. Energy absorbed was found to be 25 kJ, 26 kJ, 27 kJ, 28 kJ, and 30 kJ for embedment depths of 700 mm, 900 mm, 1100 mm, 1300 mm, and 1500 mm, respectively, in case of stiff clay. Pole embedded in loose sand absorbed 25 kJ, 26 kJ, 27 kJ, 30 kJ, and 32 kJ for embedment depths of 700 mm, 900 mm, 1100 mm, 1300 mm, and 1500 mm, respectively, as shown in Figure 4.26.b. Aluminium pole embedded in dense sand absorbed 32 kJ, 32 kJ, 36 kJ, 38 kJ, and 38 kJ for embedment depths of 700 mm, 900 mm, 1100 mm, 1300 mm, and 1500 mm, respectively, as shown in Figure 4.26.c. While aluminium pole embedded in soft clay absorbed 26 kJ, 26 kJ, 32 kJ, 36 kJ, and 37 kJ for embedment depths of 700 mm, 900 mm, 1100 mm, 1300 mm, and 1500 mm, respectively, as shown in Figure 4.26.d. In general, similar behaviour was observed for aluminium poles as in case of steel poles studies earlier; the absorbed energy by the pole increase wit increase in the embedment depth. However more energy absorption was observed in case of the aluminium pole.

Figure 4.27.a shows comparison of the intrusion of the passenger compartment for varied types of soil, for pole depth of 900 mm. It can be observed that the maximum values of intrusion obtained for dense sand, loose sand, stiff clay, soft clay, and pole with fixed support were 210 mm, 180mm, 200 mm, 180 mm, and 500 mm,

respectively. Figure 4.27.b compares the intrusion of the passenger compartment for varied types of soil, for pole with embedded depth of 1100 mm. The maximum values of intrusion obtained for dense sand, loose sand, stiff clay, soft clay, and pole with fixed support to concrete foundation were found as 210 mm, 200 mm, 220 mm, 200 mm, and 500 mm, respectively. Figure 4.27.c compares the intrusion of the passenger compartment for varied types of soil, for pole embedded depth of 1300 mm. Maximum values of the intrusion obtained for dense sand, loose sand, stiff clay, soft clay, and pole with fixed to the concrete foundation were recorded as 220 mm, 200mm, 220 mm, 200 mm, and 500 mm respectively. Similar results were recorded in Figure 4.27.d for the intrusion of the passenger compartment for varied types of soil, for pole depth of 1500 mm. It can be observed that the maximum values of the intrusion obtained for dense sand, loose sand, stiff clay, soft clay, and pole fixed to the concrete foundation were 220 mm, 200 mm, 220 mm, 200 mm, and 500 mm respectively. From the above-mentioned observations, it can be concluded that in contrast to the case of steel pole, the change in embedment depth for aluminium poles considered in this study has insignificant effect on the peak intrusion within the first 100 ms of side impact. Also, it can be observed that aluminium pole embedded in soil resulted in about half as much intrusion of the passenger compartment as that for the aluminium pole fixed to the concrete foundation.

Carrying on the investigation a bit further, nodal accelerations at five nodes numbers 523, 1317, 19589, 708, and 1122 shown in Figure 4.15 were also compared as previously presented for the aluminium pole. Figure 4.28.a compares the acceleration-time history at node number 523 for pole embedded 1500 mm, 1300 mm, 1100 mm, and 900 mm, in dense sand. Absolute peak acceleration values were observed to be 1729 g, 3735 g, 3165 g, and 1588 g, respectively. Figure 4.28.b compares accelerations with time at node number 1317 for the aluminium pole embedded 1500 mm, 1300 mm, 1100 mm, and 900 mm, in loose sand. Absolute peak acceleration values were recorded as 2393 g, 2781 g, 3791 g, and 3253 g, respectively. Figure 4.28.c compares accelerations at node number 19589 for the aluminium pole embedded 1500 mm, 1300 mm, 1100 mm, and 900 mm, in dense sand. Absolute peak values observed are 448 g, 3296 g, 527 g, and 2721 g, respectively. Figure 4.28.d compares accelerations at node number 708 for the aluminium pole embedded 1500 mm, 1300 mm, 1100 mm, and 900 mm, in dense sand. Absolute peak acceleration values were obtained as 496 g, 477 g, 666 g, and 715 g, respectively. Figure 4.28.e compares acceleration at node number 1122 for the aluminium pole embedded 1500 mm, 1300 mm, 1100 mm, and 900 mm, in dense sand. Absolute peak acceleration values were observed as 619 g, 2624 g, 576 g, and 532 g, respectively. Figures 4.29, 4.30, and 4.31 shows similar results for loose sand, stiff clay and soft clay, respectively. Similar to the behaviour of the steel pole in side impact, it is generally noted that the acceleration values at node number 19589, a nodal point directly on the impact surface, were very high in the first 10 to 20 ms, and then died out immediately to very low values for the rest of the 100 ms, whereas other nodes exhibit a fair distribution of acceleration values. Also, it can be noted that peak acceleration values are more than the norm of 50 g's associated with crash testing. Figure 4.32 (a) compares displacement of a node, lying on steel pole, on the contact surface of the pole and car in side impact for various embedment depths of pole in loose sand. Such displacement values obtained are 275 mm, 225 mm, 180 mm, and 140 mm for embedment depths of 1500 mm, 1300 mm, 1100 mm, and 900 mm. respectively. Figure 4.32 (b) compares displacement of a node, lying on steel pole, on the contact surface of the pole and car in side impact for various embedment depths of pole in dense sand. Such displacement values obtained are 55 mm, 59 mm, 62 mm, and 32 mm for embedment depths of 1500 mm, 1300 mm, 1100 mm, and 900 mm. respectively. Figure 4.32 (c) compares displacement of a node, lying on steel pole, on the contact surface of the pole and car in side impact for various embedment depths of pole in soft clay. Such displacement values obtained are 225 mm, 260 mm, 325 mm, and 265 mm for embedment depths of 1500 mm, 1300 mm, 1100 mm, and 900 mm. respectively. Figure 4.32 (d) compares displacement of a node, lying on steel pole, on the contact surface of the pole and car in side impact for various embedment depths of pole in stiff clay. Such displacement values obtained are 155 mm, 152 mm, 165 mm, and 165 mm for embedment depths of 1500 mm, 1300 mm, 1100 mm, and 900 mm.

respectively. Figure 4.33 (a) compares displacement of a node, lying on aluminium pole, on the contact surface of the pole and car in side impact for various embedment depths of pole in loose sand. Such displacement values obtained are 875 mm, 875 mm, 900 mm, and 920 mm for embedment depths of 1500 mm, 1300 mm, 1100 mm, and 900 mm. respectively. Figure 4.33 (b) compares displacement of a node, lying on aluminium pole, on the contact surface of the pole and car in side impact for various embedment depths of pole in dense sand. Such displacement values obtained are 810 mm, 815 mm, 820 mm, and 820 mm for embedment depths of 1500 mm, 1300 mm, 1100 mm, and 900 mm. respectively. Figure 4.33 (c) compares displacement of a node, lying on aluminium pole, on the contact surface of the pole and car in side impact for various embedment depths of pole in soft clay. Such displacement values obtained are 880 mm, 880 mm, 900 mm, and 925 mm for embedment depths of 1500 mm, 1300 mm, 1100 mm, and 900 mm. respectively. Figure 4.33 (d) compares displacement of a node, lying on aluminium pole, on the contact surface of the pole and car in side impact for various embedment depths of pole in stiff clay. Such displacement values obtained are 825 mm, 825 mm, 850 mm, and 900 mm for embedment depths of 1500 mm, 1300 mm, 1100 mm, and 900 mm. respectively.

Figure 4.34 compares energy absorbed by steel and aluminium poles embedded 1500 mm in soft clay. Peak values observed are 22 kJ and 33 kJ for steel and aluminium poles respectively. Interestingly aluminium pole though absorbing lesser energy is absorbing at a faster rate until first 55 ms of impact and steel pole is absorbing more afterwards. Figure 4.35 compares relative displacement between centre of steering and a point on seat for steel and aluminium poles embedded 1500 mm in soft clay. This displacement is observed to be 300 mm and 220 mm for steel and aluminium poles respectively. For aluminium pole this displacement is observed to be fairly constant after 75 ms of impact, whereas in case of steel pole the distance between seat and steering is still closing. Figure 4.36 compares displacement of a node on point of impact. Steel pole has moved less than aluminium pole. Values observed are 450 mm and 680 mm respectively. Further figure 4.37 compares decay of kinetic energy for the steel and aluminium poles system. We observe that the case of steel pole is decaying energy at a faster rate than aluminium pole. Interestingly rate of decay is constant till 35 ms for both the cases after which steel pole system is decaying faster than aluminium pole, i.e. steel pole is providing more resistance than aluminium pole.

4.6 Effect of Rubber Base on Crash Characteristics of Steel Pole

Different geometries of rubber base, as shown in Figure 3.5 and Table 3.1, were used in the finite-element simulation of vehicle crash with steel poles. The point of contact between the vehicle and the case was 1150 mm behind the front axle for side impact and 450 mm above ground level. While in case of frontal impact the point of impact was located at the centre of front bumper. Figure 4.32 show views of the simulation of steel pole supported over a cylindrical rubber base when during impact on the driver's side. Figure 4.33 shows similar views but in case of conical rubber base. It can be observed that the car was significantly deformed and a bending-shear motion is observed in the rubber base, during side impact with car travelling at a speed of 50 km/hr.

Figure 4.34 shows the absorbed energy by the steel pole supported over rubber base of different configurations, in frontal impact. Peak absorbed energy value obtained for rubber case 1, case 4, and case 7 shown in Table 3.1 was observed to be around 4 kJ for each case. It should be noted that the height of the rubber base for cases 1, 4 and 7 was 500 mm. For rubber support cases 2, 5, and 8, the peak absorbed energy value was found to be 8 kJ. It should be noted that the height of the rubber base for cases 2, 5 and 8 was 350 mm. For rubber support cases 3, 6, and 9, the absorbed energy was 9 kJ, 9.5 kJ, and 10 kJ, respectively. It should be noted that the height of the rubber base for cases 3, 6 and 9 was 200 mm. It can be observed that the energy absorbed by the steel pole increases with the decrease in the height of the rubber base. This may be attributed to the fact that the steel pole was directly impacted by the vehicle when the height of the rubber base is 500 mm. However, the pole was impacted at 100 mm over the front bumper location when the height of the rubber base is 350 mm and at 250 mm over the front bumper of the car when the height of the rubber base is 200 mm.

Interestingly significant energy absorption is observed only after first 30 ms, till then all cases exhibit same energy absorption. This 30 ms time interval is interesting to all the cases (studied in previous sections), wherein energy absorption curves is alike. Figure 4.35 compares acceleration at centre point of steering, between the nine rubber bases cases crash simulated. Absolute maximum acceleration values observed for case 1, 2, 3, 4, 5, 6, 7, 8, and 9 are 161 g, 296 g, 228 g, 93 g, 512 g, 276 g, 175 g, 154 g, and 120 g, respectively, with case # 4 having a least value of 93 g. These values are compared to the values obtained in the case of steel pole embedded in soft clayey soil and fixed on base plate. Figure 4.36 shows this comparison. It is observed that pole supported on rubber base case # 9 is exhibiting lowest acceleration levels at the centre of steering. Figure 4.37 compares change in distance between centre point of steering and corresponding point on seat. For case 1 to 9 values are .We observe that this distance varies by around 200mm (8") to 250 mm (10"). This distance is almost same for all the cases studied. Figure 4.38 compares this relative distance for case # 6, steel pole fixed on base plate using anchor bolts and embedded 1500 mm in soft clayey soil, in frontal impact. Maximum relative displacement observed is 200 mm, 225 mm, and 300 mm respectively. Figure 4.39 compares acceleration at a point on driver's seat for steel pole supported on rubber base and supported on fixed base. We observe peak values for each case to be 30 g and 45 g respectively. This shows a decrease of almost 33% in acceleration value by using a rubber base supported pole. Interestingly the curve for rubber base supporting pole is following the pattern of other two curves up to 55 ms after which there is a sudden decrease in the rate of increase of such displacement and is observed to have least maximum value of displacement in all the cases considered during the 100 ms time period.

Figure 4.40 compares energy absorbed by steel pole, in side impact, for all the nine rubber base supported steel poles, impacted at 50 km/hr speed. Peak energy absorbed in case 1, case 2, case 3, case 4, case 5, case 6, case 7, case 8, and case 9 energy absorbed is 0.1 kJ, 0.11 kJ, 0.11 kJ, 0.1 kJ, 0.12 kJ, 0.11 kJ, 0.07 kJ, 0.07 kJ, and 0.06 kJ respectively. We observe that pole is not absorbing a considerable energy in case of side impact when compared with frontal impact. This low energy absorption could be due to non interaction of the pole and car, and also we are observing that side impact is relatively absorbing much less energy in comparison to frontal impact. This could also be due to the fact that car is as much laterally stiff as it is longitudinally. The case of side impact is like a bending and twisting of car around its weaker axis. Carrying analysis further acceleration at roof beam level for side impact case is compared for all of these nine cases. Figure 4.41 (a) compares acceleration at a point on the roof beam level for case 1 to 3. Absolute peak values observed are 180 g, 300 g, and 210 g respectively. Figure 4.41 (b) compares acceleration at a point on the roof beam level for case 4 to 6. Absolute peak values observed are 90 g, 500 g, and 250 g respectively. Figure 4.41 (c) compares acceleration at a point on the roof beam level for case 7 to 9. Absolute peak values observed are 160 g, 150 g, and 120 g respectively. Case number 4 is observed to be generating least acceleration of 90 g among all the cases. Figure 4.42 compares intrusion of passenger compartment for case number 1 to 9. Maximum intrusion observed at 100 ms is 700 mm, 640 mm, 650 mm, 640 mm, 690 mm, 690 mm, 650 mm, 690 mm, and 700 mm. We observe that the intrusion is independent of rubber base geometry. Figure 4.43 compares intrusion of passenger compartment for the cases of steel pole supported on base plate, embedded 1500 mm in soft clayey soil, and supported on a rubber base. We observe that the case of fixed support is still causing less intrusion followed by rubber base case # 4 and pole embedded in soft clay with maximum intrusion. Figure 4.44 (a) compares decay of kinetic energy in the case of rubber base supported pole and supported on a fixed steel base plate. Interestingly energy dissipated in rubber base is more than the case of fixed steel base supported pole. Figure 4.44 (b) shows relative difference between energy absorbed for both the cases. It is observed that the rubber base system is absorbing energy at a higher rate and much faster than the case of fixed support.

CHAPTER 5

CONCLUSIONS & RECOMMENDATIONS FOR FUTURE RESERACH

5.1 Conclusions

Vehicle crash simulations were conducted for both side and frontal impacts with steel and aluminium poles. Based on results from this study, the following conclusions were drawn:

1- Aluminium poles are found to be more energy absorbing as compared to steel poles.

2- Embedding pole in soft clayey soil rather than using the conventional breakaway steel base over concrete foundation, as specified by the Canadian Highway Bridge Design Code [2], was found to be favourable in absorbing the energy resulting from vehicle-steel pole crash for frontal impact and side impact scenarios.

3- In side impact the energy absorbed by a pole is almost 10% of what it absorbed during frontal impact suggesting that the vehicle is not laterally stiff enough to induce sufficient deformations in pole and thus energy absorbed by pole is far less than that in case of frontal impact. Car stiffness should be increased laterally by using stronger side impact beams, stronger roof perimeter beam and underside of car.

4- Side impact crash has proved the most critical case since occupant accelerations and movement are more significant and deformations in the vehicle passenger compartment is severe, when compared to the case of frontal impact crash with steel pole.

5- Aluminium pole embedded in clayey soil has been observed to cause less intrusion of passenger compartment by approximately 500 mm.

6- Rubber-base is reducing the accelerations at various levels in car but found to be non-effective in terms of energy absorbed by pole. This needs further research.

7- It could also be concluded that fixed support case is more effective in limiting passenger compartment intrusion. This needs to be further investigated.

5.2 Recommendations for Future Research

1- We were able to successfully model and simulate Car-Pole crashes using LS-Dyna and get various deformations and other results but validation of finite element models is a critical aspect which cannot be overlooked. Validation of results provides much more insight into the problem, thereby, refining the model and hence more realistic results.

2- Currently, simulations FRP (Fibre Reinforced Polymer) poles in both side and frontal impacts are underway. The key issue in the computer simulation is to develop accurate models to evaluate the amount of energy absorbed by the pole and determine the time rate of energy transferred and sudden acceleration induced to the occupants. Impact performance of the existing poles and proposed pole systems will be judged in terms of the safety performance evaluation criteria of the National Cooperative Highway Research Program (NCHRP) as well as the Euro-NCAP. The proper system of pole supports is expected to be strong enough to offer protection during minor impacts and remain flexible enough to avoid influencing the air bag deployment characteristics of the vehicle.

3- These results should be further evaluated by introducing actual driver's dummy as well as child dummy on the back seat. Also, these results should be validated for wind loads, snow loads and other load combinations discussed. This would provide a more reliable relative displacement, acceleration, intrusion of passenger compartments values etc. which when standardised would serve as a guidelines for ensuring "Safety of Life" of those involved in vehicle crashes and development of a "**Crashworthy Traffic Light Pole**".

4- More investigations may be required to further evaluate the best shape of the proposed rubber base, and industry partner may be contacted to fabricate a rubber base for experimental testing in the laboratory under pendulum impact.

REFERENCES

1. Road Safety Vision, 2001, Transport Canada

2. Canadian Standard Association, (2000), "Canadian Highway Bridge Design Code 2000", Etobicoke, Ontario.

3. Highway Subcommittee on Bridges and Structures (2001), "Standard Specifications for Structural Supports for Highway Signs, Luminaries and Traffic Signals", Federal Highway Administration, US-DOT.

4. AASHTO-AGC-ARTBA Joint Cooperation Committee on New Highway Materials Task Force (1980), "Standardized Highway Lighting Pole Hardware Guide".

5. Ross, H. E., Sicking, D. L., Zimmer, R. A., and Michie, J. D. (1993), "NCHRP Report 350: Recommended Procedures for the Safety Performance Evaluation of Highway Features". Transportation Research Board, National Research Council, Washington, D.C.

6. American Association of State Highway and Transportation Officials, (1989) "Roadside Design Guide".

7. Gilani, A., and Whittaker, A. (2000), "Fatigue Evaluation of Steel Post Structures; I: Background and Analysis", Journal of Structural Engineering, pp. 322-330.

8. Gilani, A., and Whittaker, A. (2000), "Fatigue Evaluation of Steel Post Structures; II: Experimentation, Journal of Structural Engineering", pp. 331-339.

9. Hamilton, H. R., Riggs, G. S., and Puckett, J. A., (2000), "Increased Damping in Cantilevered Traffic Signal Structures", Journal of Structural Engineering, ASCE, 126(4), pp. 530-537.

10. Genda, C., Jingning, W., Jiaqing, Y., Lokeshwarrapa, R. D., and Barker M. (2001), "Fatigue Assessment of Traffic Signal Mast Arms Based on Field Test Data Under natural Wind Gusts", Transportation Research Record-1770, paper no. 01-2801, pp. 188-194.

11. Cook, R. A., Bloomquist, D., Richard, D. S., and Kalajian, M. A. (2001), "Damping of Cantilevered Traffic Signal Structures", Journal of Structural Engineering, pp. 1476-1482.

12. Pagnini, L. C., Solari, G., (2001), "Damping measurements of steel poles and tubular towers." Engineering Structures 23, pp. 1085-1095.

13. Harrison, IV B. F., Roschke, P. N., (2000), "Laboratory Simulation of Wind Vibrations in Roadside Structures", Journal of Structural Engineering, pp. 1238-1245.

14. Pinelli, J., Subramanian, C. S., Tabora, J, (2002), "Experimental Study of

Breakaway Highway Sign Connection", Journal of Transportation Engineerin

pp. 17-20.

15. Alberson, D. C., Ivey, D., (1993), "Improved Breakaway Utility Pole, AD-IV" Transportation Research Record 1468, pp. 84-94.

16. Ivey, D., (1990), "AD IV the next Design Step in Breakaway Devices for Timbe Utility Poles", Progress Report, Texas.

17. National Cooperative Highway Research Program Report 230, Transportatio Research Board, Washington, D.C.

18. Nunez, E., Fouhad, F. H., Durden, H., (2000), "Evaluation of Concrete Pole Type Substation Structures Subjected to Shock Loads".

19. Elsafi, O., Alampalli, S., Owens F., (2001), "New Procedure for Design of End Plates and Base Plates of Cantilevered Traffic Support Structures", Journal of Structural Engineering, pp. 1153-1163.

20. Kocer, Y. F., Arora, J. S.,(1996), "Optimal Design of Steel Transmission Poles", Journal of Structural Engineering, pp. 1347-1356.

21. Kocer, Y. F., Arora, J. S.,(1996), "Design of Prestressed Concrete Transmission Poles: Optimization Approach", Journal of Structural Engineering, pp. 804-814.

22. PCI Committee on Prestressed Concrete Poles. (1983). "Guide for Design of

Prestressed concrete poles." Journal of *PCI*, pp. 22-88.

23. Kraulhemmer, T., (1987). "A Numerical Study of Wind-Induced Tower Vibrations." *Composites and Structures.*, pp. 223-241.

24. ASCE Committee on Electrical Transmission Structures of the Committee on Analysis and Design of Structures of the Structural Division. (1991)." Guidelines for transmission line structural loading." ASCE, New York, N.Y.

25. Sicking, D. L., Rohde, J. R., Reid J. D., (2000), "Design and Development of Steel Breakaway Posts", Transportation Research Record 1720, pp. 59-66.

26. Nunez, E., Fouad, F. H., (2000), "Estimation of Second-Order Effects for Pole Type Structures", Transportation Research Record-1740, pp. 151-156.

27. Standard Specifications for Structural Supports for Highway Signs, Luminaries and Traffic Signals. AASHTO, Washington, D.C. 1994.

28. Yang, J., DeWolf, J. T., (2002), "Reliability Assessment of Highway Truss Sign Supports", Journal of Structural Engineering, pp. 1429-1438.

29. Reid, J. D., Paulsen, G. W., (1998),"Design and Simulation of Large Breakaway Signs" , Journal of Transportation Engineering, pp. 59-64.

30. Azim, E., Dhafer M., Nabih, E. B., (2000), "Impact Finite Element Analysis of Slip-Base Sign Support Mechanism", Journal of Transportation Engineering, pp. 143-153.

31. Austin Energy, 721 Barton Springs Road, Austin, Texas 78704

32. Mamalis, A. G., Robinson, M., Manolakos, D. E., Demosthenous, G. A., Ioannidis, M. B., and Carruthers, J., (1997), "Crashworthy Capability of Composite Material Structures.", Composite Structures 37, pp. 109-134.

33. Nelson G. Bingel III, (1999), "Code Issues And Applications for FRC Utility Poles", Preprint Proposals for National Electric Safety Code, 2002 Edition, IEEE.

34. Foedinger R., Boozer J. F., Bronstad M. E., Davidson Dr. J. W., (2003), "Development of an Energy Absorbing Composite Utility Pole", TRB Annual Meeting 2003, CD-ROM.

35. Ray, M. H., Troxel, L. A., and Camey, J. F. III. (1991), "Characteristics of Side Impact Accidents Involving Fixed Roadside Objects." Journal of Transportation Engineering, ASCE, Vol. 117(3), pp. 281-297.

36. Ross, H. R. Jr., Perera, H. S., Sicking, D. L., and Bligh R. P., (1989), "NCHRP Report 318: Roadside Safety Design for Small Vehicles". Transportation Research Board, National Research Council, Washington, D.C.

37. Zaouk, A. K., Bedewi, N. E., and Meczkowski, L., (1996), "Development and Validation of a Detailed Chevrolet C-1500 Pickup Truck Model for Multiple Impact Applications", FHWA / NHSTA, George Washington University,

USDOT.

38. Hignett, H. J. (1969) "A Sideway Impact Test into a 12.2-m Lighting Column Fitted with a Breakaway Joint." Report RRL LR241. Road Research Laboratory, Ministry of Transport, United Kingdom.

39. National Research Council Committee on Trauma Research, "Injury in America: A Continuing Public Health Problem", (1985), National Academy Press, Washington, D.C.

40. Troxel, L. A., Ray, M. H. and Carney, J. F. III.(1994), "Accident Data Analysis of Side-Impact Fixed-Object Collisions." Report FHWA-RD-91-122. FHWA, U.S. Department of Transportation.

41. European New Car Assessment Program (2003), "Pole Side Impact Testing Protocol", www.euroncap.com.

42. Ray, M. H., and J. F. Carney III. (1993). "Side Impact Test and Evaluation Procedures for Roadside Structure Crash Tests." Report FHWA-RD-92-062. FHWA, U.S. Department of Transportation.

43. Hiranmayee, K., (1998), "Occupant Injury in Side Impacts with Roadside Hardware," Ph.D. Thesis, University of Iowa, Iowa.

44. Michie, J. D., (1981),"Collision Risk Assessment Based on Occupant Flail-Space

Model," Transportation Research Record No. 796, TRB, Washington, D.C.

45. Michie, J. D., (1981), "National Cooperative Highway Research Program Report 230, Transportation Research Board, Washington, D.C.

46. NHTSA, (1997), "Federal Motor Vehicle Safety Standards: Side Impact protection," Code of Federal Regulations, 49 CFR 571.214, Washington D.C.

47. Gabler, H. C. and Willke, D. T., (1991), "Upper Interior Head Impacts: The Safety Performance of Passenger Vehicles," Presented at the 13th International Technical Conference on Experimental Safety Vehicles, Paris.

48. NHTSA, (1997), "Federal Motor Vehicle Safety Standards: Side Impact protection," Code of Federal Regulations, 49 CFR 571.208, Washington D.C.

49. Fan, W. R., (1971), "Internal Head Injury Assessment," Proceeding of the 15th Stapp Car Crash Conference, SAE paper 710870.

50. Fan, W. R., (1971), "Internal Head Injury Assessment," Proceeding of the 15th Stapp Car Crash Conference, SAE paper 710870.

51. Side Impact Protection, NHTSA FMVSS 214.

52. Hinch, J., G. Manhard, D. Stout, and R. Owings. (1987), "Laboratory Procedures to Determine the Breakaway Behaviour of Luminary Supports in Minisize Vehicle Collisions." Report FHWA-RD-86-106. FHWA, U.S. Department of

Transportation.

53. Society of Automobile Engineers (1988), "SAE Journal-211.", Warrendale, Pa.

54. Hallquist, J. D., Stillman, D. W., Lin, T. L., (1998), "LS-DYNA Theoretical Mannual", Livermore Software Technology Corporation.

55. Bailey Tsay, Lin, J., and Tsay, C. S., (1984), "Explicit Algorithms for Non Linear Dynamics of Shells", Comp. Meth. Appl. Mech. Engg, pp 225-251.

56. ASTM International 10th Edition, (1990), "Metals Handbook, Vol.2 - Properties and Selection: Nonferrous Alloys and Special-Purpose Materials".

57. Ferritto, J., Dickenson, S., Priestley, N., Werner, S., and Taylor, C., (1999), "Seismic Criteria for California Marine Oil Terminals", Naval Facilities Engineering Center, Shore Facilities Department, Structures Division, California, USA, pp 153 -170.

58. Plaxico, C., Ray, M., Hiranmayee, K., (1997), "Fidelity of the EASi Ford Taurus Model", Department of Civil and Environmental Engineering, Worcester Polytechnic Institute, Worcester, MA 01609-2280

59. Buth, C. E., Samuelson, G. R., and Olson, R. M., (1979) "Crash Tests and Evaluation of Highway Appurtenances," FHWA-RD-79-92, Federal Highway Administration, Washington, D.C.

Table 1.1: Single vehicle side-impact passenger car collisions where most harmful object was roadside hardware [43]

Most Harmful event	1980-1985 FARS Fatalities		1982-1985 NASS			
			Injuries		Exposure	
	Frequency	%	Frequency	%	Frequency	%
(1)	(2)	(3)	(4)	(5)	(6)	(7)
(a) Narrow Objects						
Tree	784	47.6	19,865	32.2	41,516	24.7
Utility pole	434	26.3	18,593	30.2	35,996	21.4
Other post/pole	39	2.3	1,365	2.2	7,405	4.4
Light support	45	2.7	3,072	5.0	5,518	3.3
Sign support	12	0.7	1,935	3.1	6,958	4.1
Mailbox	—	—	311	0.5	2,189	1.3
Delineator post	—	—	142	0.2	413	0.2
Fire hydrant	1	0.1	—	—	—	—
Total narrow objects	1,315	79.9	45,283	73.4	99,995	59.4
(b) Broad Objects						
Guardrail	70	4.3	3,445	5.6	15,996	9.4
Bridge pier/abutment	44	2.7	344	0.6	1,796	1.1
Fence	15	0.9	723	1.2	4,572	2.7
Bridge rail	11	0.7	407	0.7	1,921	1.1
Wall	18	1.1	580	0.9	2,288	1.4
Bridge parapet	24	1.4	200	0.3	414	0.2
Concrete barrier	4	0.2	671	1.1	1,287	0.8
Other long. barrier	2	0.1	270	0.4	1,852	1.1
Impact attenuator	1	0.1	210	0.3	239	0.1
Total broad objects	189	11.5	6,850	11.1	30,365	17.9
(c) Other Object Types						
Ditch	15	0.9	2,962	4.8	10,042	6.0
Other fixed object	30	1.8	1,942	3.2	6,784	4.0
Culvert	30	1.8	450	0.7	970	0.6
Building	25	1.5	384	0.6	1,064	0.7
Unknown	22	1.3	—	—	—	
Earth embankment	12	0.8	2,480	4.0	6,608	3.9
Curb	2	0.1	586	1.0	11,051	6.6
Rock embankment	6	0.4	706	1.2	1,480	0.9
Shrubbery	1	0.1	—			
Total of other objects	143	8.6	9,510	15.5	37,999	22.7
Total of all objects	1,647	100.0	61,643	100.0	168,359	100.0

Table 2.1 Group load combinations [3]

Group Load	Load Combination	Percent of Allowable Stress (see note 1)
I	*DL*	100
II	*DL+W*	133
III	DL+Ice+1/2(W) (see note 2)	133

Notes:

1. The given percentages of allowable stress are applicable for the allowable stress design method. No load reduction factors shall be applied in conjunction with these increased allowable stresses.
2. *W* shall be computed on the basis of the wind pressure equation. A minimum value of 1200 Pa (25 psf) shall be used for W in group load III.
3. See Section 2.2.3 regarding application of live load.

DL : Dead Load

W = Wind Load

Ice = Ice Load

Table 2.2.: Wind importance factors, Ir

Recurrence Interval Years	*V*= 38 -45 m/s (85-100 mph)	*V*> 45 m/s (100 mph) (Hurricane)
100	1.15	1.23
50	1.00	1.00
25	0.87	*0.80
10	0.71	*0.54
* Note: The design wind pressure for hurricane wind velocities greater than 45 m/s (100 mph) should not be less than the design wind pressure using *V*=45 m/s (100 mph) with the corresponding non-hurricane Ir value.		

Table 2.3 Recommended minimum design life

Design Life	Structure Type
50 years	• Luminary support structures exceeding 15m (49.2ft) in height • Overhead sign structures
25 years	• Luminary support structures less than 15 m (49.2 ft) • Traffic signal structures
10 years	• Roadside sign structures

Table 2.4 Velocity conversion factors (C_v)

Recurrence intervals years, Interval Years	V=38-45 m/s (85-100 mph)	V> 45 m/s (100 mph) (Hurricane)
100	1.07	1.105
50	1.00	1.00
25	0.93	0.89
10	0.84	0.73

Table 2.5 Height and exposure factors, K_z

Height, m(ft)	K_z
5.0 (16.4) or less	0.87
7.5 (24.6)	0.94
10.0 (32.8)	1.00
12.5 (41.0)	1.05
15.0 (49.2)	1.09
17.5 (57.4)	1.13
20.0 (65.6)	1.16
22.5 (73.8)	1.19
25.0 (82.0)	1.21
27.5 (90.2)	1.24
30.0 (98.4)	1.26
35.0 (114.8)	1.30
40.0 (131.2)	1.34
45.0 (147.6)	1.37
50.0 (164.0)	1.40
55.0 (180.5)	1.43
60.0 (196.9)	1.46
70.0 (229.7)	1.51
80.0 (262.5)	1.55
90.0 (295.3)	1.59
100.0 (328.1)	1.63

Table 2.6 Dimension Table

Steel Pole Shaft				
Mounting Height (m)	Shaft Length (m)	Shape	90 MPH	80 MPH
9.15	8.23	Round	190 x 89 x 3.05*	Same
		Octagon	190 x 101 x 3.05	Same
		Dodecagon	190 x 100 x 3.05	Same
10.67	9.75	Round	180 x 90 x 3.05	Same
		Octagon	216 x 101 x 3.05	190 x 100 x 3.05
		Dodecagon	190 x 100 x 3.05	Same
12.2	11.3	Round	183 x 89 x 3.05	Same
		Octagon	254 x 100 x 3.05	230 x 100 x 3.05
		Dodecagon	190 x 100 x 3.05	Same
13.72	12.80	Round	196 x 89 x 3.05	175 x 89 x 3.05
		Octagon	254 x 100 x 3.4	254x100 x 3.05
		Dodecagon	210 x 100 x 3.05	190 x 100 x 3.05
Aluminium Pole Shaft				
Mounting Height (m)	Shaft Length (m)	Alloy	90MPH	80MPH
9.14	8.38	6063	200 x 150 x 3.9	Same
		6005	200 x 150 x 3.9	Same
10.67	9.9	6063	200 x 150 x 4.8	Same
		6005	200 x 150 x 3.9	Same
12.2	11.43	6063	254 x 150 x 3.9	Same
		6005	254 x 150 x 3.9	Same
13.72	12.95	6063	254 x 150 x 4.8	Same
		6005	254 x 150 x 3.9	Same

*Bottom Diameter x Top Diameter x Thickness (mm)

Table 2.7 Impact conditions

Test Level	Feature	Test Designation of NCHRP Report 350	Vehicle	Nominal Speed km/h (mph)	Nominal Angle deg.
2	Support Structures	2-60 S2-60 2-61 S2-61	820C 700C 820C 700C	35 (21.7) 35 (21.7) 70 (43.5) 70 (43.5)	0-20 0-20 0-20 0-20
3 Basic Level	Support Structures	3-60 S3-60 3-61 S3-61	820C 700C 820C 700C	35 (21.7) 35 (21.7) 100 (62.1) 100 (62.1)	0-20 0-20 0-20 0-20

Table 2.8 Injury as function of lateral change in velocity for side impacts centered on passenger compartment

ΔV total (km/h)	Minor $0 \leq AIS < 2$		Moderate $2 \leq AIS < 3$		Severe $AIS \geq 4$		Unknown	Total	
	(no.)	(%)	(no.)	(%)	(no.)	(%)	(no.)	(no.)	(%)
(1)	(2)	(3)	(4)	(5)	(6)	(7)	(8)	(9)	(10)
0-10	34	65	7	33	2	25	2	44	54
11-20	4	8	1	5	0	0	0	5	6
21-30	9	17	0	0	0	0	0	9	11
31-40	2	4	6	29	1	12	0	9	11
41-50	3	6	1	5	1	13	0	5	6
51-60	0	0	5	23	3	38	0	8	10
60>	0	0	1	5	1	12	0	2	2

Table 2.9: LS-DYNA Material Models Used

No.	Material Type	No of Components
1	Elastic	25
7	Blatz-ko Rubber	5
20	Rigid	27
24	Piecewise Linear Isotropic Plastic	154
26	Metallic Honeycomb	2

Table 2.10 Elastic and Blatz-Ko Material Models

	Elastic	Blatz-ko rubber
Density	7.85 g/cc	1.27 g/cc
Young's Modulus	210,000 MPa	28 MPa
Poisson's ratio	0.3	-

Table 2.11 Piecewise Linear Isotropic Plasticity Material Model

Density	7.85 g/cc
Young's Modulus	210,000 MPa
Poisson's Ratio	0.3
Yield Stress	270 MPa
Load Curve	See Figure 3.8
Plastic Strain at Failure	∞ (no failure)

Table 2.12 Weight of various components

Component	Actual Weight (kg)	FEM Weight (kg)
Door assembly	25.85	26.54
Bumper	19.59	20.49
assembly	14.42	13.38
Fender	25.7	27.09
Hood	21.99	24.33

Table 2.13 Centre of gravity location

	X mm	Y mm	Z mm
FEM	-2220.00	-19.75	803.00
TEST	-2100.00	0.00	690.00

Table 2.14 Roadside hardware side-impact crash test evaluation criteria

Structural Adequacy	NCHRP-B	The test article shall readily activate in a predictable manner by collapsing, breaking away, fracturing or
Occupant Risk	NCHRP-F	The vehicle shall remain upright during and after the collision although moderate rolling, pitching and yawing
	SI-H	The Head Injury Criteria (HIC) measured using a side impact dummy (Part 572 subpart F) shall be less than 1000.
	SI-T	The Thoracic Trauma Index (TTI) measured using a side impact dummy (part 572 subpart F) shall be less than 90.
	SI-P	The pelvic acceleration measured using a side impact dummy (part 572 subpart F) shall be less than 130 g's.
Vehicle Trajectory	SI-V	After the collision the vehicle trajectory shall not intrude into the adjacent traffic lanes.
In side impacts, roadside structures are expected to breakaway, fracture, collapse or yield allowing the vehicle to either stop or bypass. This table shows the acceptable evaluation criteria for Roadside structures as per FHWA Publication# FHWA-RD-92-062 May 1993.		

Table 2.15 Comparison of impact conditions for side impact crash tests.

	FMVSS 214	EU	ISO	Table 1
Test Device	Vehicle	Vehicle	Vehicle	Roadside Hardware
Velocity (km/hr)	50	30	30	0
Orientation angle, θ	0°	0°	0°	0°
Side-slip angle, θ_i	0°	0°	0°	0°
Impact point	Longitudinal cg			Centre leading edge of device
Impactor	MDB	MDB	Rigid Pole	820-kg vehicle
Velocity (km/hr)	54	50	0	50
Orientation, θ	90°	90°	90°	90°
Side-slip angle, θ_i;	63°	0°	0°	90°
Impact point	Centre Crushable Face			Centre of Door

Table 3.1 Pole supported on rubber base (refer to Figure 3.5):

Case No.	Height (H)	Top Diameter D_t	Bottom Diameter D_b	Inside Diameter D_i	Number of Solid Elements
1	500	280	280	40	1680
2	350	280	280	40	1120
3	200	280	280	40	700
4	500	280	280	70	1536
5	350	280	280	70	1024
6	200	280	280	70	640
7	500	280	350	70	840
8	350	280	350	70	1000
9	200	280	350	70	960

All sizes in "mm"

Table 3.2 Values of ε_c and corresponding shear strengths for clayey soils.

Shear Strength lb/sq ft	ε_c %
250-500	2.0
500-1000	1.0
1000-2000	0.7
2000-4000	0.5
4000-8000	0.4

Table 3.3 Properties of cohesive soils

Type	Undrained Shear Strength	Strain at 50% maximum shear stress. ε_c	Effective Unit Weight, γ_b (lb/cu ft)
Under-consolidated Clays	0.35-1.0	2	20-25
Normally consolidated soils at depth z, inches.	1.0+0.0033z	2-1	25-50
Over-consolidated soils based on consistency:			
Medium stiff	3.5-7	1.0	50-65
Stiff	7-14	0.7	50-65
Very stiff	14-28	0.5	50-65
hard	Over28	0.4	50-65

Table 3.4 Test matrix for side impact tests 95S008 and 95S014

	FOIL Test 95S008	FOIL Test 95S014
Vehicle	1990 Ford Taurus	1990 Ford Taurus
Weight	1,639kg	1,588kg
SID(modified neck)	One in Driver Seat (Hybrid III neck)	One in Driver Seat
Crab Angle	90°	90°
Speed (nominal)	35km/hr	35 km/hr
Impact Location	1,150 mm rearward of front axle	1,150 mm rearward of front axle
Test Article	FOIL instrumented rigid pole	FOIL instrumented rigid pole

Figure 1.1 View of car impact to wooden pole (VSRC, Ryerson University)

Figure 1.2 View of damaged prestressed concrete traffic light pole after car impact

Figure 1.3 View of deformed traffic light steel pole after car impact

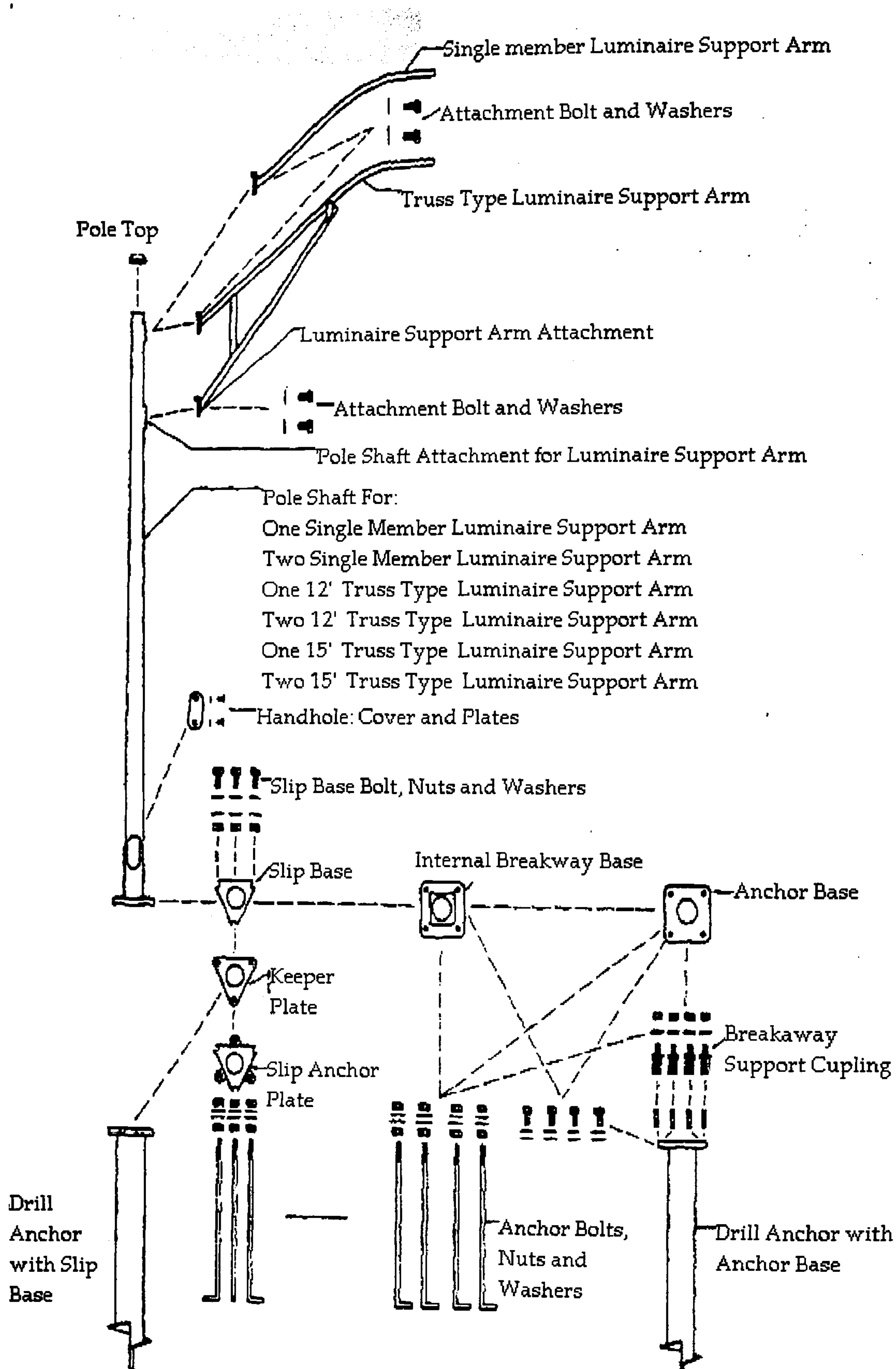

Figure 2.1 Steel pole shaft assemblies [4]

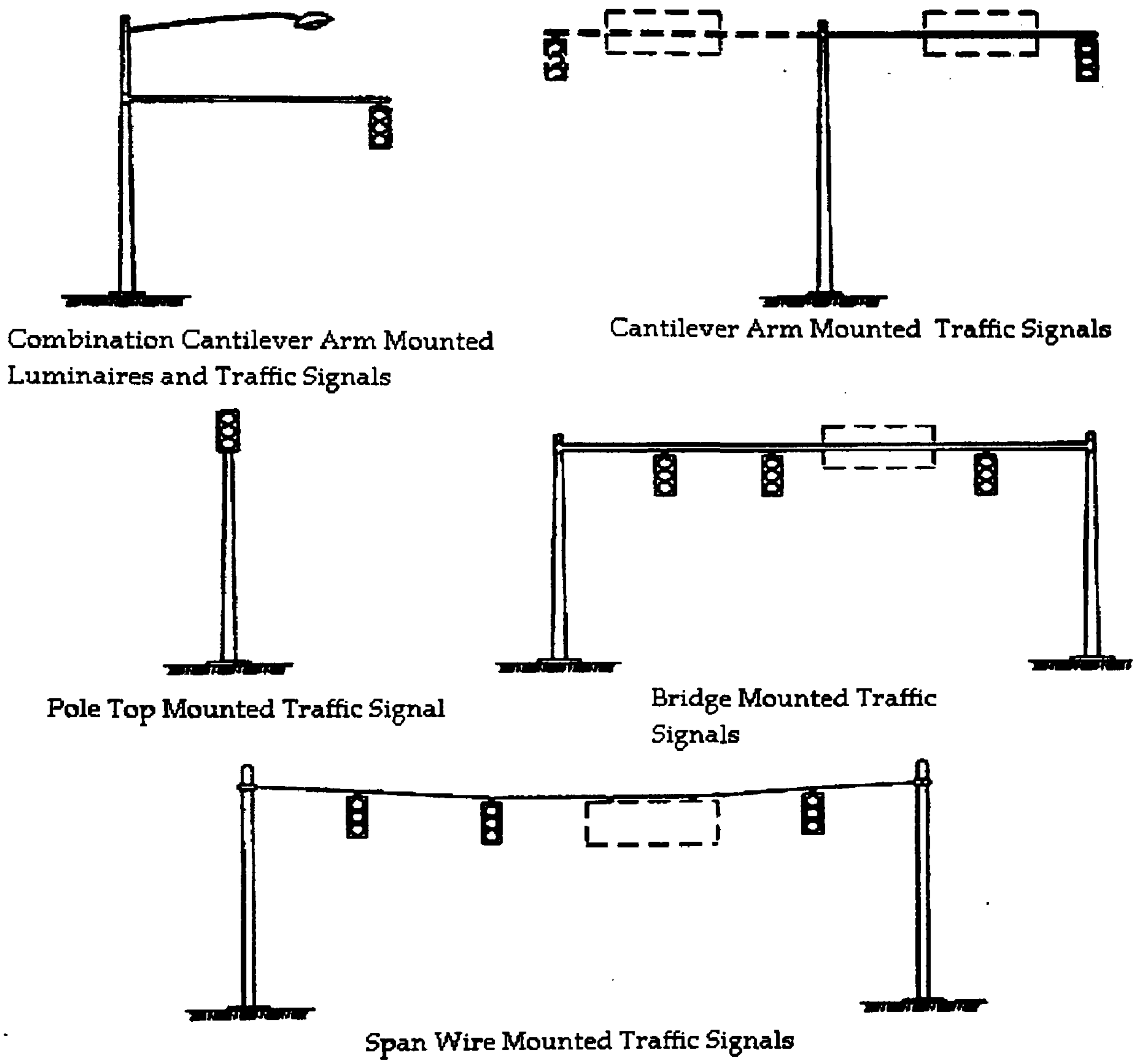

Figure 2.2: Traffic signal support structures.

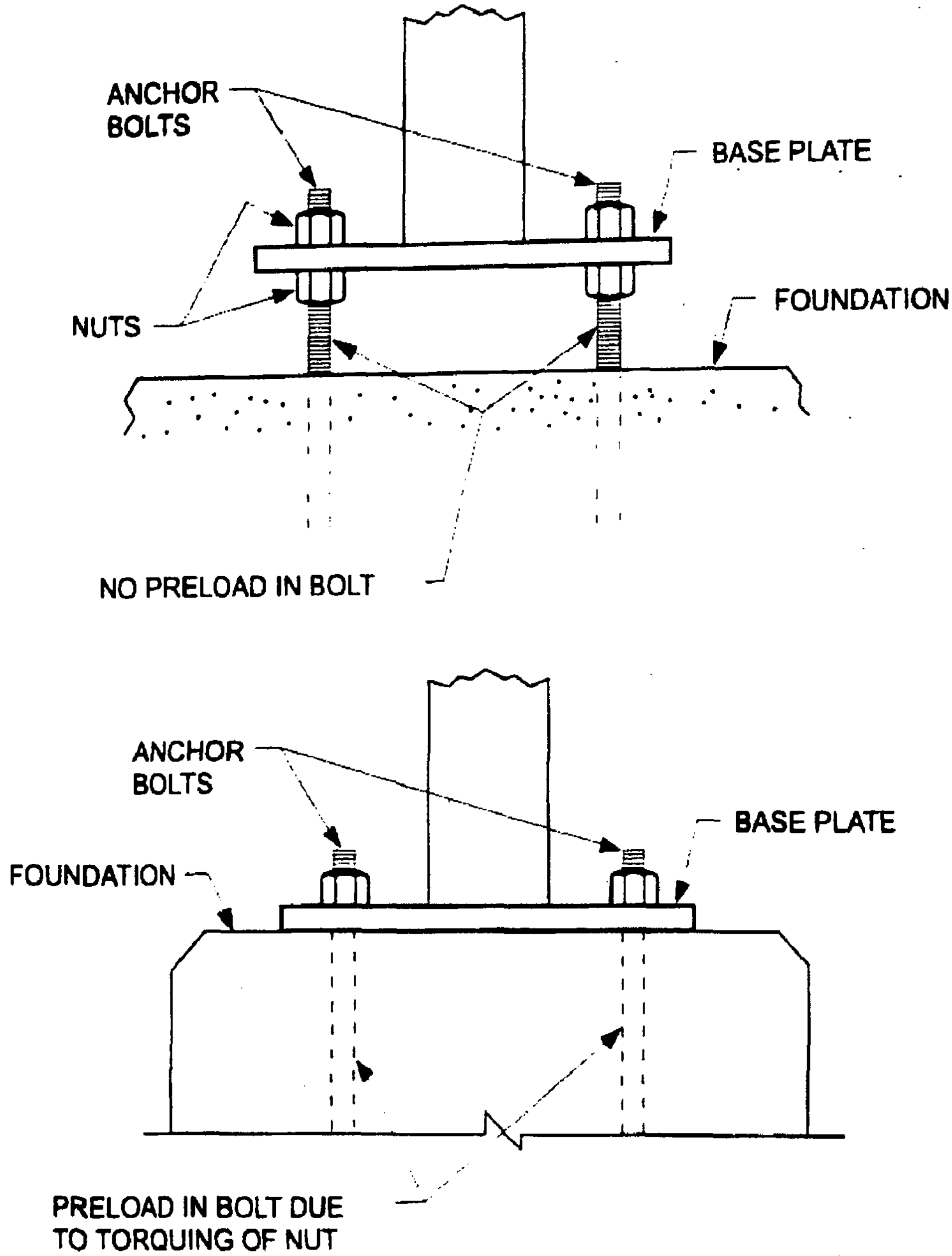

Figure 2.3 (a) CHBDC pole supports details with and without anchor bolt preload.

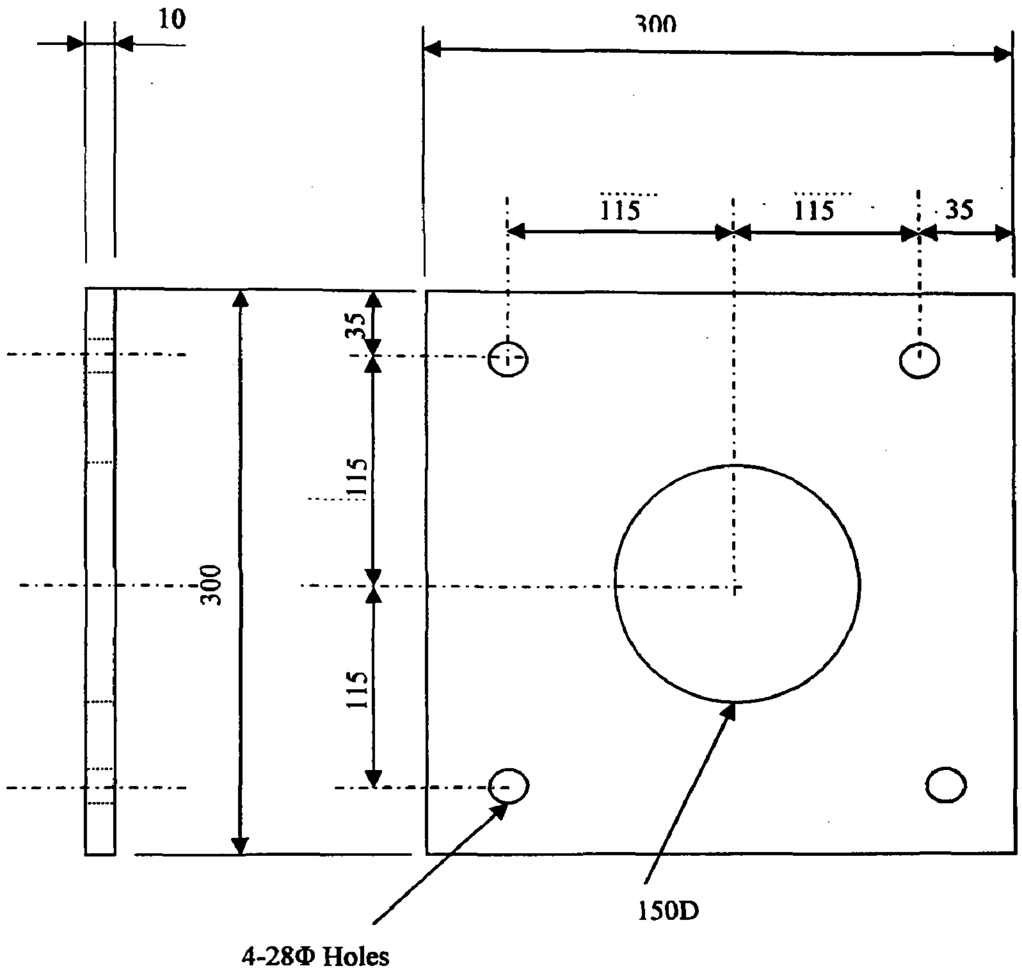

Figure 2.3 (b) Anchor bolt bearing plate (units in mm)

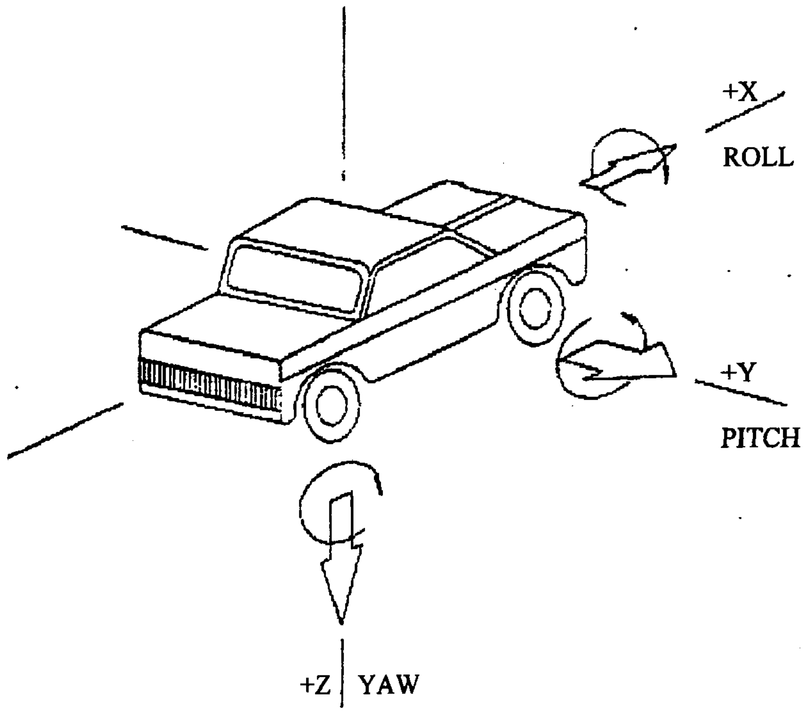

Figure 2.4 Positive sign convention for yaw, pitch and roll.

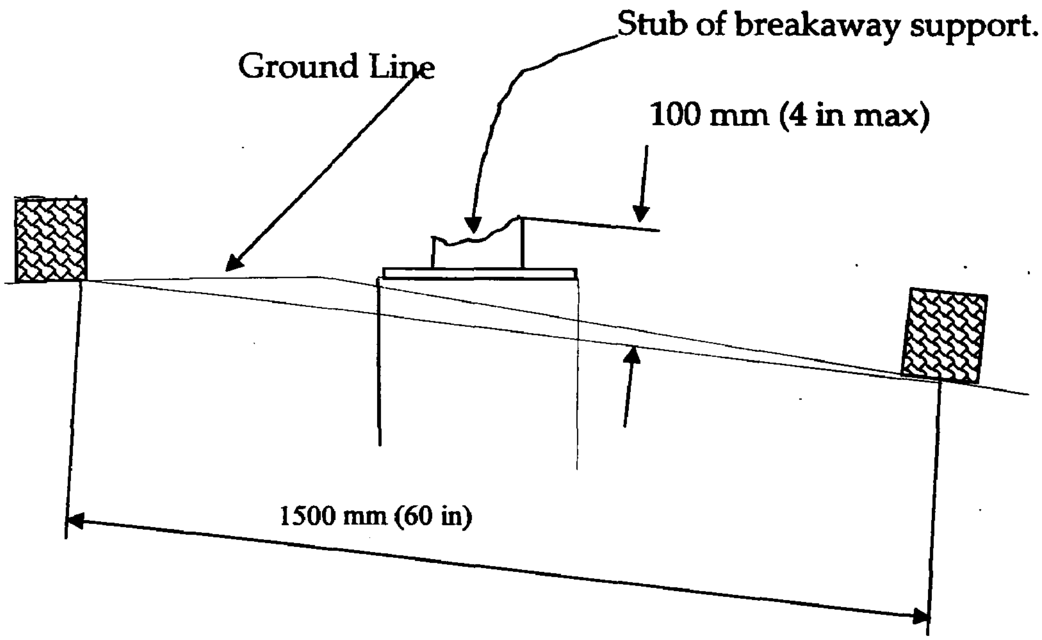

Figure 2.5 Stub height requirements.

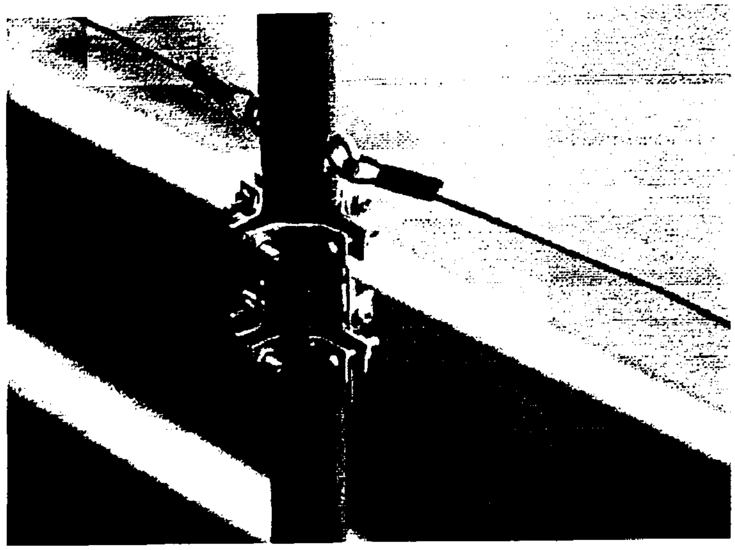

(a) Upper Hinge

(b) Base

Figure 2.6 AD-IV Pole

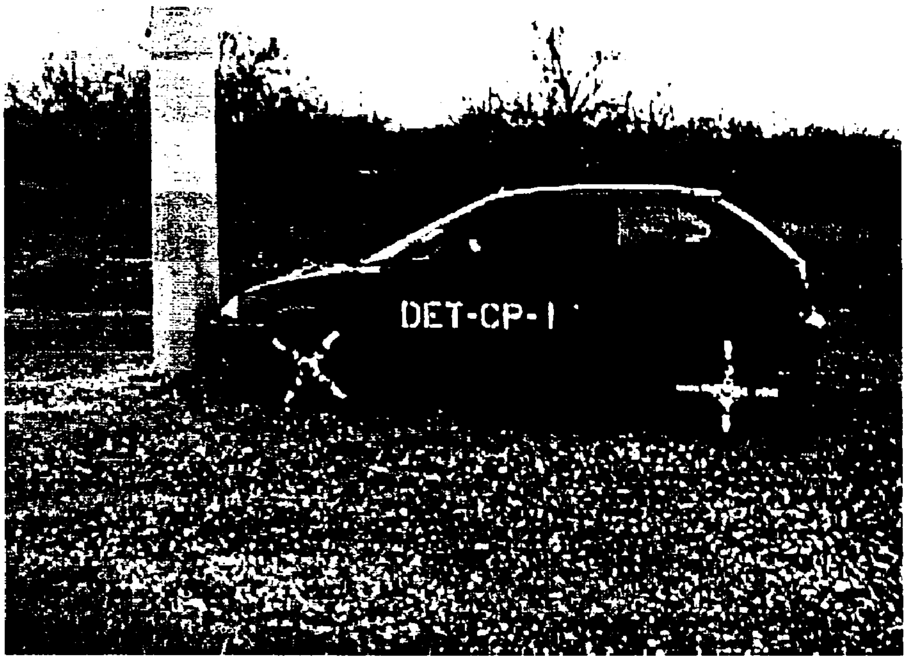

(a) Before

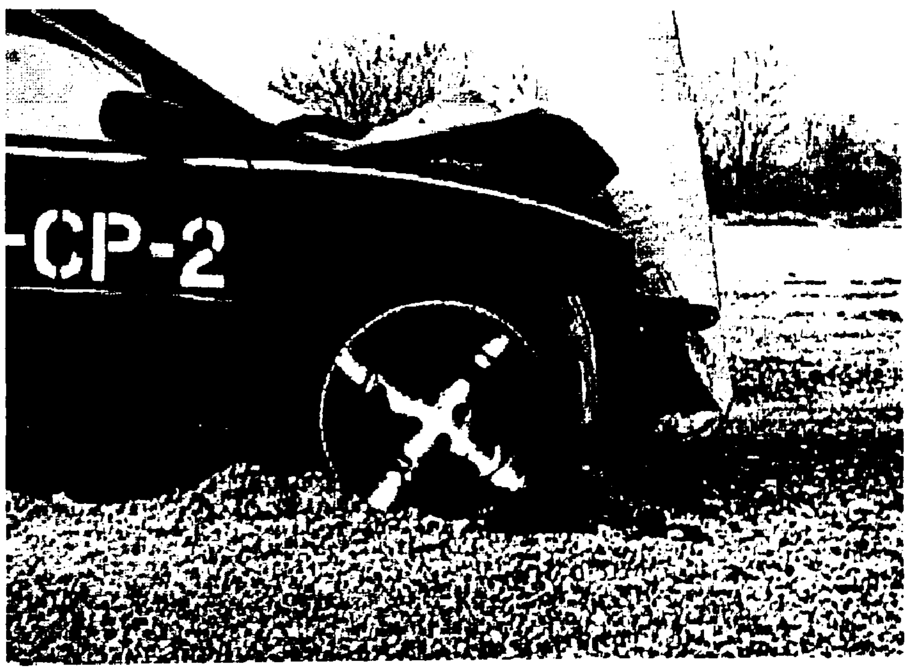

(b) After

Figure 2.7 Post test photograph of composite pole and vehicle following crash test at 70 km/hr.

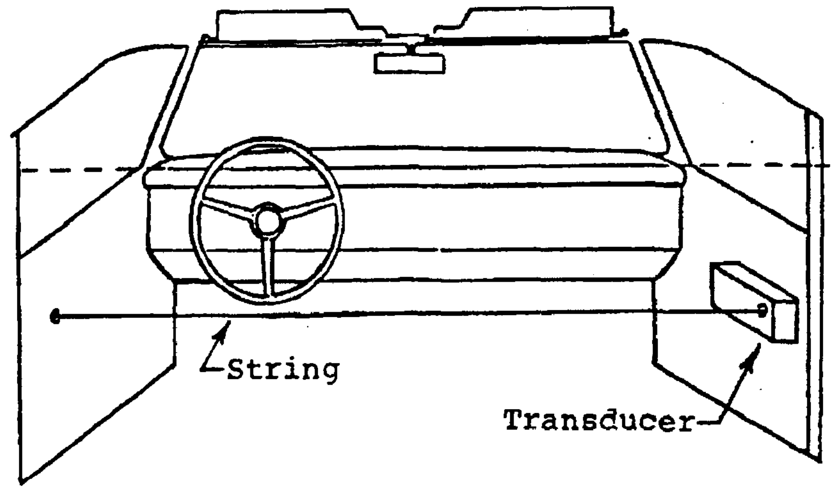

Figure 2.8 Displacement transducer to measure passenger compartment intrusion.

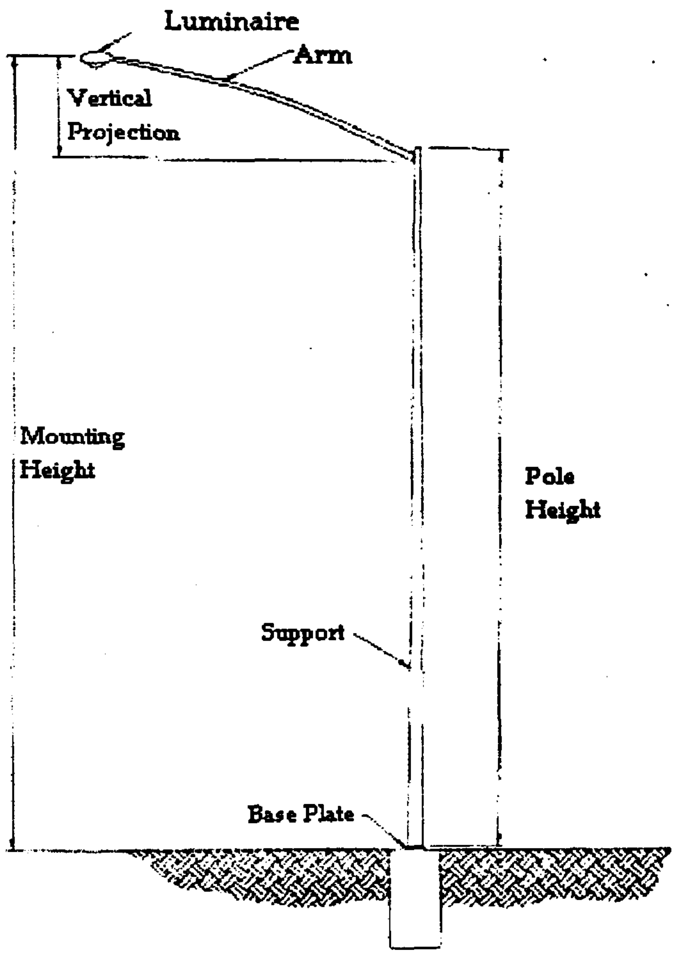

Figure 2.9 Typical breakaway luminary [36]

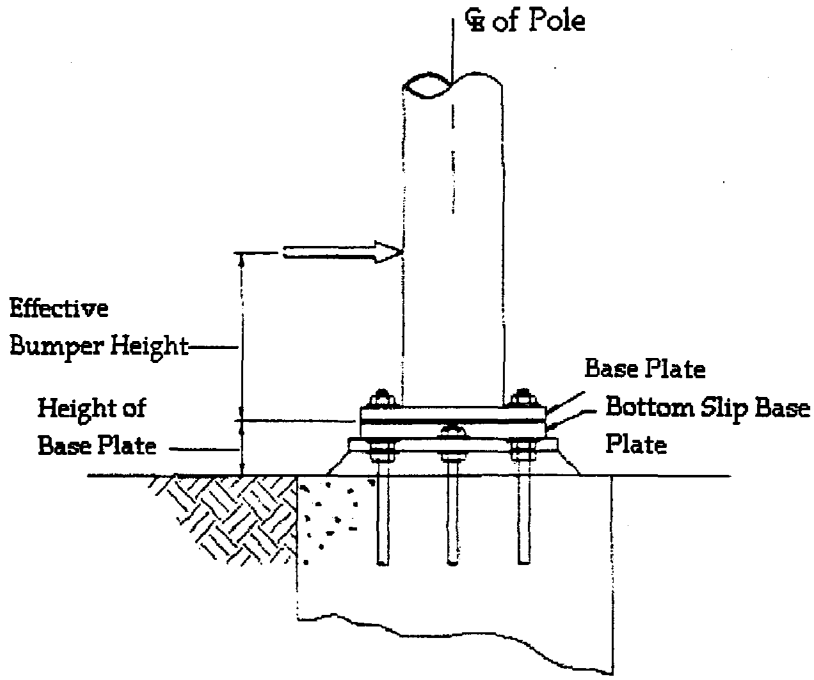

Figure 2.10 Effective bumper height [36]

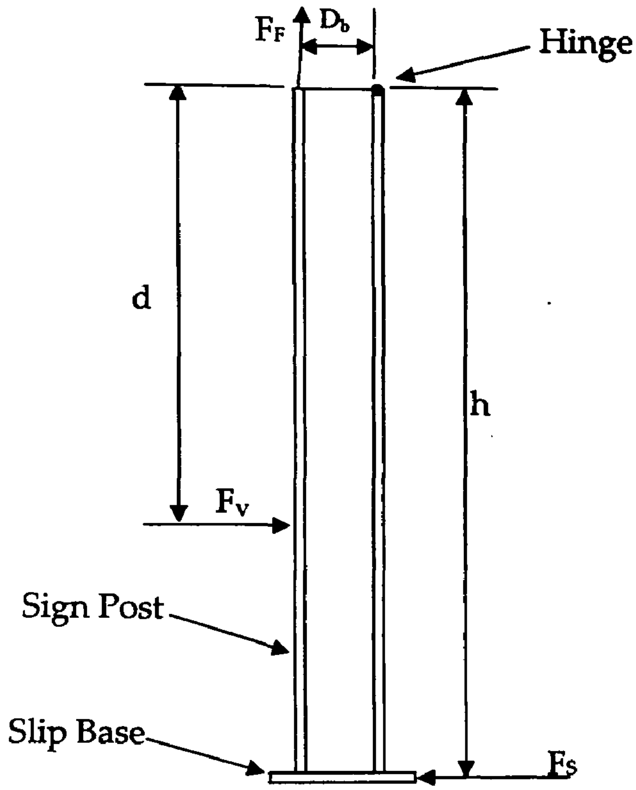

Figure 2.11 Free body of breakaway sign support. [36]

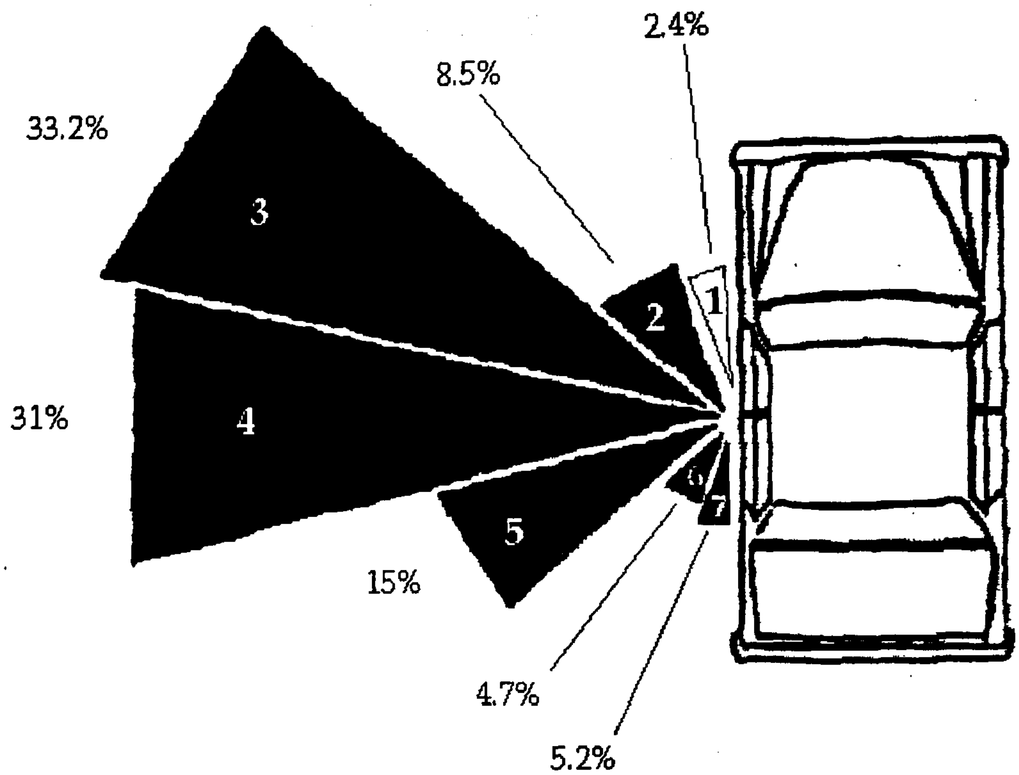

	IMPACT ANGLE
#1	0 ° - 15 °
#2	15 ° - 45 °
#3	45 - 75 °
#4	75° - 105°
#5	105° - 135°
#6	135° - 165°
#7	165° - 180°

Figure 2.12 Directions of force in side-impact collisions with fixed roadside objects involving passenger compartment. [5]

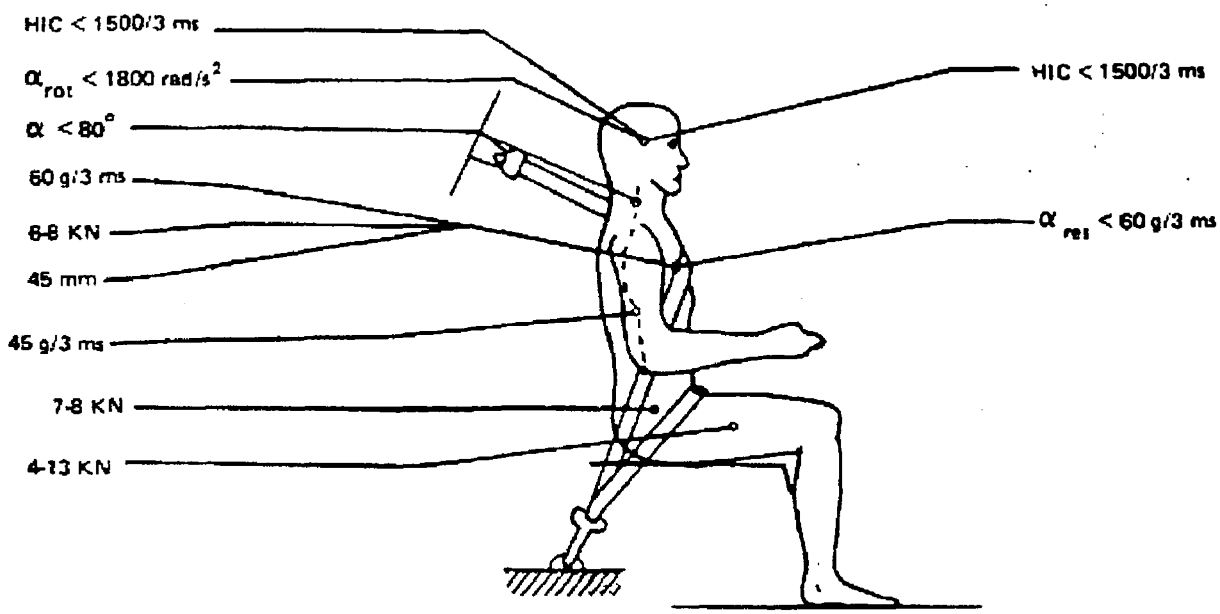

Figure 2.13 Biomechanical limits and protection limits.

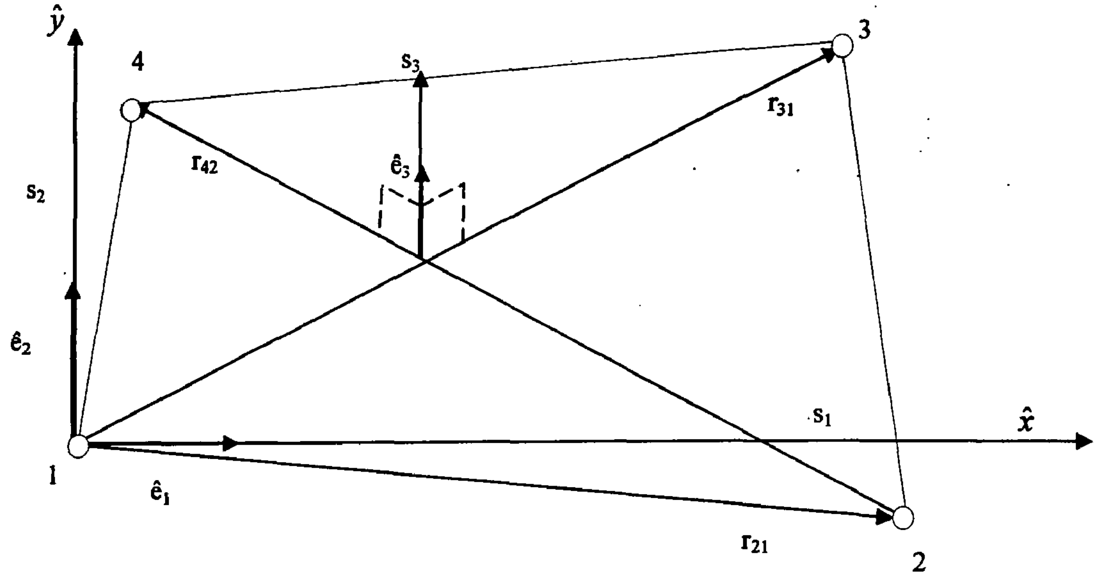

Figure 3.1 Construction of element coordinate system.

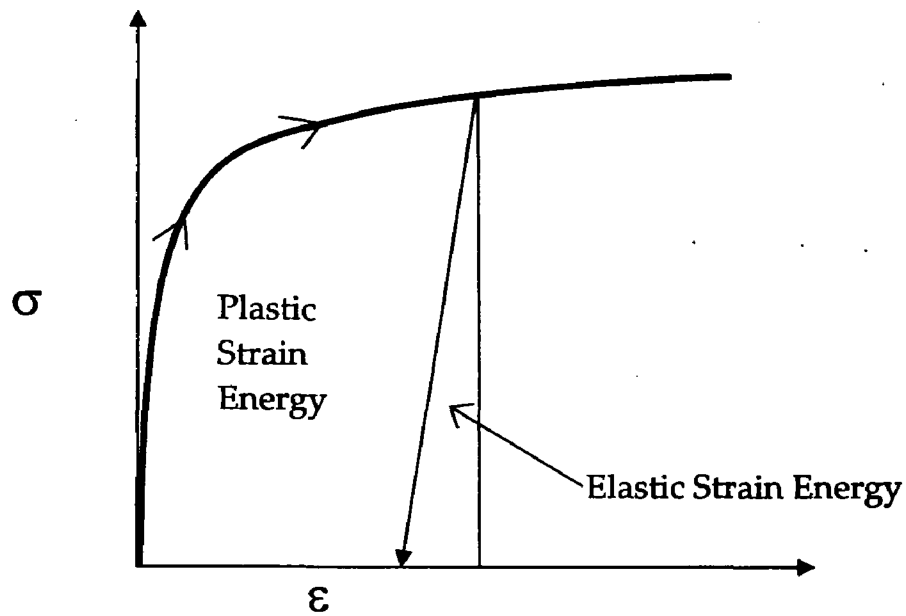

Figure 3.2 Plastic and Elastic Strain Energies

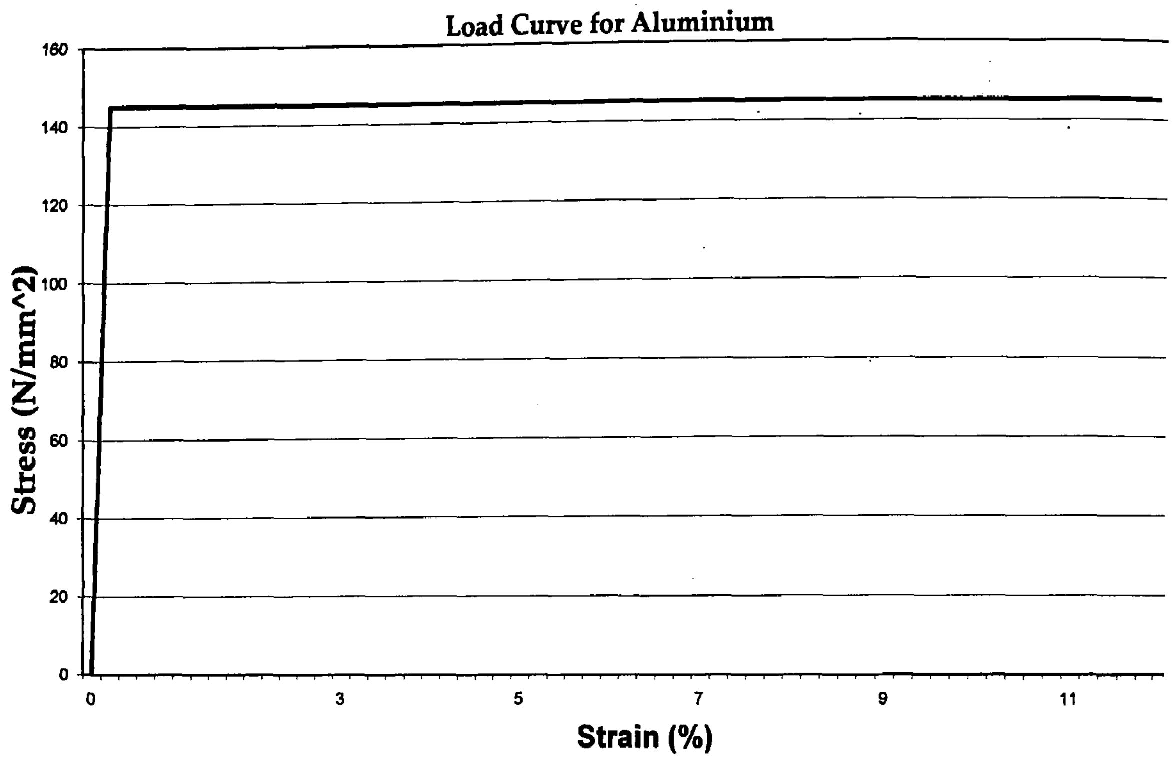

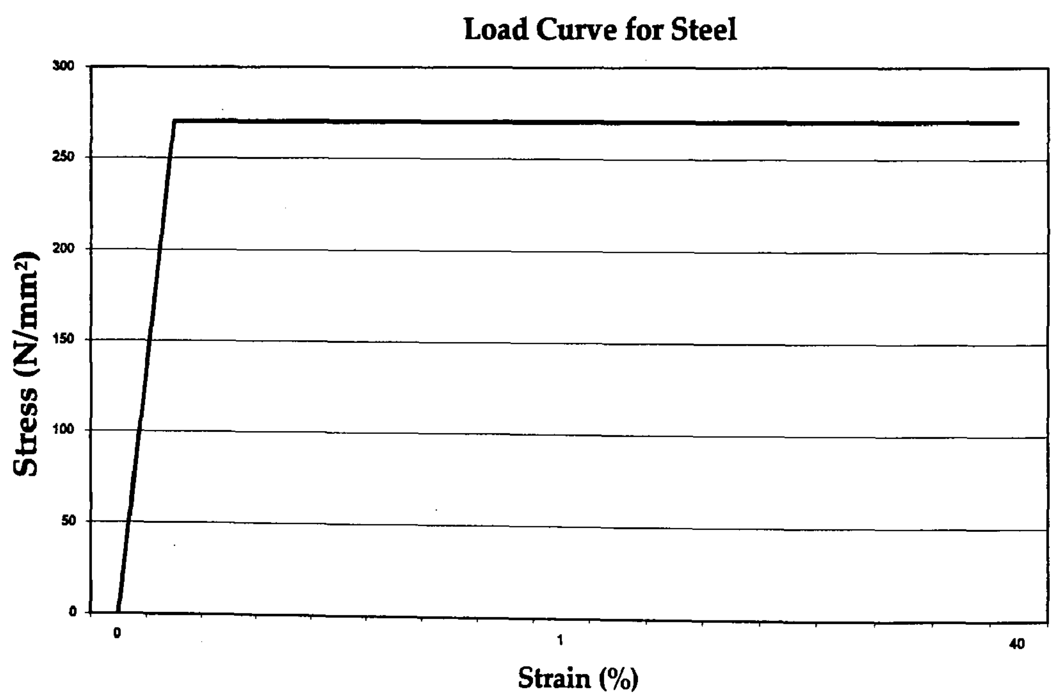

Figure 3.3 Load curve for aluminium and steel.

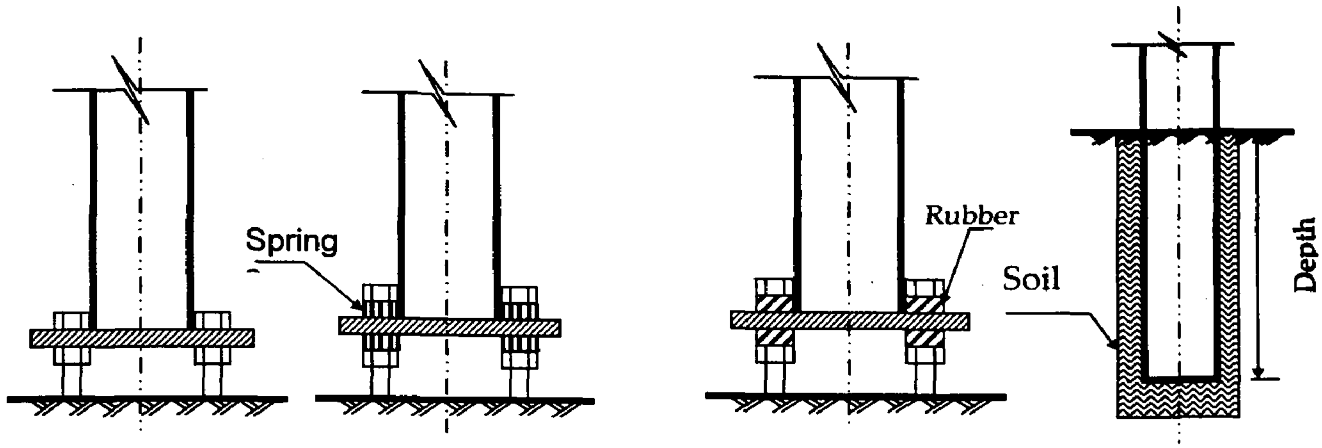

a) Fixed Support b) Fixed with springs c) Fixed with Rubber Dampers d) Embedded in Soil

Figure 3.4 Pole support types considered

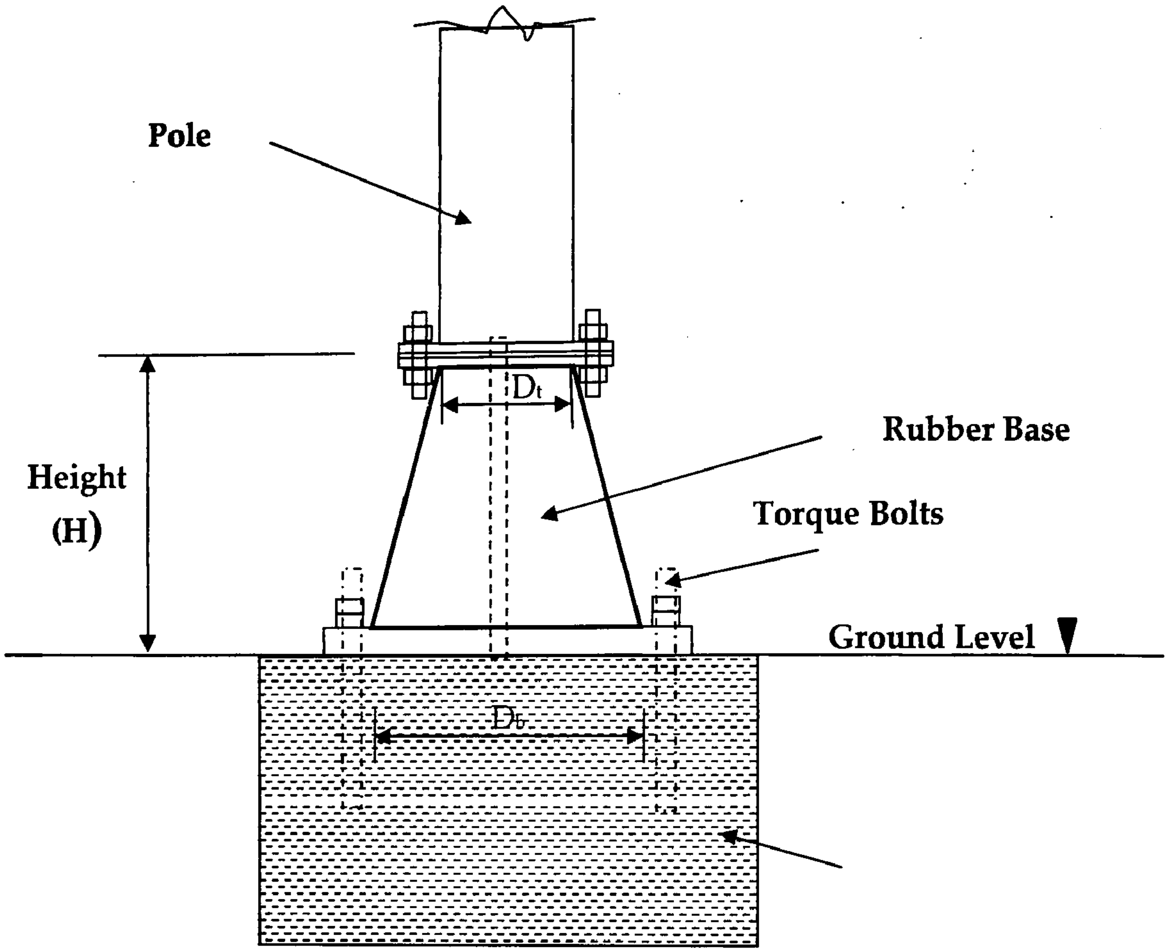

Figure 3.5 Rubber base supporting steel pole

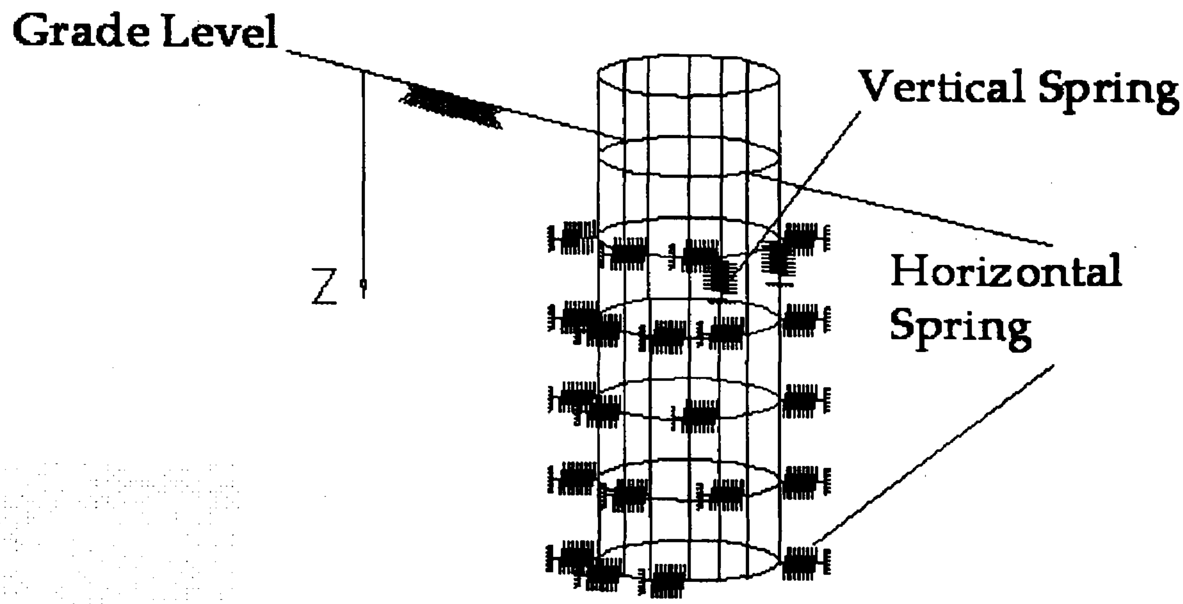

Figure 3.6: Schematic representation of spring elements to simulate soil pole interaction.

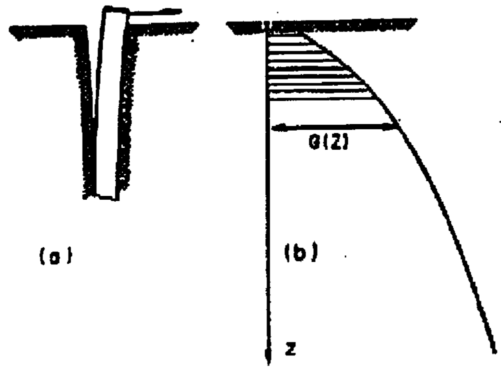

Pole Embedded in Soil

a) Faliure Mode
b) Subgrade Reaction

Figure 3.7 Typical pole soil separations and horizontal sub grade reaction. [57]

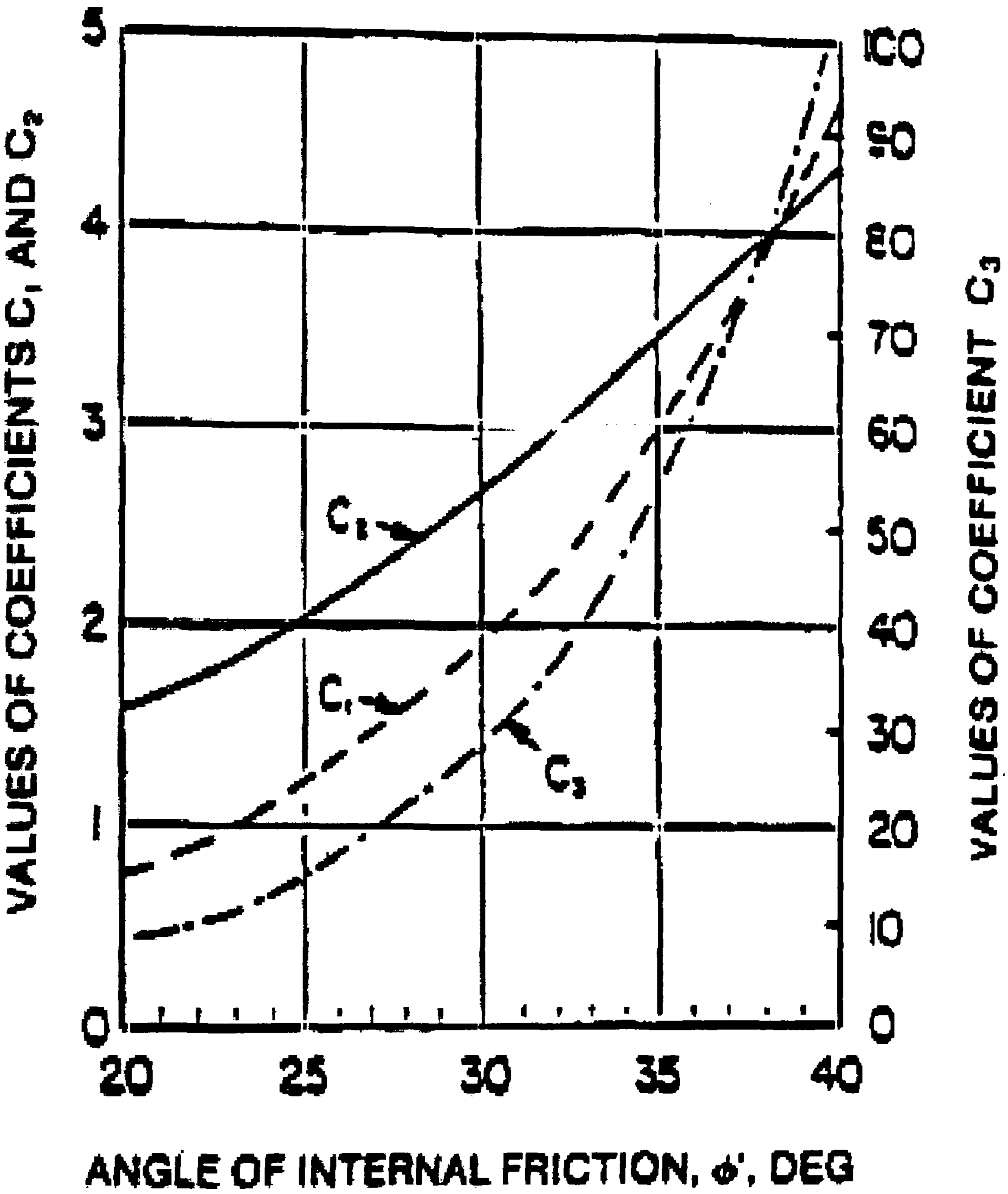

Figure 3.8: American Petroleum Institute (API) coefficients for sand. [57]

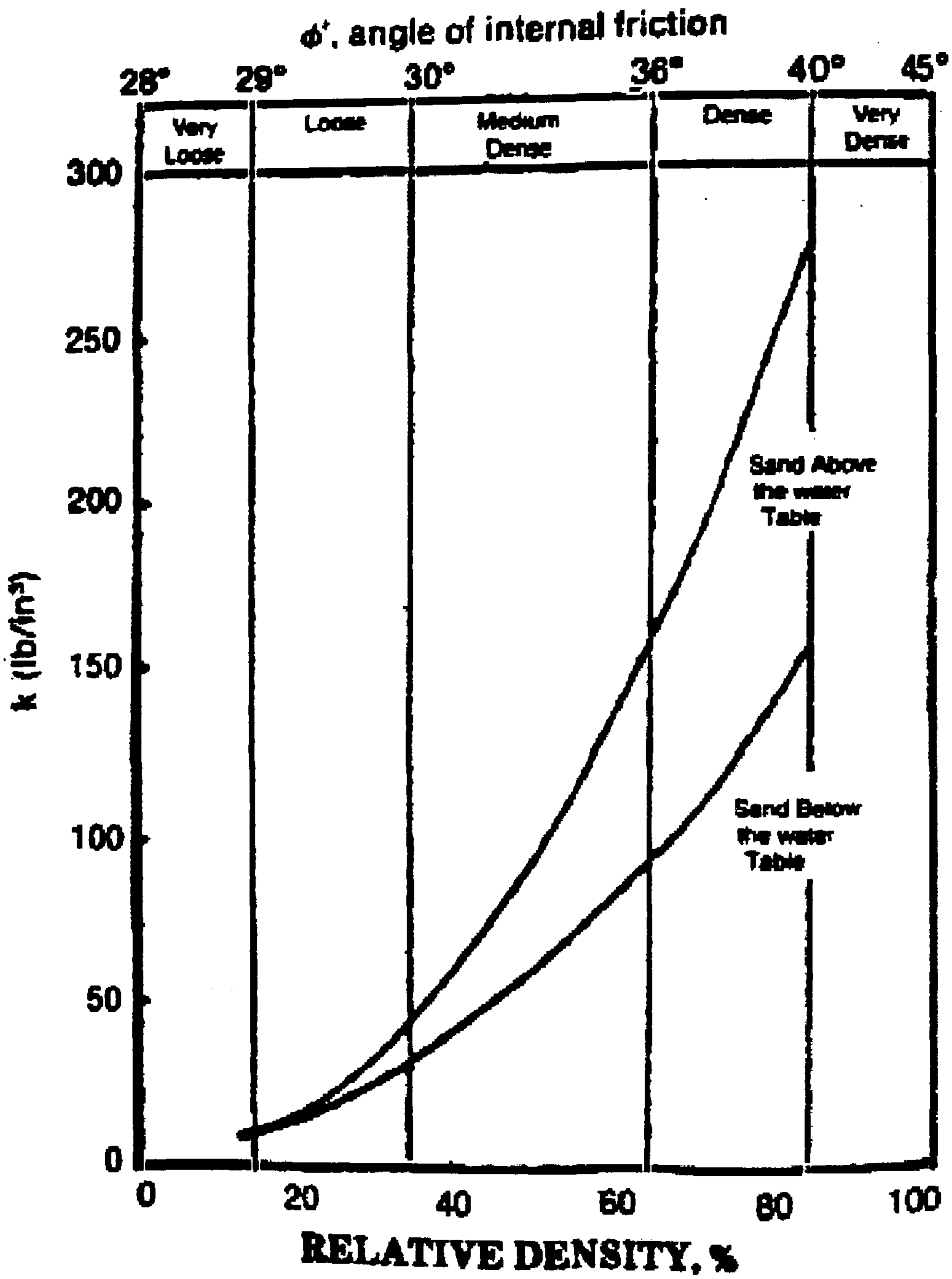

Figure 3.9 API initial modulus of subgrade reaction. [57]

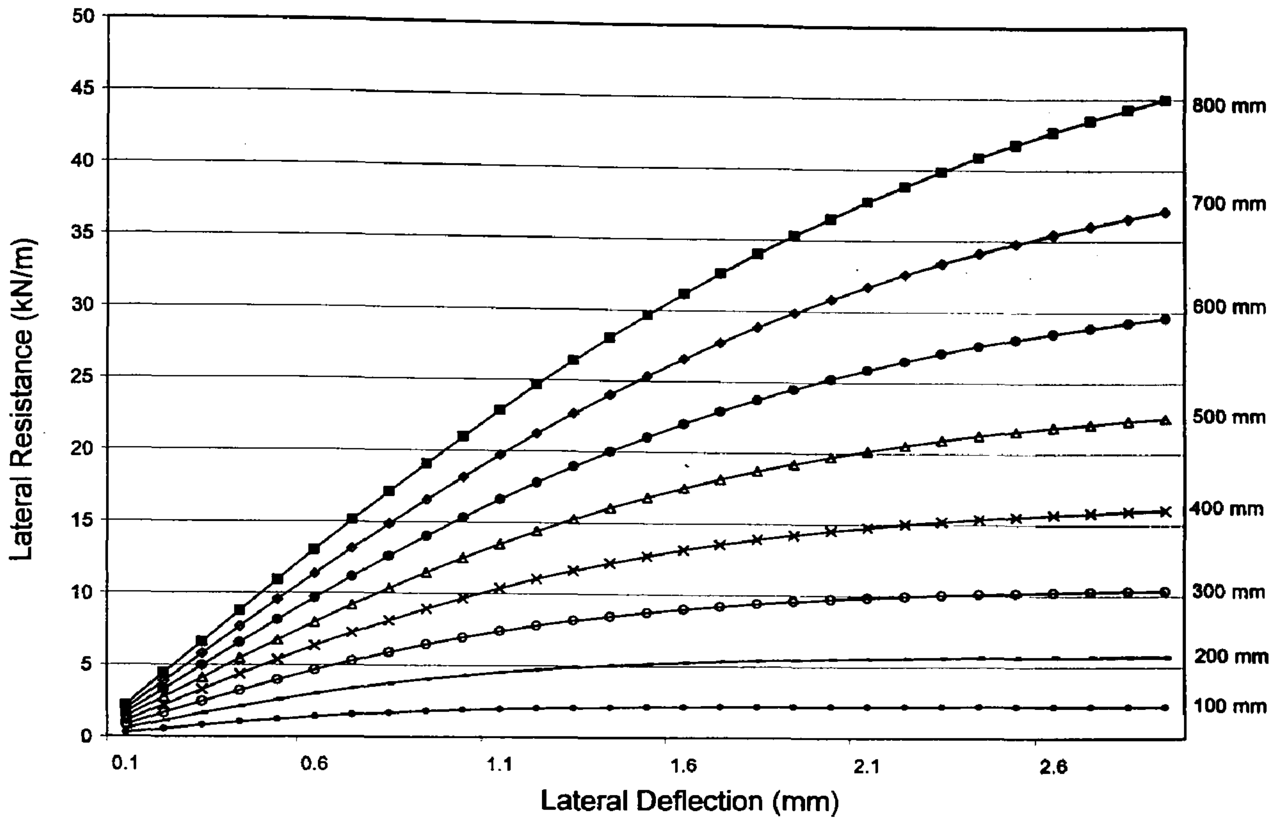

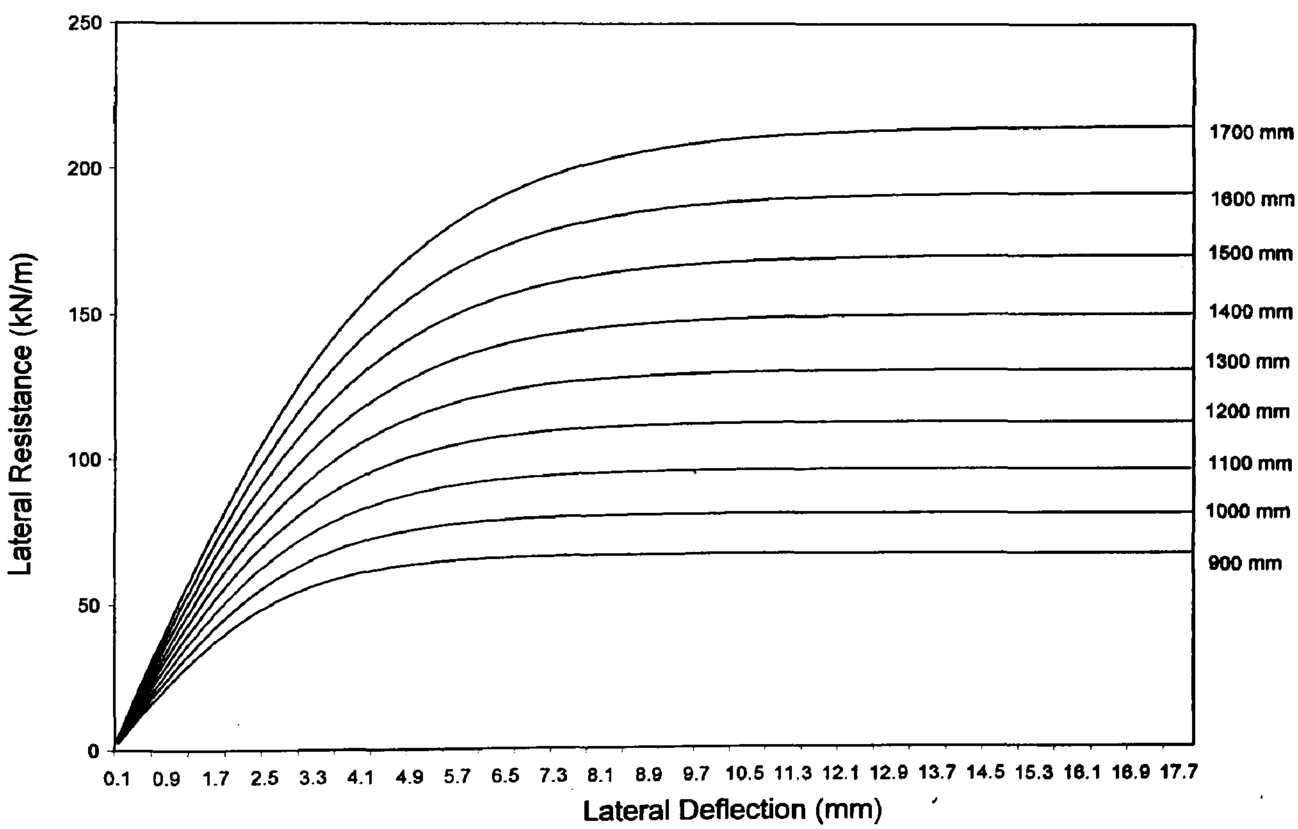

Figure 3.10: Spring coefficient (k_h) for dense sand

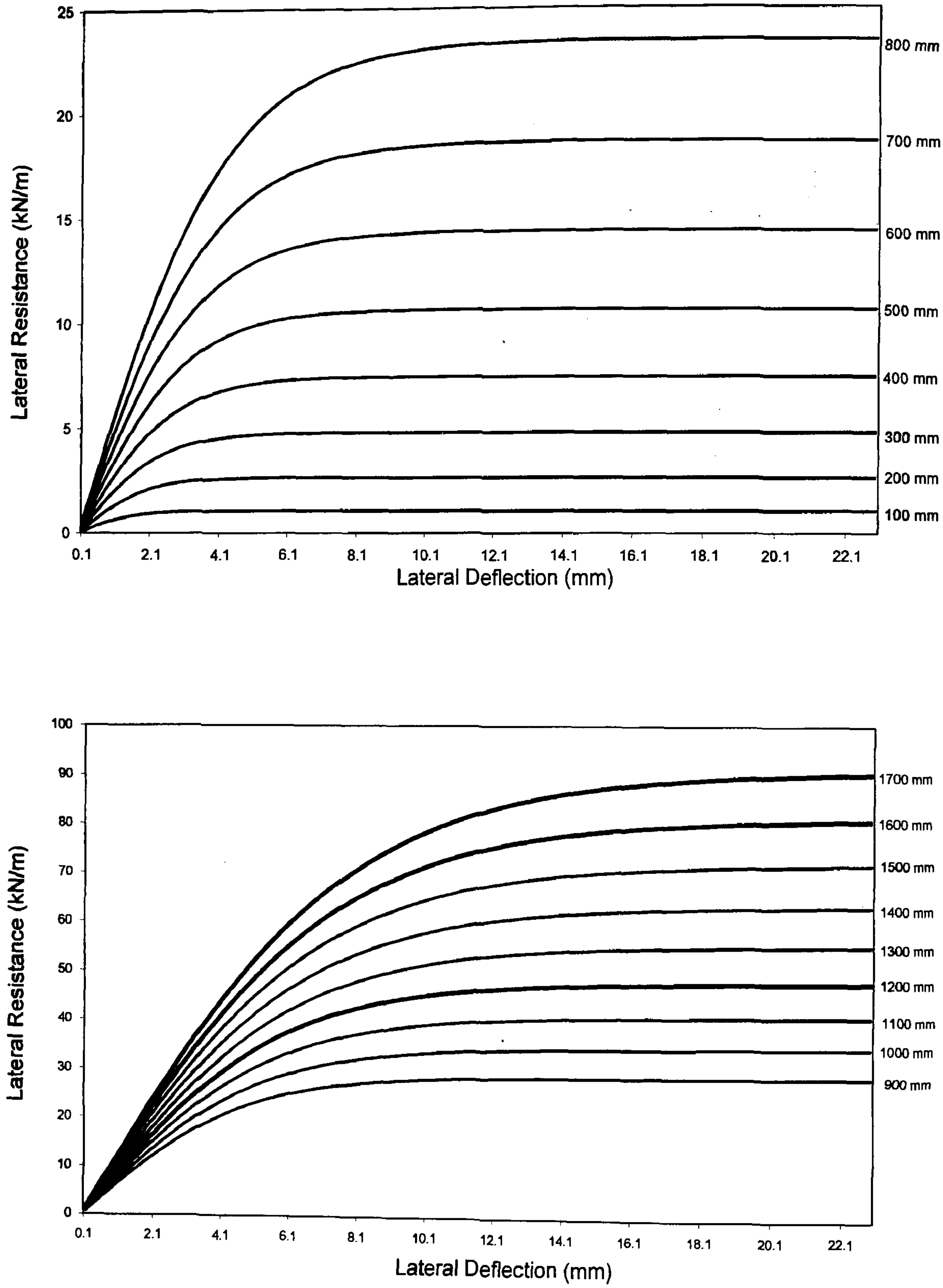

Figure 3.11 Spring coefficient (k_h) for loose sand at different depths.

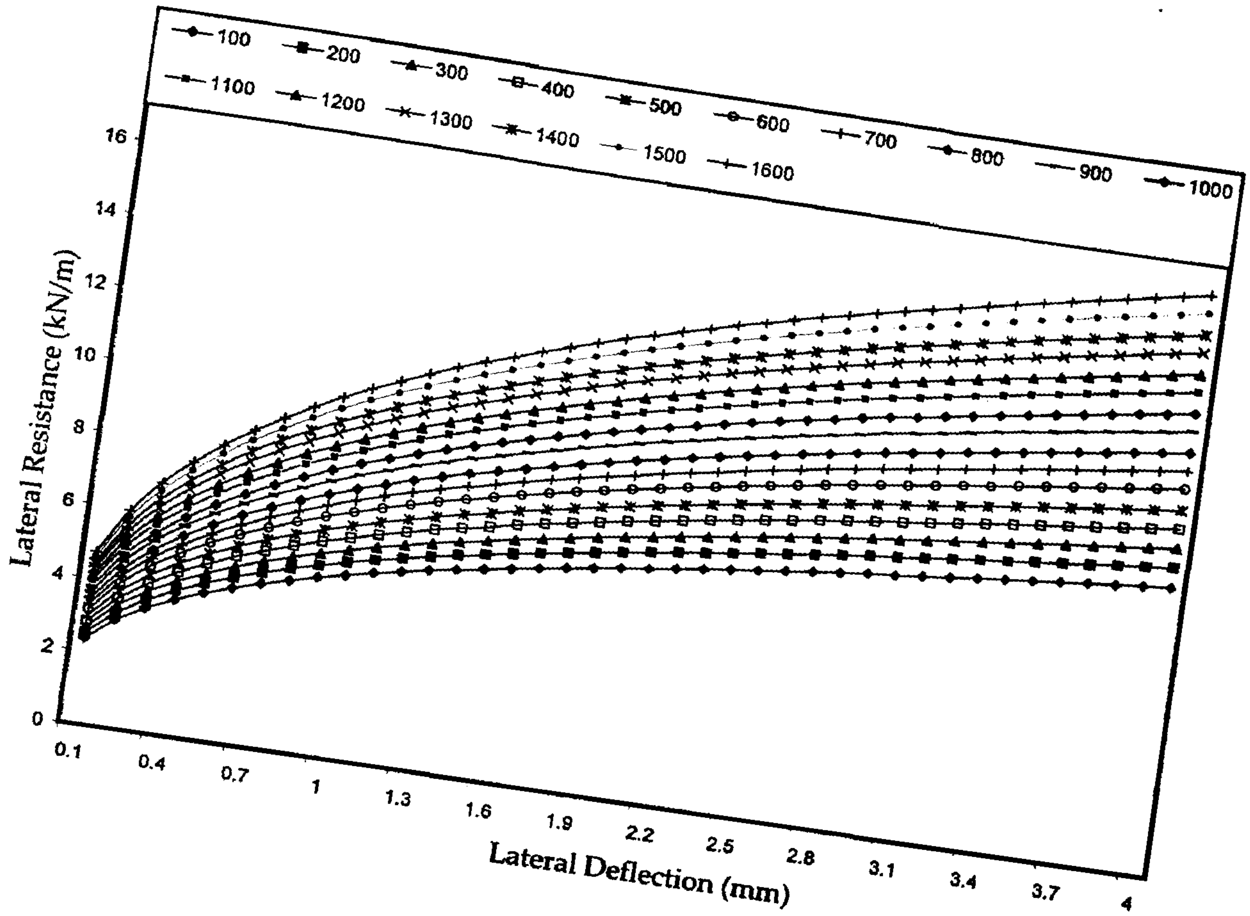

Figure 3.12 Spring coefficient (k_h) for soft clay

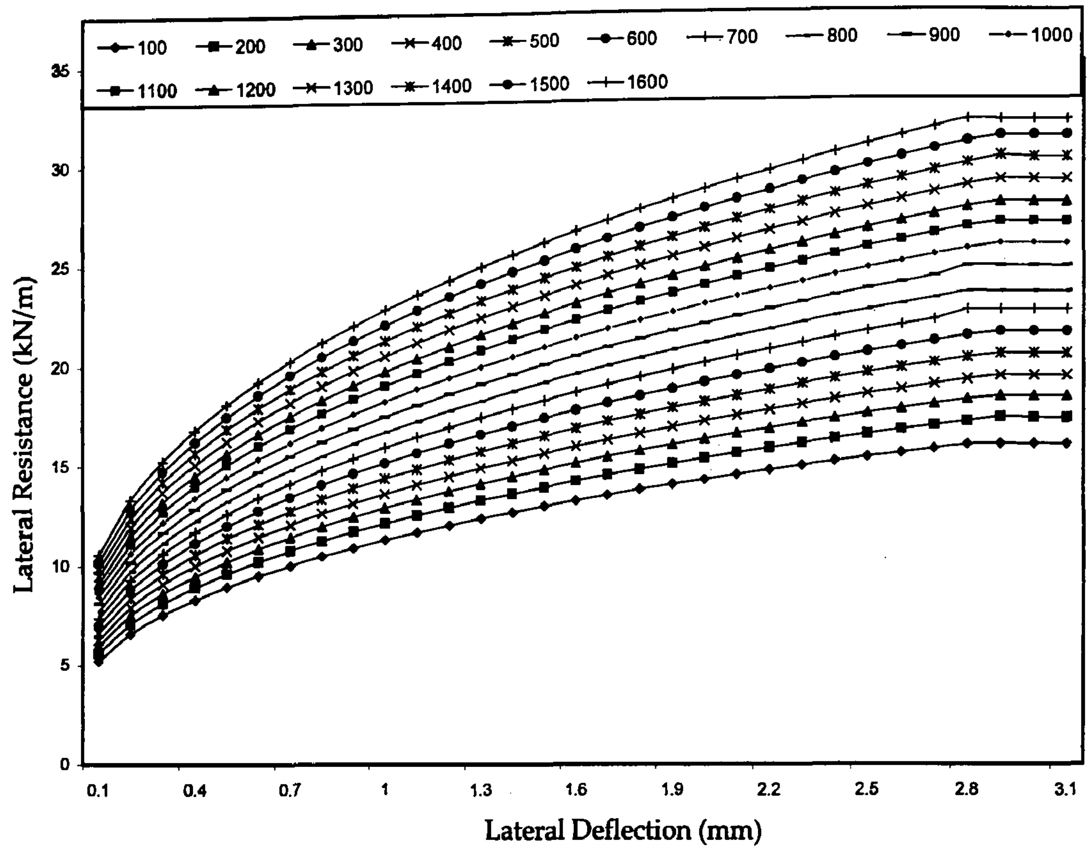

Figure 3.13 Spring coefficient (kh) for stiff clay

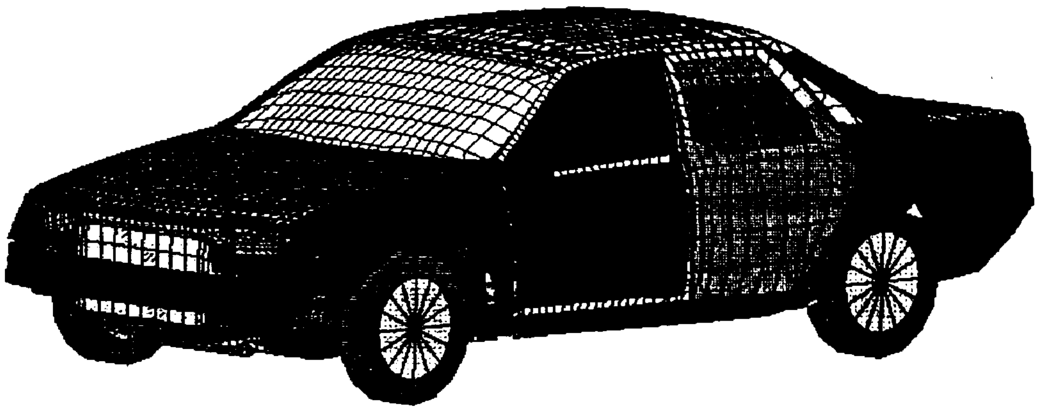

Figure 3.14 Finite element model of the car used in the current study.

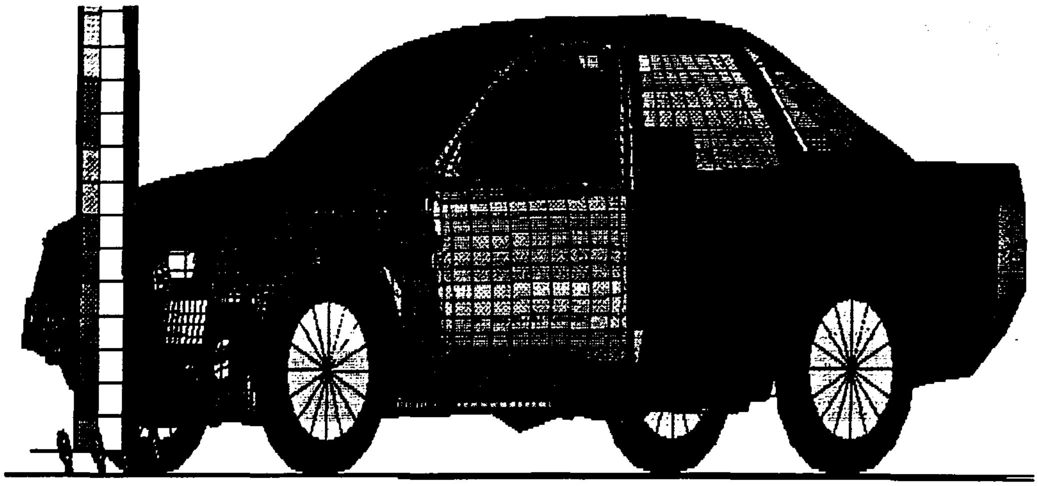

t = 25 ms

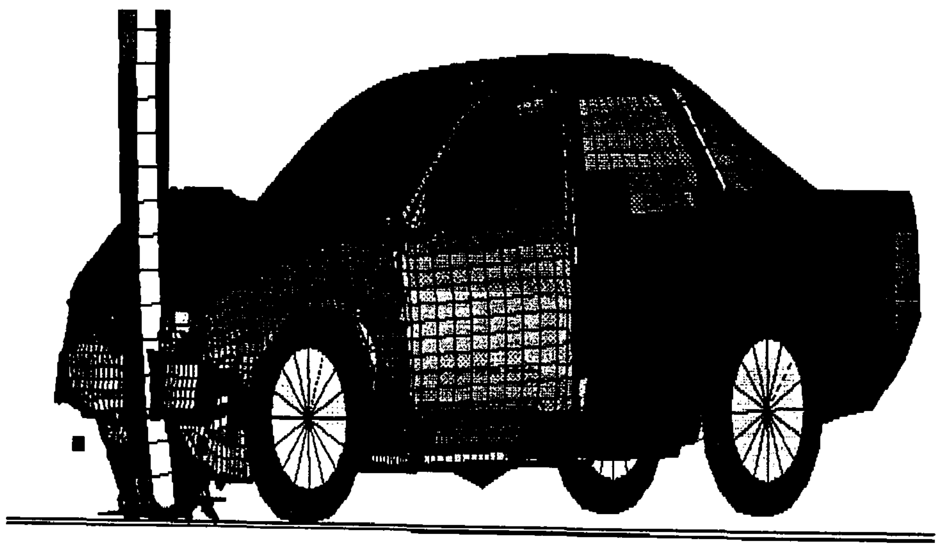

t = 50 ms

Figure 4.1 (a): Deformed shapes of the vehicle and steel pole at different time increments.

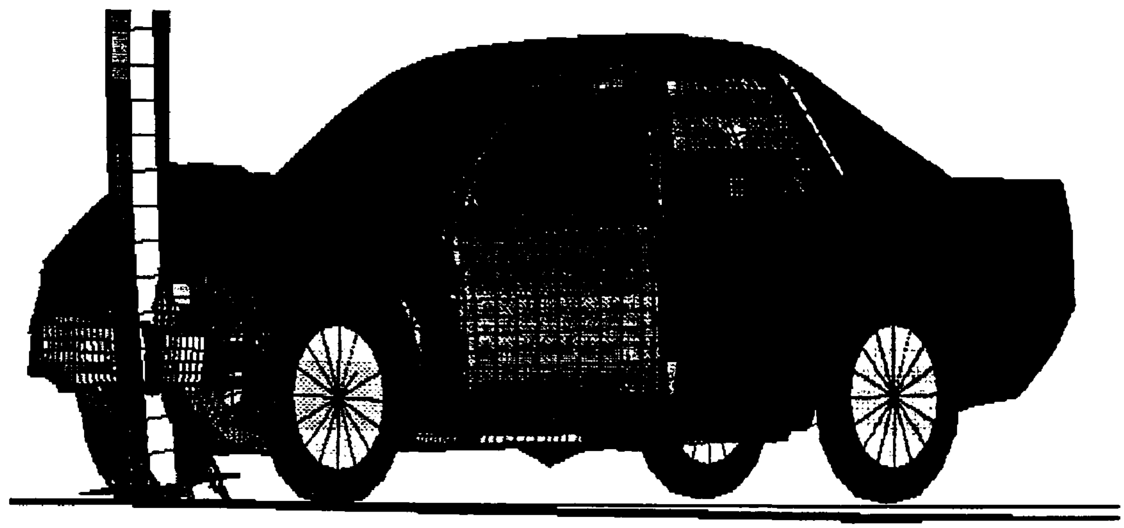

t = 75 ms

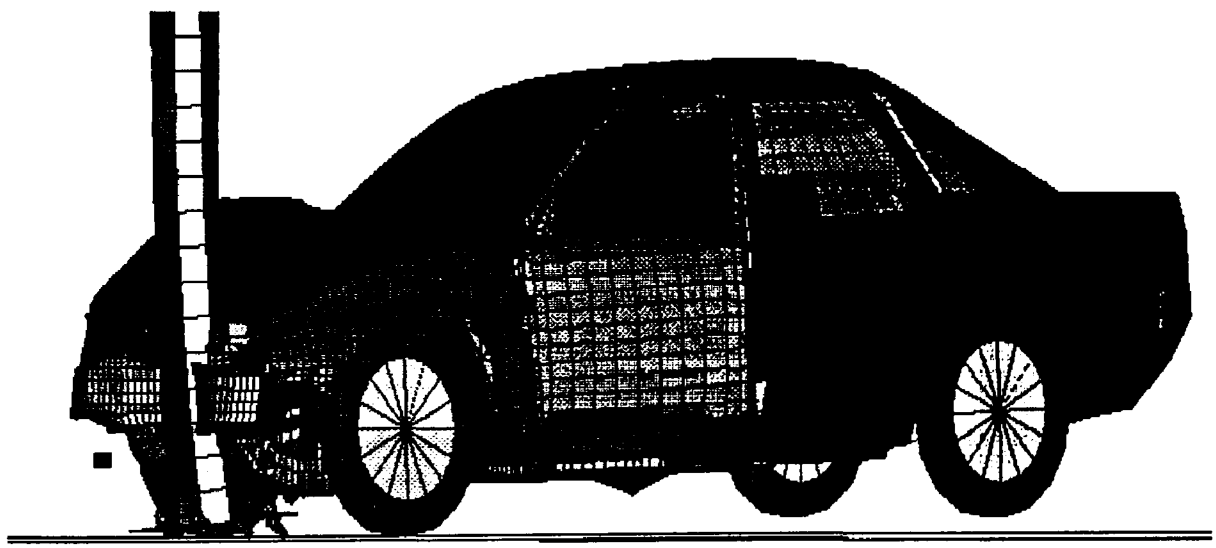

t = 100 ms

Figure 4.1 (b) Deformed shapes of the vehicle and steel pole at different time increments.

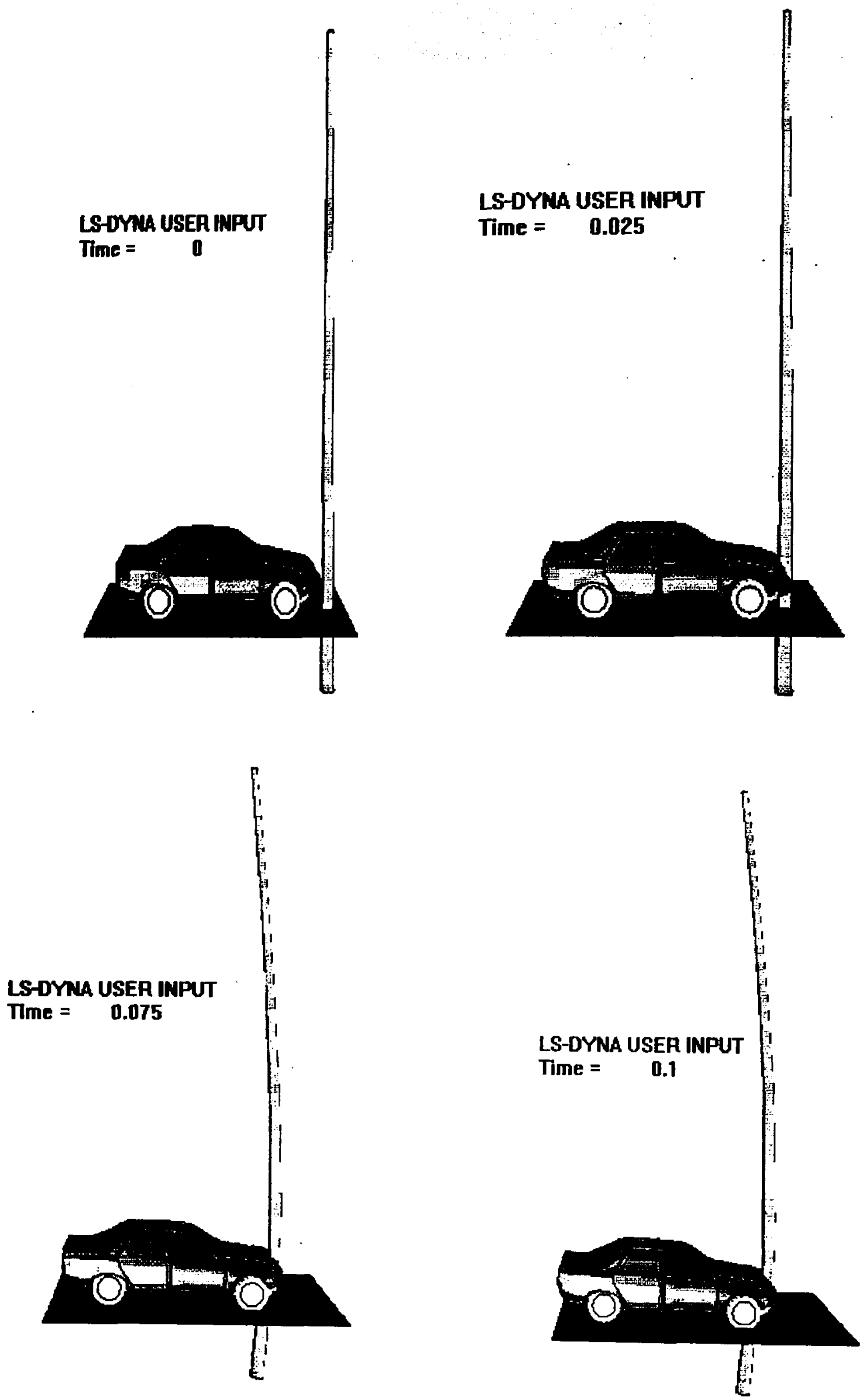

Figure 4.2: Frontal impact to steel pole embedded into soil

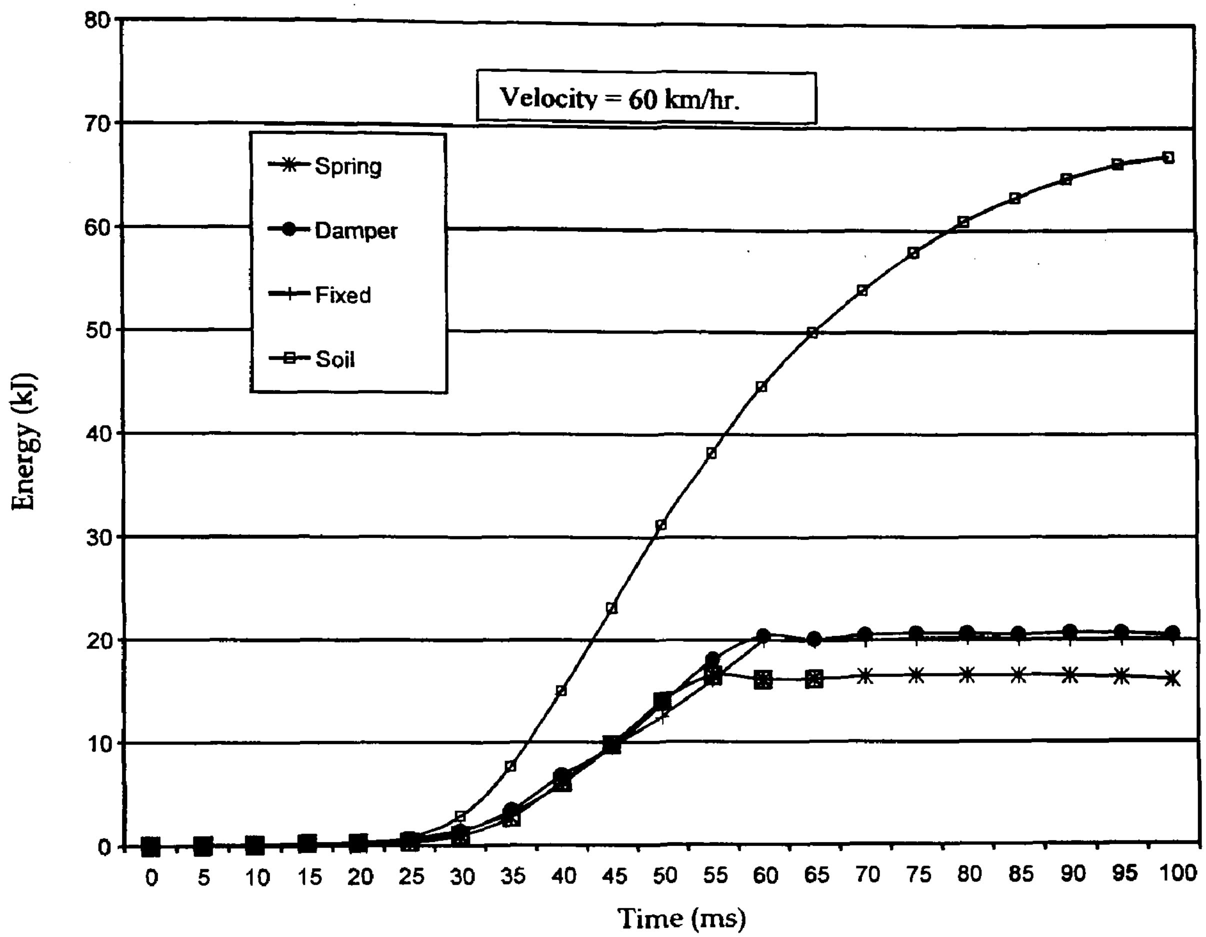

Figure 4.3 Energy absorbed by the steel pole for different support conditions in frontal impact.

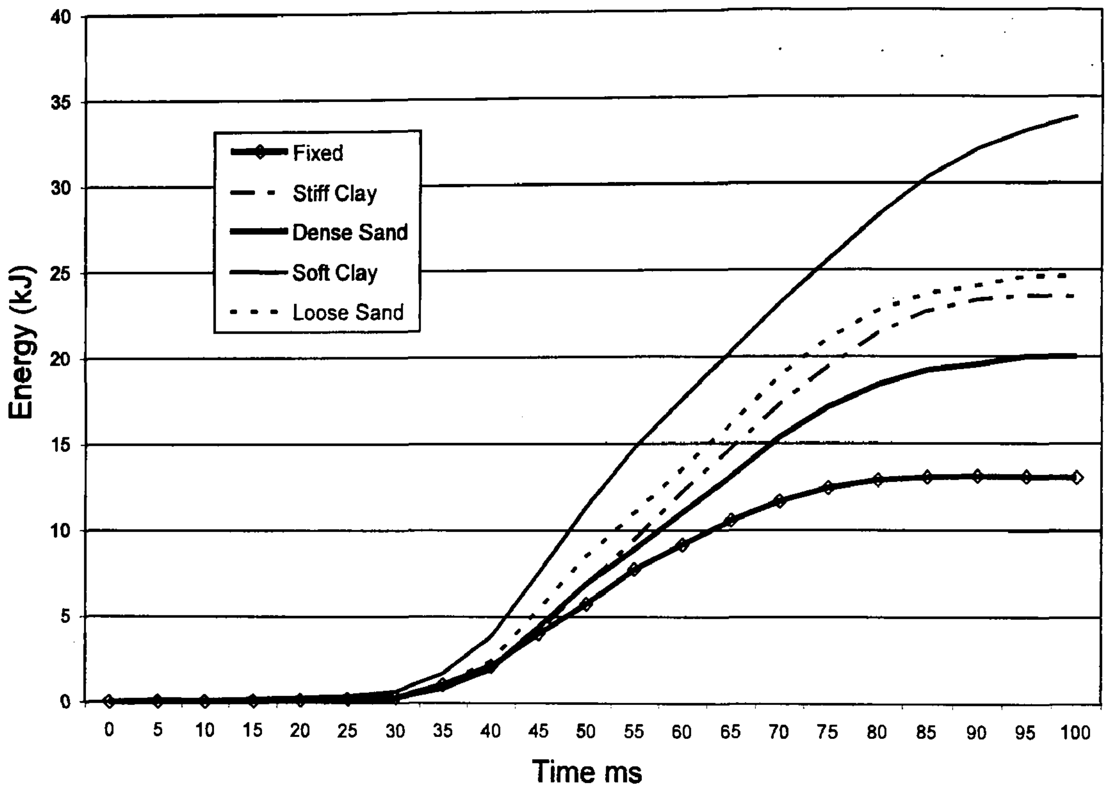

Figure 4.4 Energy absorbed by the steel pole embedded in different types of soil in frontal impact.

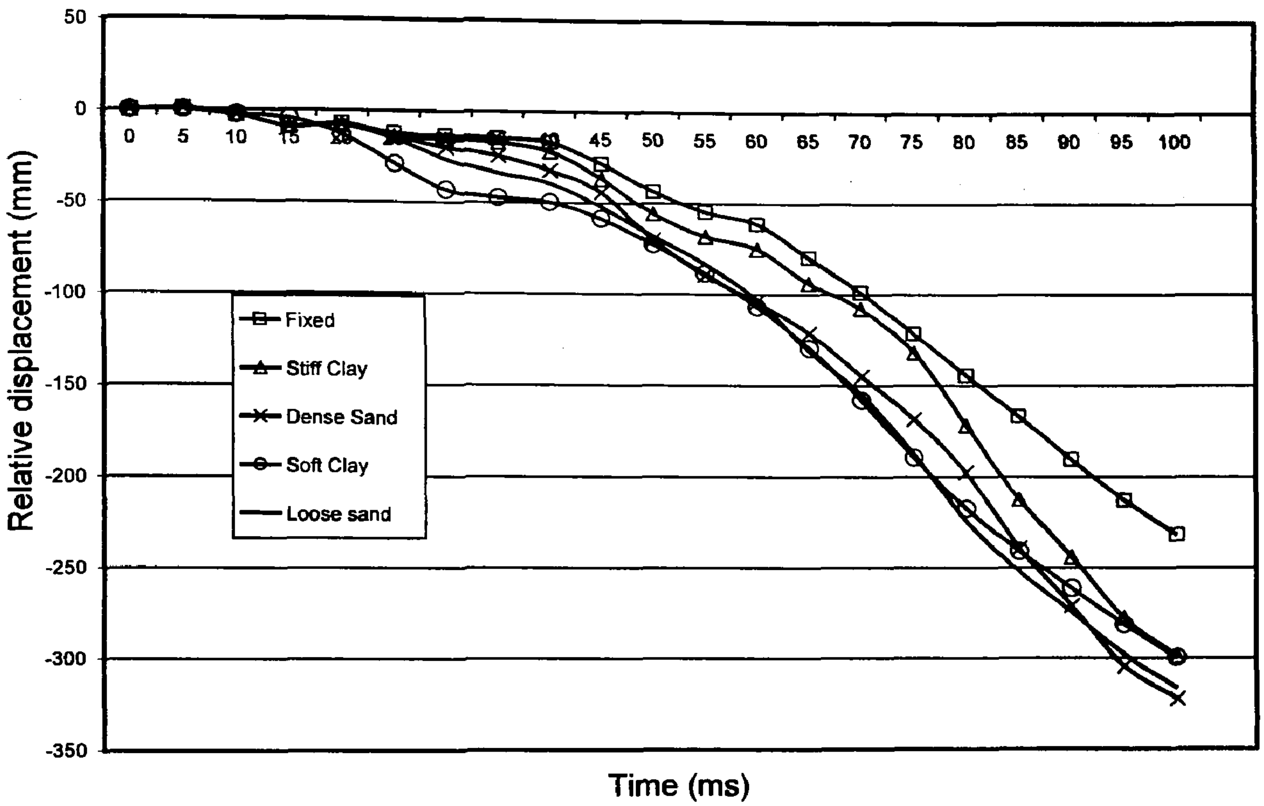

Figure 4.5 Relative displacements between centre of steering wheel and corresponding point on the driver's seat, in frontal impact.

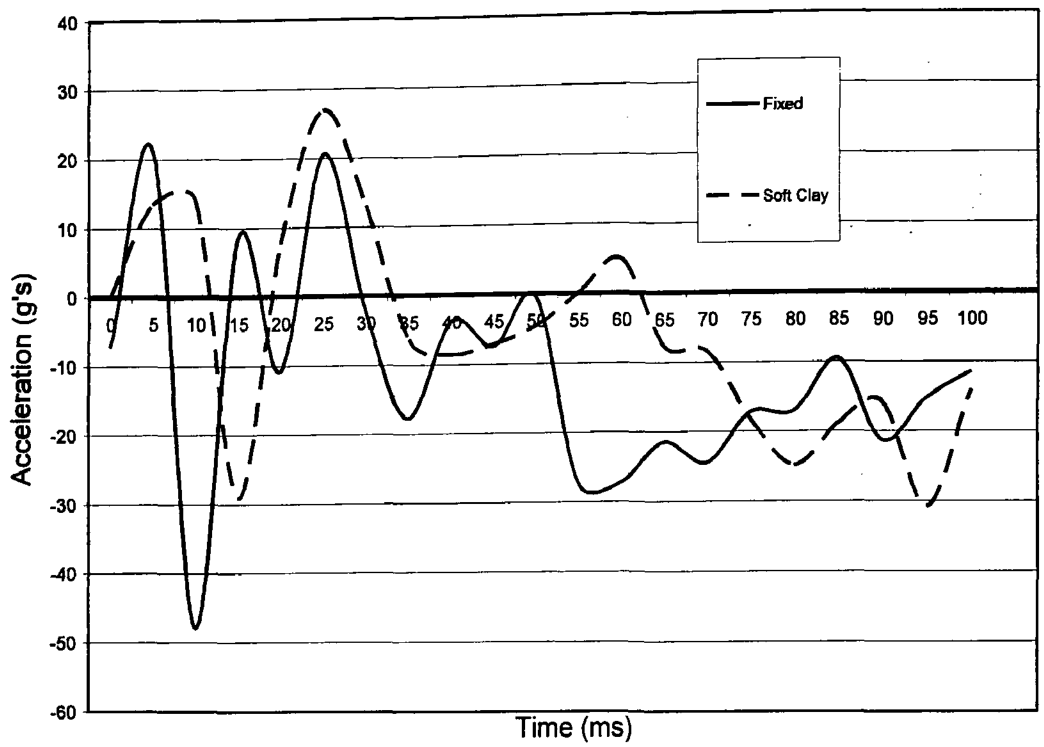

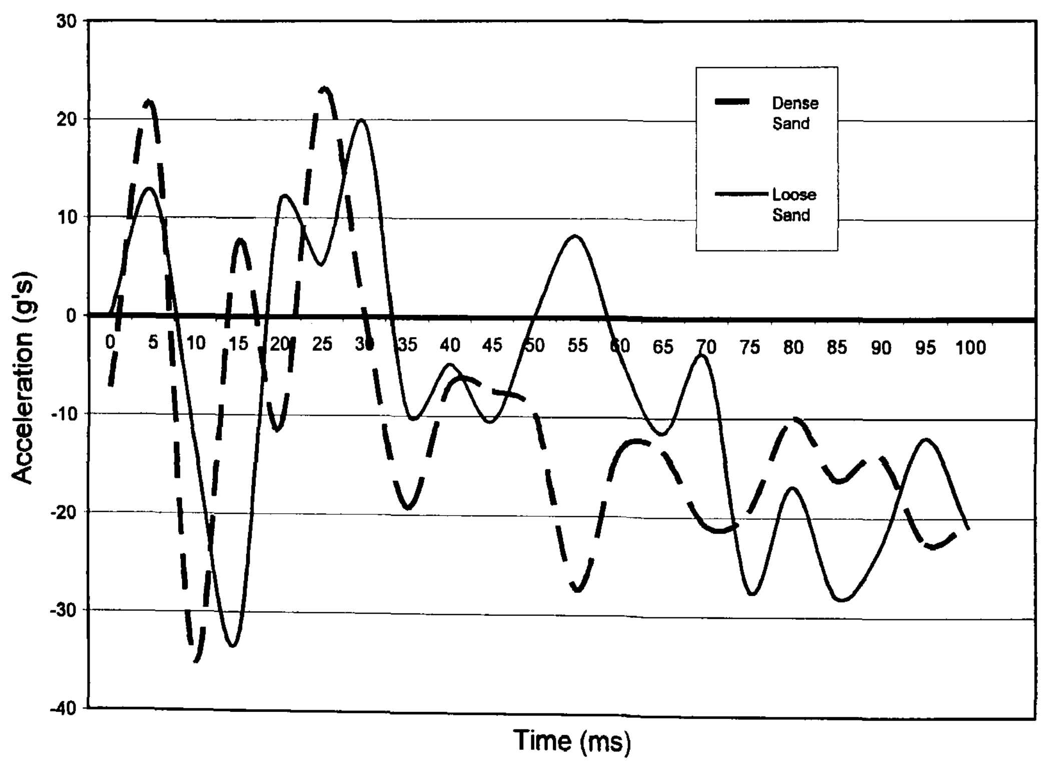

Figure 4.6: Resultant acceleration-time histories at a point on the driver's seat in frontal impact, pole embedded 1500mm in soil.

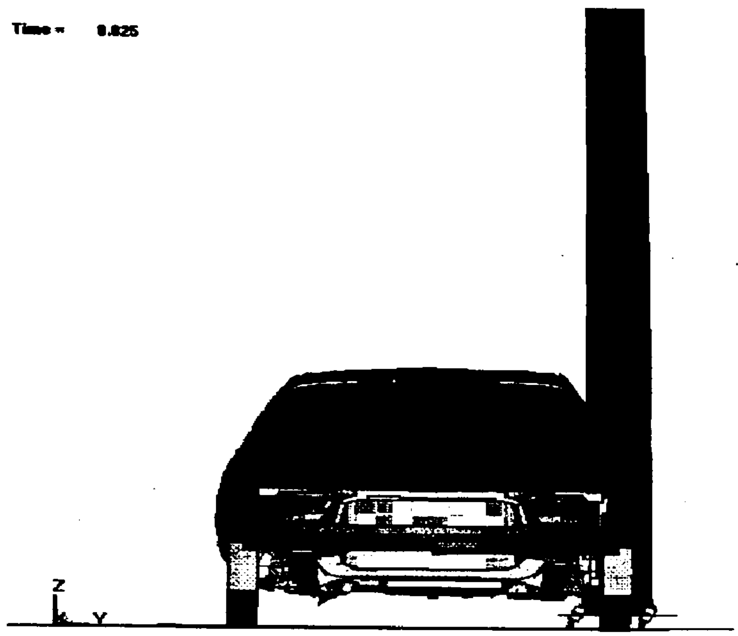

t = 25 ms

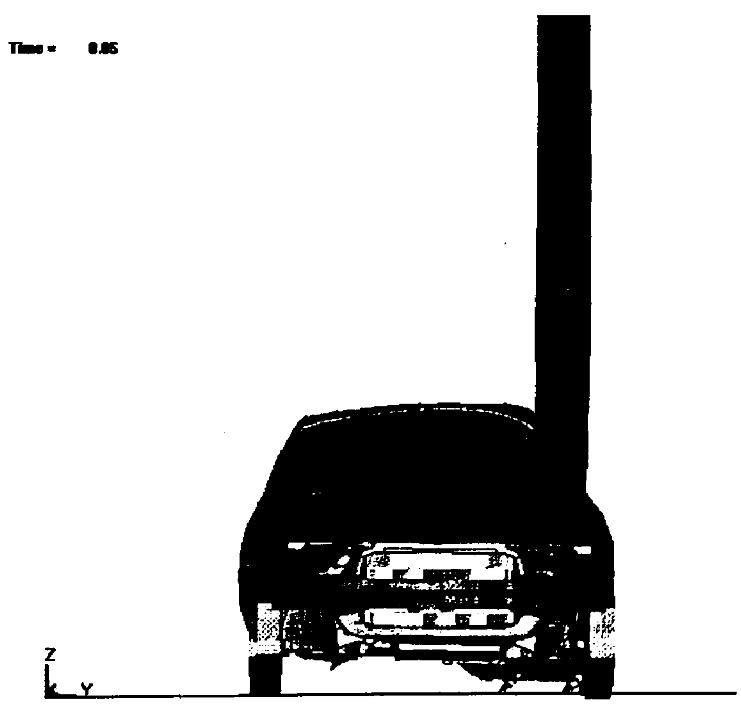

t = 50 ms

Figure 4.7 (a) Deformed shape of the vehicle side impact with the pole.

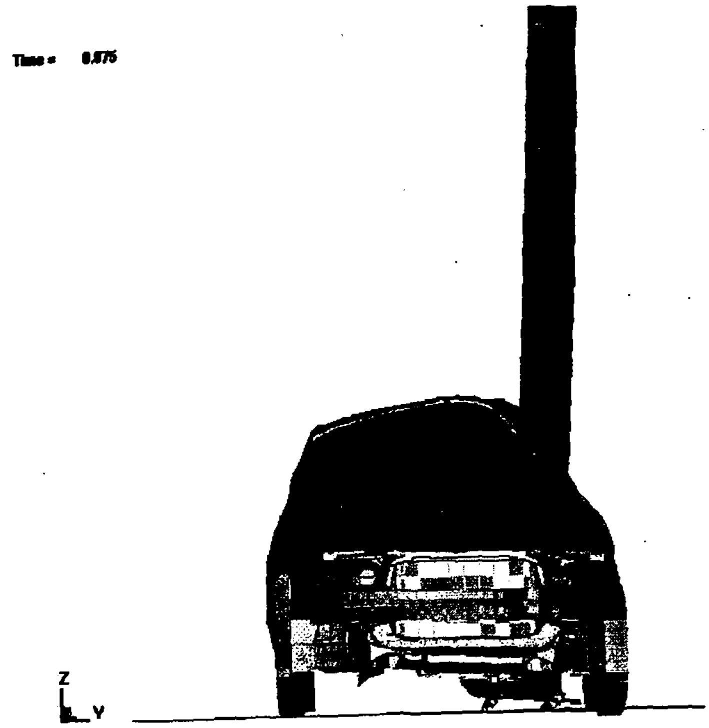

t = 75 ms

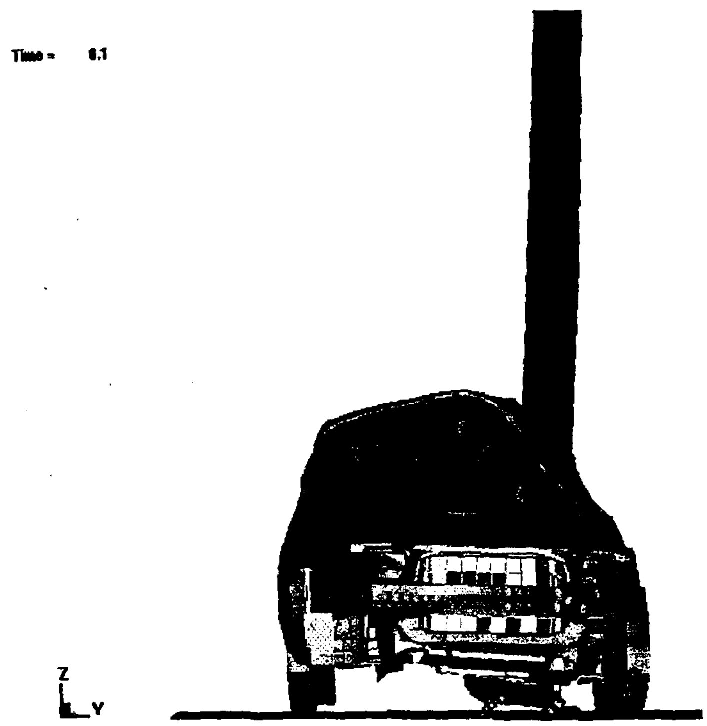

t = 100 ms

Figure 4.7 (b) Deformed shape of the vehicle in side impact with the pole.

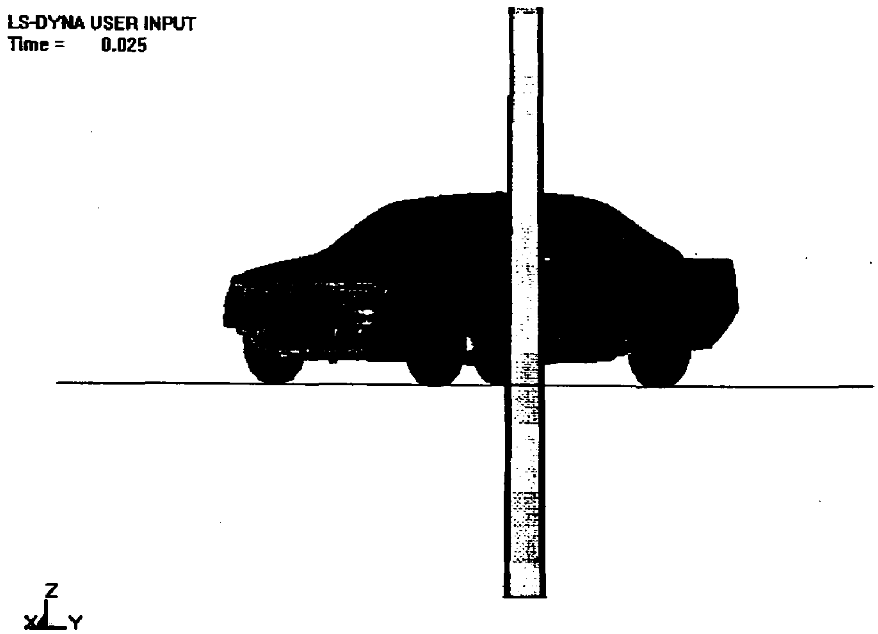

t = 25 ms

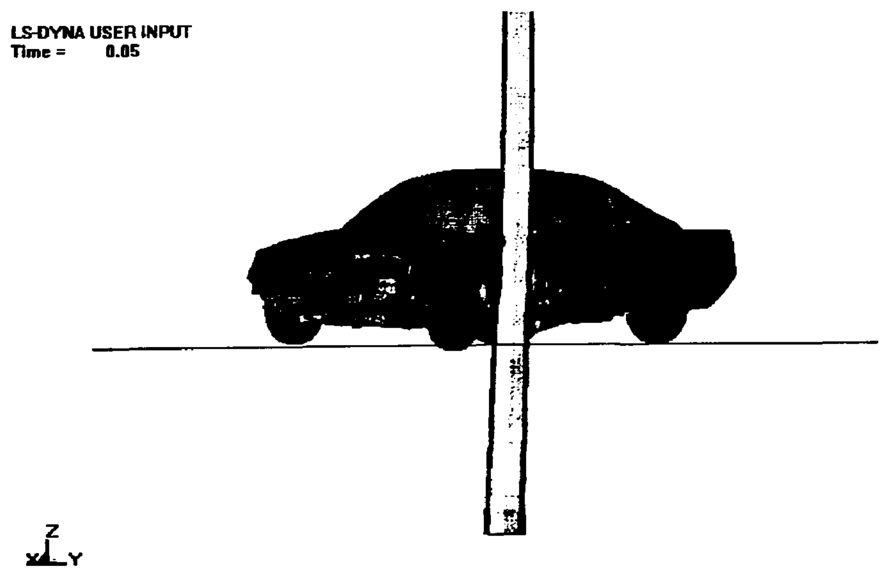

t = 50 ms

Figure 4.8 (a) Pole Embedded in Soil

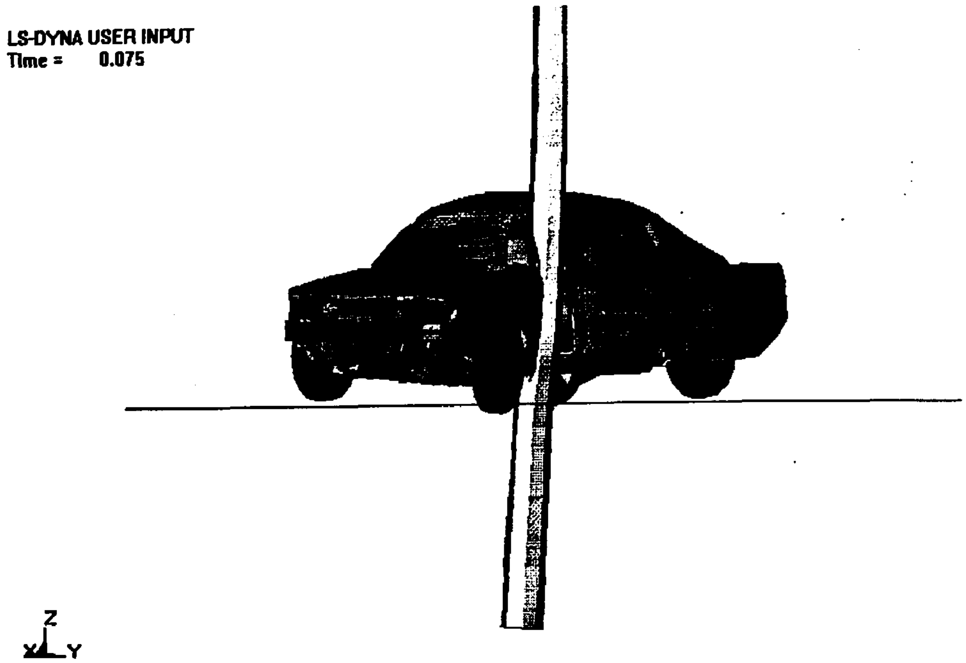

t = 75 ms

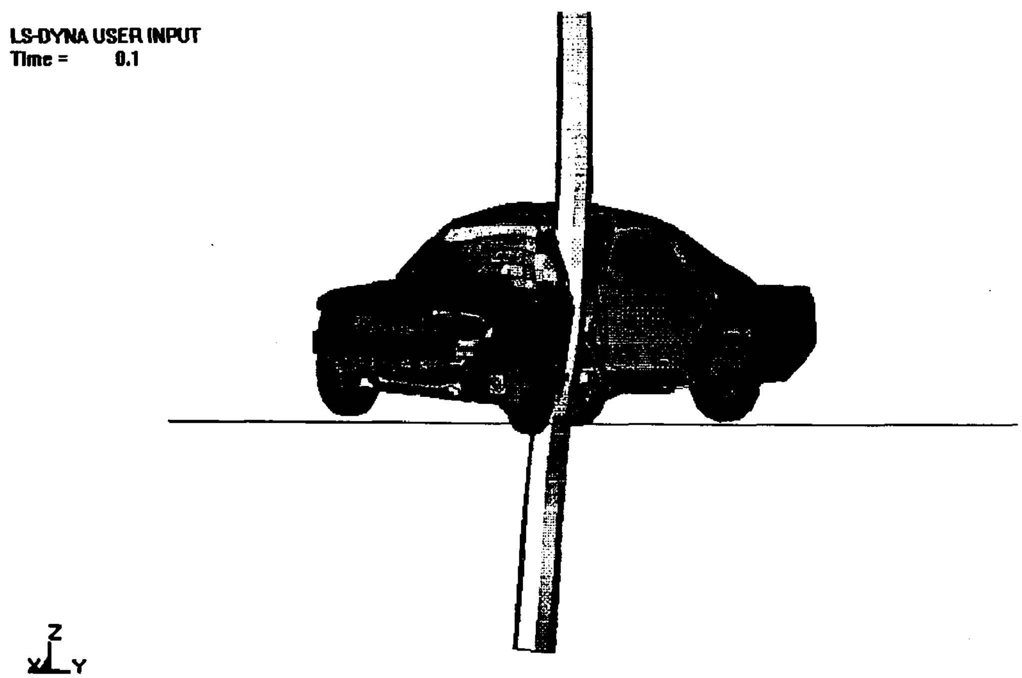

t = 100 ms

Figure 4.8 (b) Pole embedded in soil

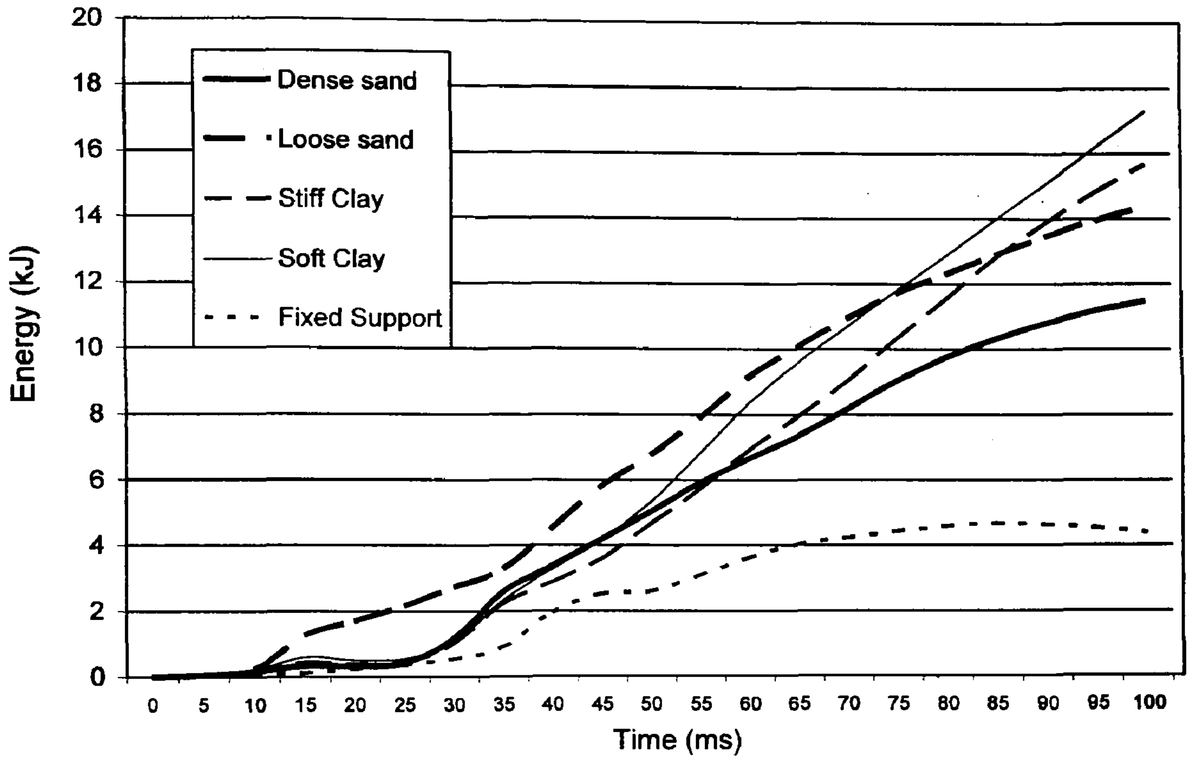

Figure 4.9 Energy absorbed by the steel pole for different support conditions in side impact.

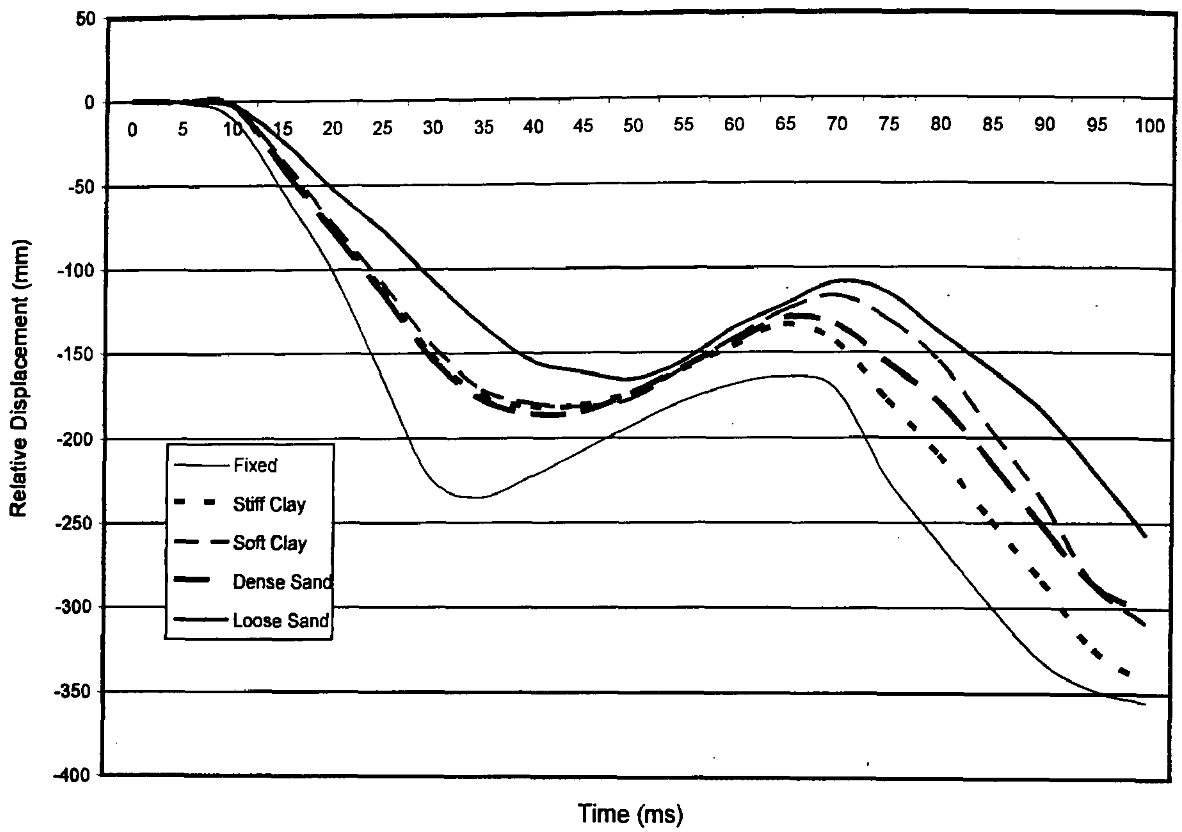

Figure 4.10 Relative displacements between a point on the driver's door and the corresponding point on the driver's seat during side impact.

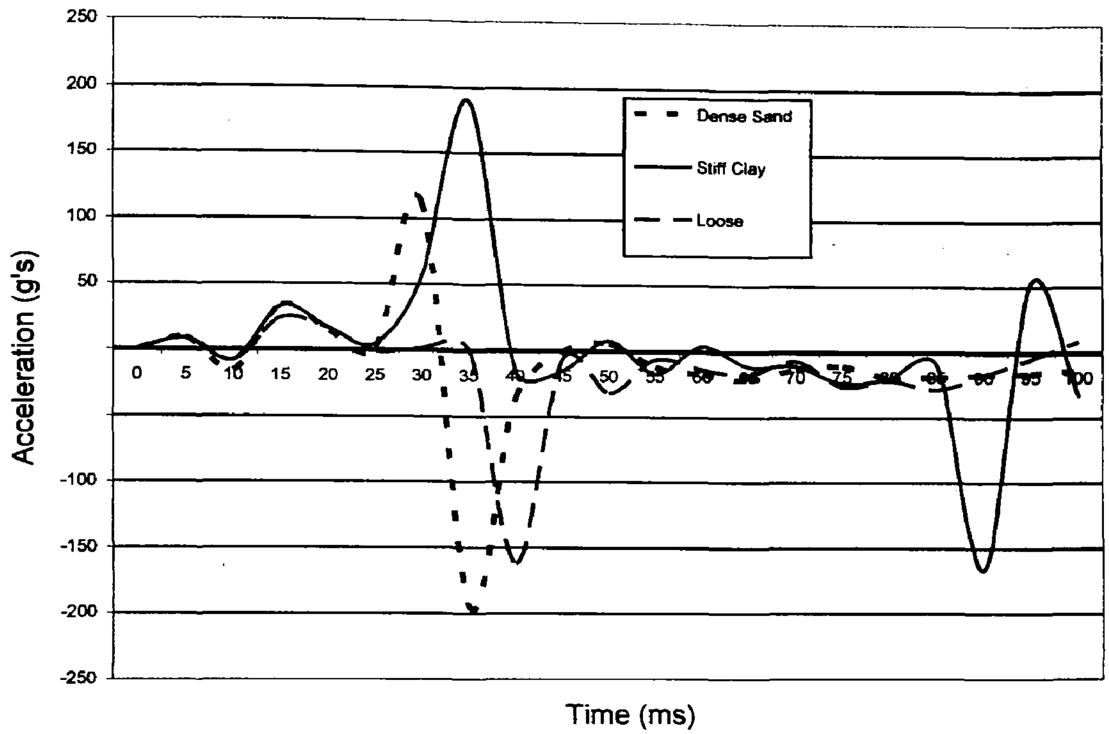

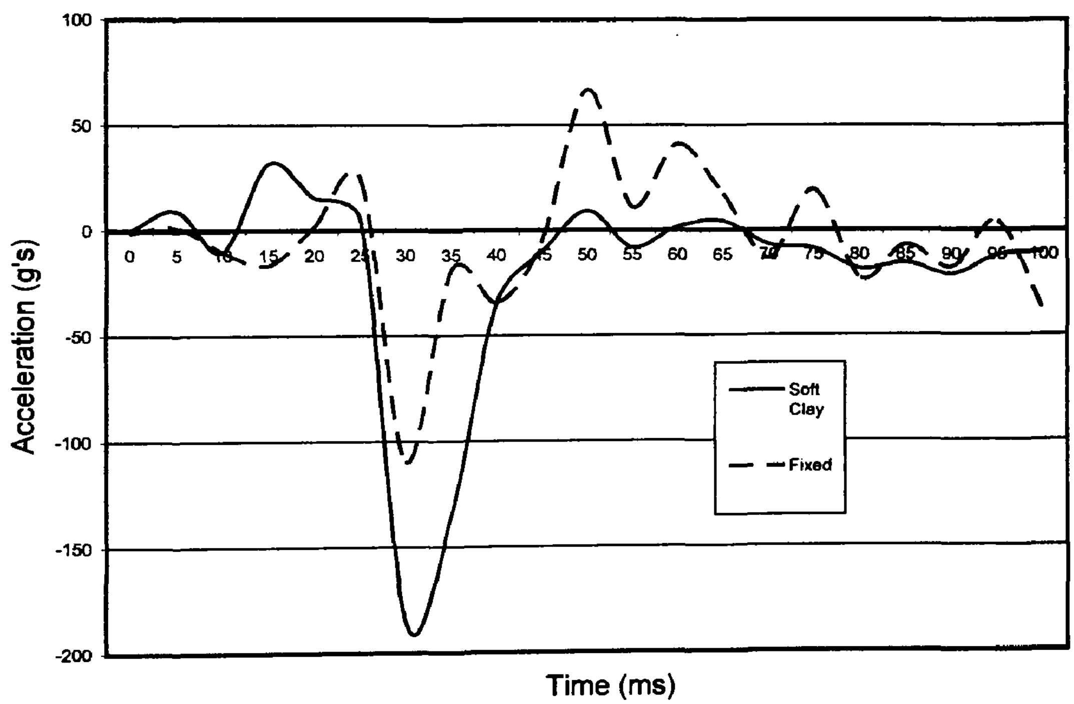

Figure 4.11 Resultant acceleration-time histories at a point on the driver's seat during side impact.

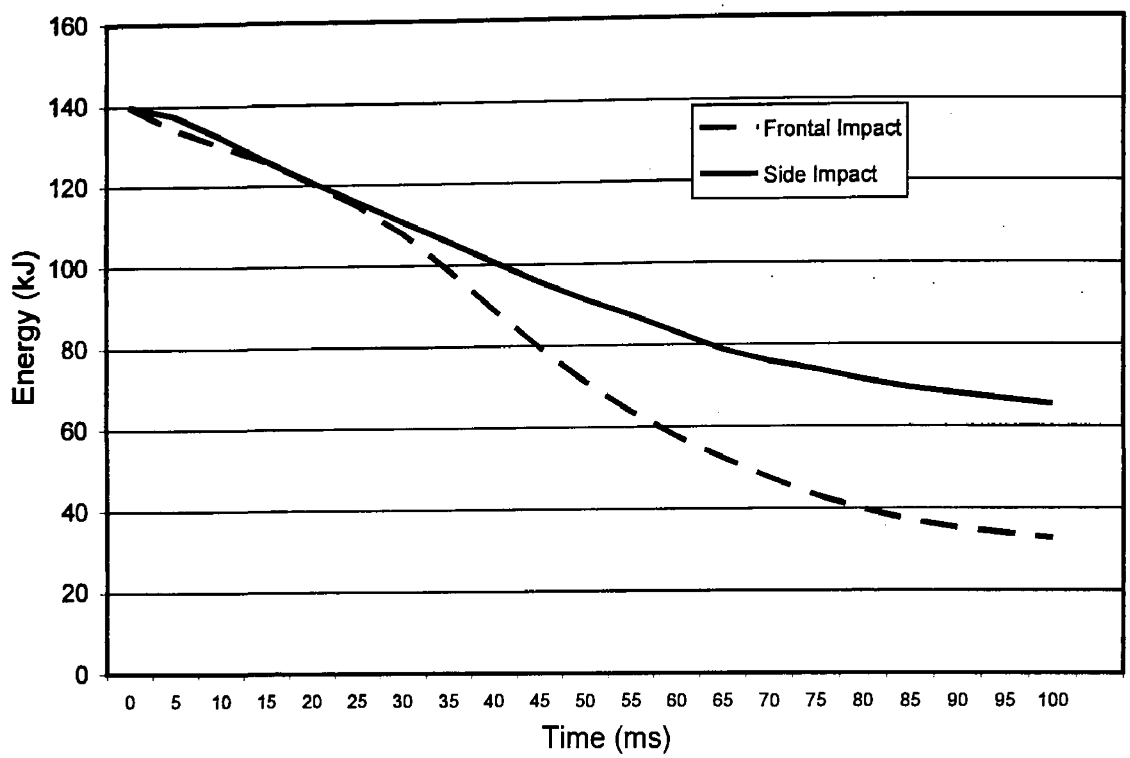

(a) Energy decay in frontal and side impact.

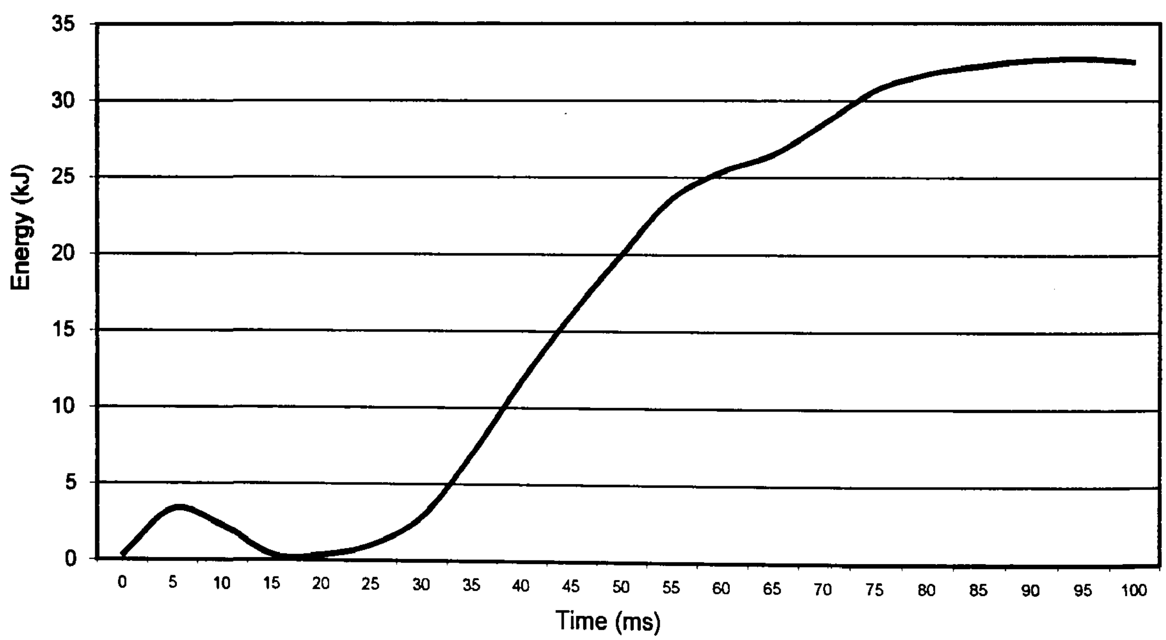

(b) Relative difference in kinetic energy.

Figure 4.12 Decay of kinetic energy in frontal and side impact.

(a) Energy Absorbed by the Steel Pole Embedded in Soft Clay
Impact Speed 50 km/hr

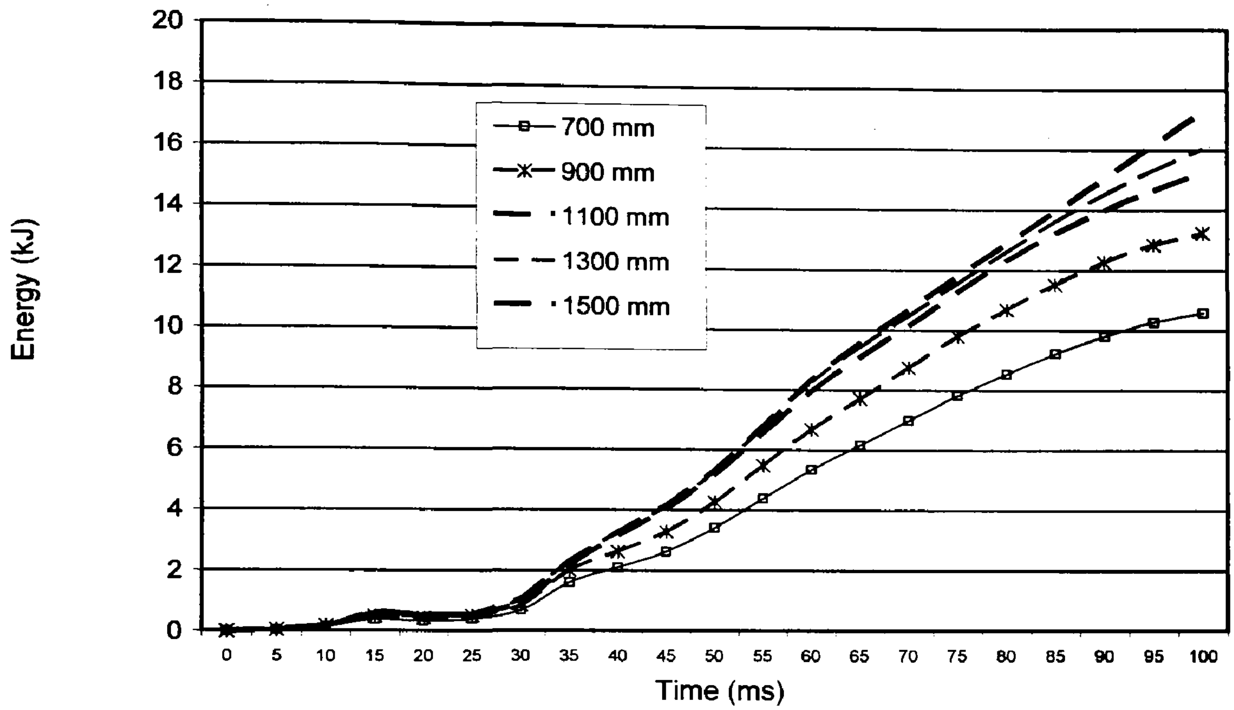

(b) Energy Absorbed by the Steel Pole Embedded in Stiff Clay
Impact Speed 50 km/hr

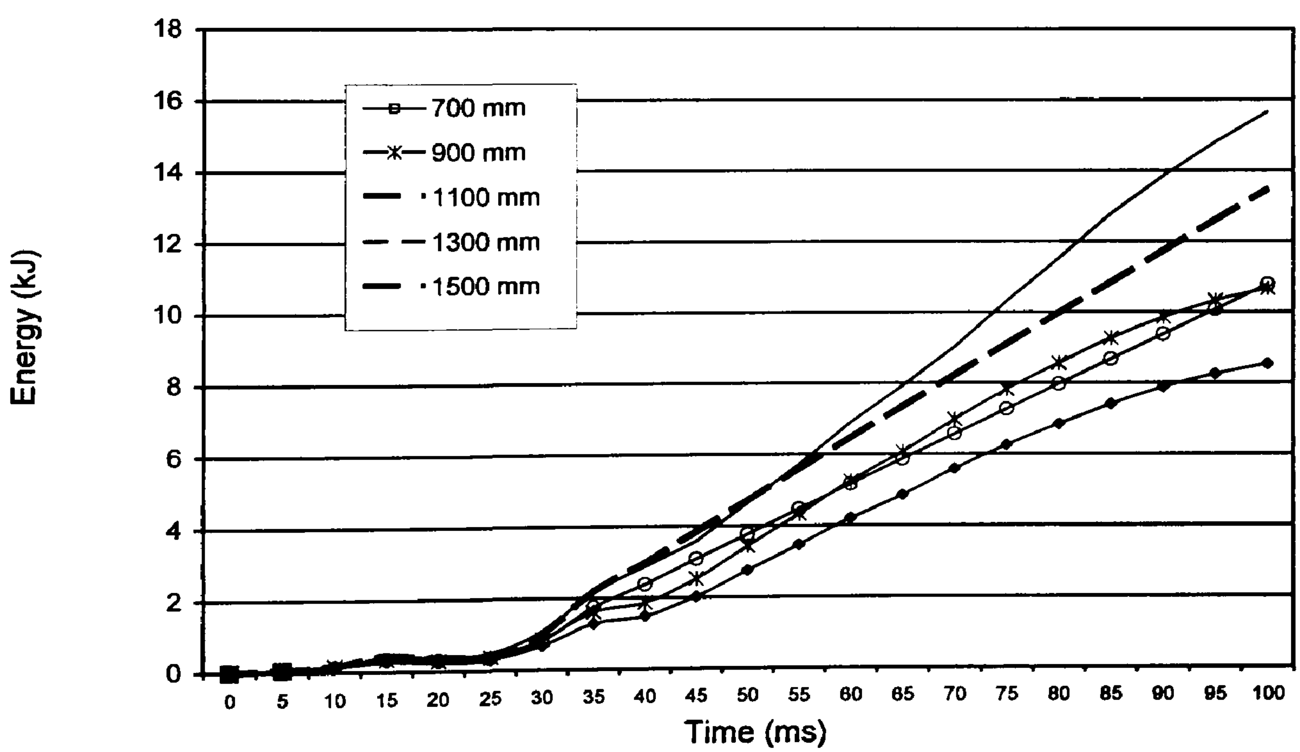

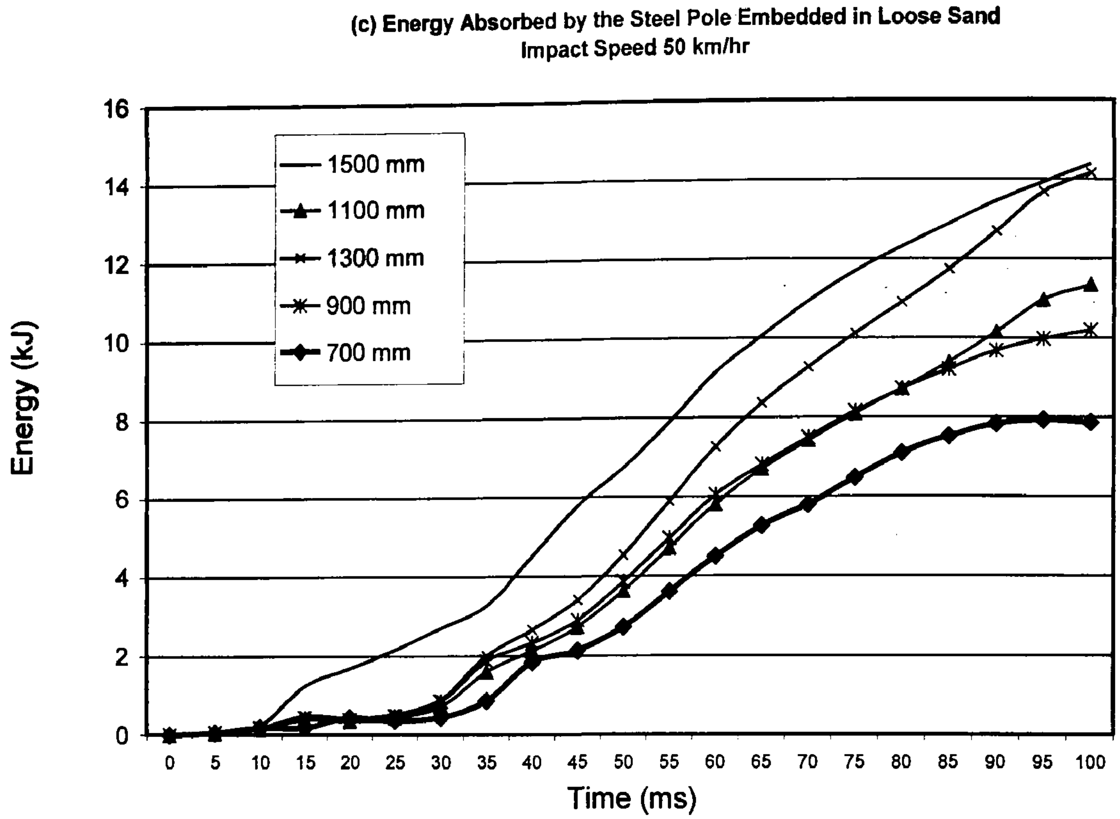

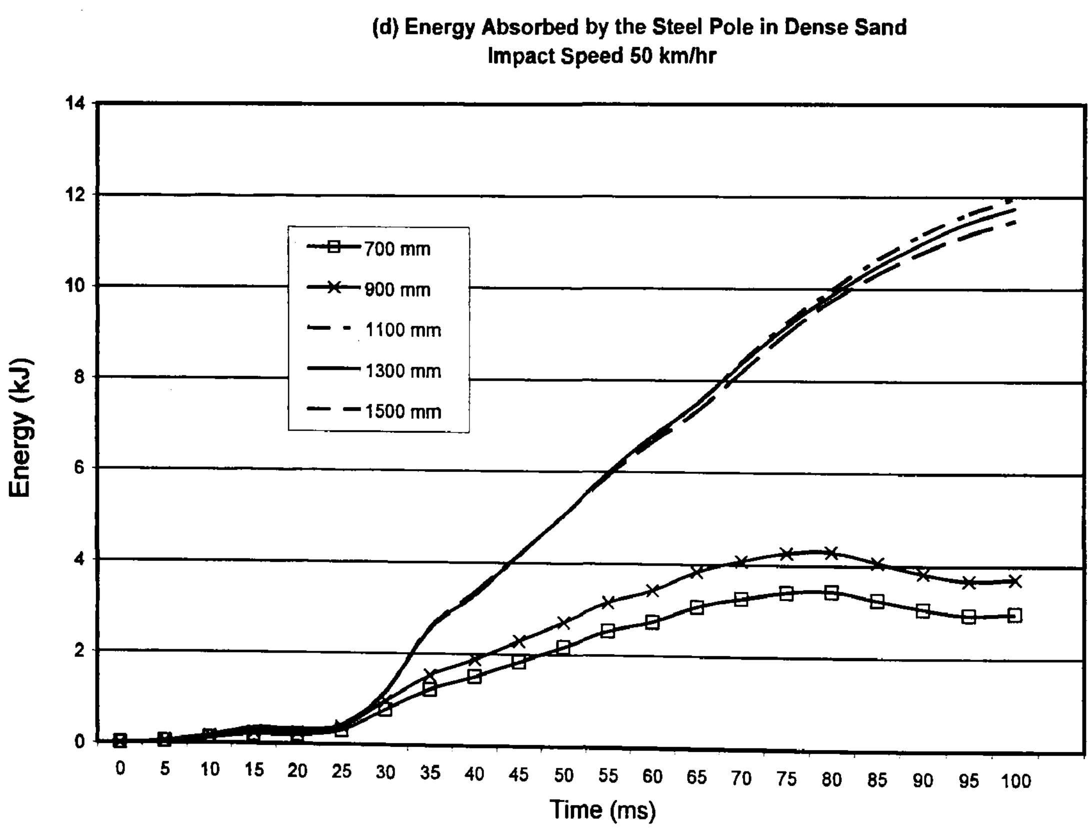

Figure 4.13 Effect of embedment depth on energy absorbed by the steel pole during side impact.

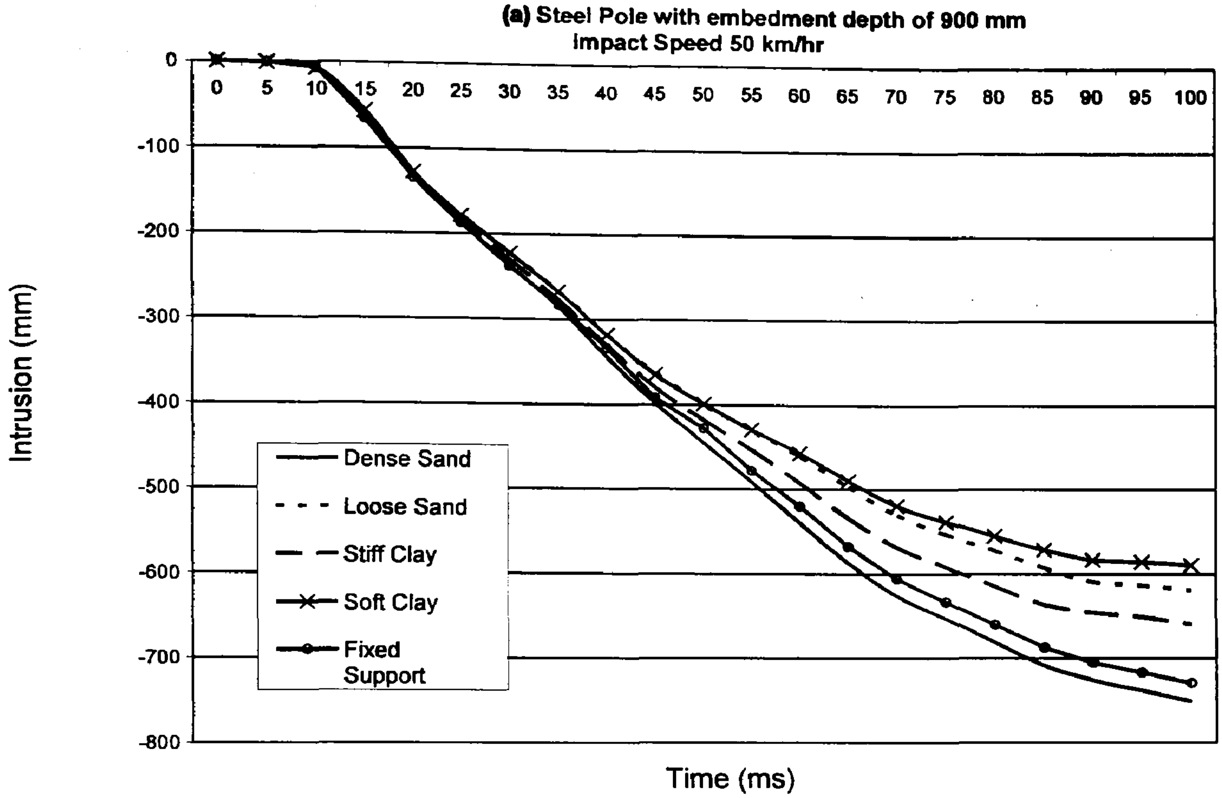

(a) Steel Pole with embedment depth of 900 mm
Impact Speed 50 km/hr
Intrusion (mm)
0
-100
-200
-300
-400
-500
-600
-700
-800
0 5 10 15 20 25 30 35 40 45 50 55 60 65 70 75 80 85 90 95 100
Dense Sand
Loose Sand
Stiff Clay
Soft Clay
Fixed Support
Time (ms)

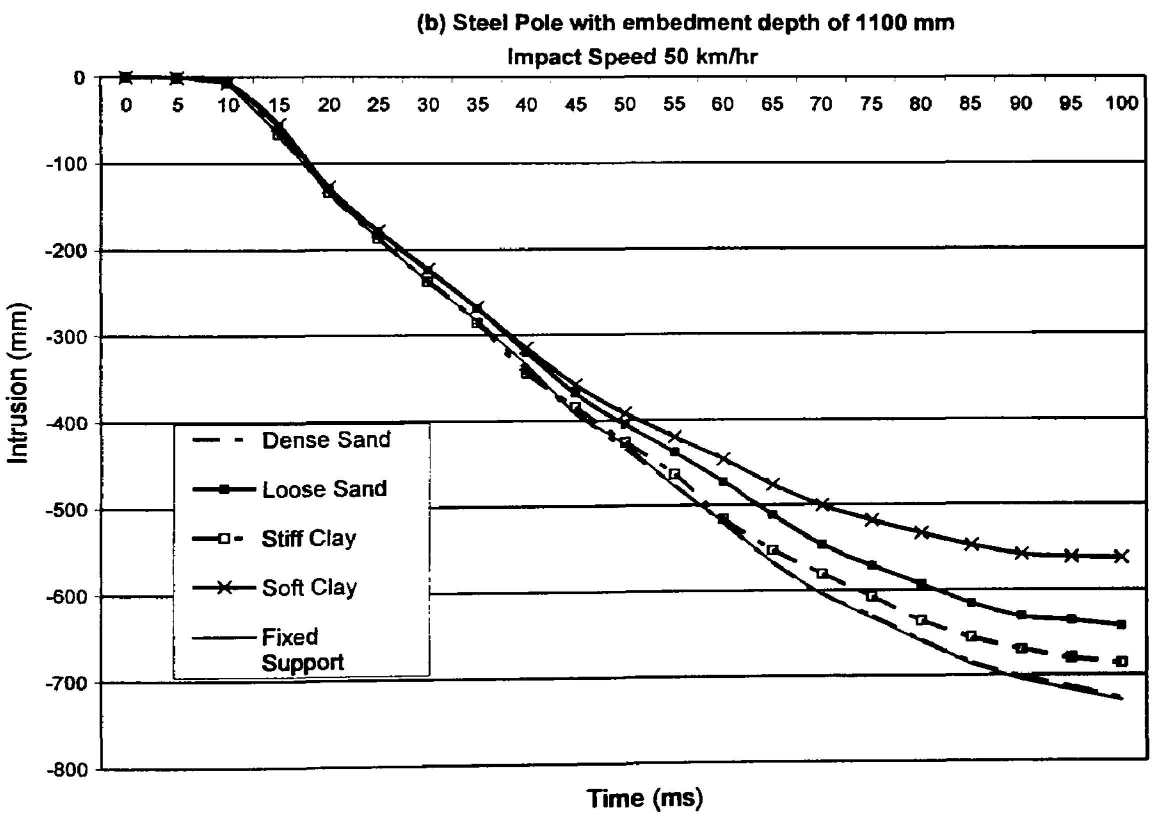

(b) Steel Pole with embedment depth of 1100 mm
Impact Speed 50 km/hr
Intrusion (mm)
0
-100
-200
-300
-400
-500
-600
-700
-800
0 5 10 15 20 25 30 35 40 45 50 55 60 65 70 75 80 85 90 95 100
Dense Sand
Loose Sand
Stiff Clay
Soft Clay
Fixed Support
Time (ms)

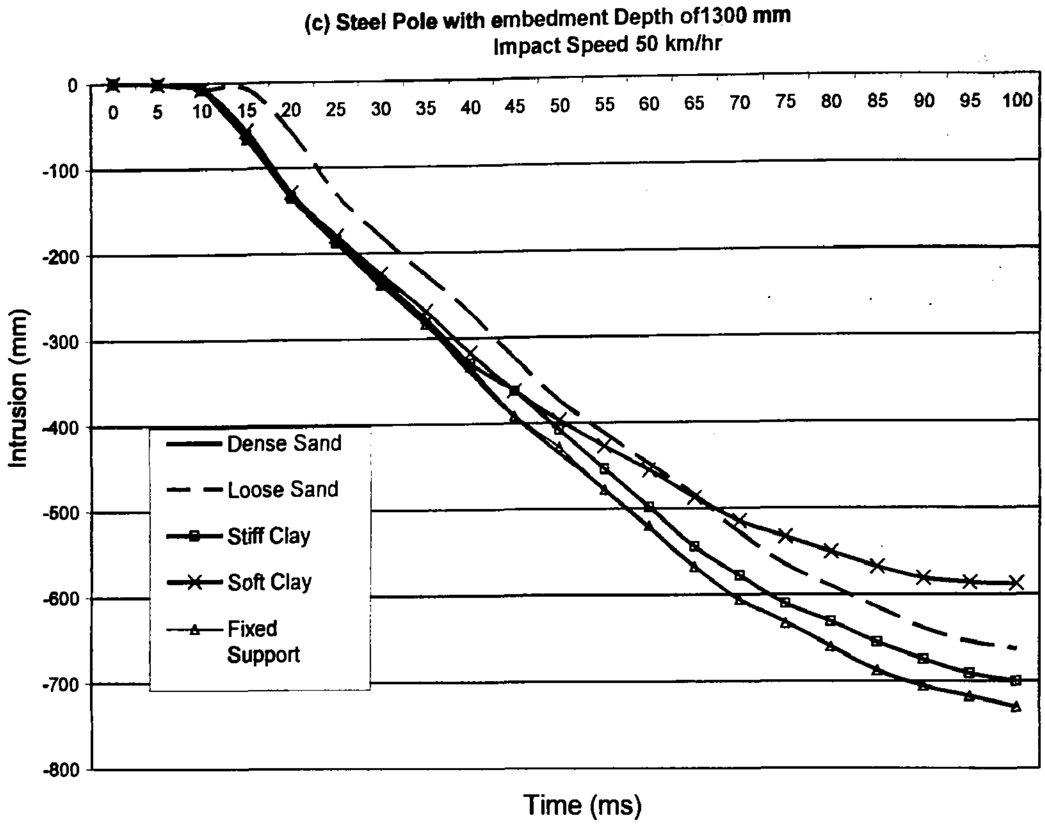

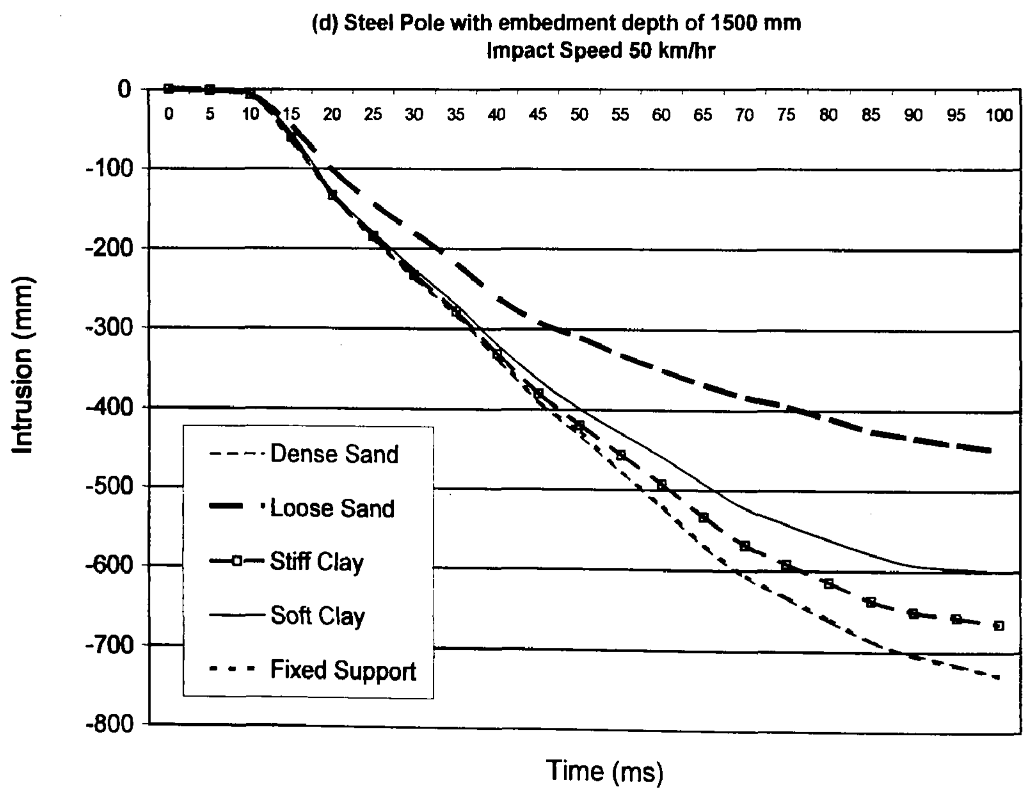

Figure 4.14 Intrusion of passenger compartment for the steel poles in side impact.

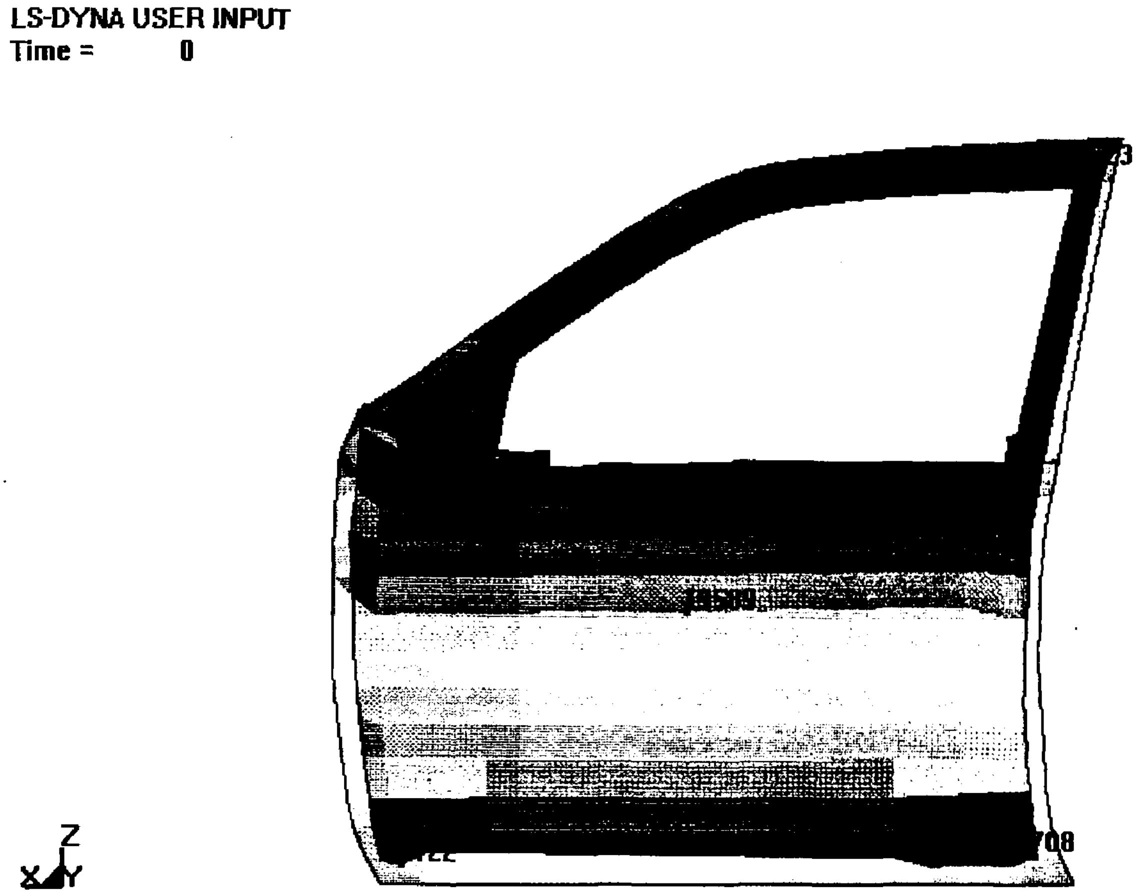

Figure 4.15 Location of nodes on the driver side door in side impact.

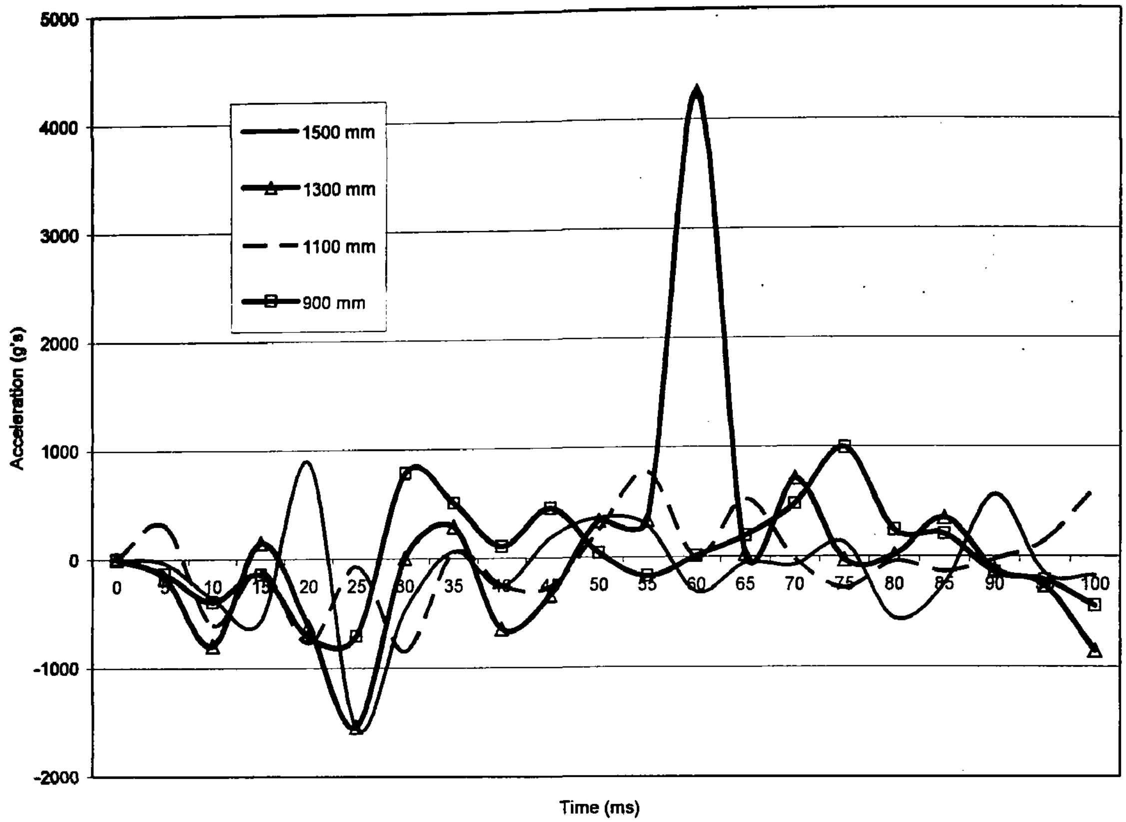

a) Steel pole embedded in dense sand: Node #523

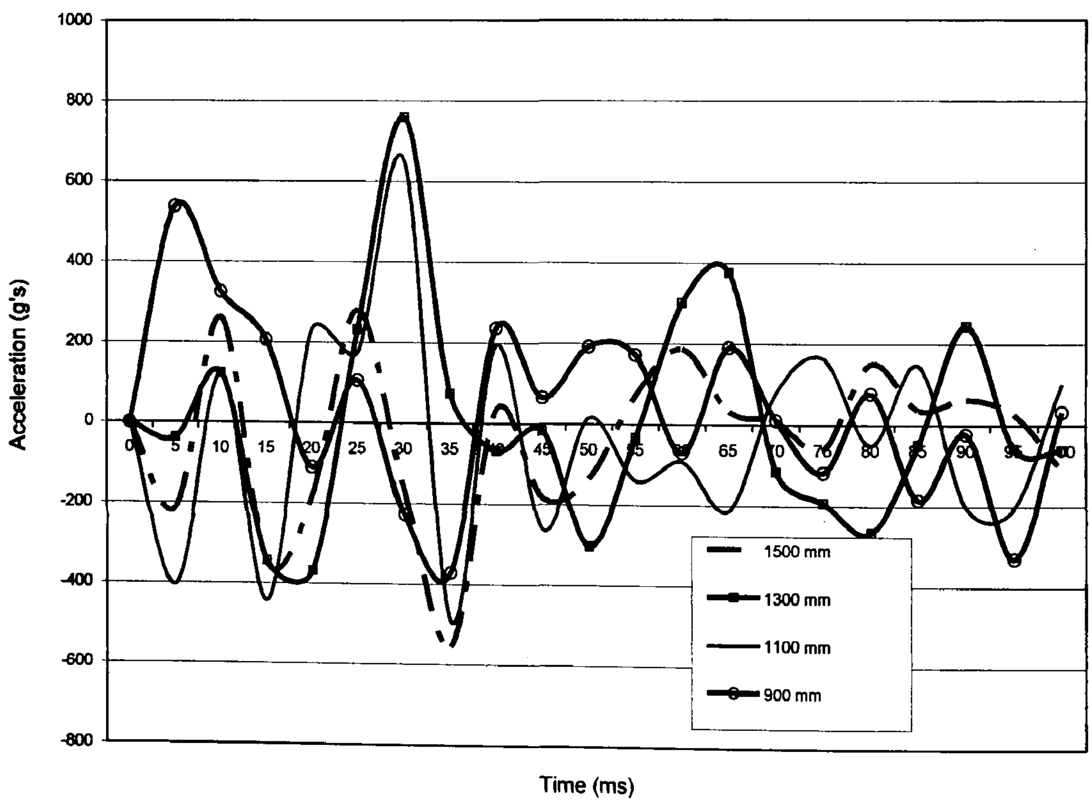

b) Steel pole embedded in dense sand: Node #1317

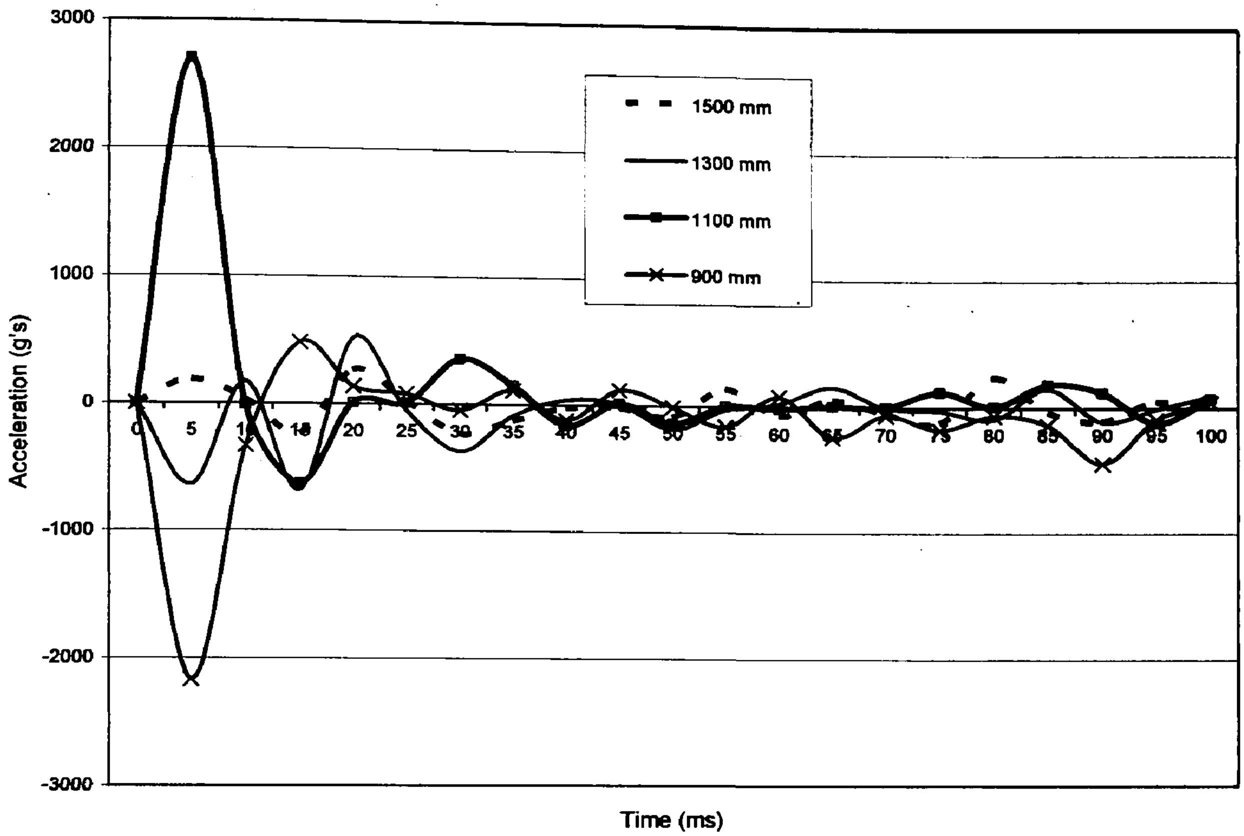

c) Steel pole embedded in dense sand : Node # 19589

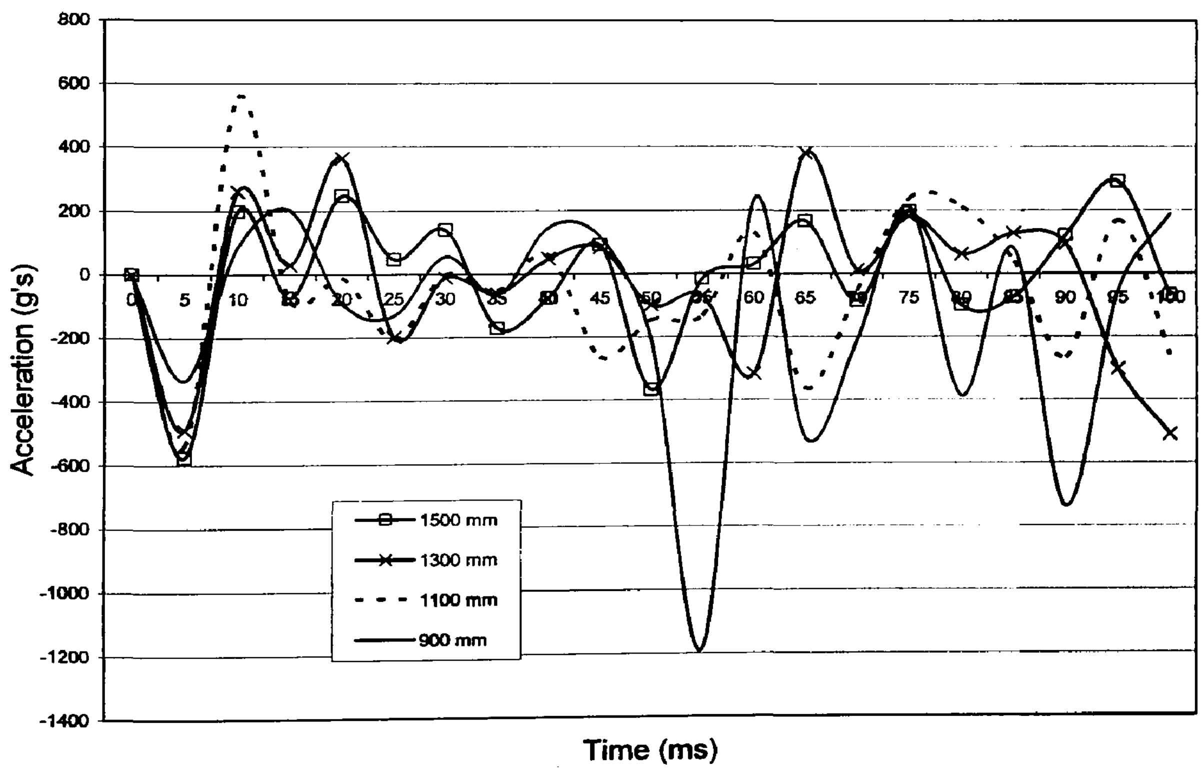

d) Steel pole embedded in dense sand: Node #708

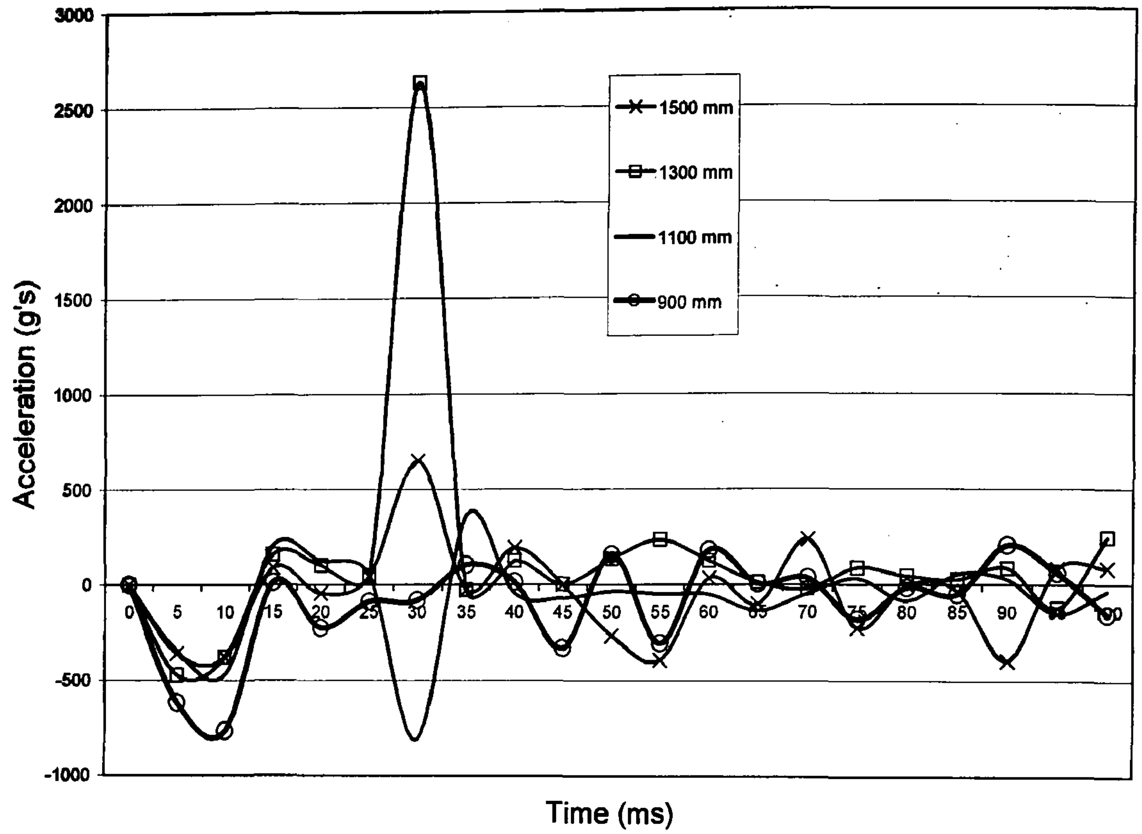

(e) Steel pole embedded in dense sand: Node # 1122

Figure 4.16: Comparative acceleration-time histories in dense sandy soil.

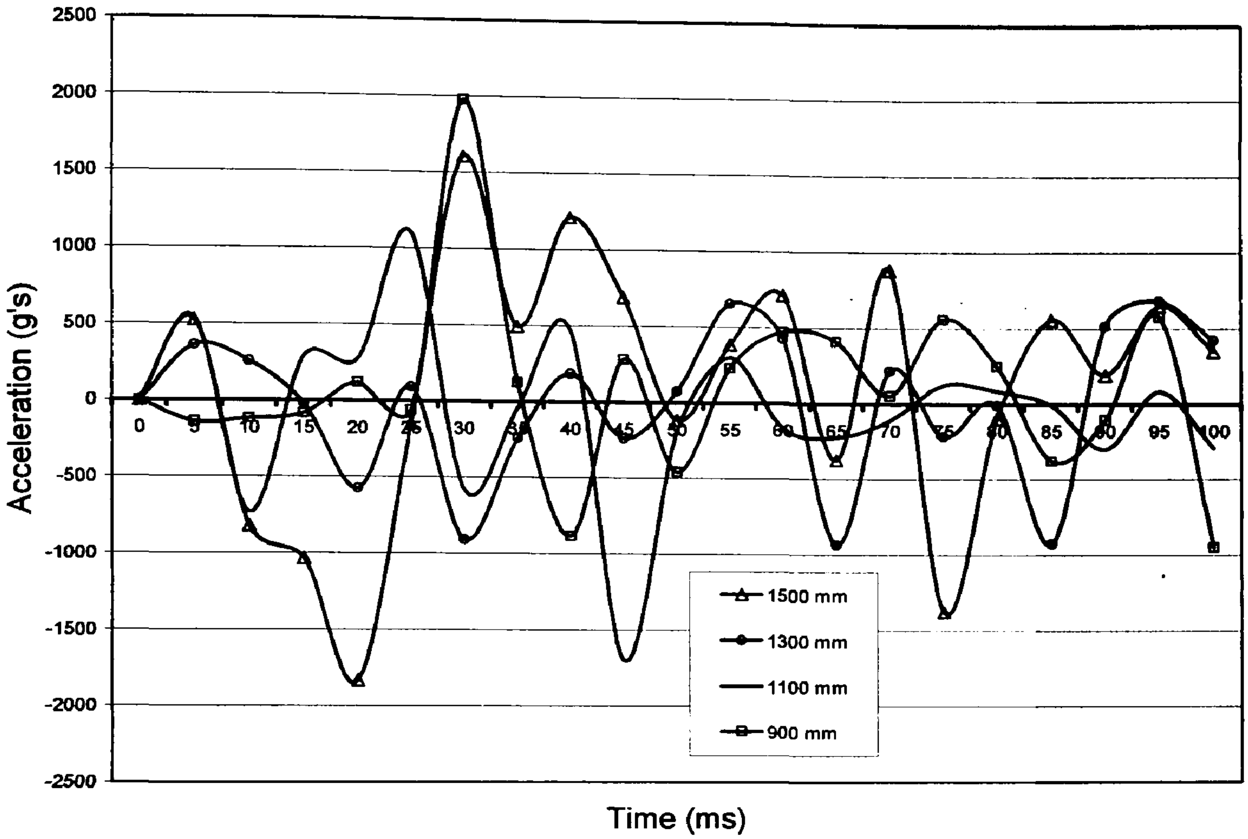

(a) Steel pole embedded in loose sand: Node #523

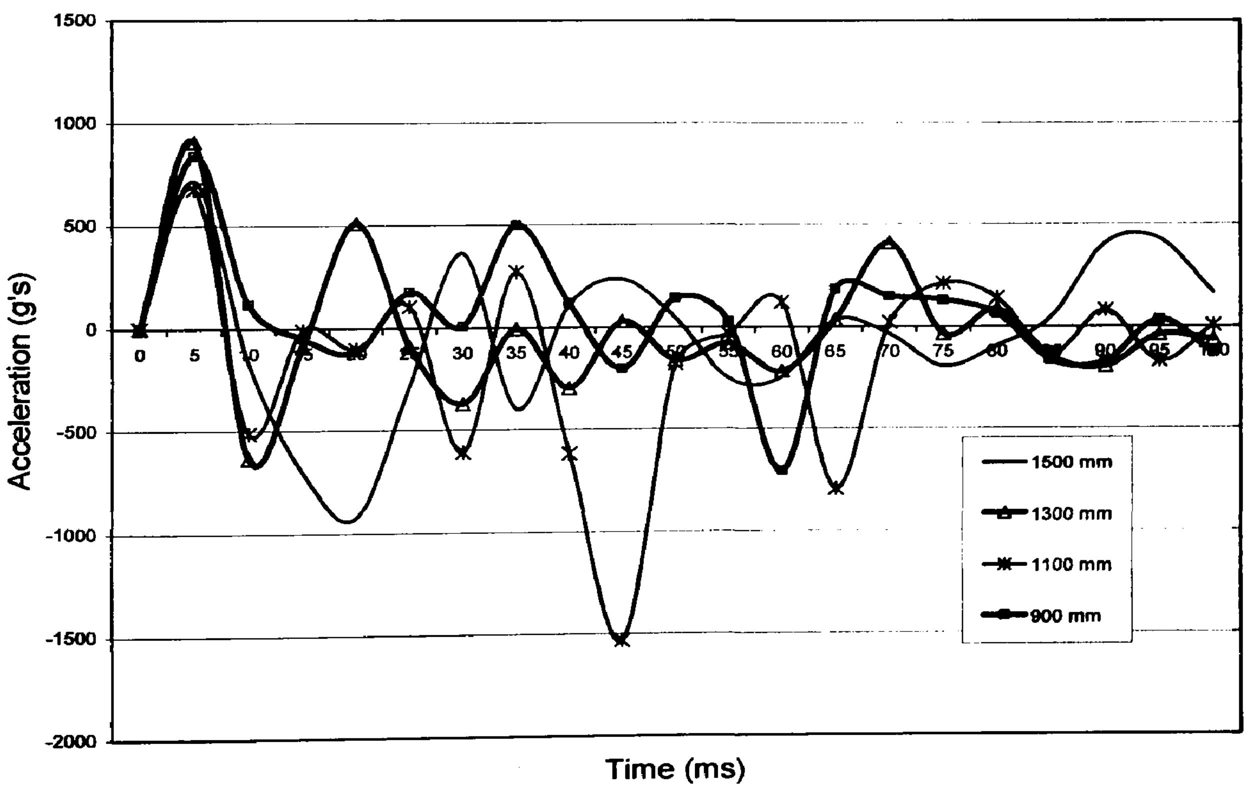

(b) Steel pole embedded in loose sand: Node #1317

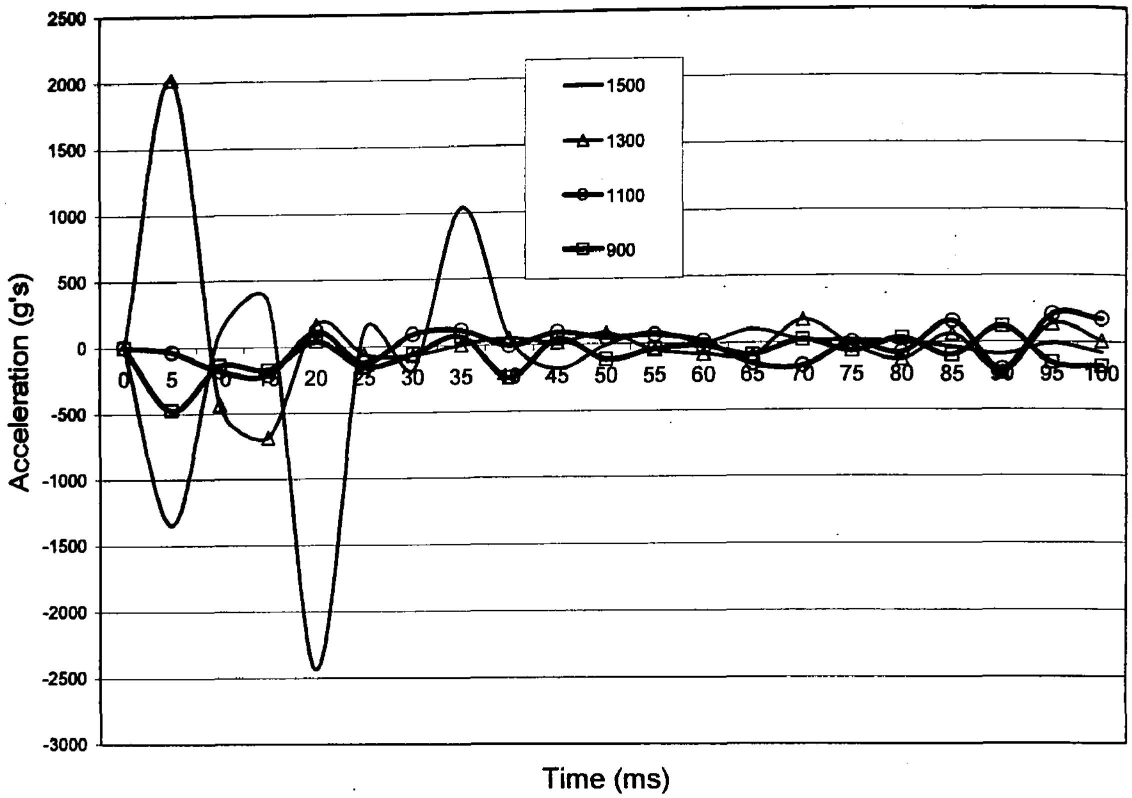

(c) Steel pole embedded in loose sand: Node # 19589

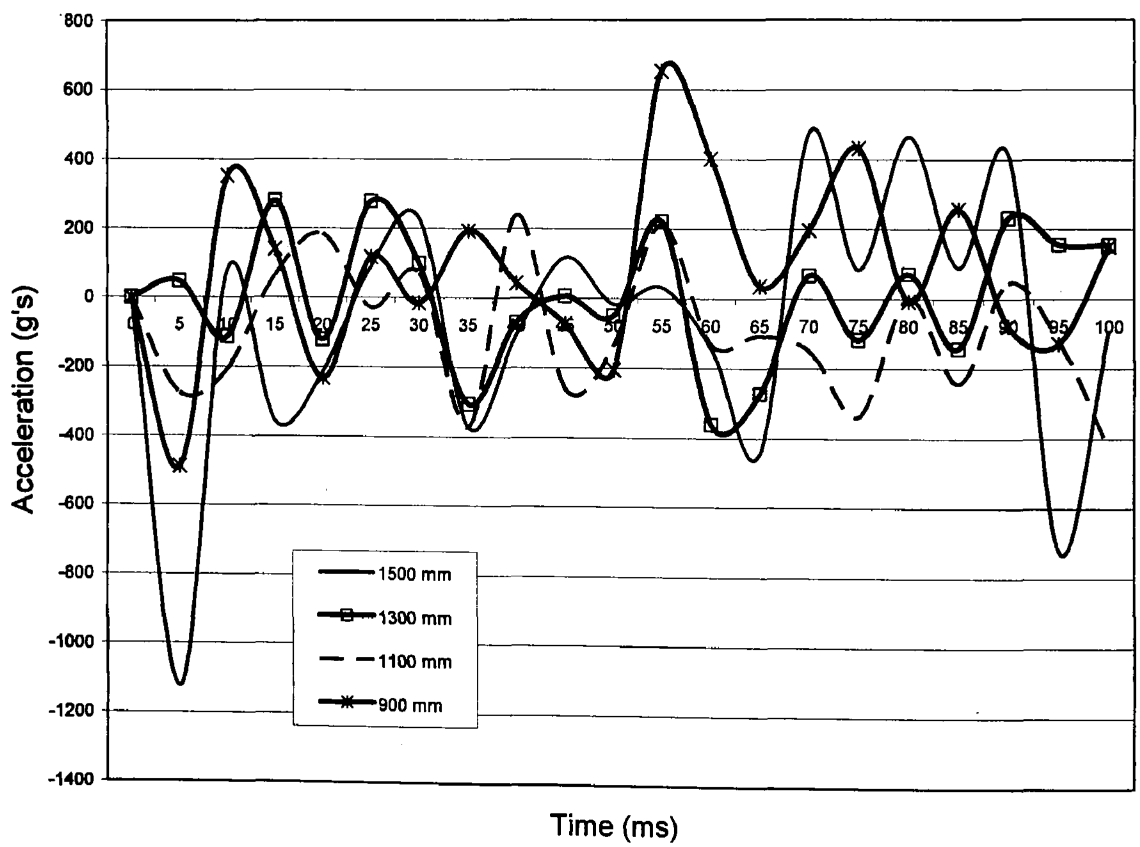

(d) Steel pole embedded in loose sand: Node #708

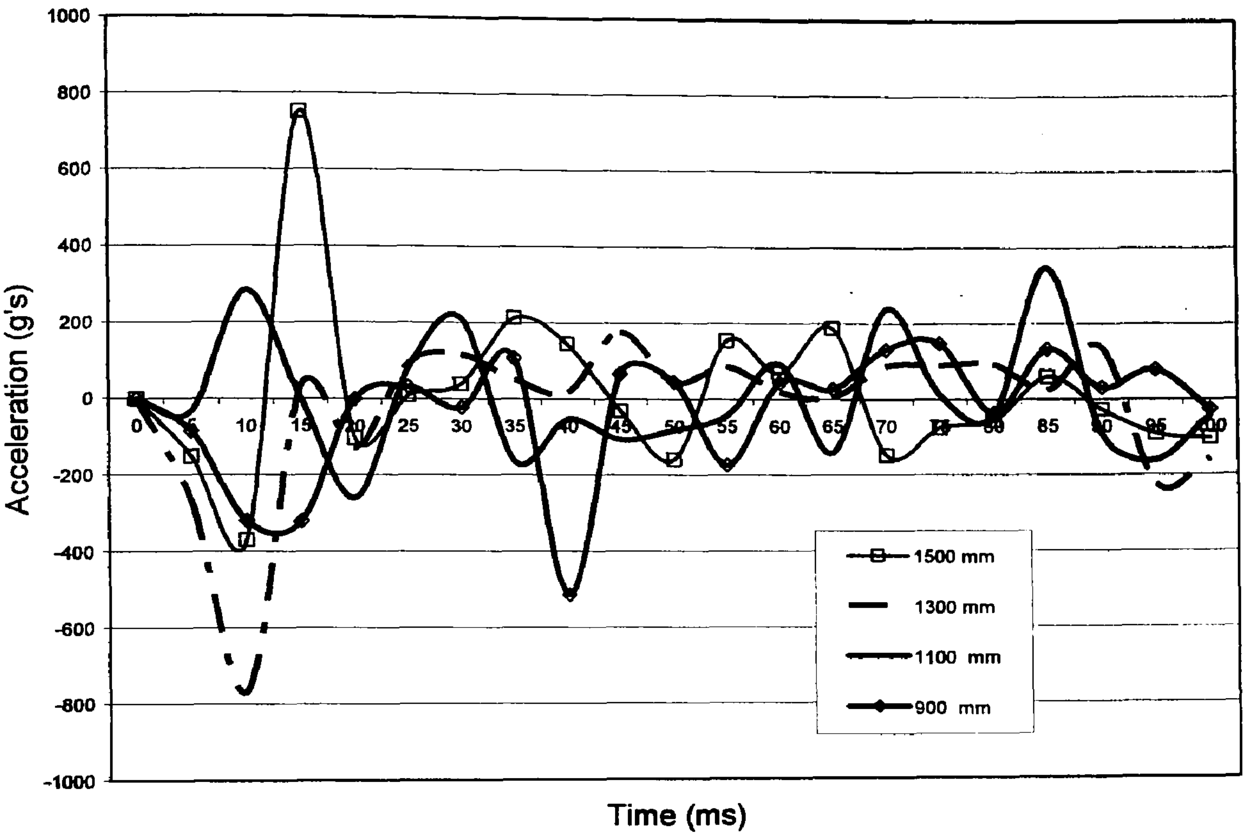

(e) Steel pole embedded in loose sand: Node # 1122

Figure 4.17: Comparative acceleration-time histories in case of loose sandy soil.

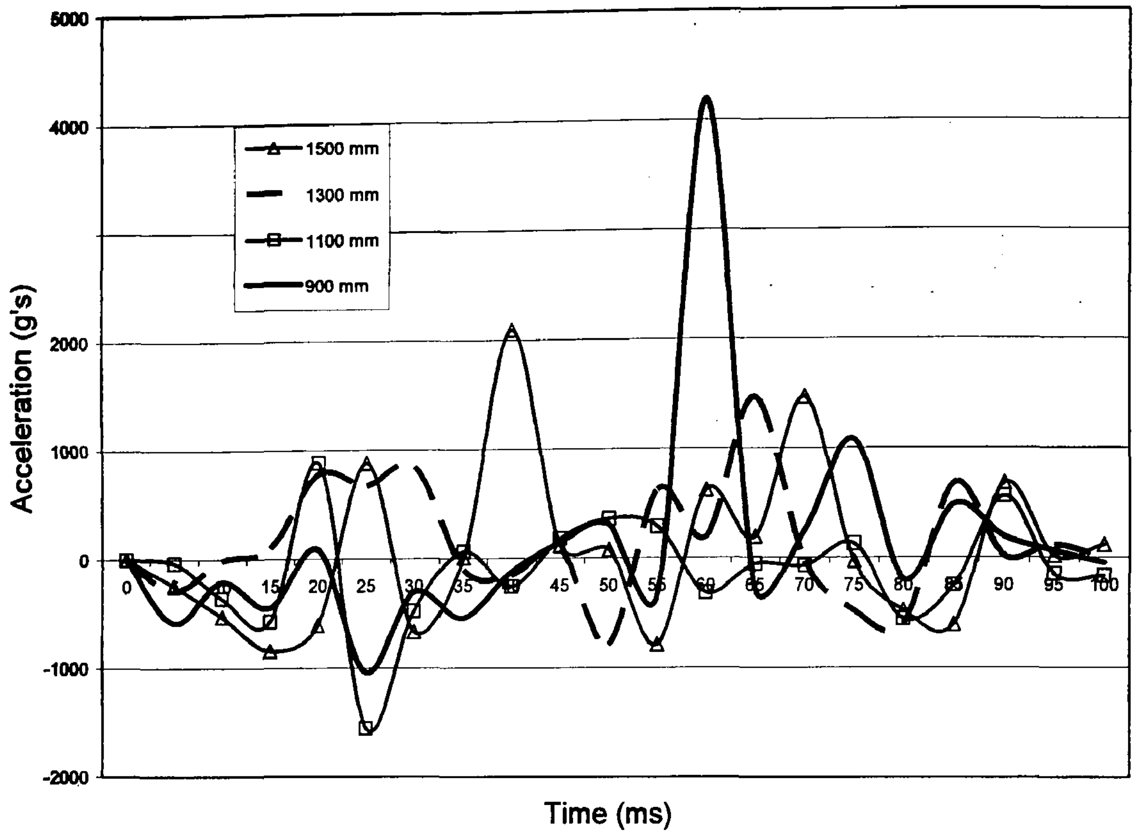

(a) Steel pole embedded in stiff clay: Node #523

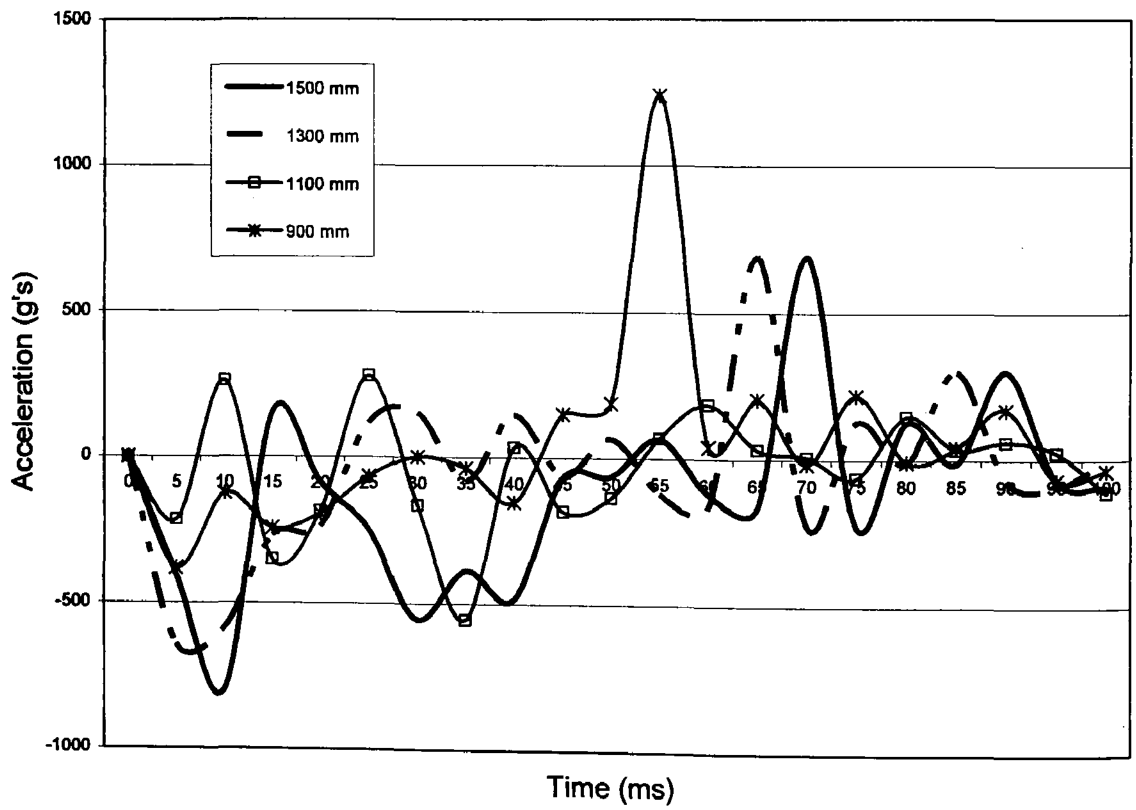

(b) Steel pole embedded in stiff clay: Node #1317

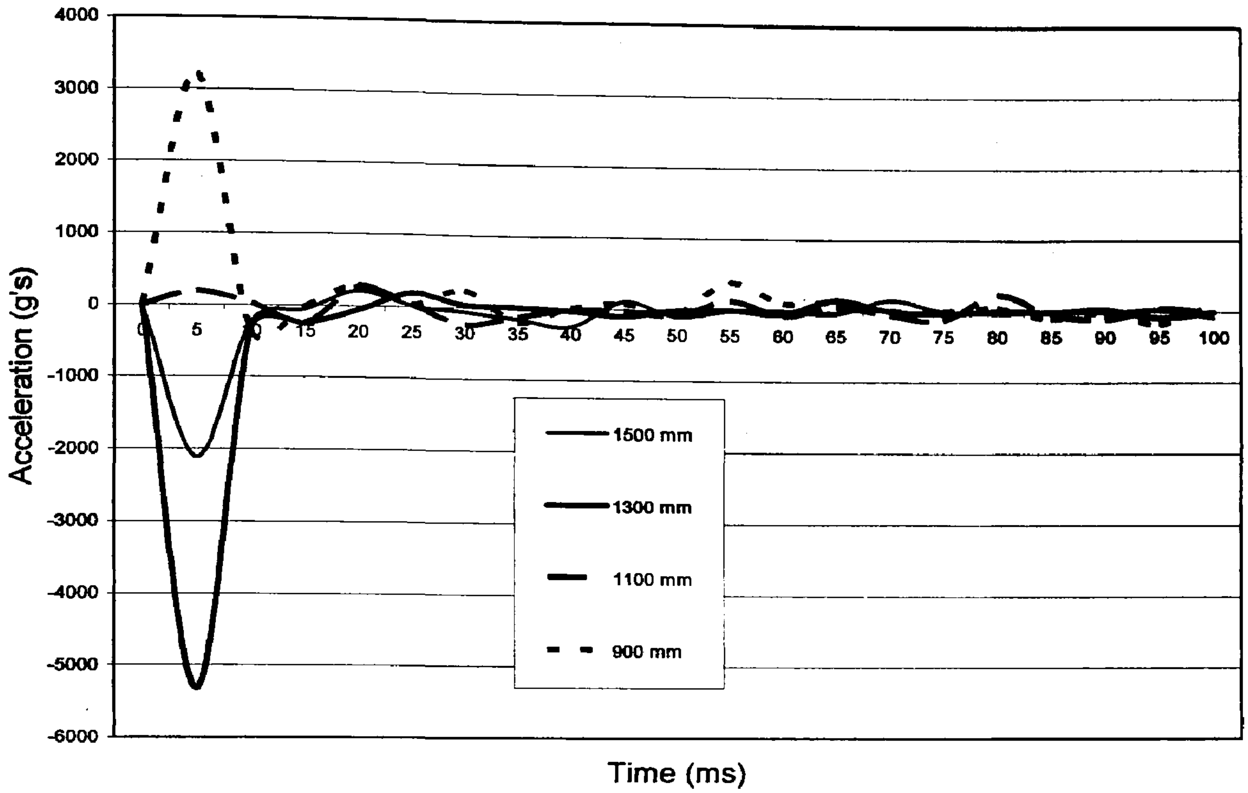

(c) Steel pole embedded in stiff clay: Node # 19589

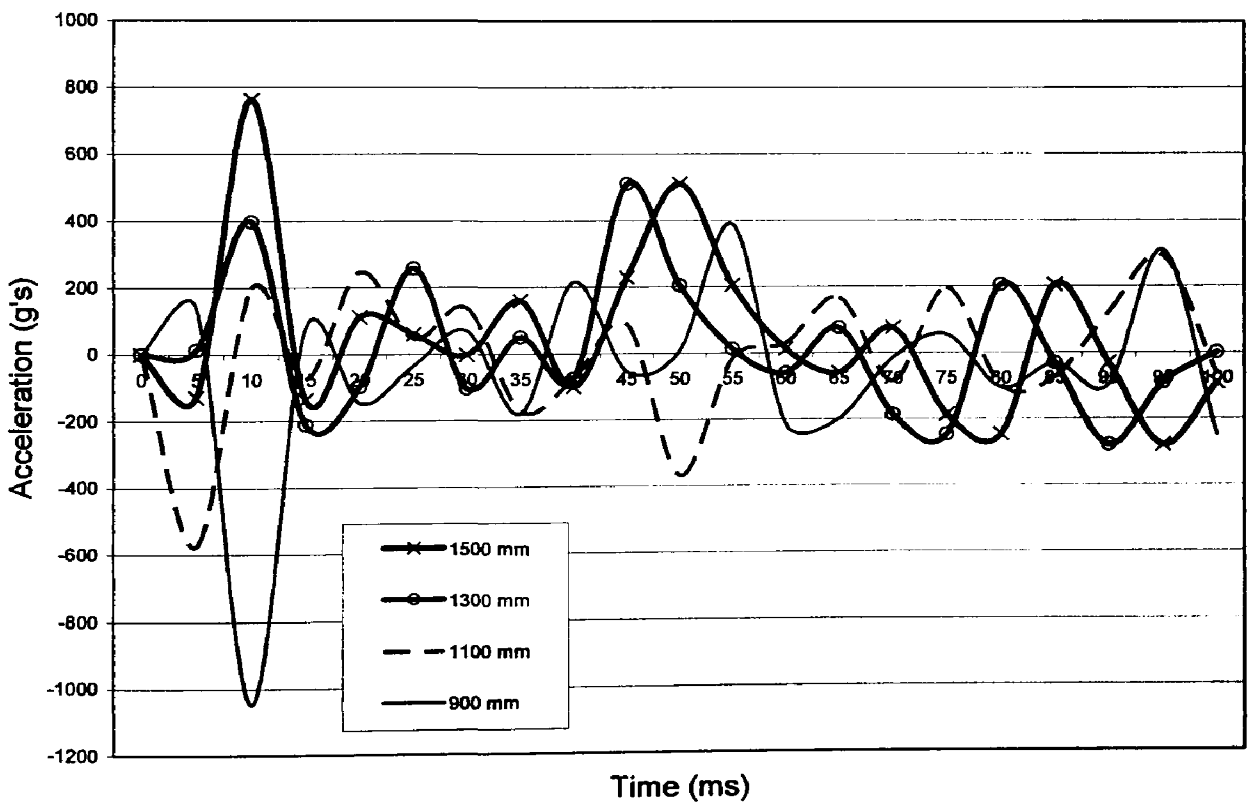

(d) Steel pole embedded in stiff clay: Node #708

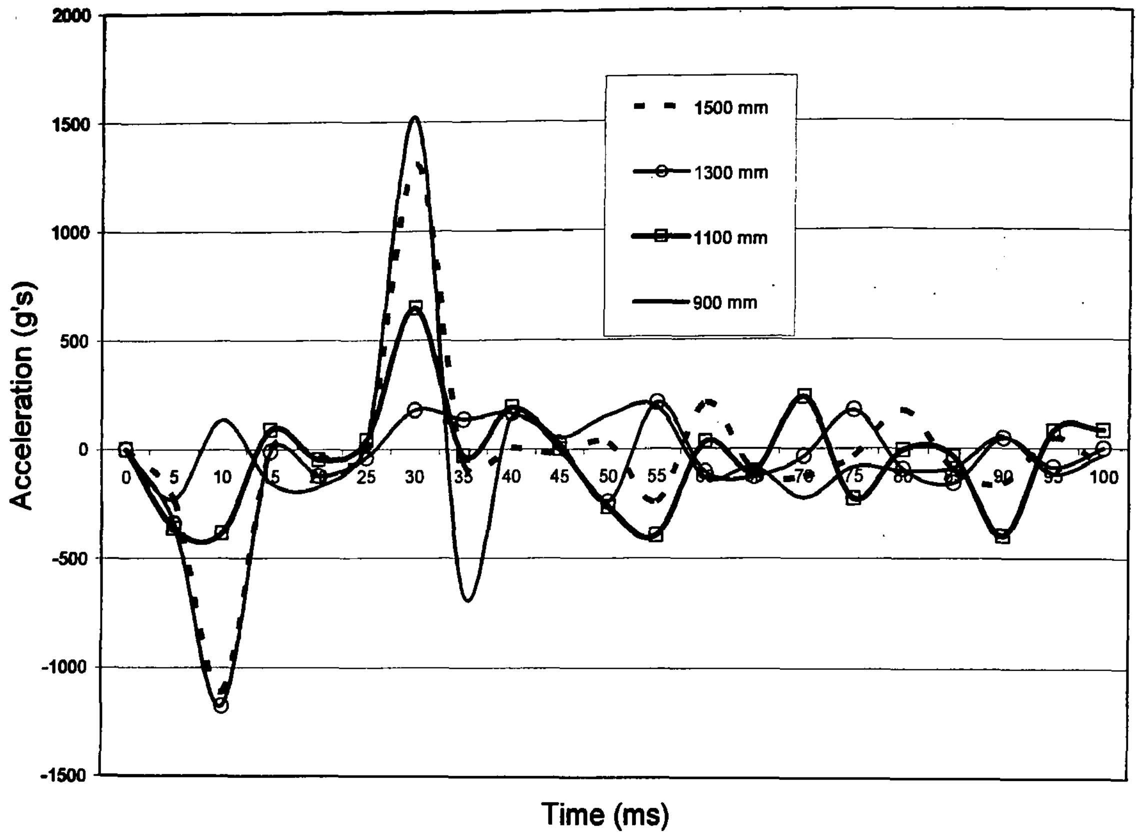

(e) Steel pole embedded in stiff clay: Node # 1122

Figure 4.18 Comparative acceleration-time histories in case of stiff clay soil.

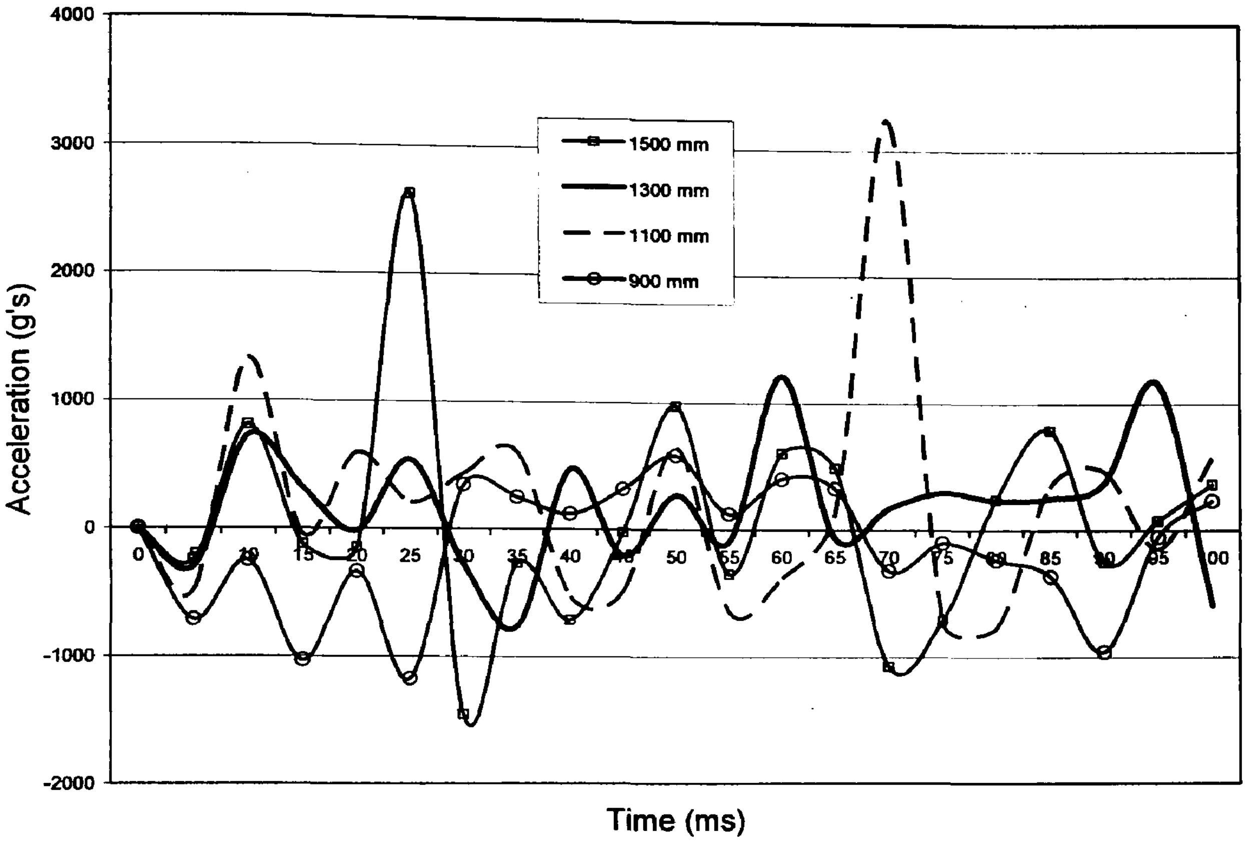

(a) Steel pole embedded in soft clay: Node #523

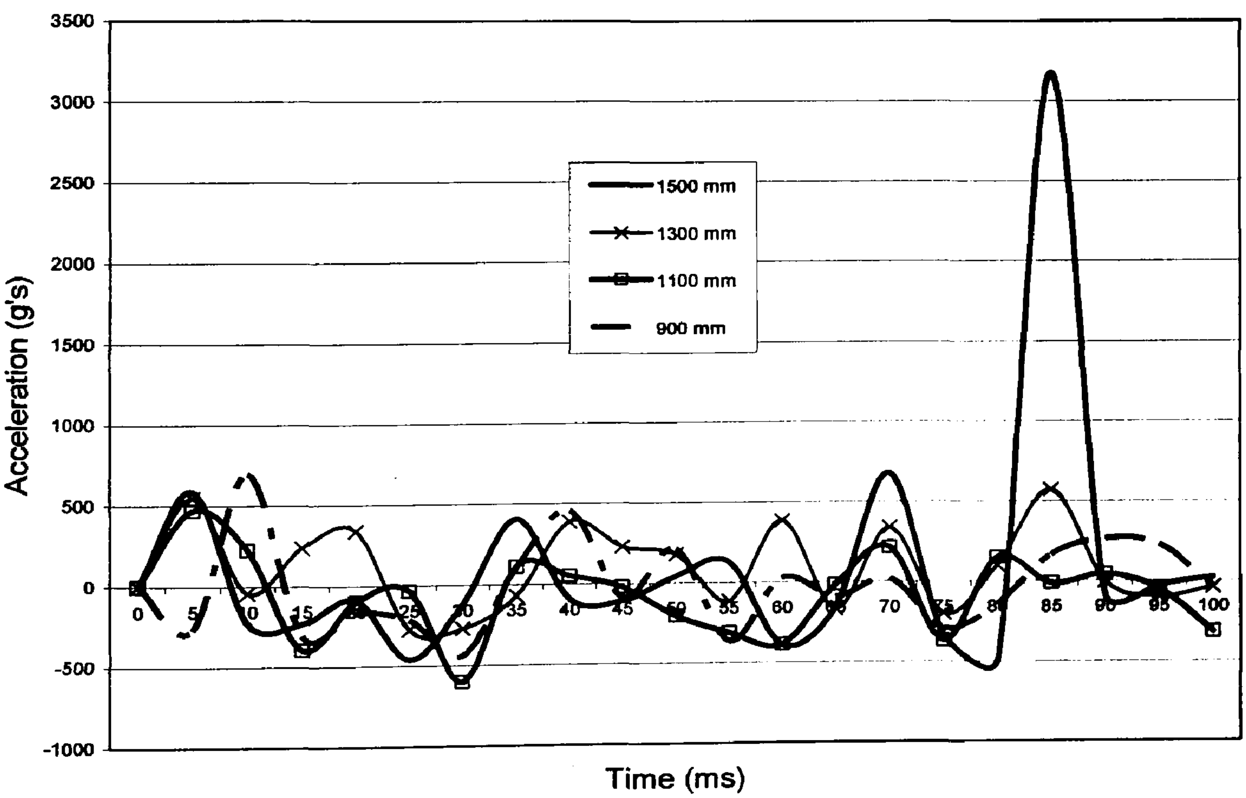

(b) Steel pole embedded in soft clay: Node #1317

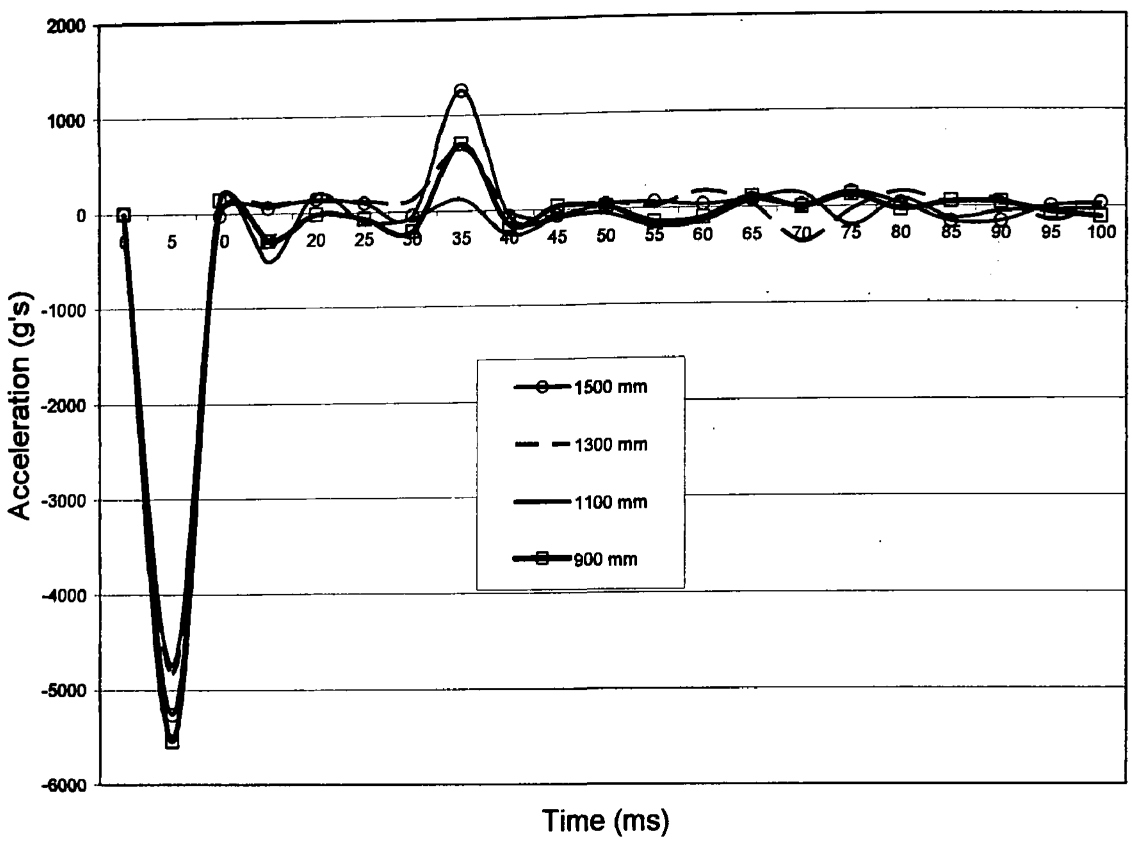

(c) Steel pole embedded in soft clay: Node # 19589

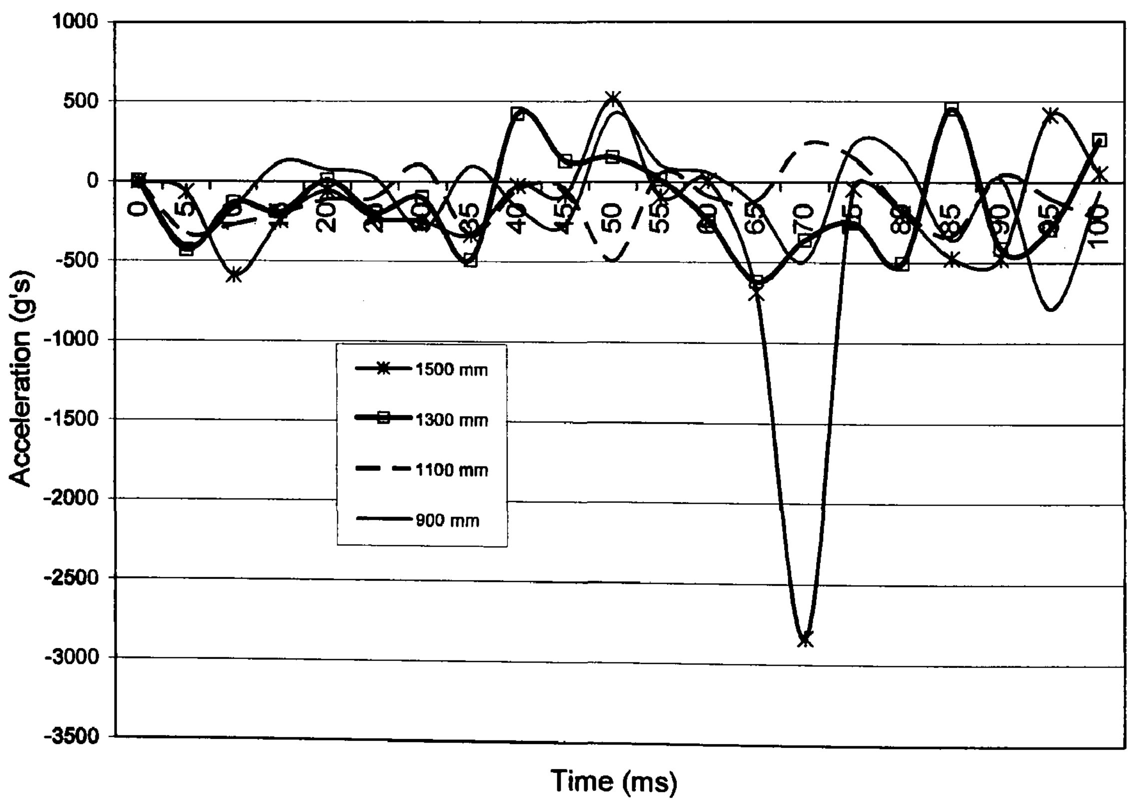

(d) Steel pole embedded in soft clay: Node #708

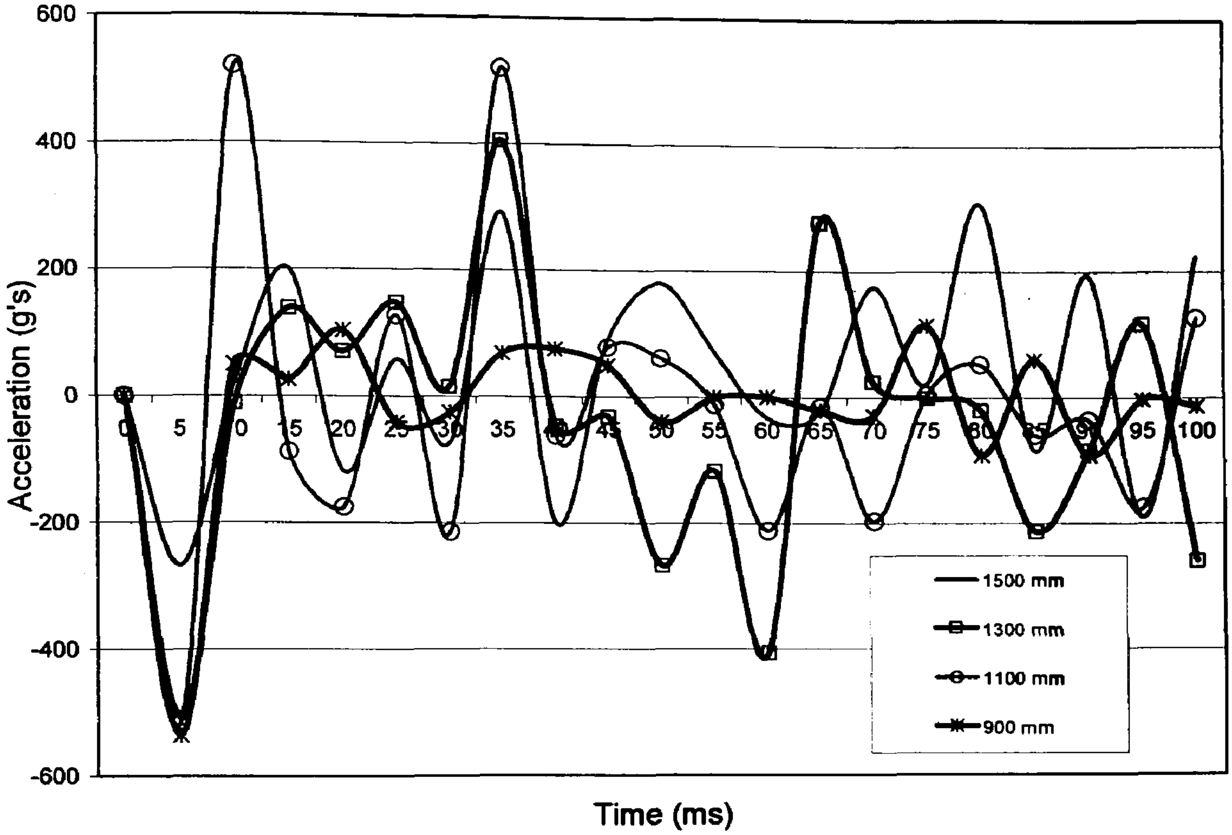

(e) Steel pole embedded in soft clay: Node # 1122

Figure 4.19 Comparative acceleration-time histories in case of soft clayey soil.

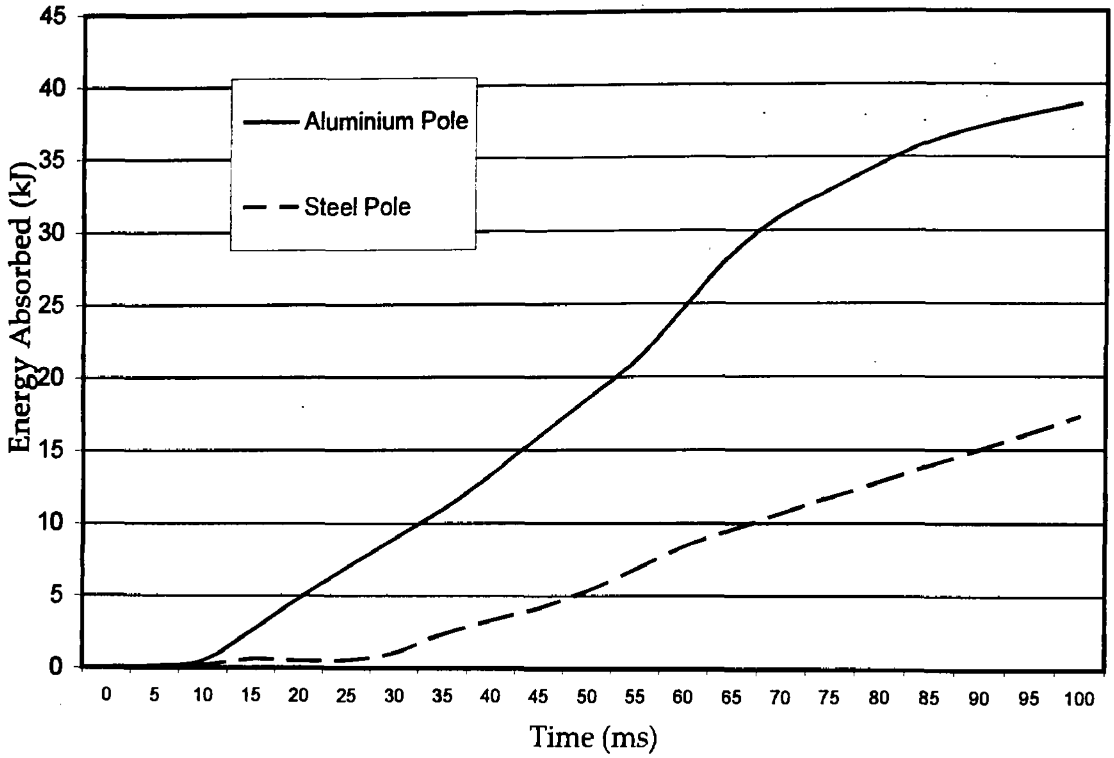

Figure 4.20 Energy absorbed by steel and aluminium poles embedded 1500 mm in soft clayey soil in side impact.

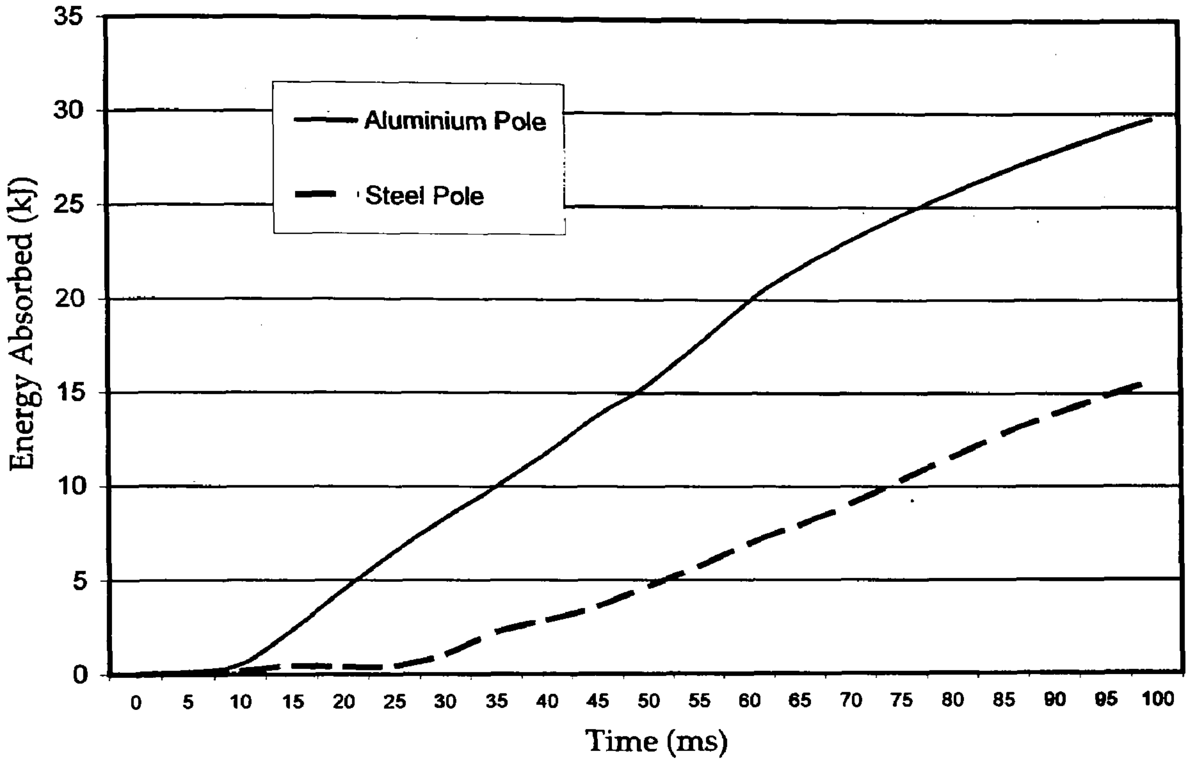

Figure 4.21 Energy absorbed by steel and aluminium poles embedded 1500 mm in stiff clayey soil in side impact.

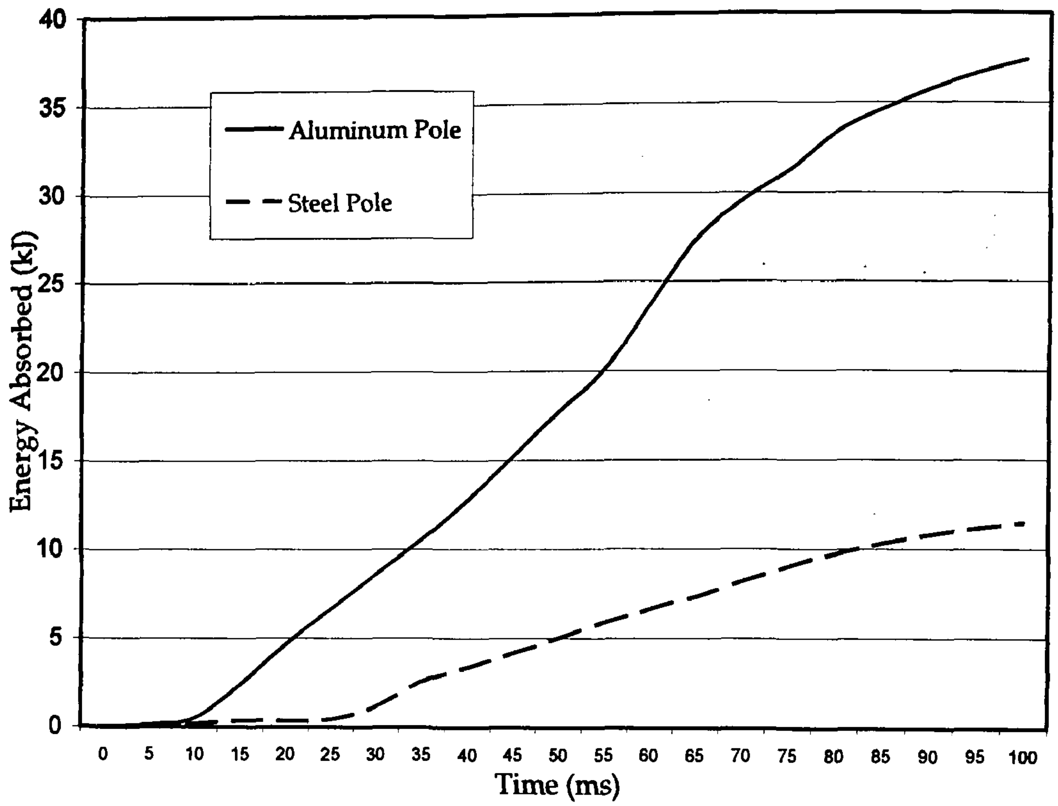

Figure 4.22 Energy absorbed by steel and aluminium poles embedded 1500 mm in dense sandy soil in side impact.

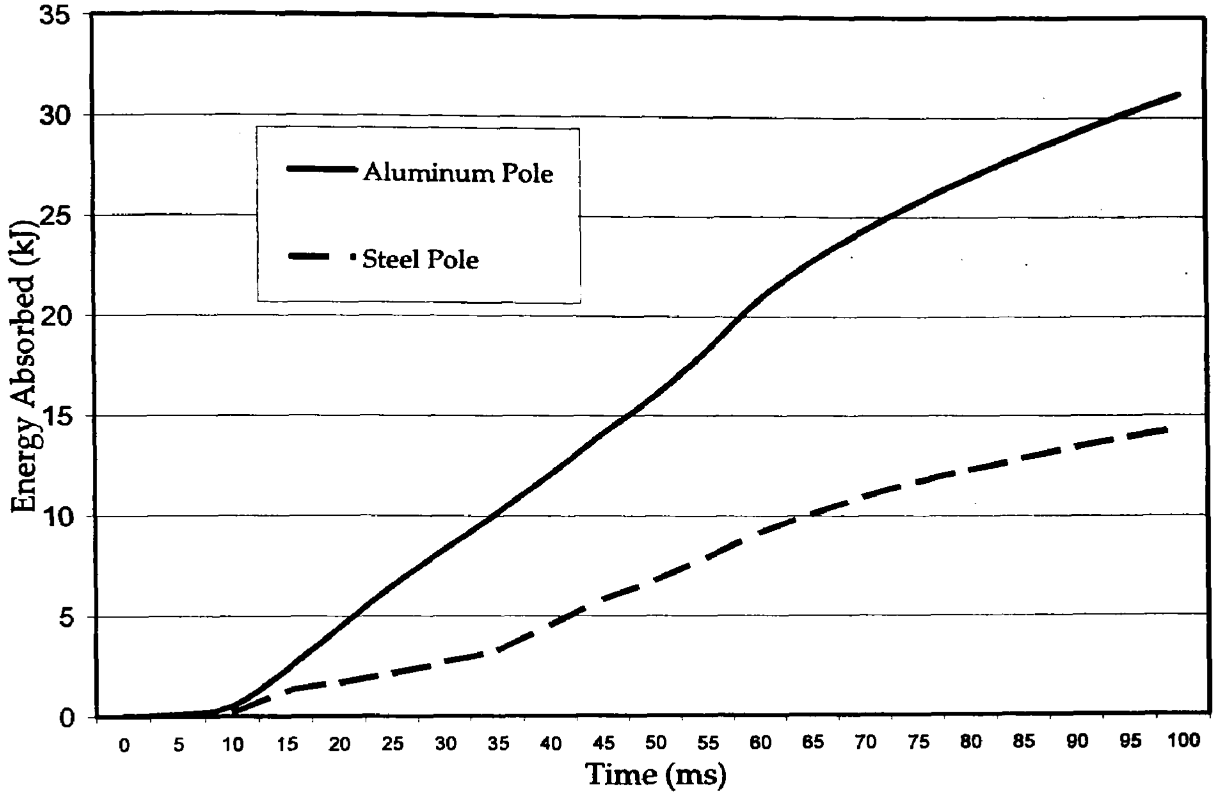

Figure 4.23 Energy absorbed by steel and aluminium poles embedded 1500 mm in loose sand soil in side impact.

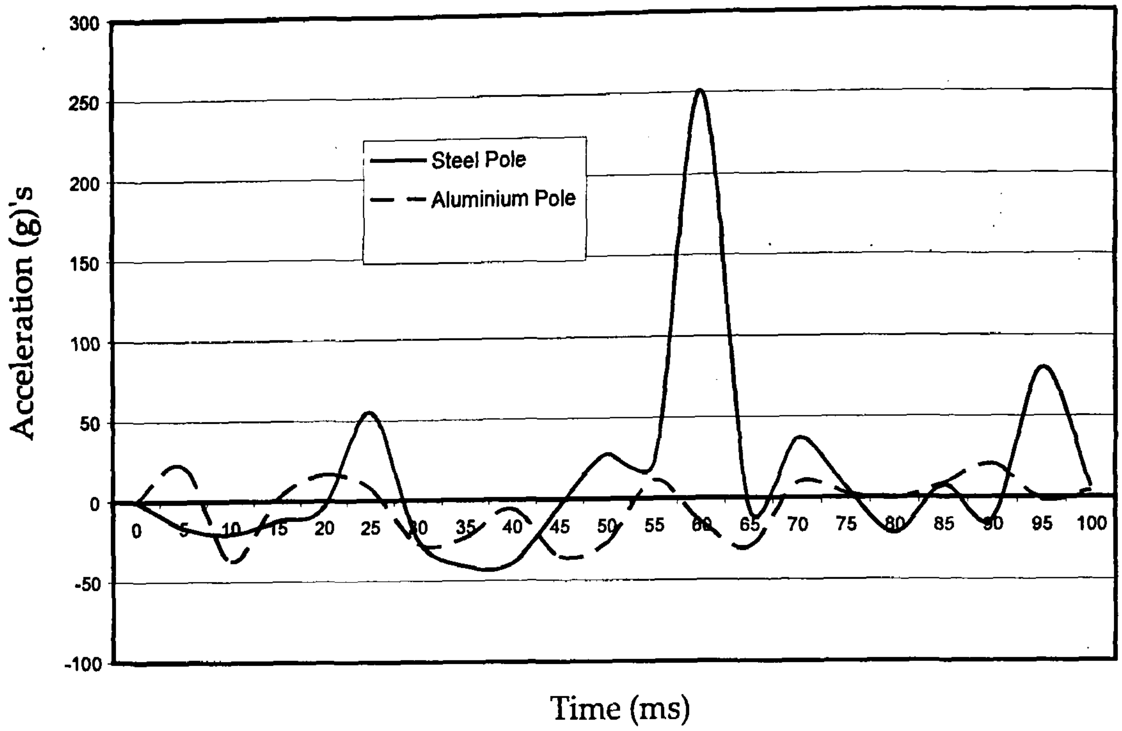

(a) Dense Sand

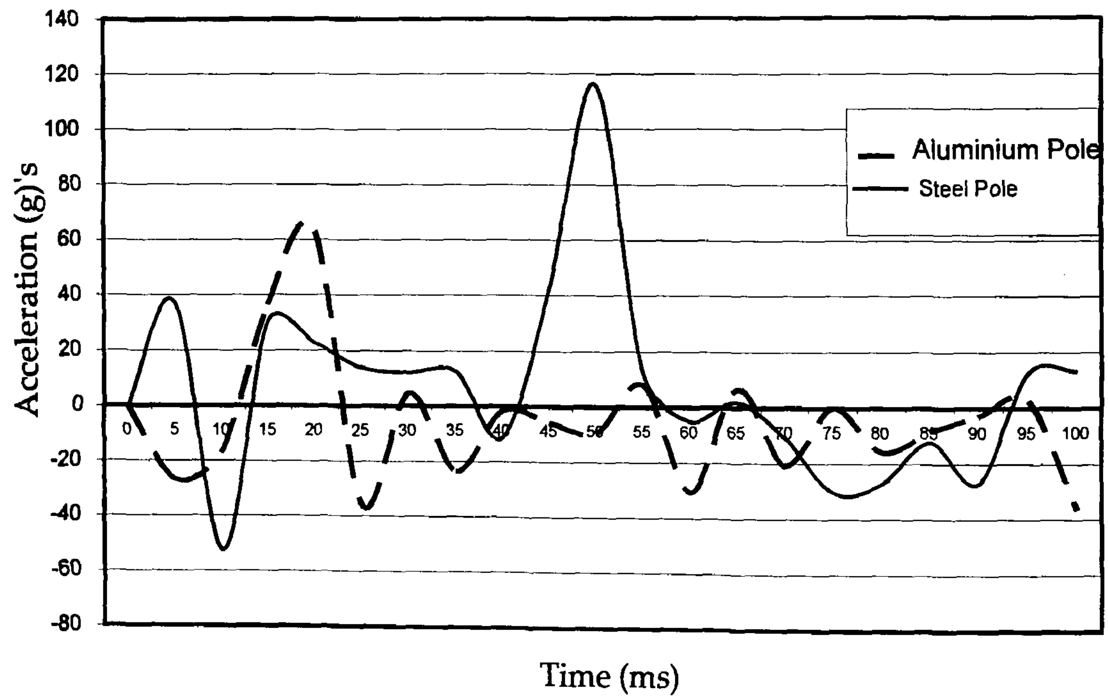

(b) Loose Sand

Figure 4.24 Comparative acceleration for aluminium pole and steel pole at a node on roof beam when pole is embedded 1500 mm in soil and impacted sideways.

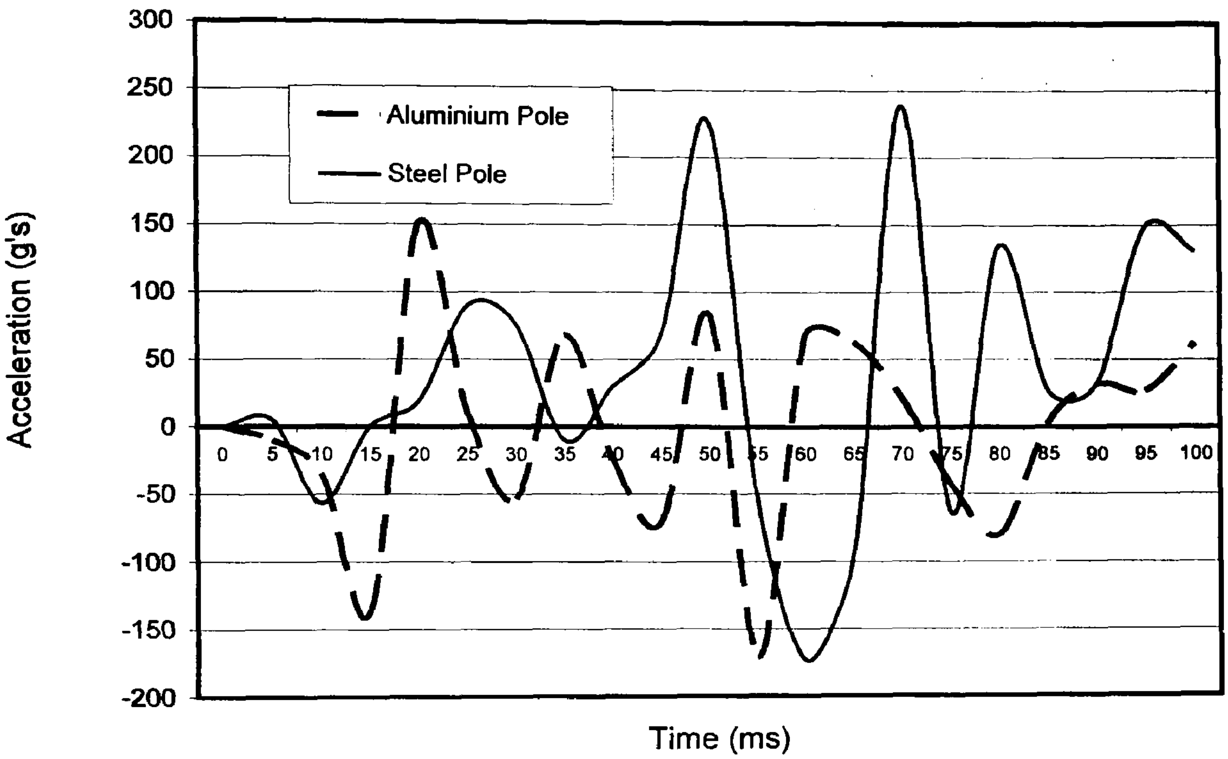

Figure 4.25 Comparative acceleration for steel and aluminium poles at a point on the B pillar when poles are embedded 1500 mm in dense soil and impacted sideways.

(a) Energy Absorbed by the Aluminium Pole Embedded in Stiff Clay
Impact Speed 50 km/hr

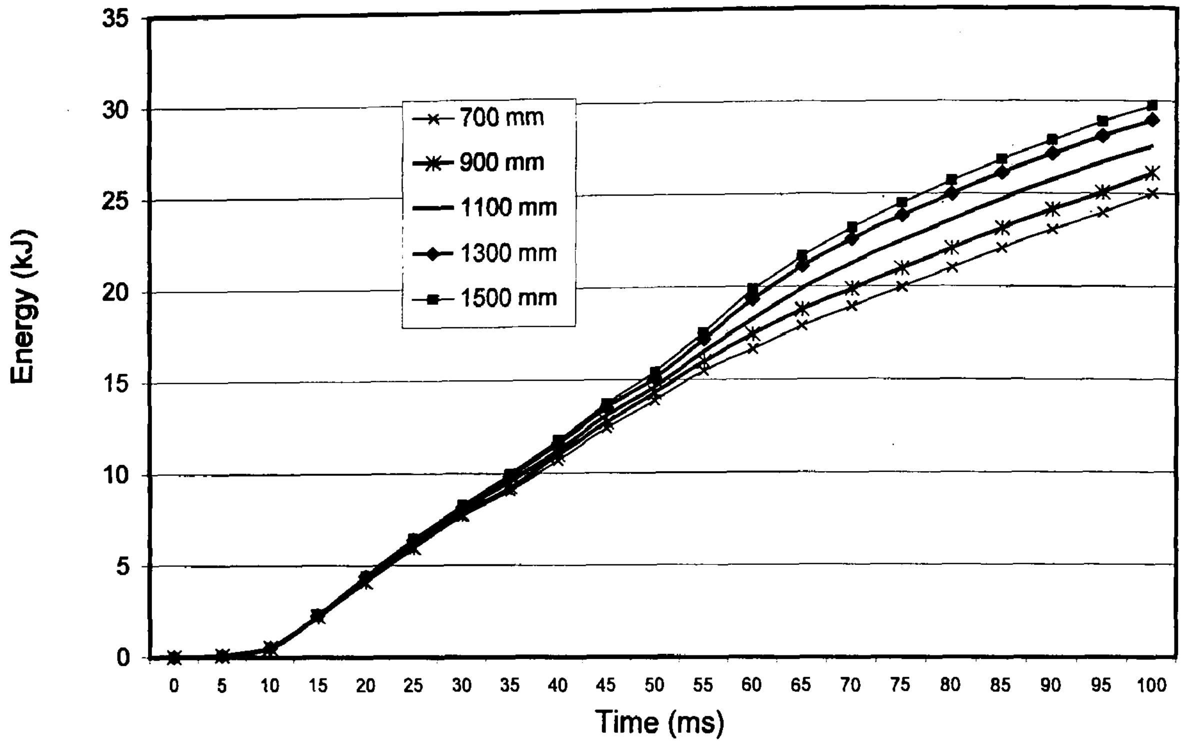

(b) Energy Absorbed by the Aluminium Pole Embedded in Loose Sand
Impact Speed 50 km/hr

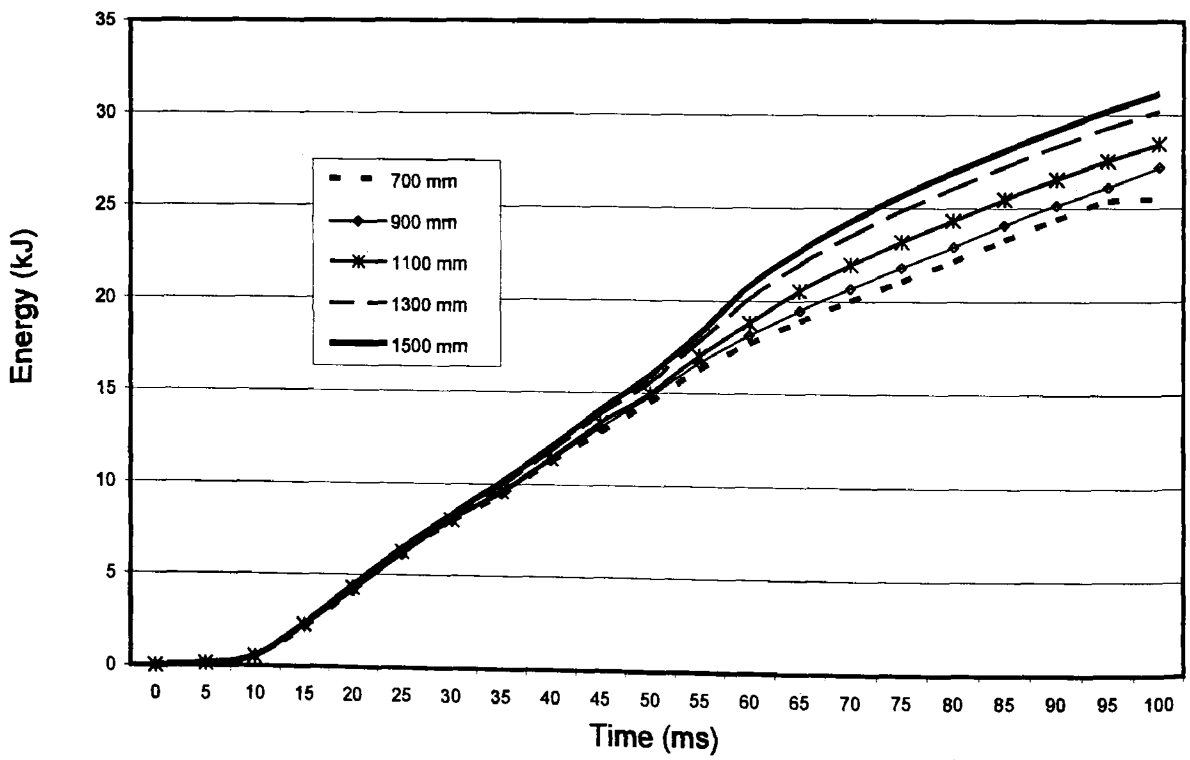

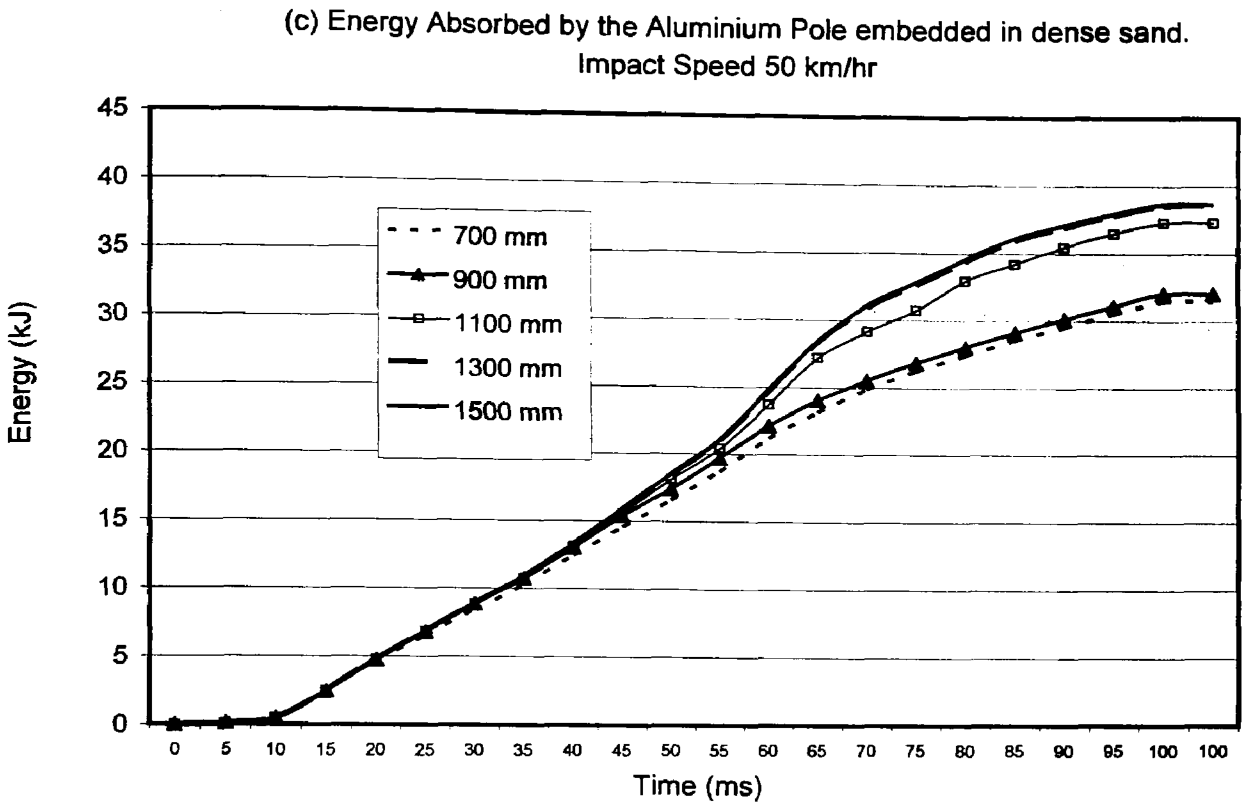

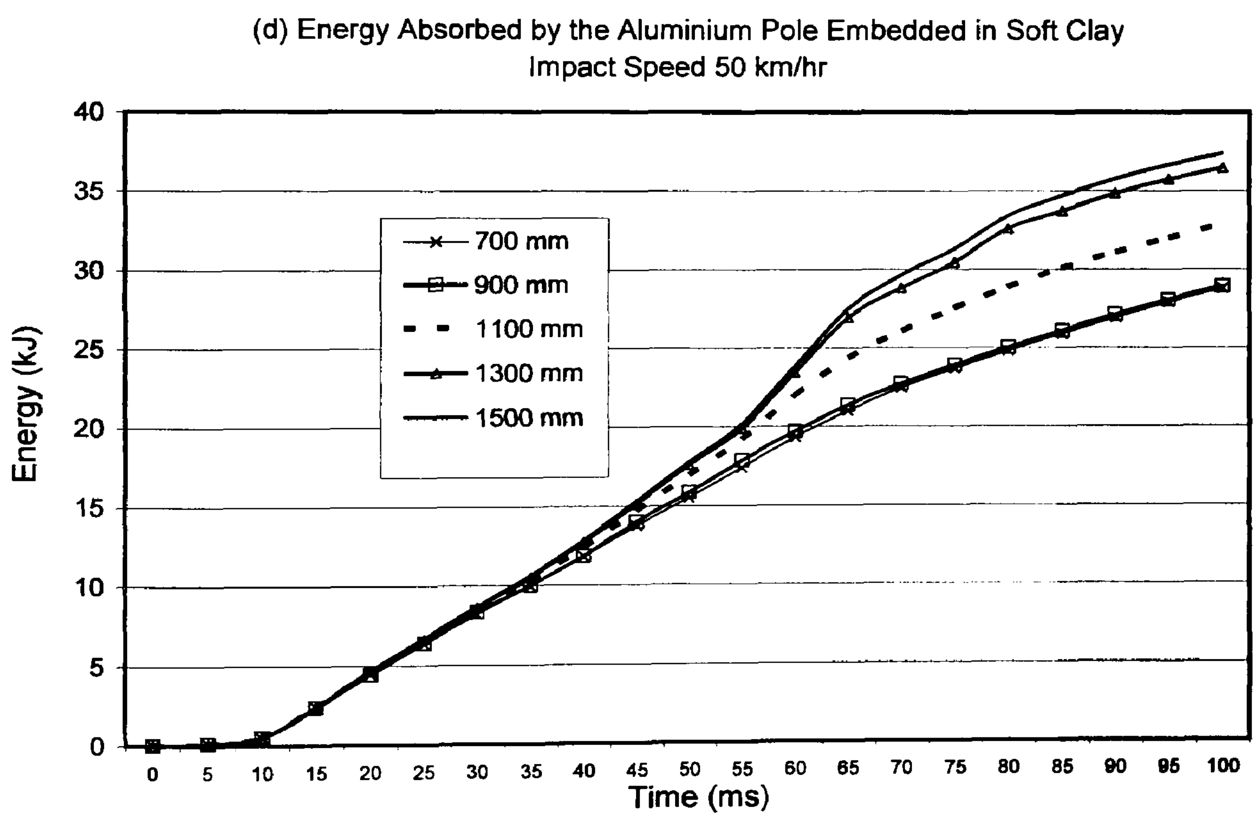

Figure 4.26 Effect of embedment depth on energy absorbed by aluminium pole during side impact.

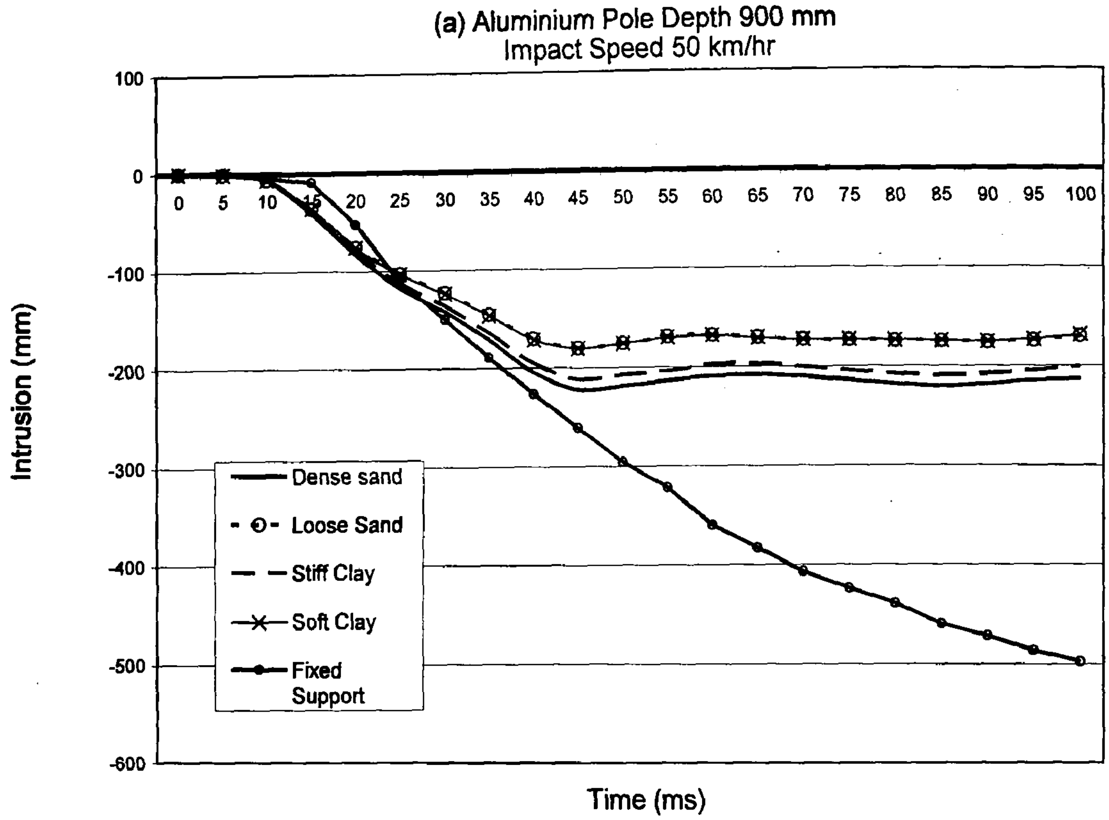
(a) Aluminium Pole Depth 900 mm
Impact Speed 50 km/hr
Intrusion (mm)
Time (ms)
100
0
-100
-200
-300
-400
-500
-600
0 5 10 15 20 25 30 35 40 45 50 55 60 65 70 75 80 85 90 95 100
Dense sand
Loose Sand
Stiff Clay
Soft Clay
Fixed Support

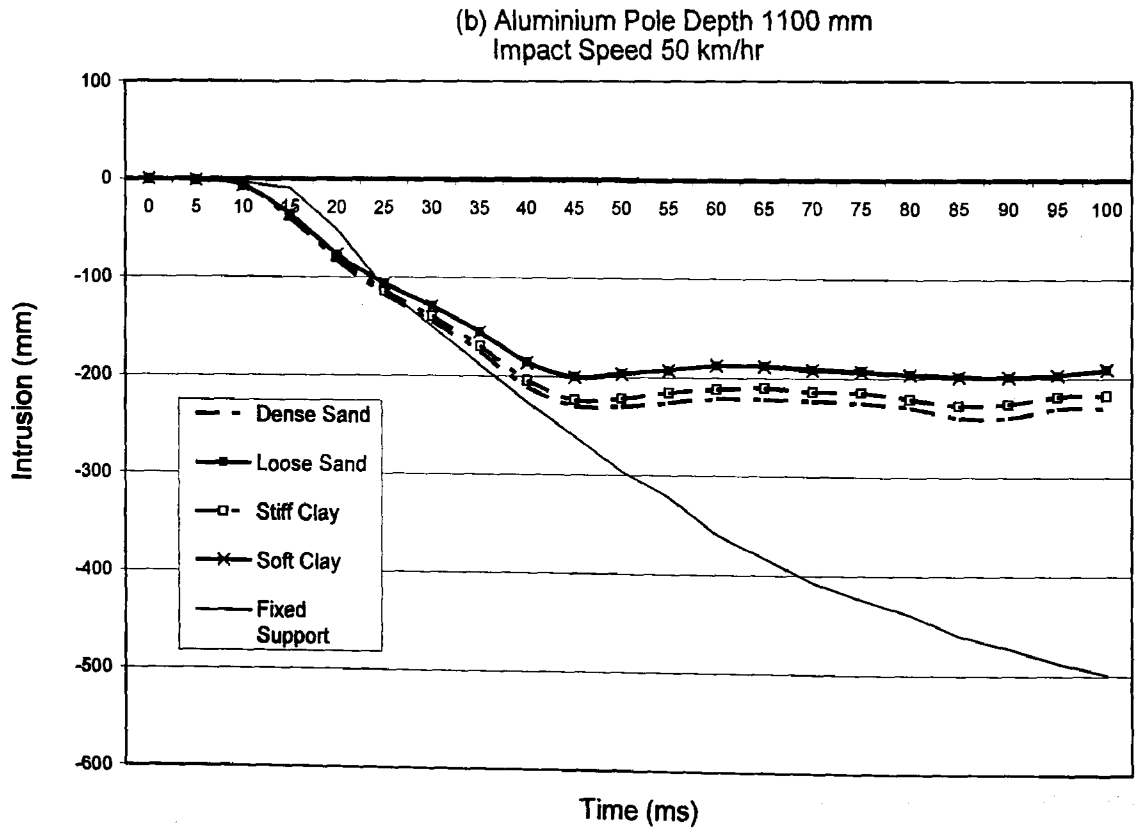
(b) Aluminium Pole Depth 1100 mm
Impact Speed 50 km/hr
Intrusion (mm)
Time (ms)
100
0
-100
-200
-300
-400
-500
-600
0 5 10 15 20 25 30 35 40 45 50 55 60 65 70 75 80 85 90 95 100
Dense Sand
Loose Sand
Stiff Clay
Soft Clay
Fixed Support

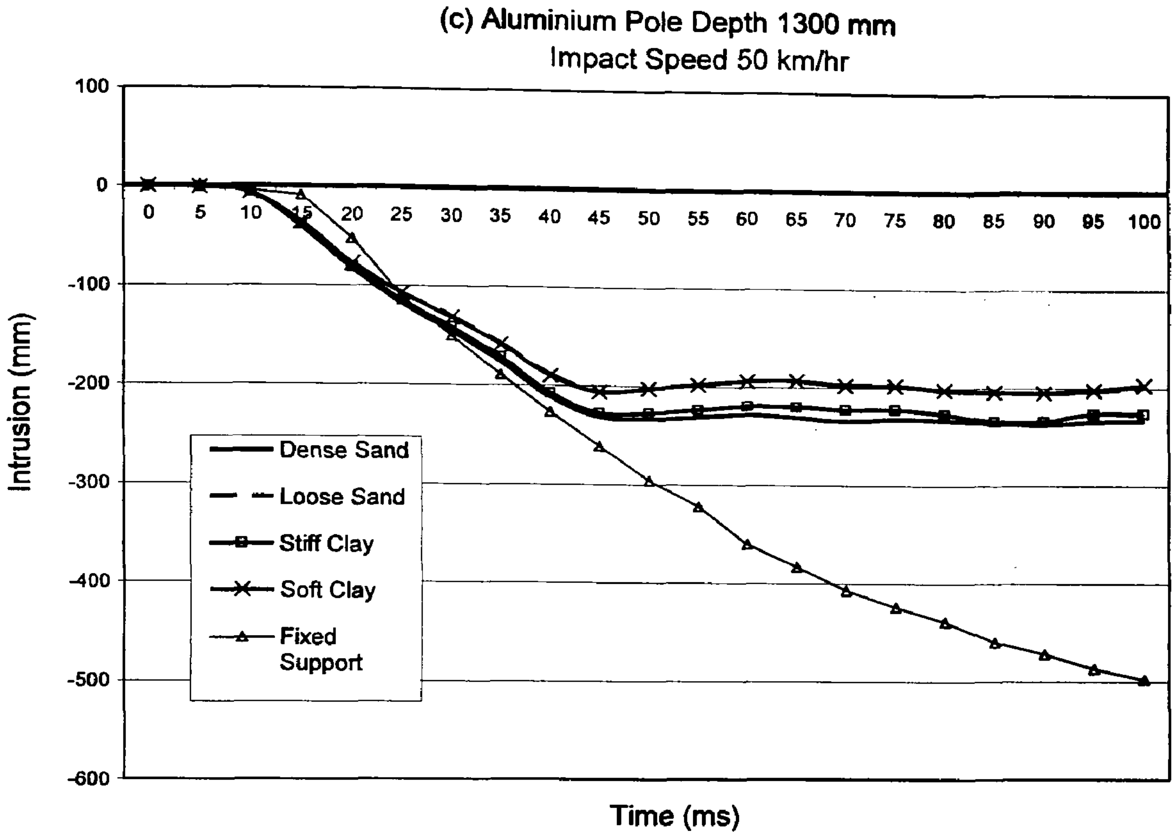

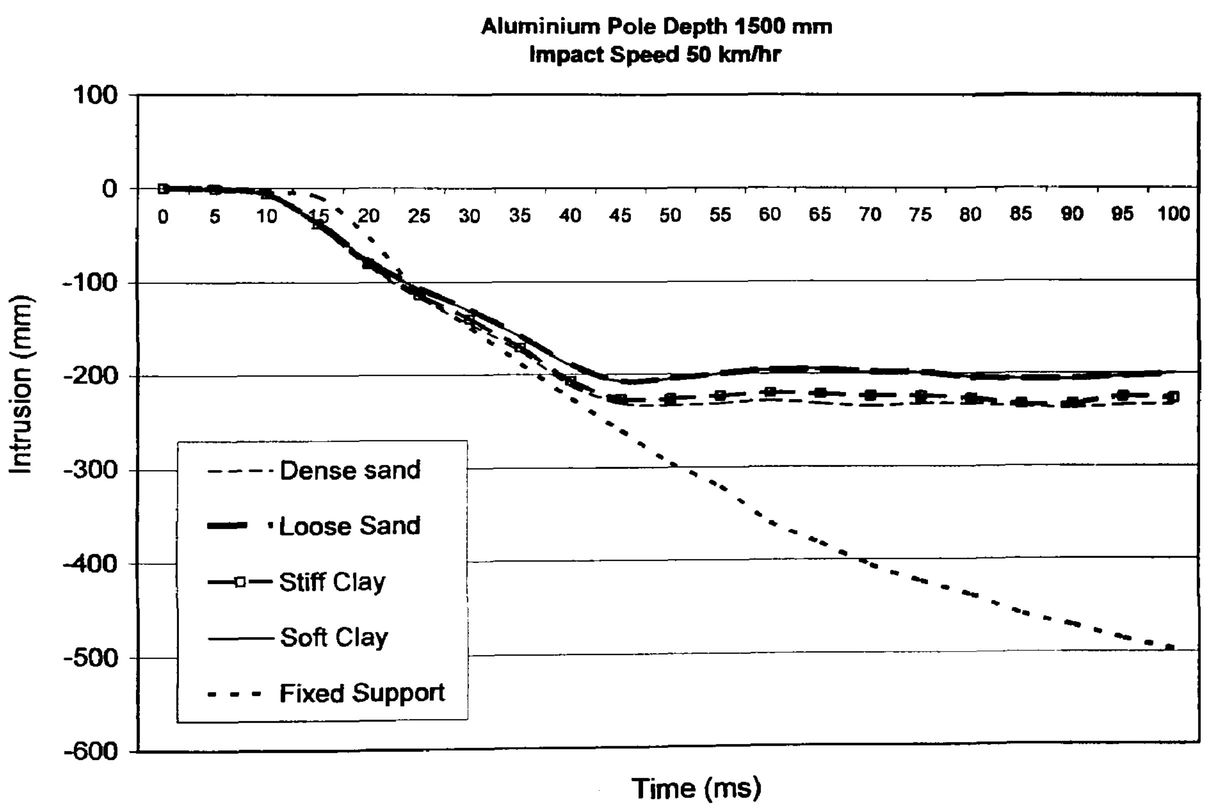

Figure 4.27 Intrusion of passenger compartment for aluminium poles in side impact.

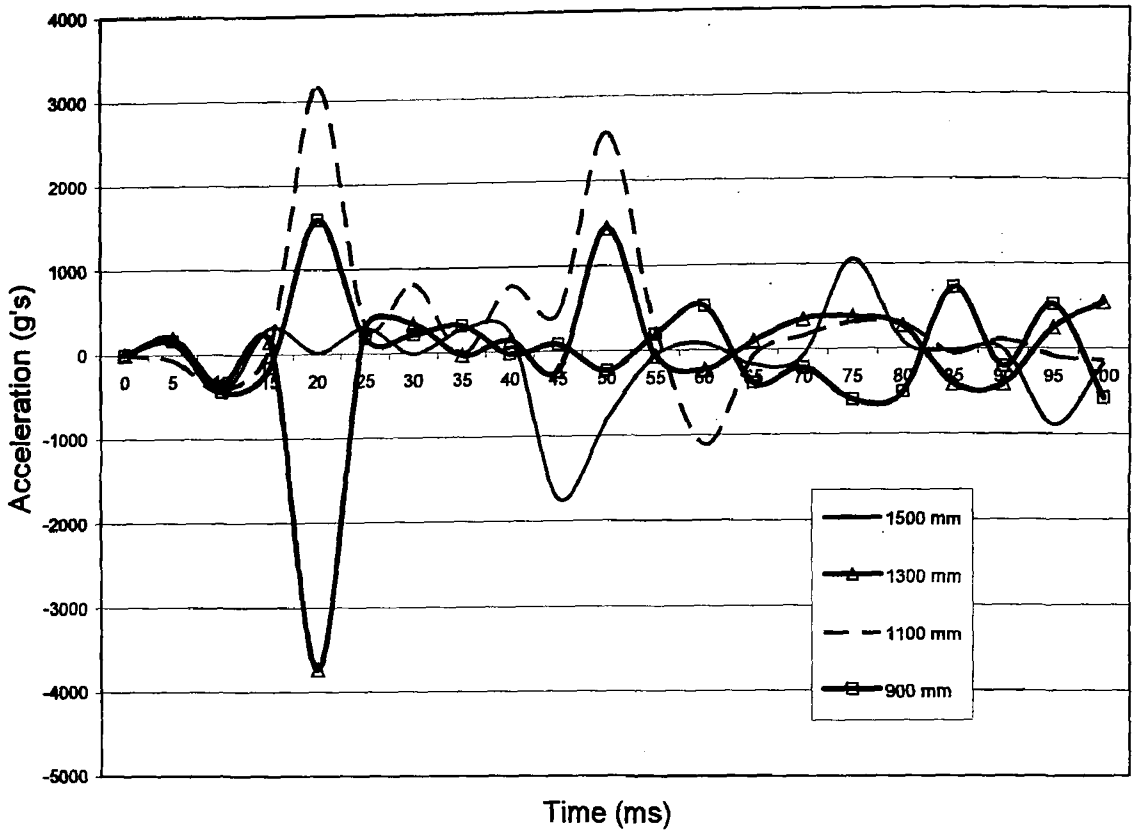

(a) Aluminium pole embedded in dense sand : Node #523

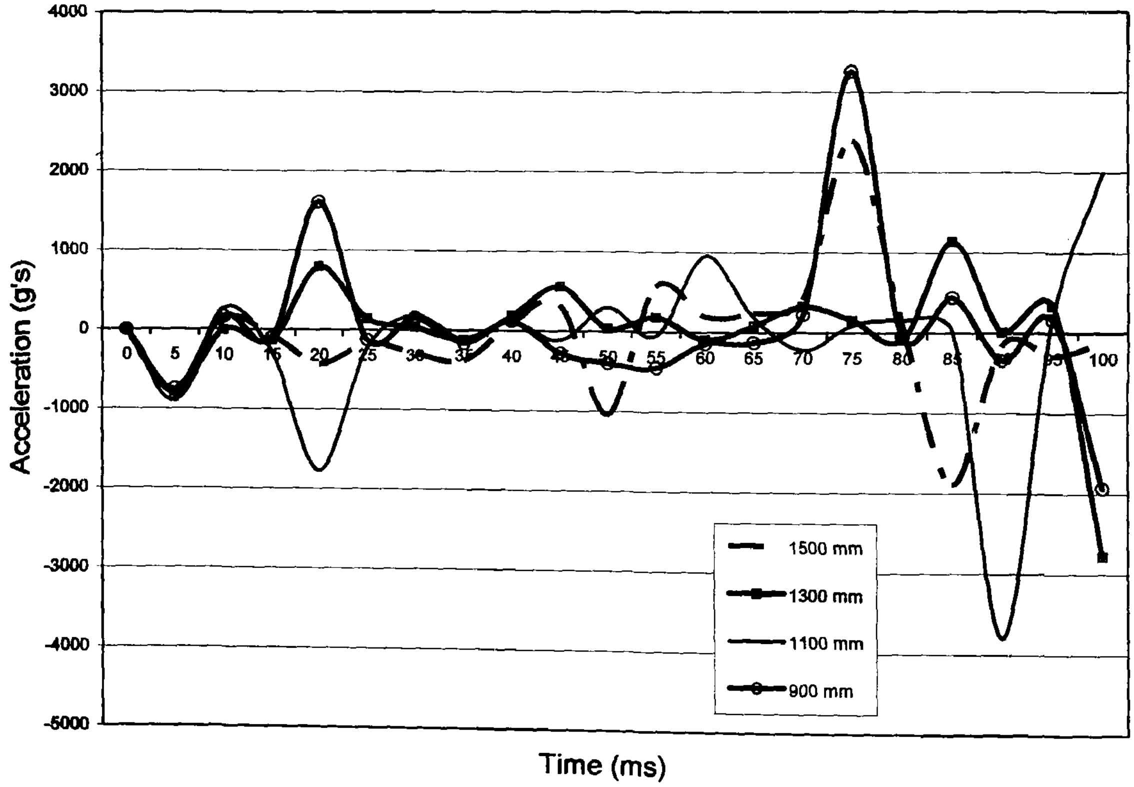

(b) Aluminium pole embedded in dense sand: Node #1317

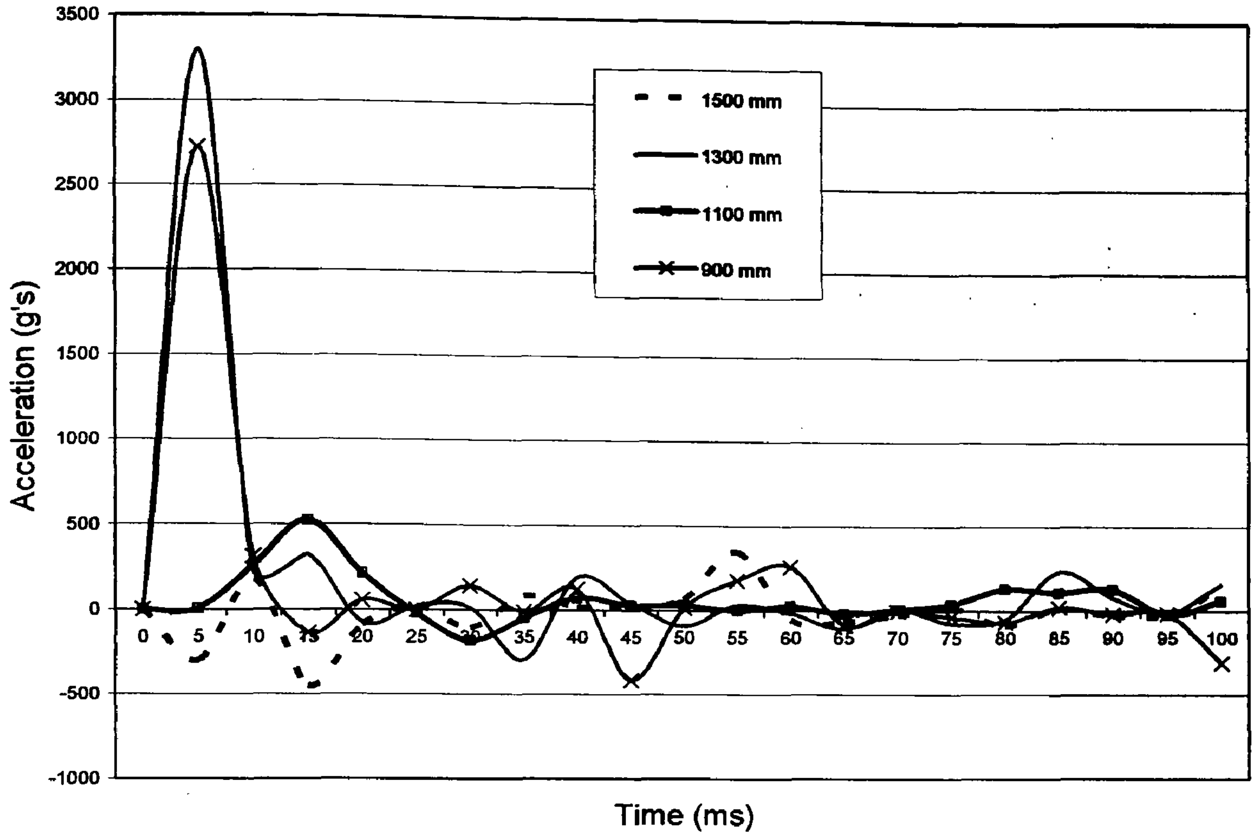

(c) Aluminium pole embedded in dense sand: Node # 19589

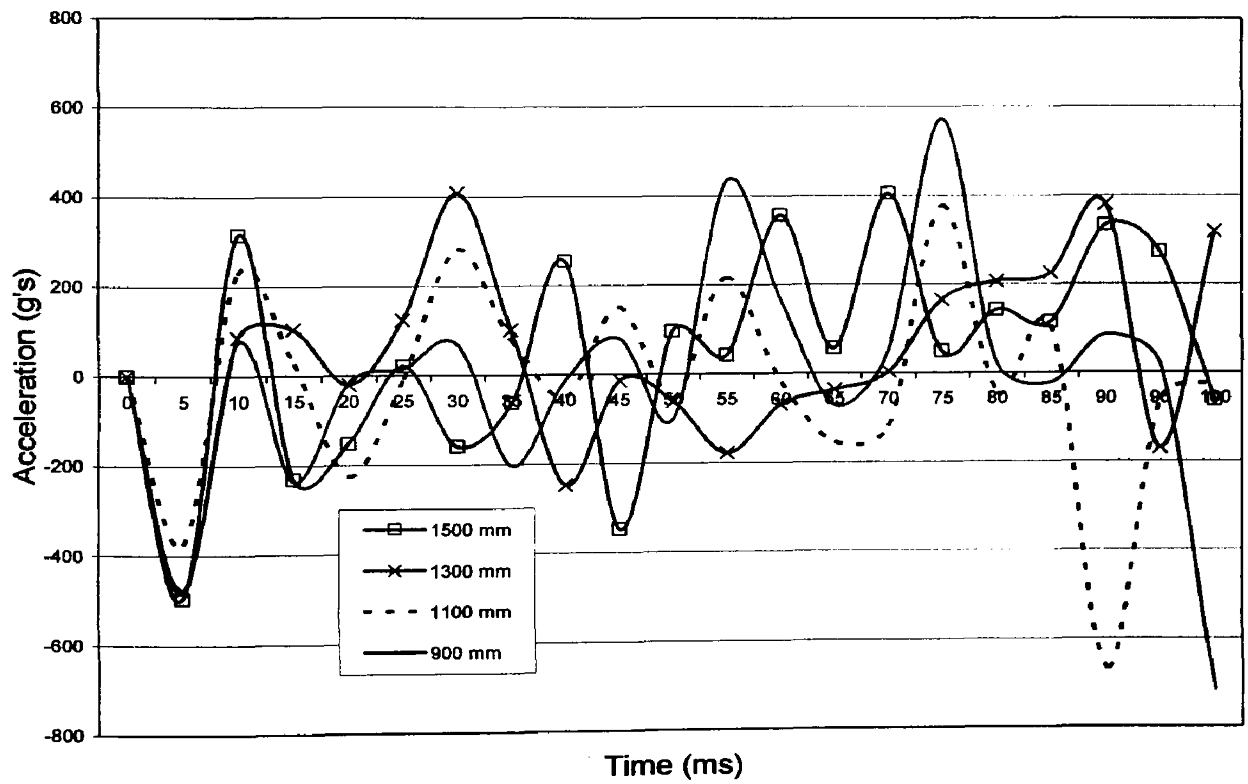

(d) Aluminium pole embedded in dense sand : Node #708

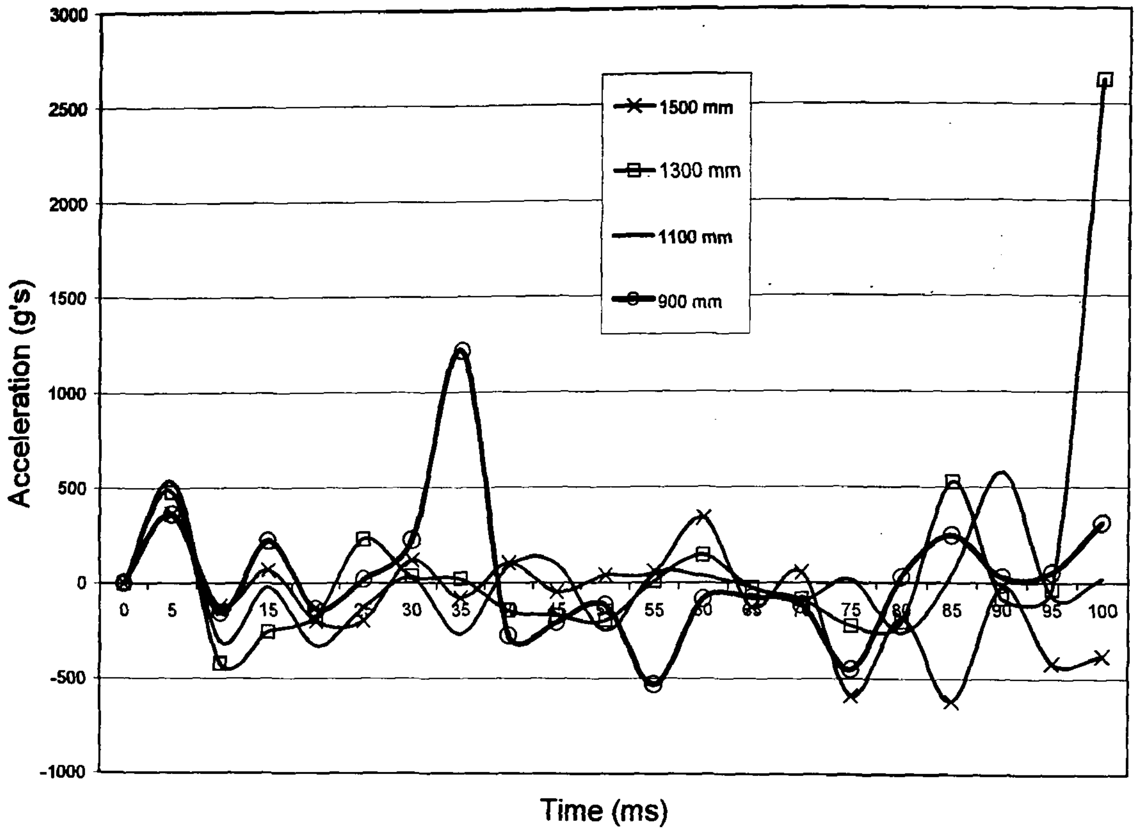

(e) Aluminium pole embedded in dense sand : Node # 1122

Figure 4.28 Comparative accelerations at the nodes on driver side door for aluminiun pole embedded in dense sandy soil.

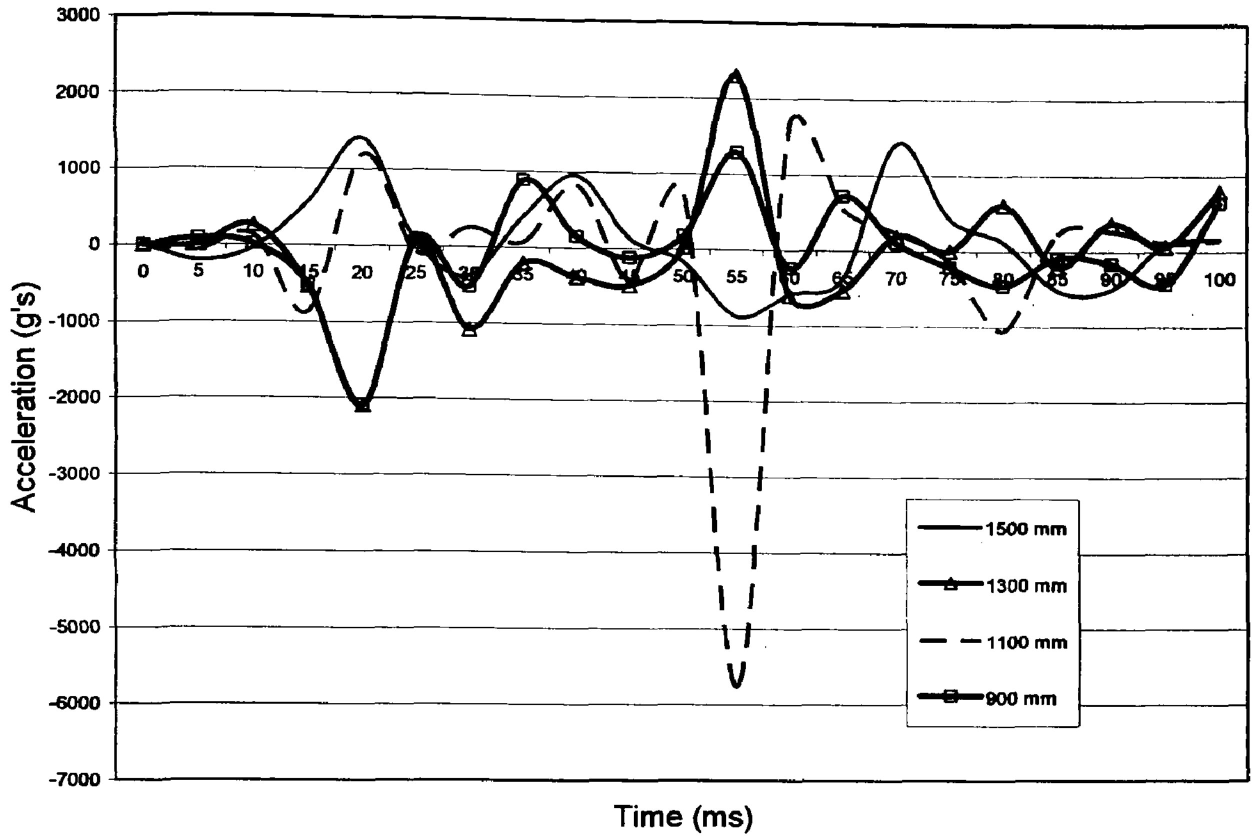

(a) Aluminium pole embedded in loose sand: Node #523

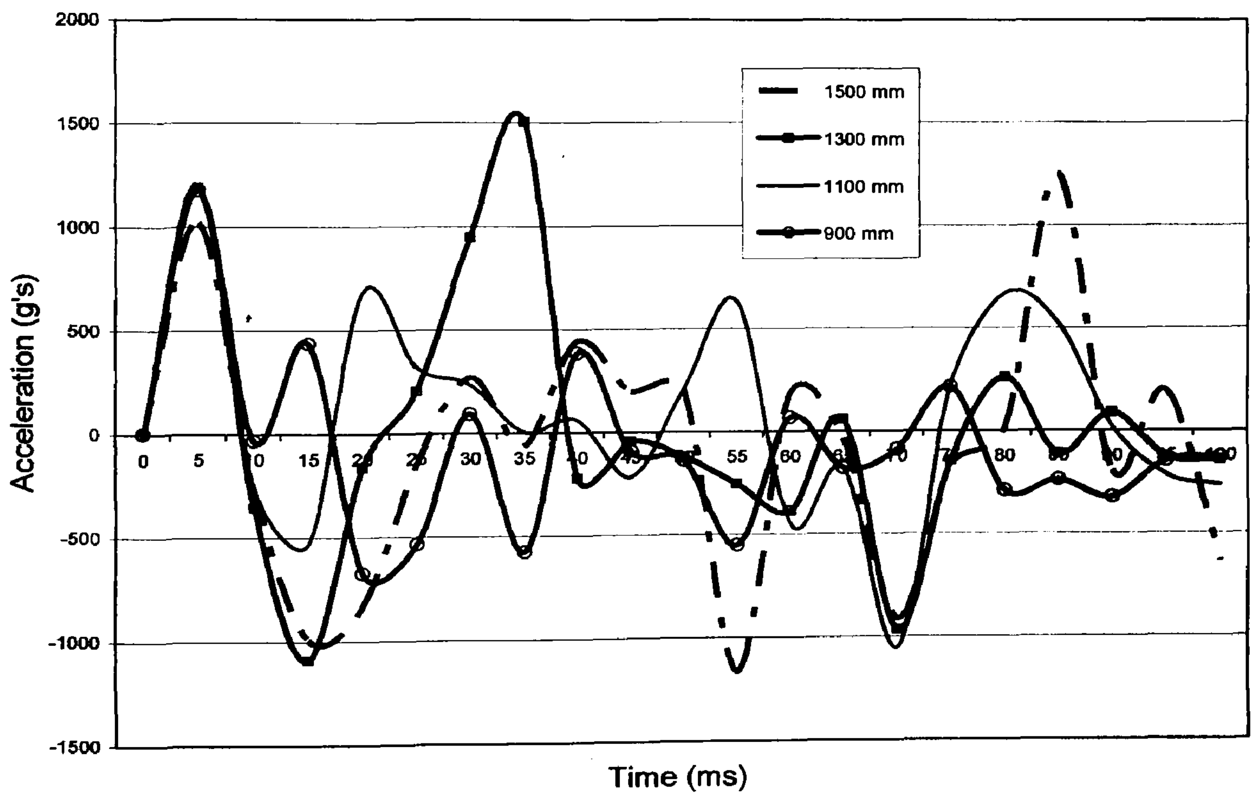

(b) Aluminium pole embedded in loose sand: Node #1317

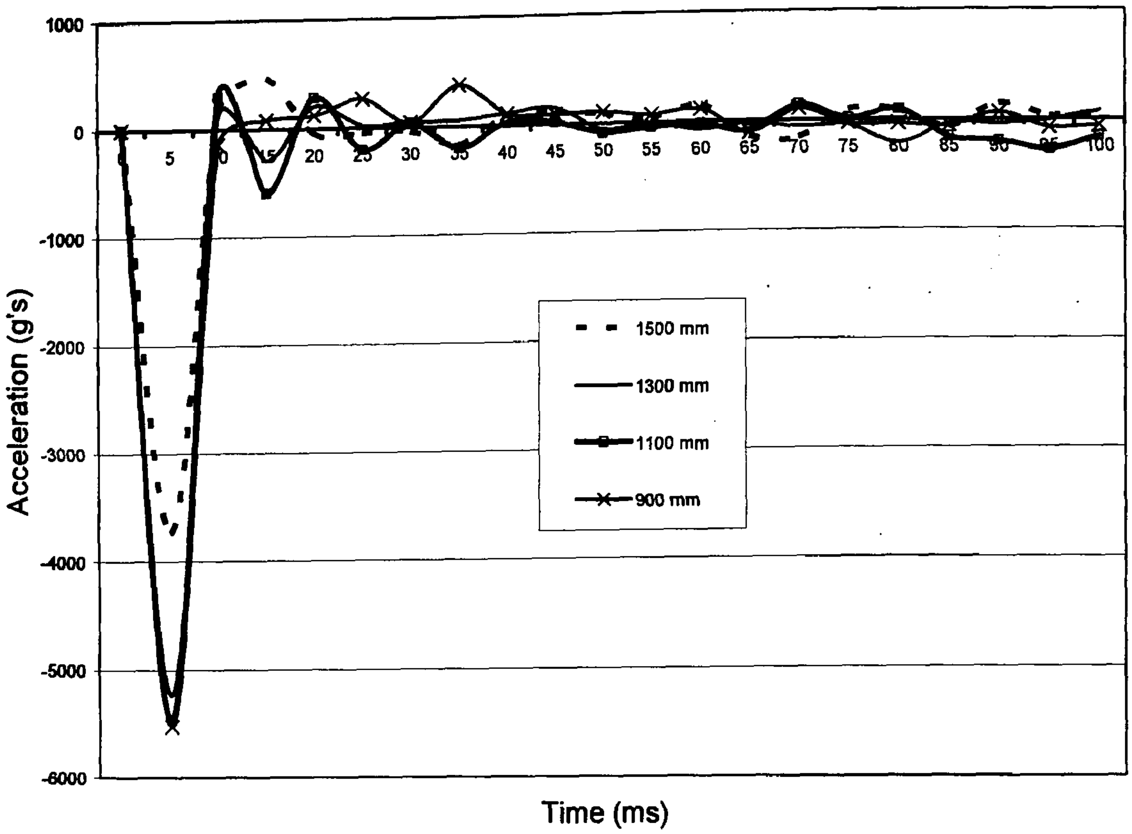

(c) Aluminium pole embedded in loose sand: Node # 19589

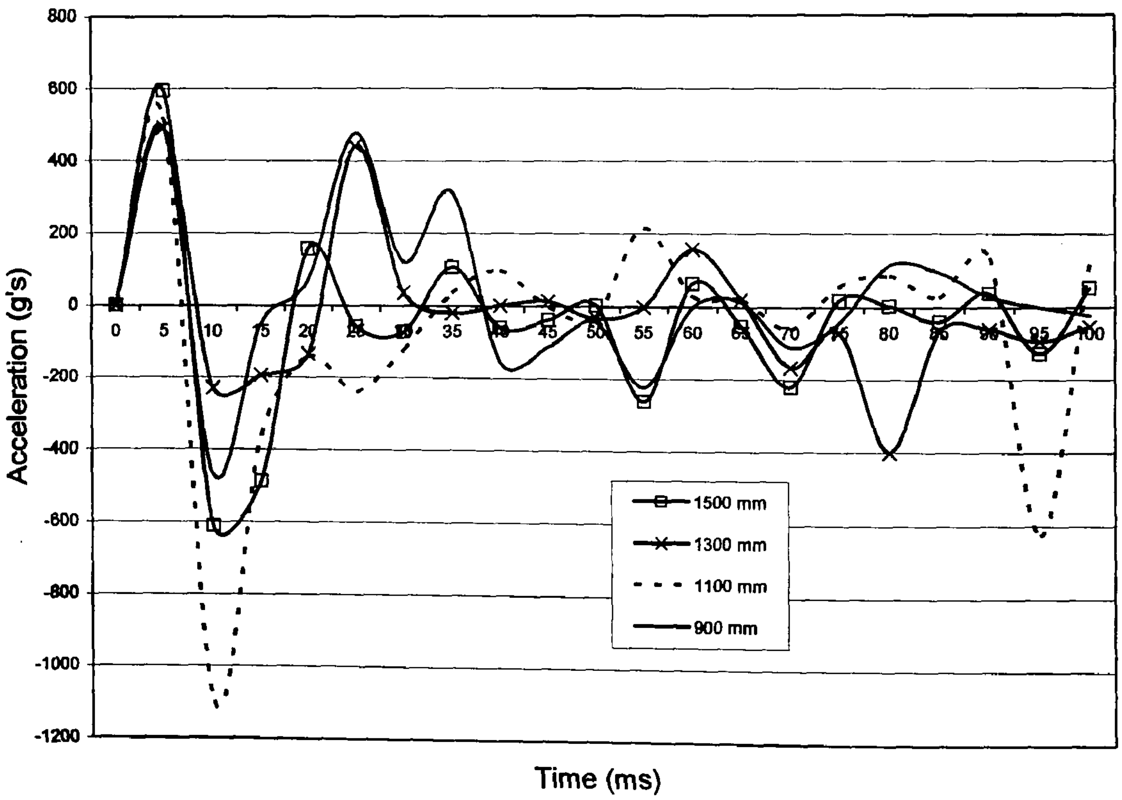

(d) Aluminium pole embedded in loose sand: Node #708

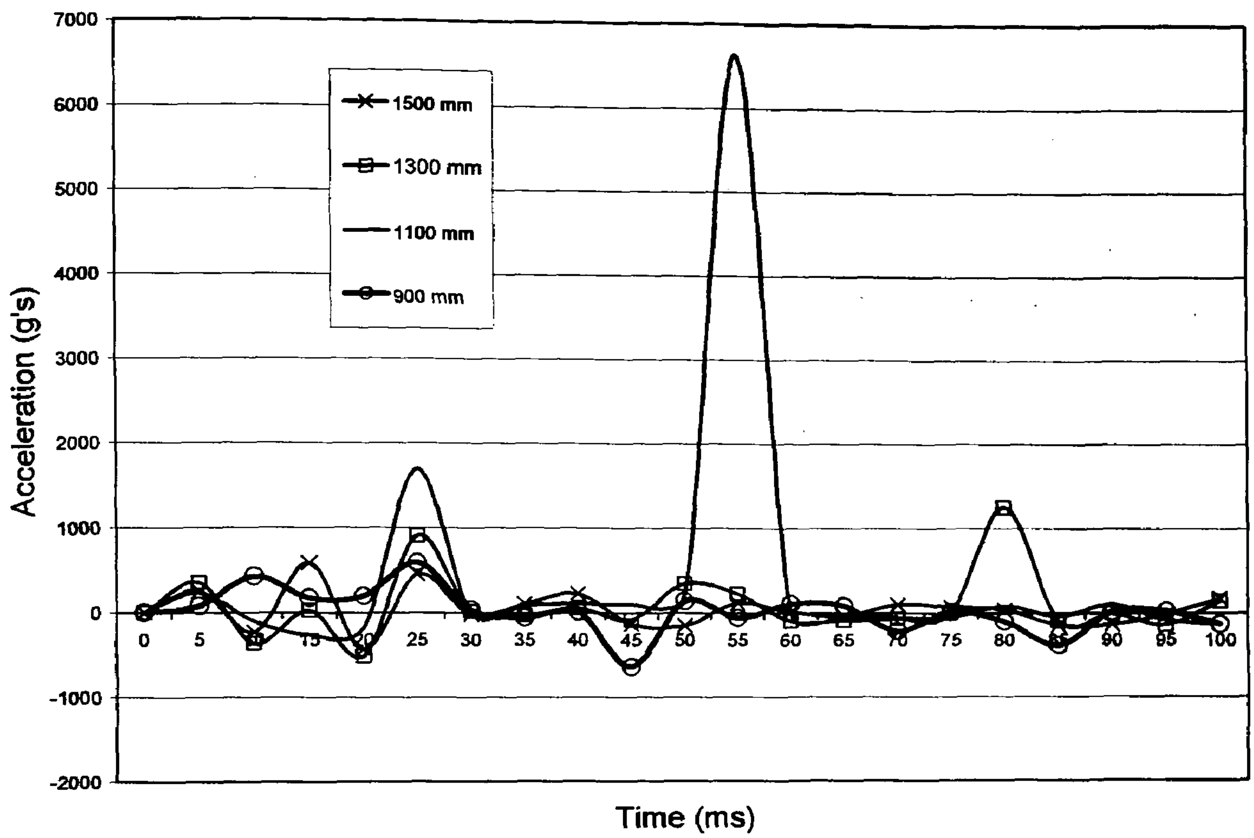

(e) Aluminium pole embedded in loose sand: Node # 1122

Figure 4.29 Comparative accelerations at the nodes on driver side door for aluminium pole embedded in dense sandy soil.

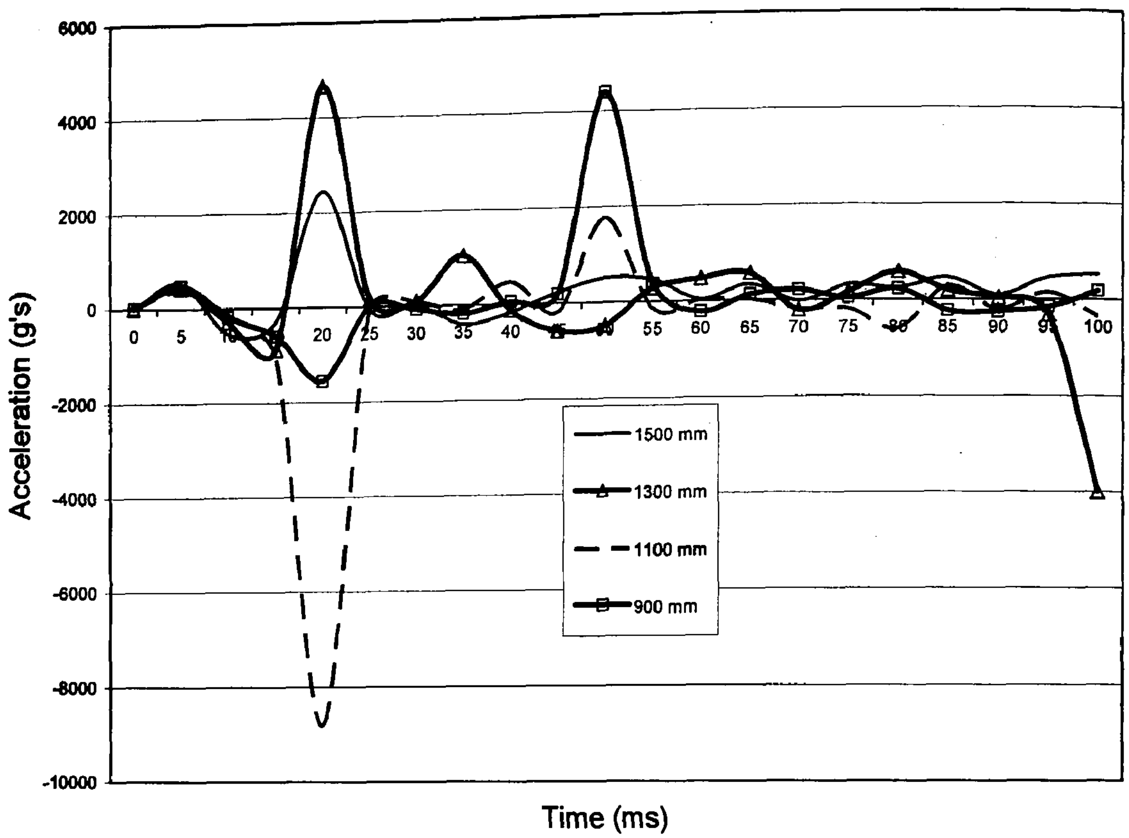

(a) Aluminium pole embedded in stiff clayey soil: Node #523

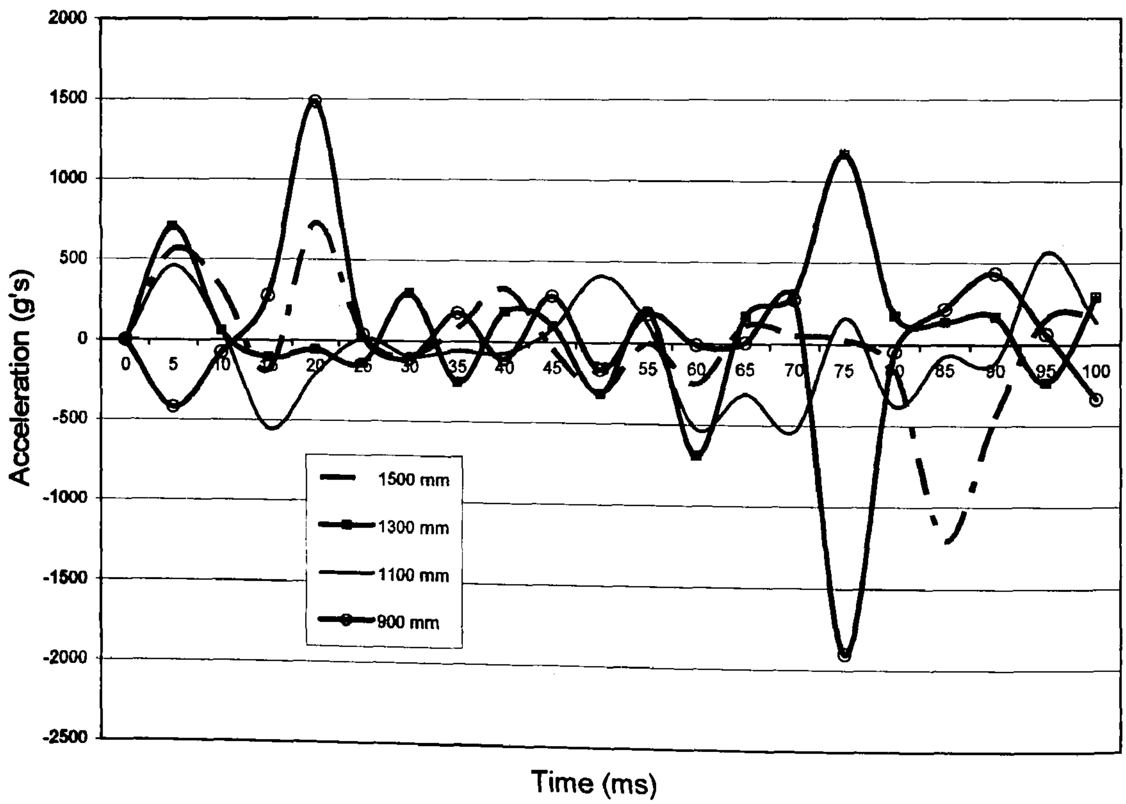

(b) Aluminium pole embedded in stiff clayey soil: Node #1317

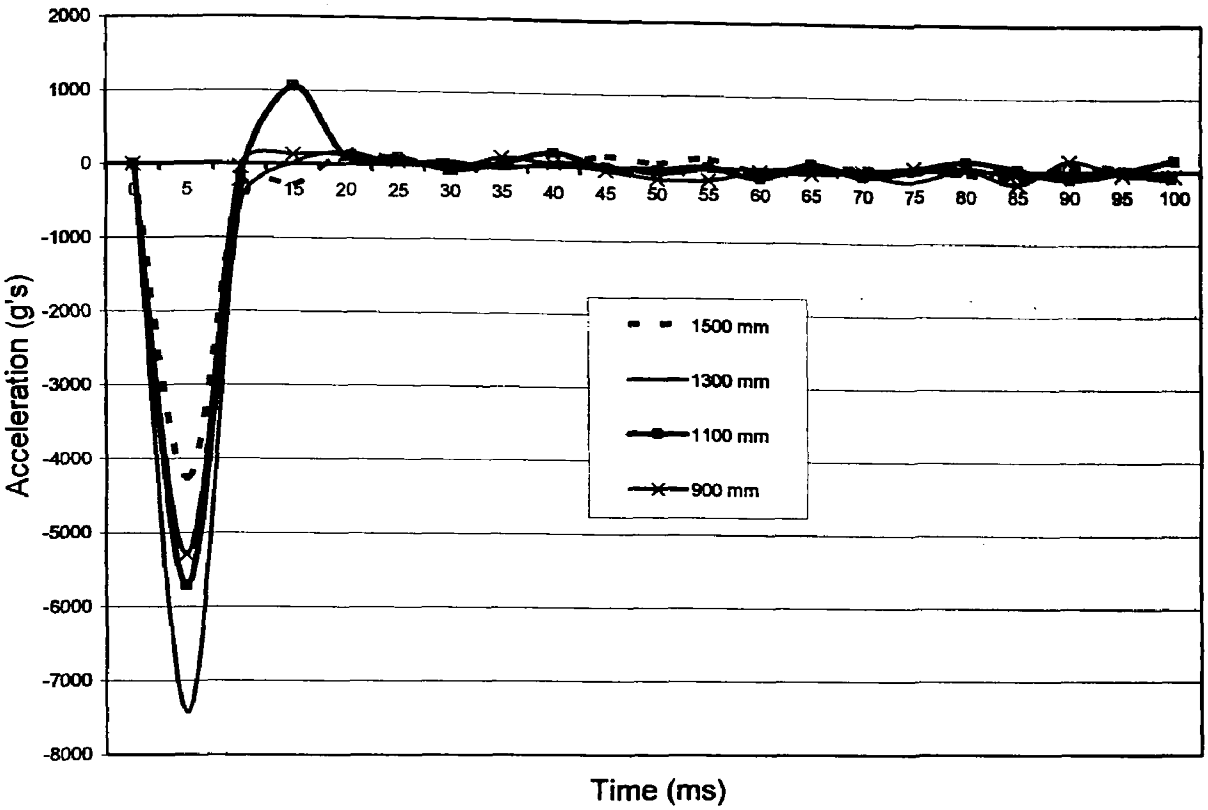

(c) Aluminium pole embedded in stiff clayey soil: Node # 19589

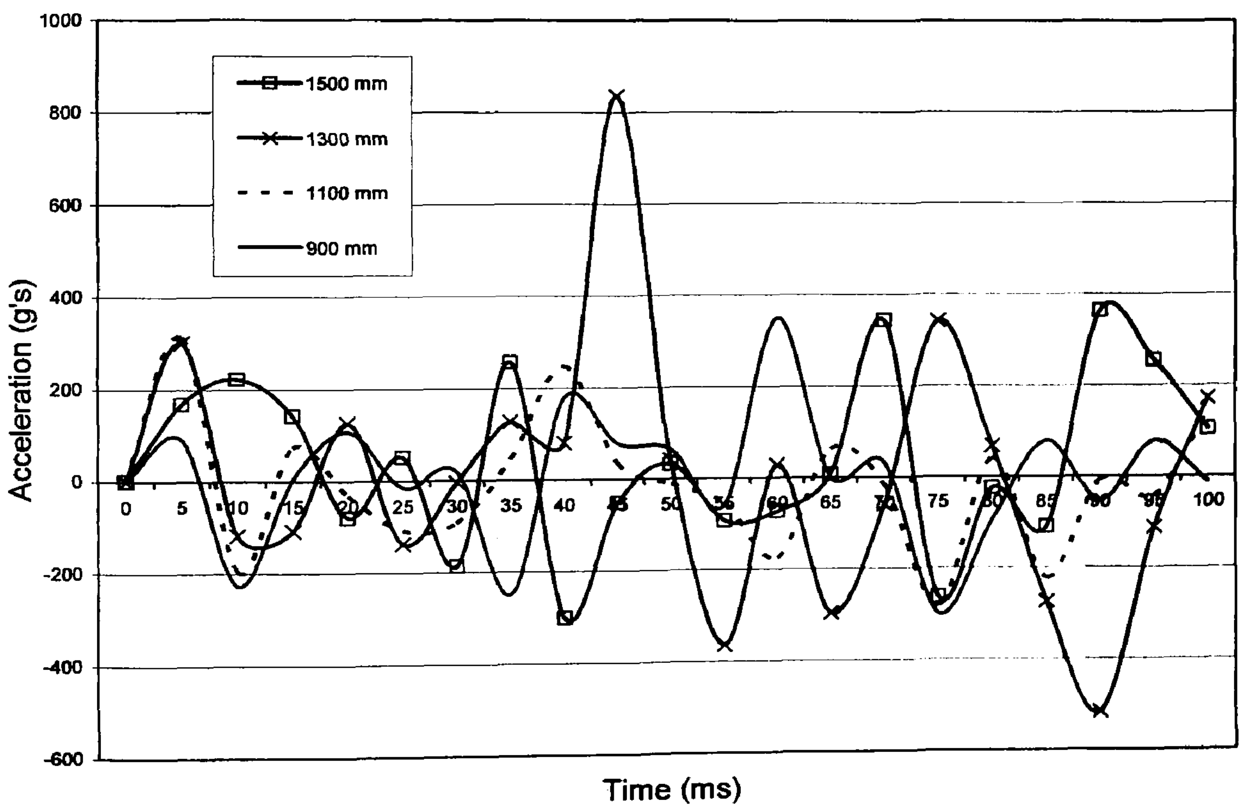

(d) Aluminium pole embedded in stiff clayey soil: Node #708

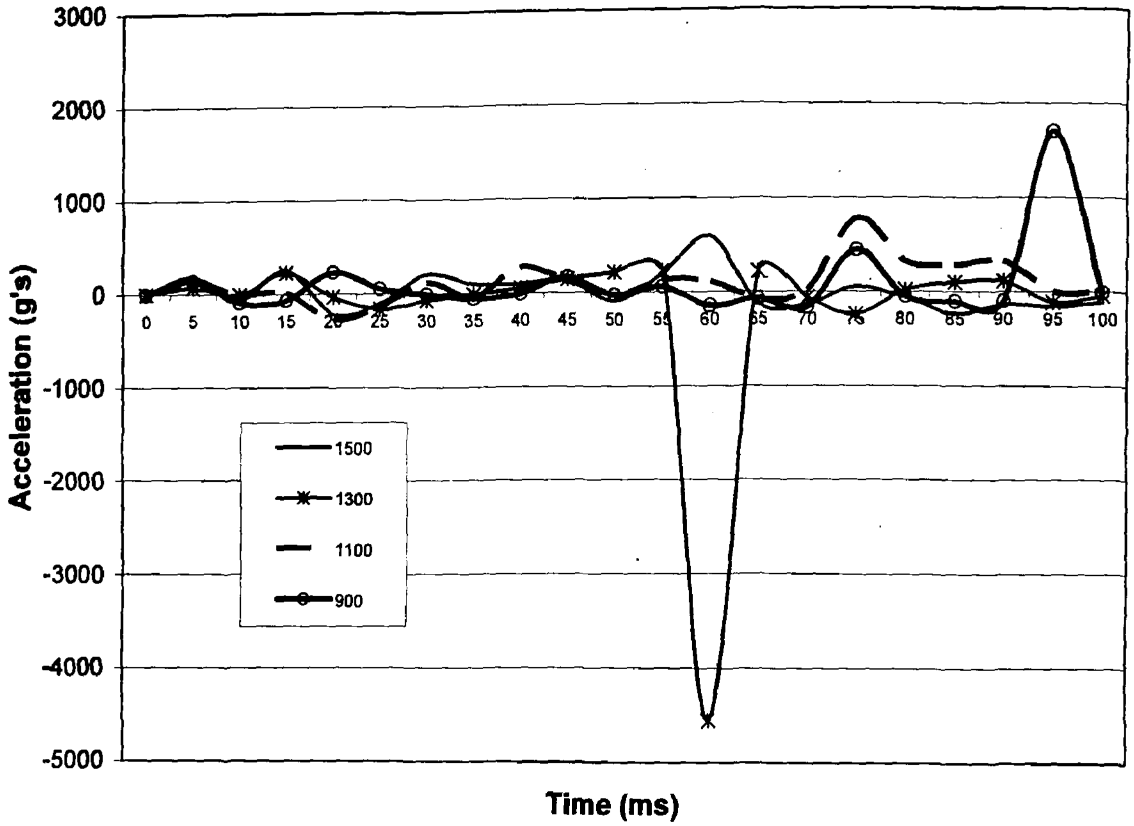

(e) Aluminium pole embedded in stiff clayey soil: Node # 1122

Figure 4.30 Comparative accelerations at the nodes on driver side door for the aluminium pole embedded in stiff clayey soil.

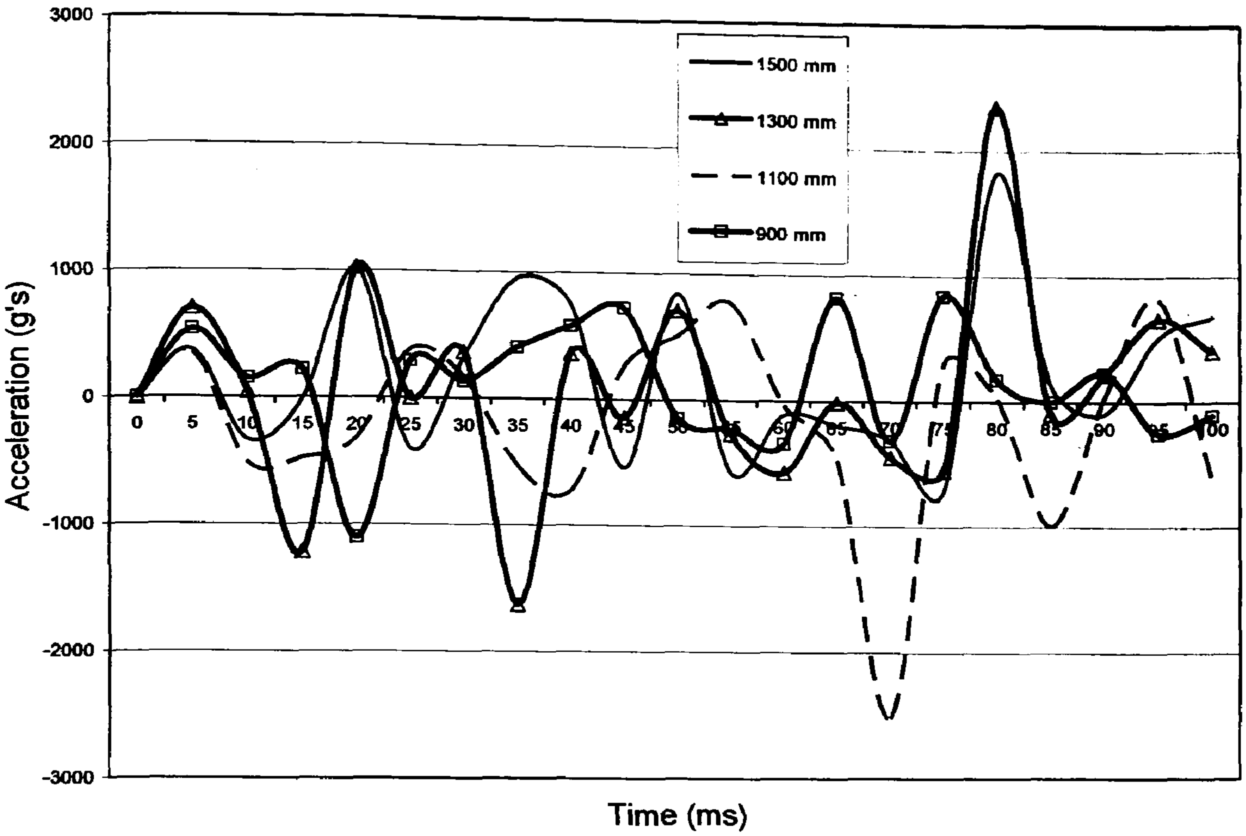

(a) Aluminium pole embedded in soft clayey soil: Node #523

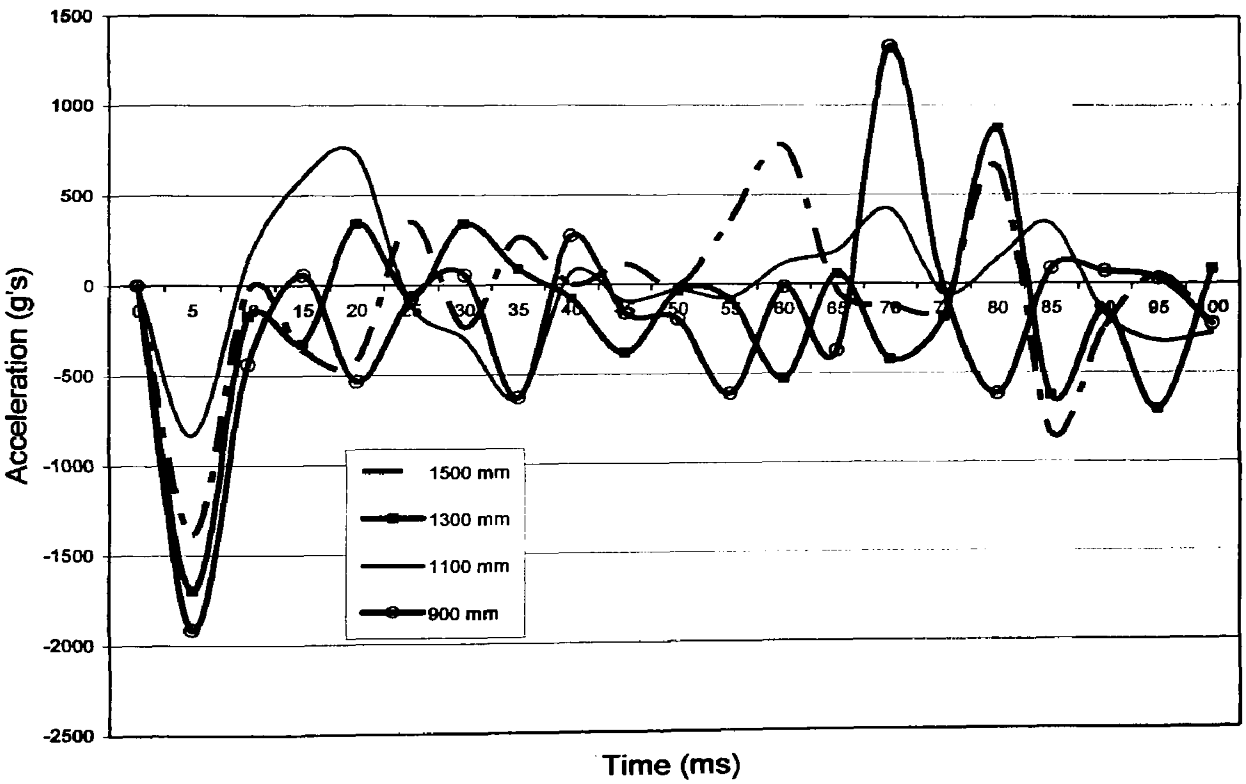

(b) Aluminium pole embedded in soft clayey soil: Node #1317

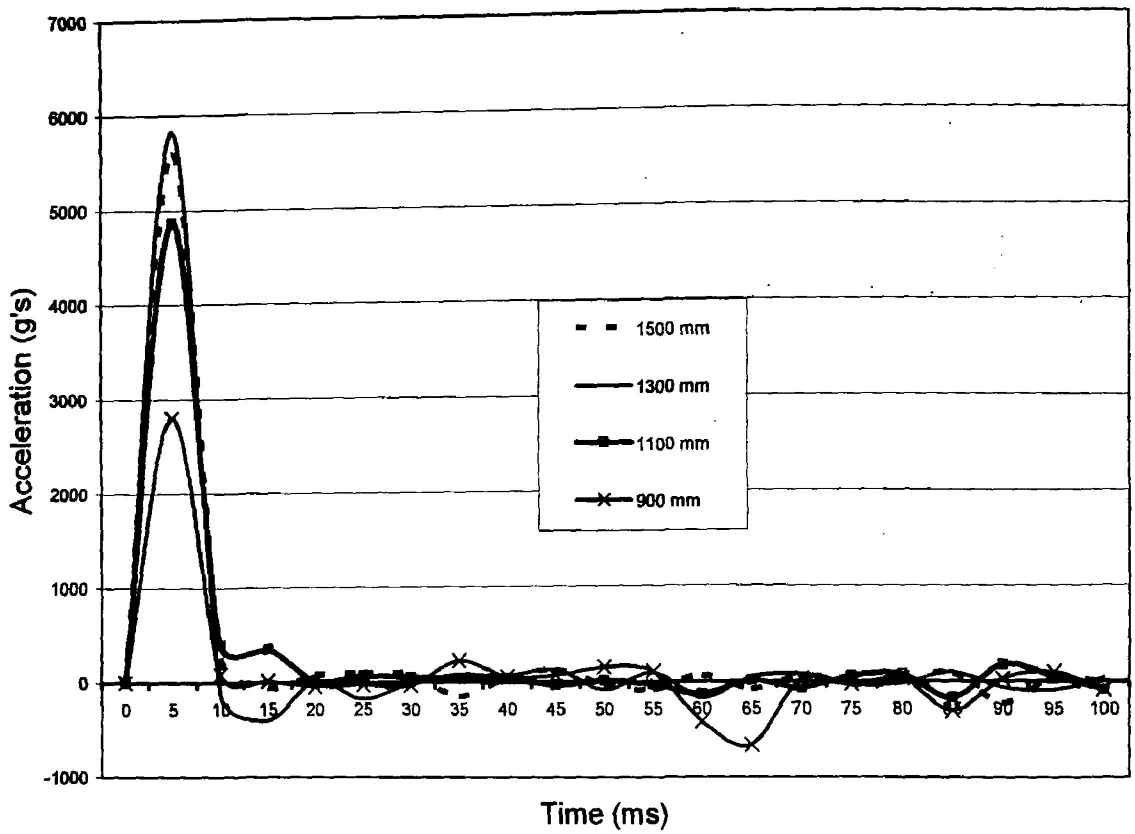

(c) Aluminium pole embedded in soft clayey soil: Node # 19589

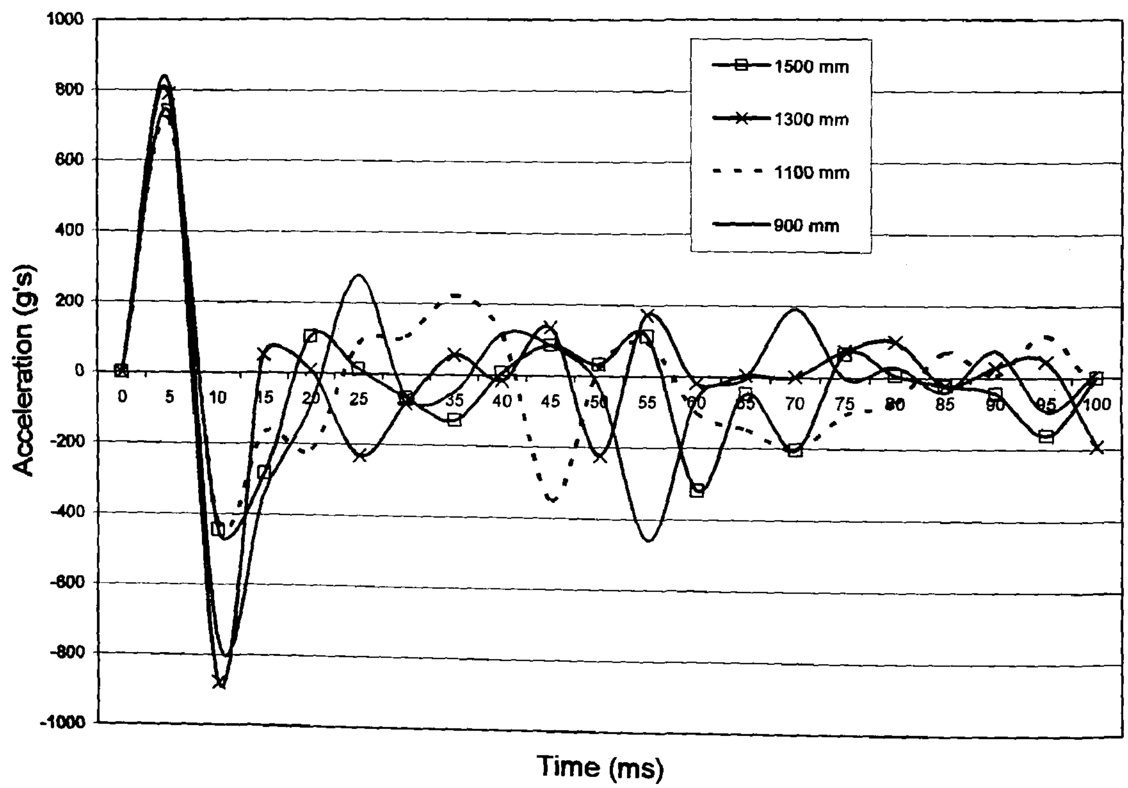

(d) Aluminium pole embedded in soft clayey soil: Node #708

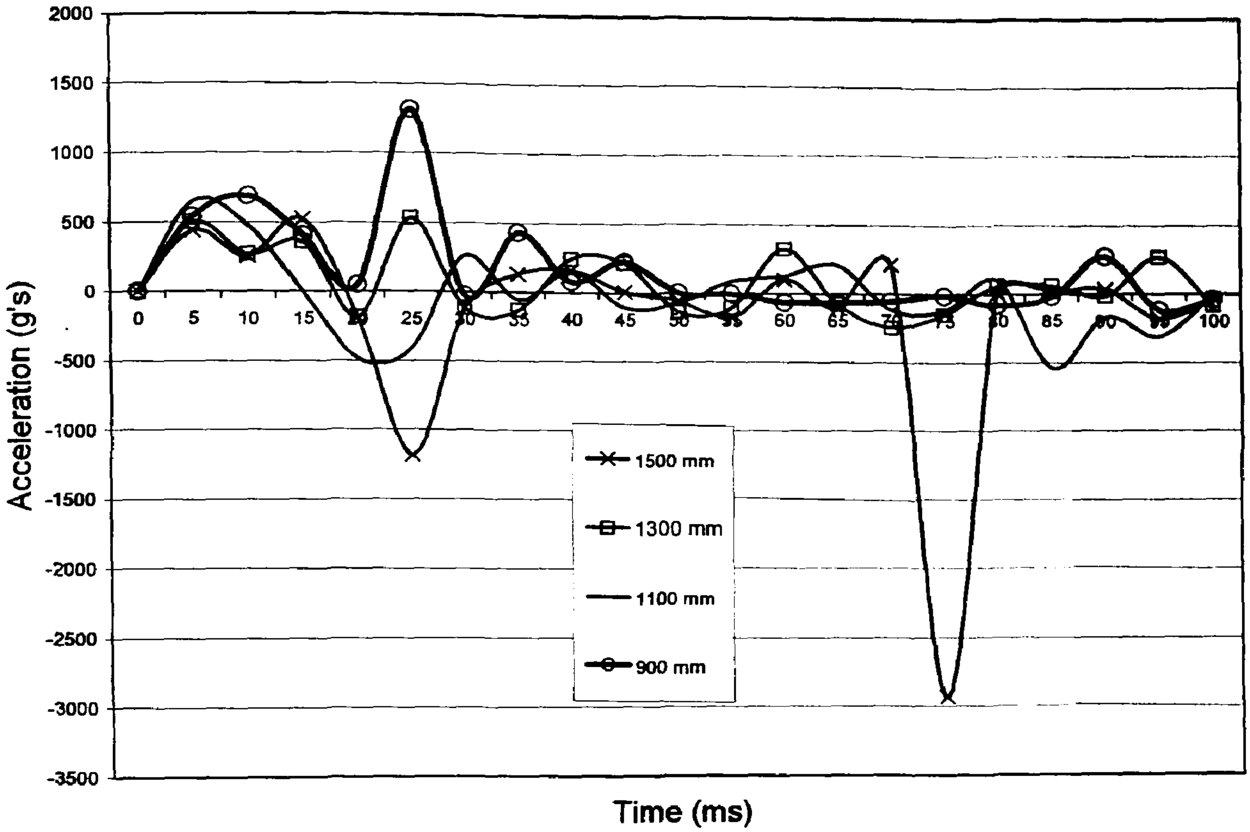

(e) Aluminium pole embedded in soft clayey soil: Node # 1122

Figure 4.31 Comparative accelerations at nodes on the driver side door for aluminium pole embedded in soft clayey soil.

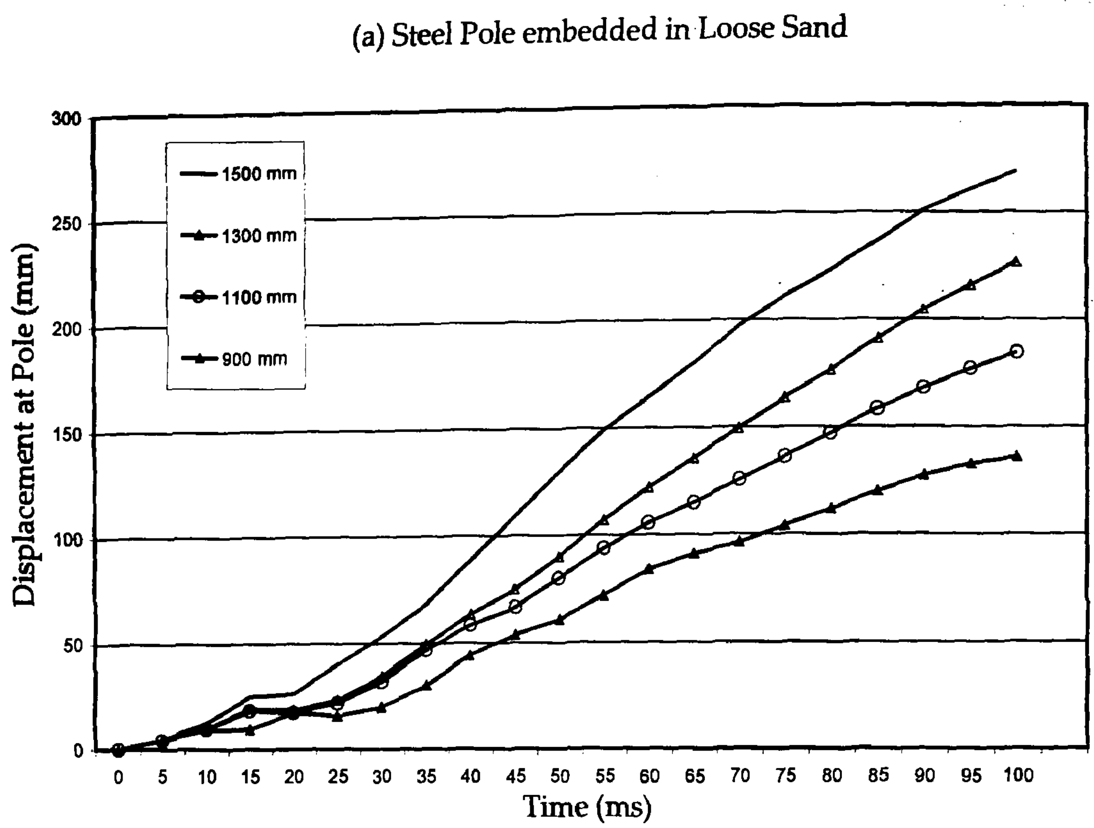
(a) Steel Pole embedded in Loose Sand
1500 mm
1300 mm
1100 mm
900 mm
Displacement at Pole (mm)
Time (ms)

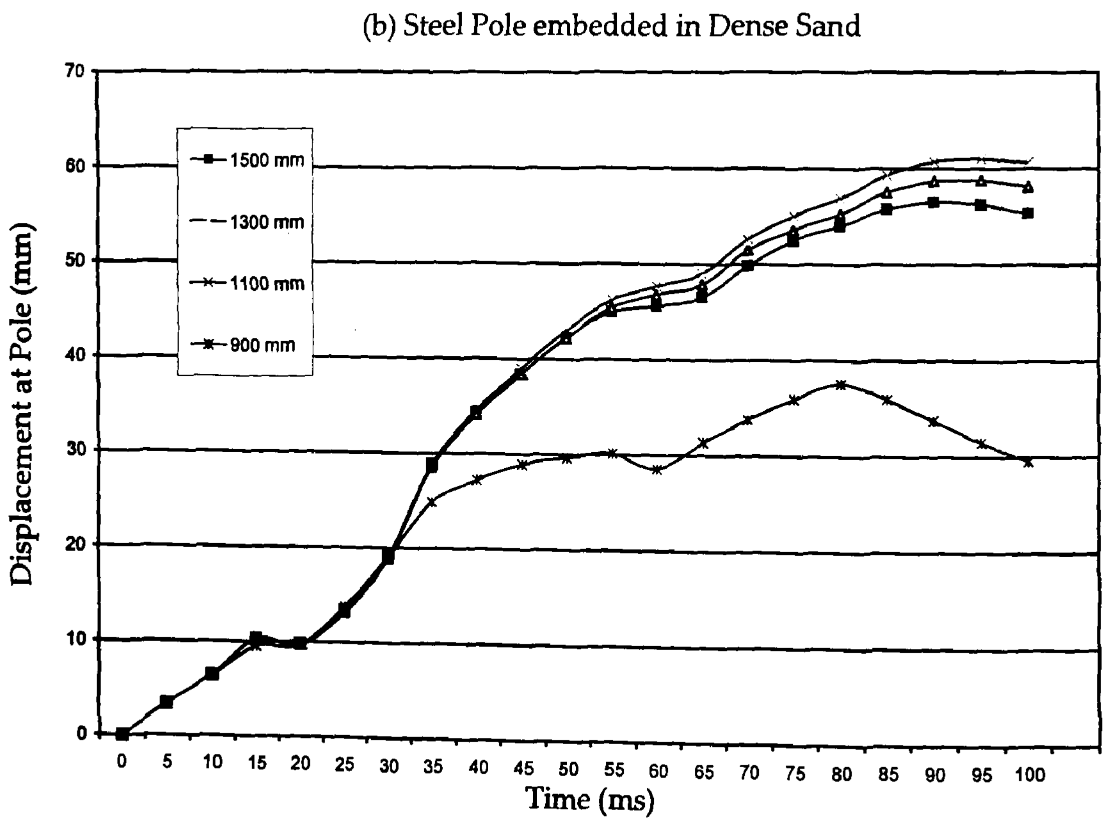
(b) Steel Pole embedded in Dense Sand
1500 mm
1300 mm
1100 mm
900 mm
Displacement at Pole (mm)
Time (ms)

(c) Steel Pole embedded in Soft Clay

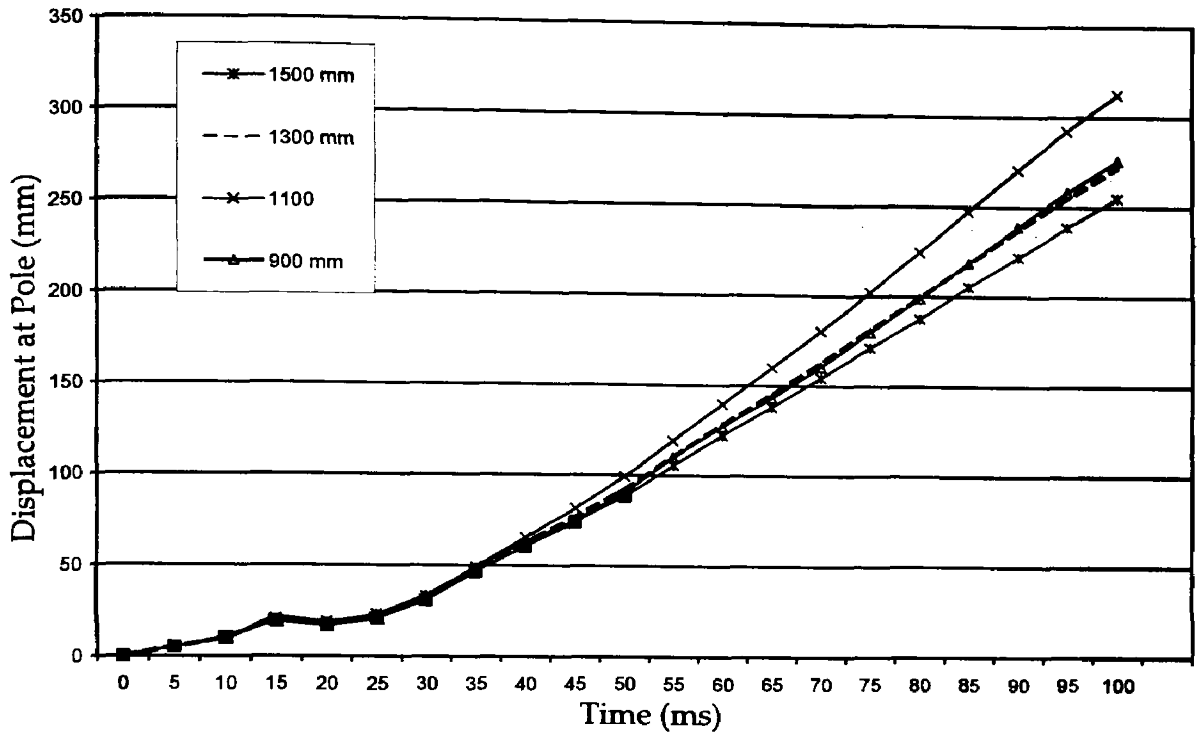

(d) Steel Pole embedded in Stiff Clay

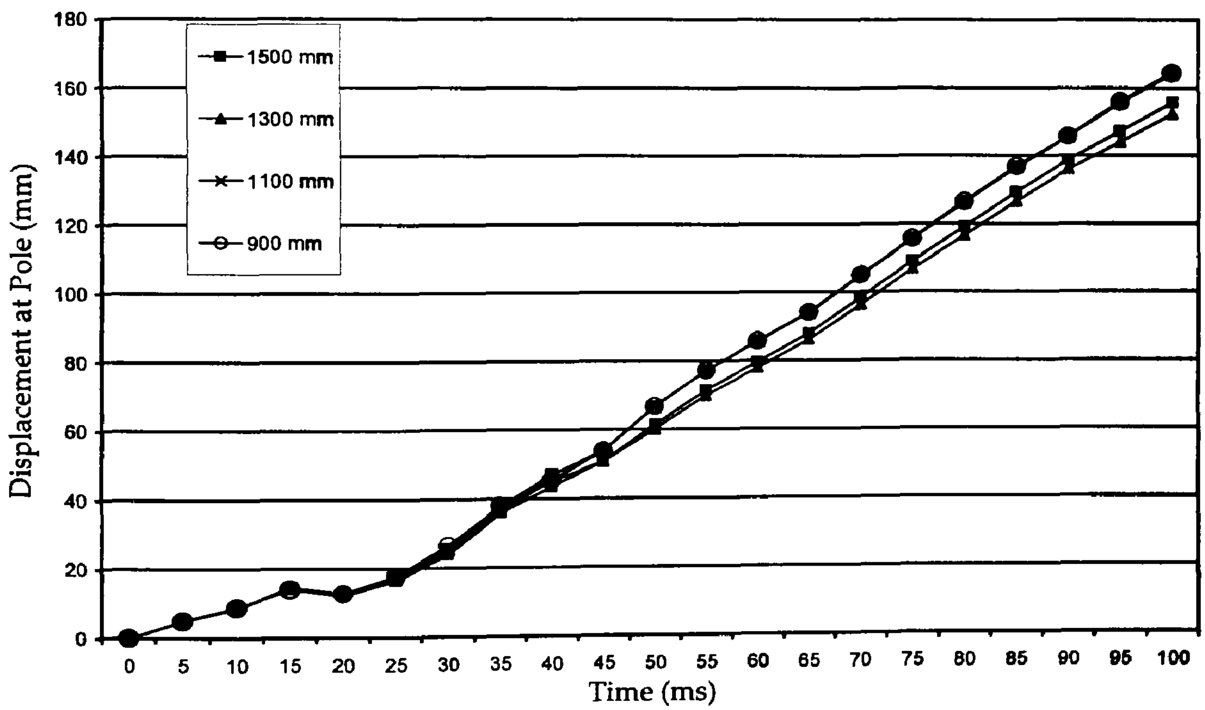

Figure 4.32 Nodal displacement time histories at a point of contact between car and steel pole in side impact.

(a) Aluminium Pole embedded in Soft Clay

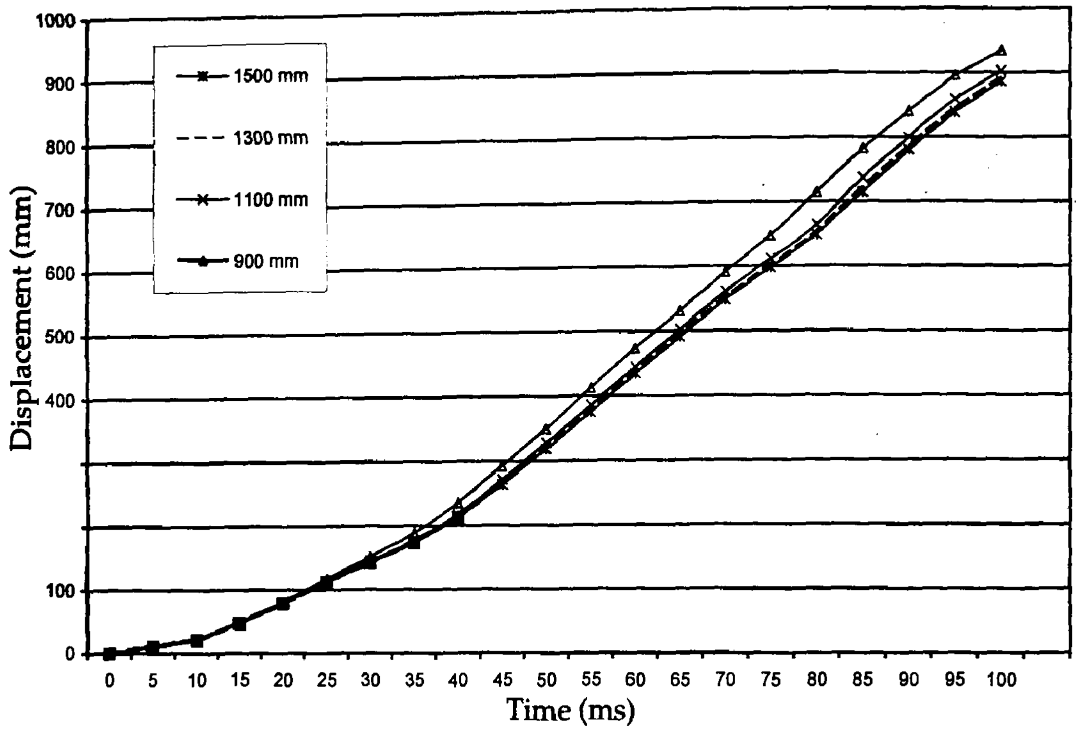

(b) Aluminium Pole embedded in Stiff Clay

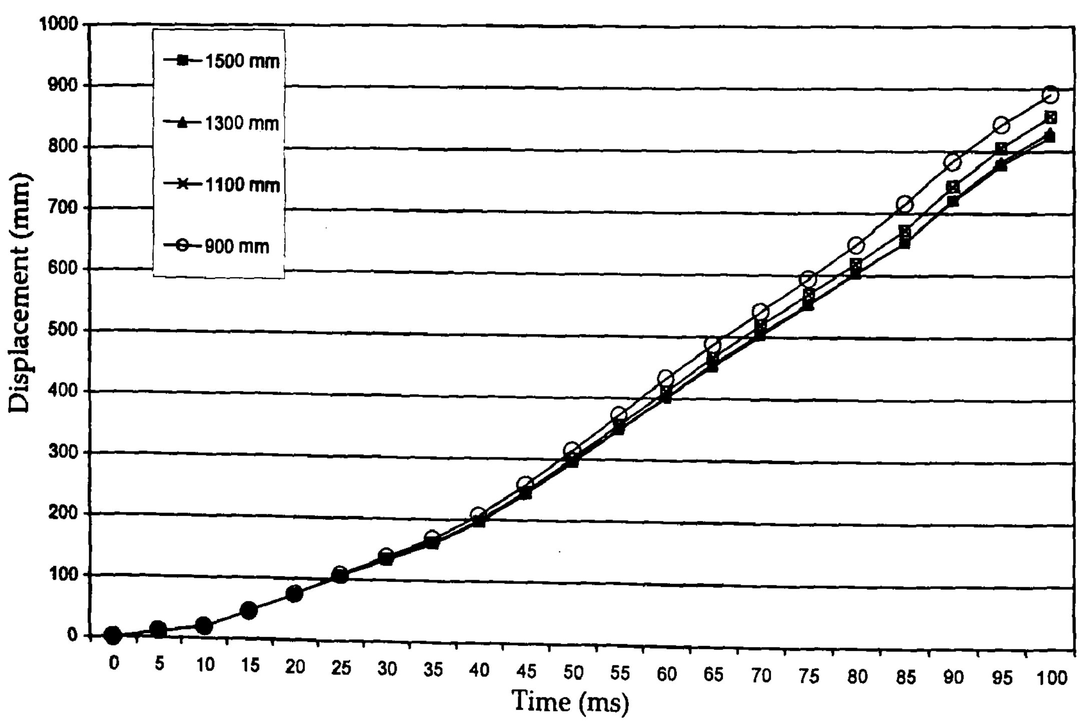

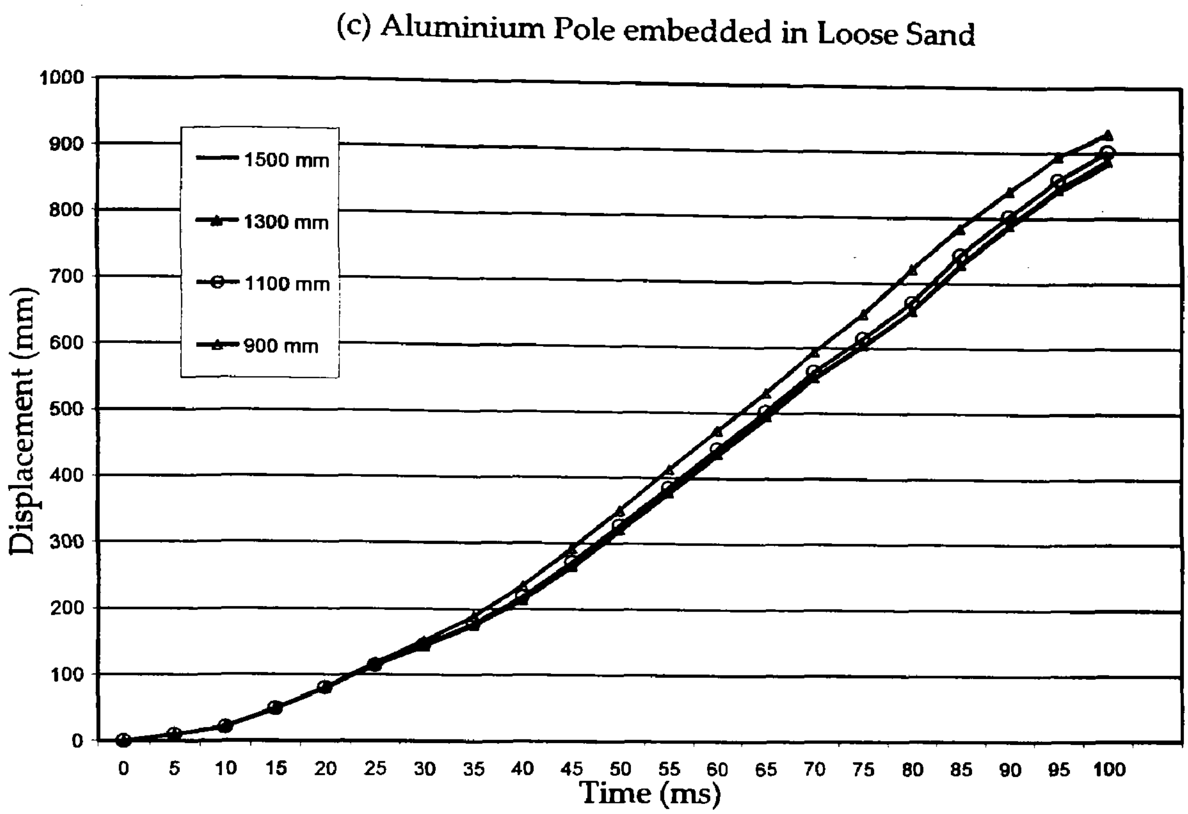

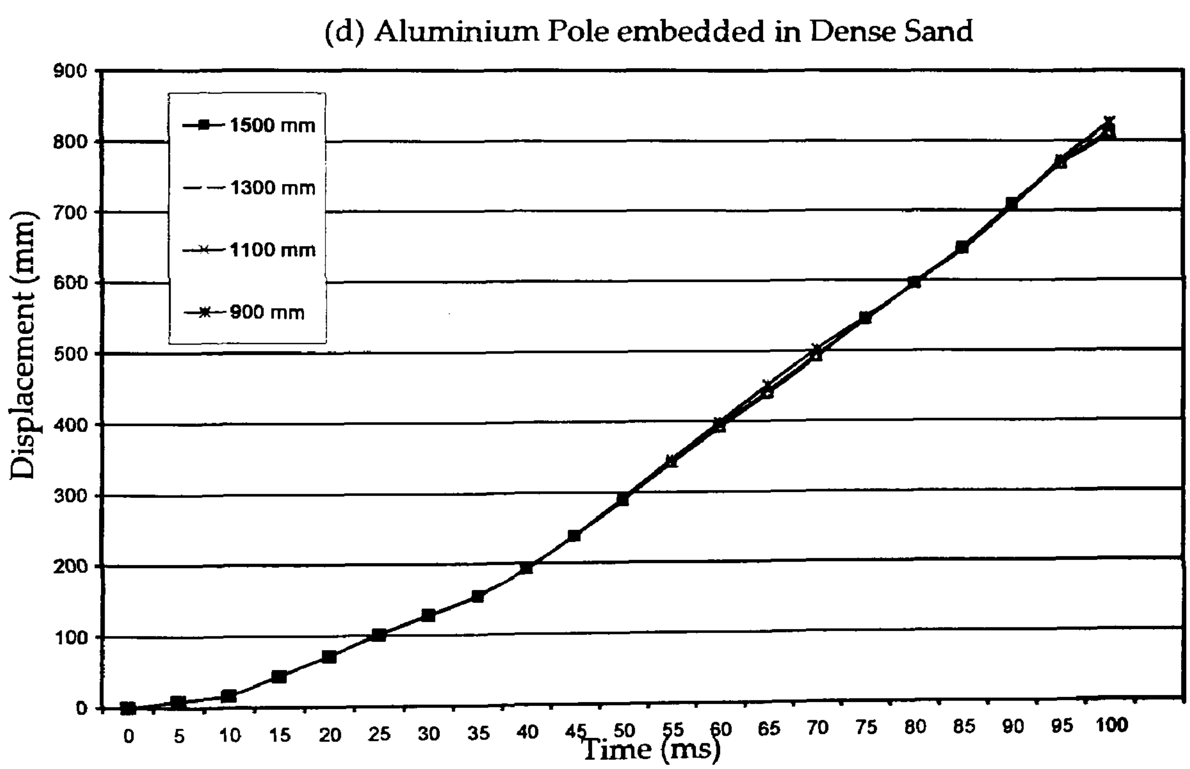

Figure 4.33 Nodal displacement time histories at a point of contact between car and aluminium pole in side impact.

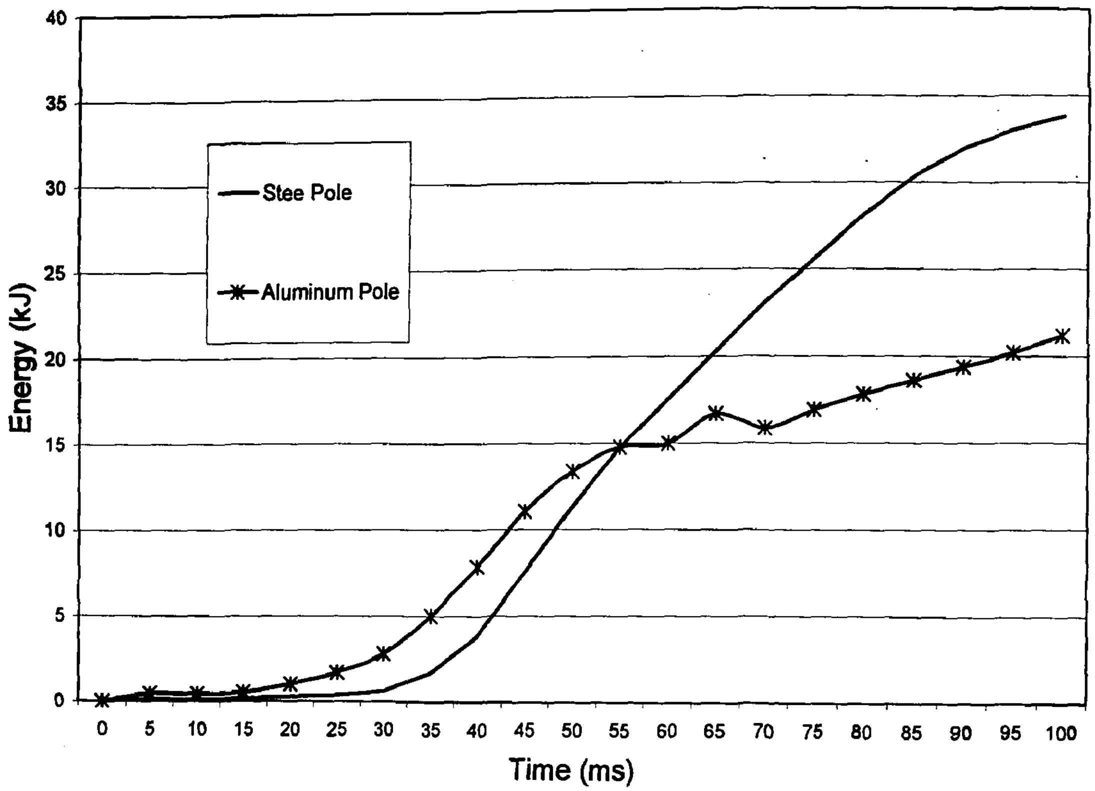

Figure 4.34 Energy absorbed by steel and aluminium poles embedded 1500 mm in soft clay in frontal impact.

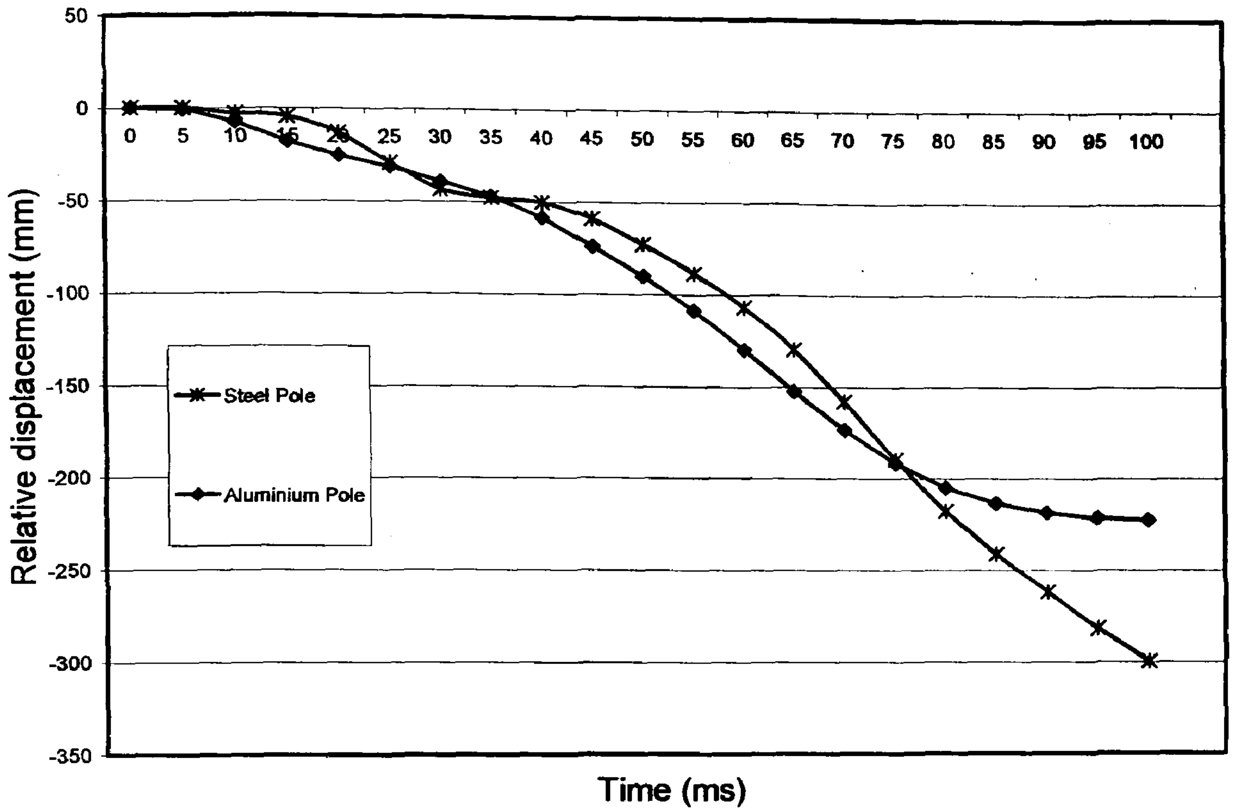

Figure 4.35 Comparative relative displacement between seat and steering for steel and aluminium poles embedded 1500 mm in soft clay in frontal impact.

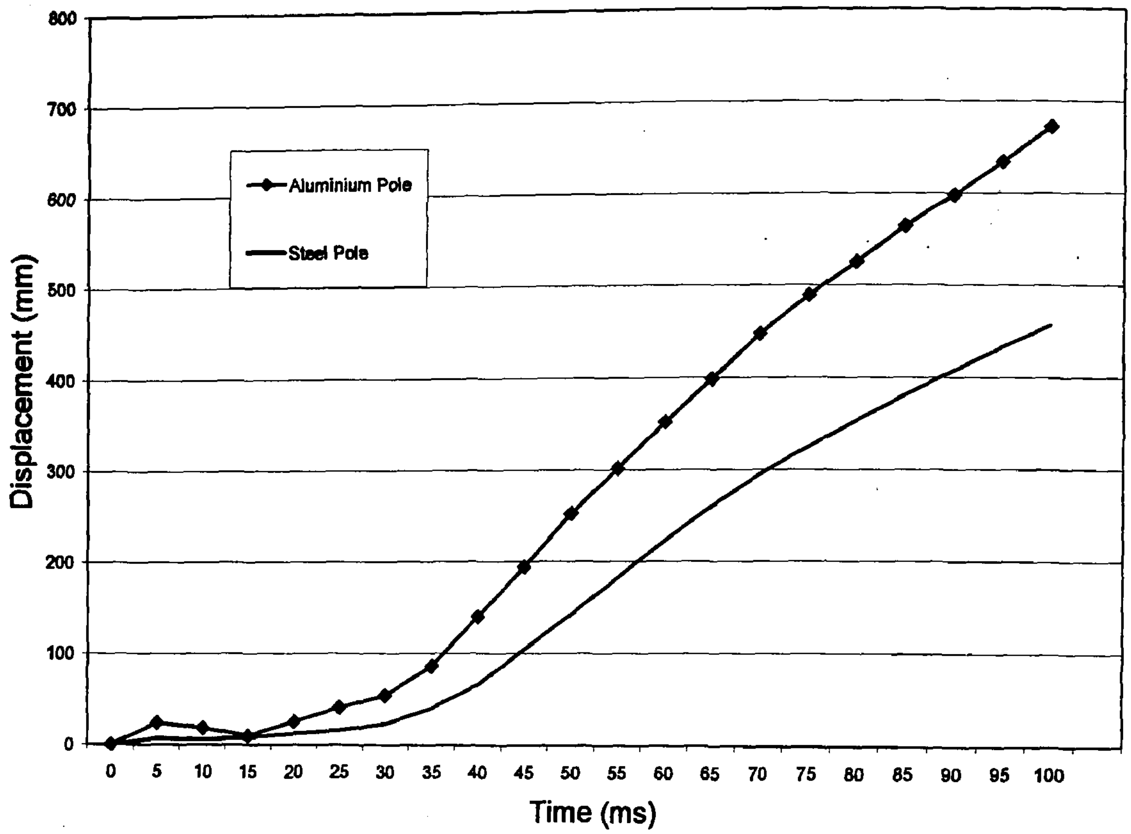

Figure 4.36 Comparative displacements of steel and aluminium poles at point of contact in frontal impact.

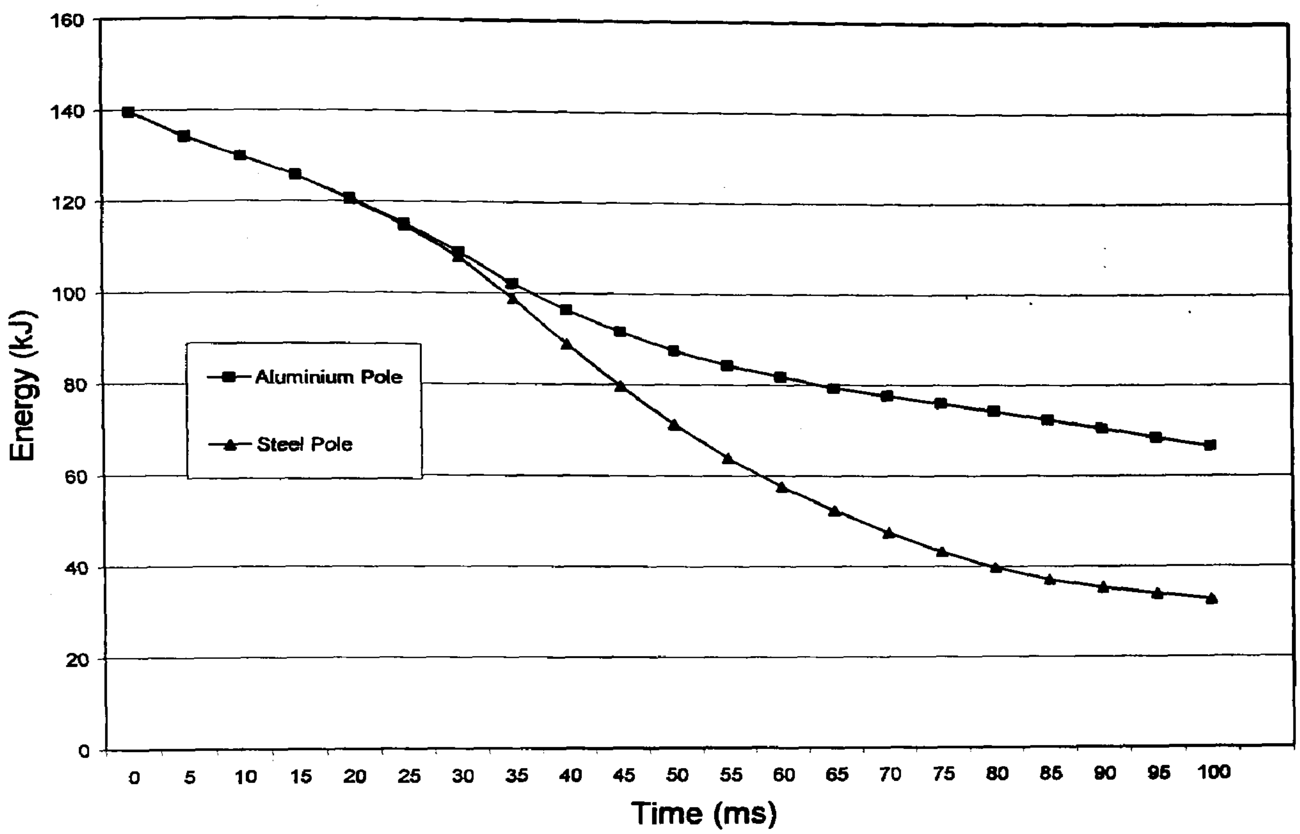

Figure 4.37 Comparative decay of kinetic energy for steel and aluminium poles embedded 1500 mm in soft clay in frontal impact.

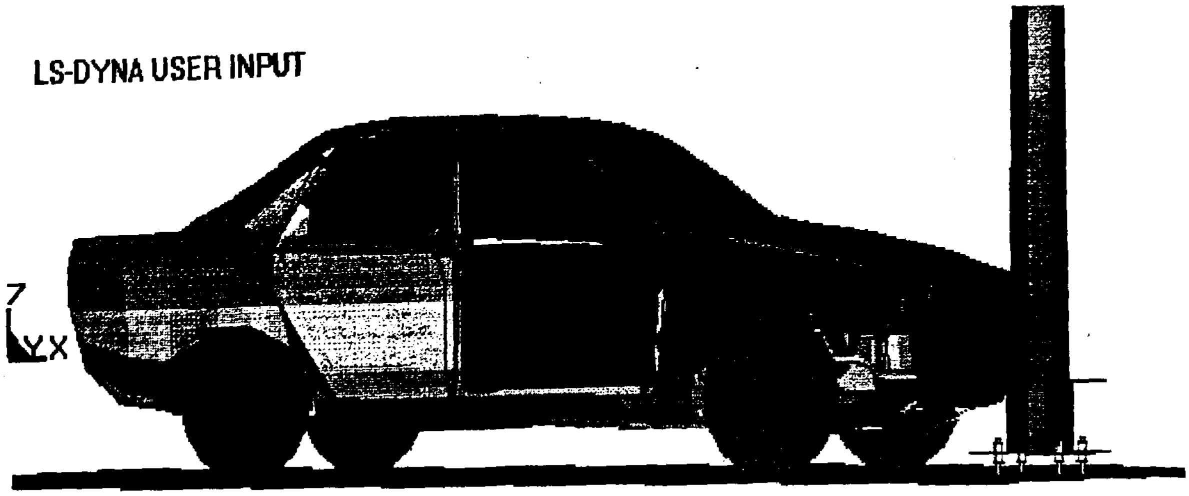

t = 0 ms

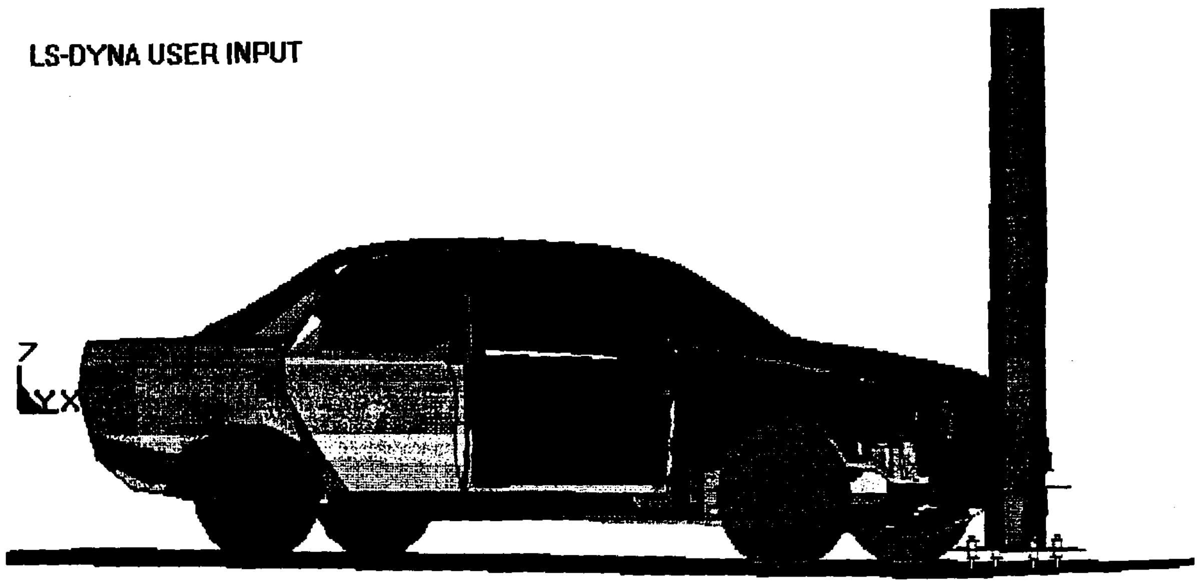

t = 25 ms

Figure 4.38 (a)

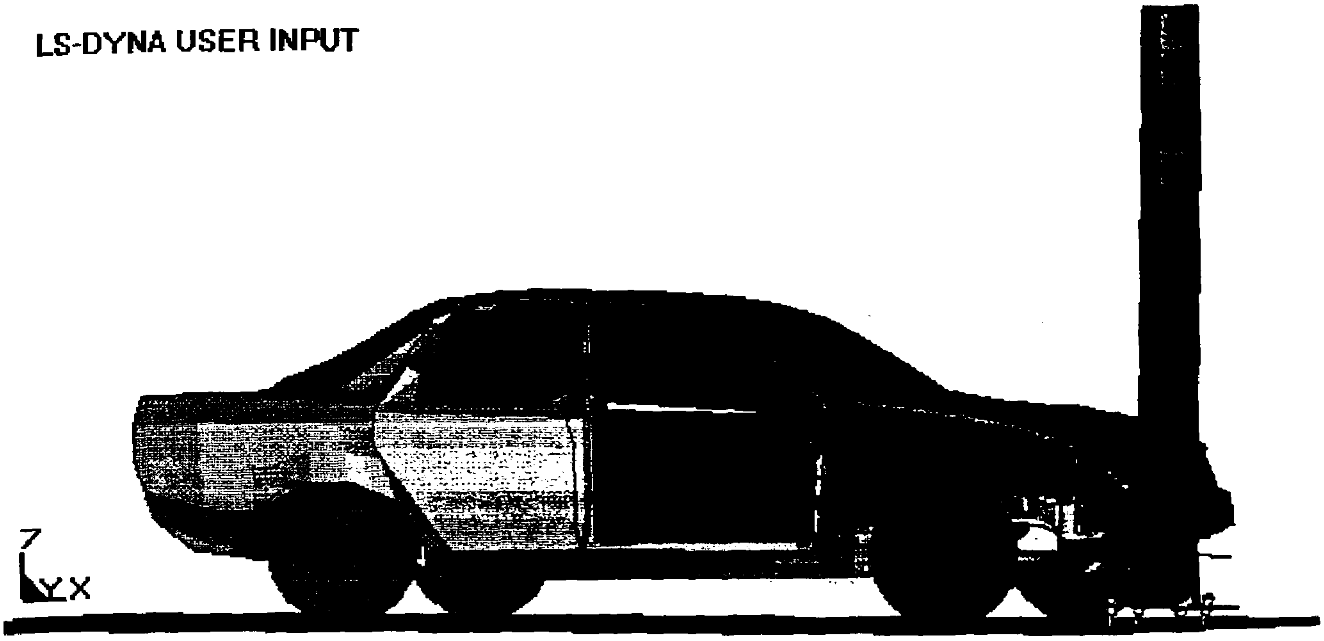

t = 50 ms

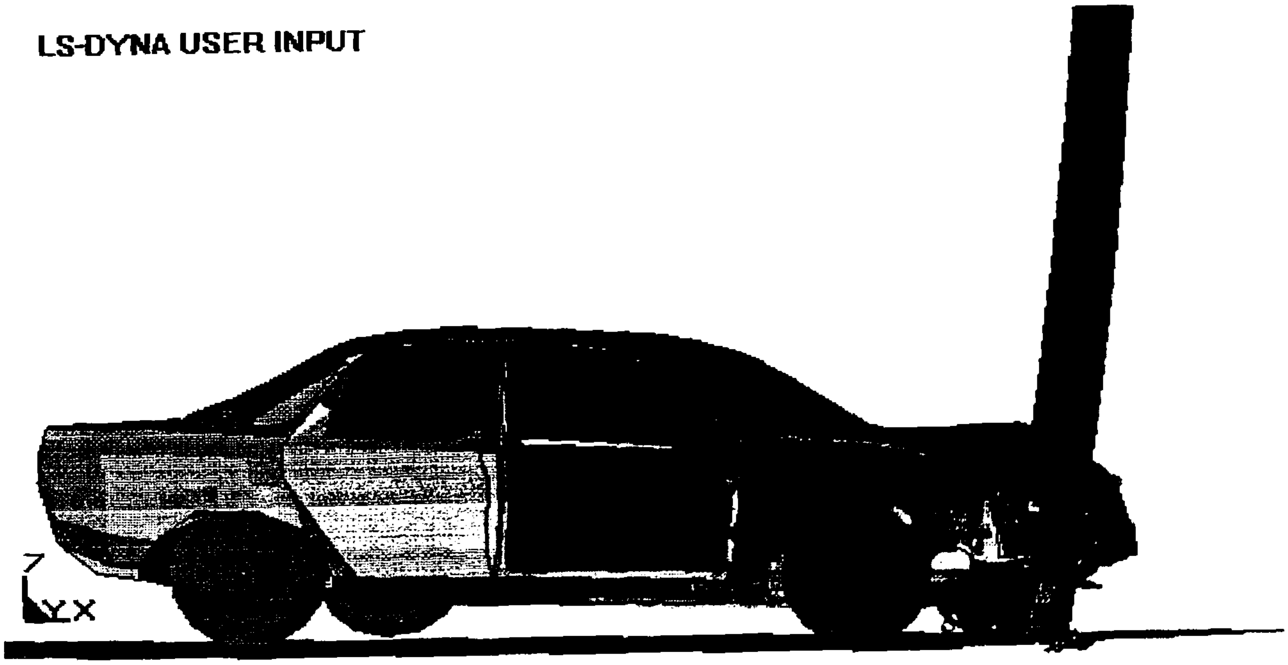

t = 100 ms

Figure 4.38 (b) Simulation results for steel pole supported on rubber base in frontal impact.

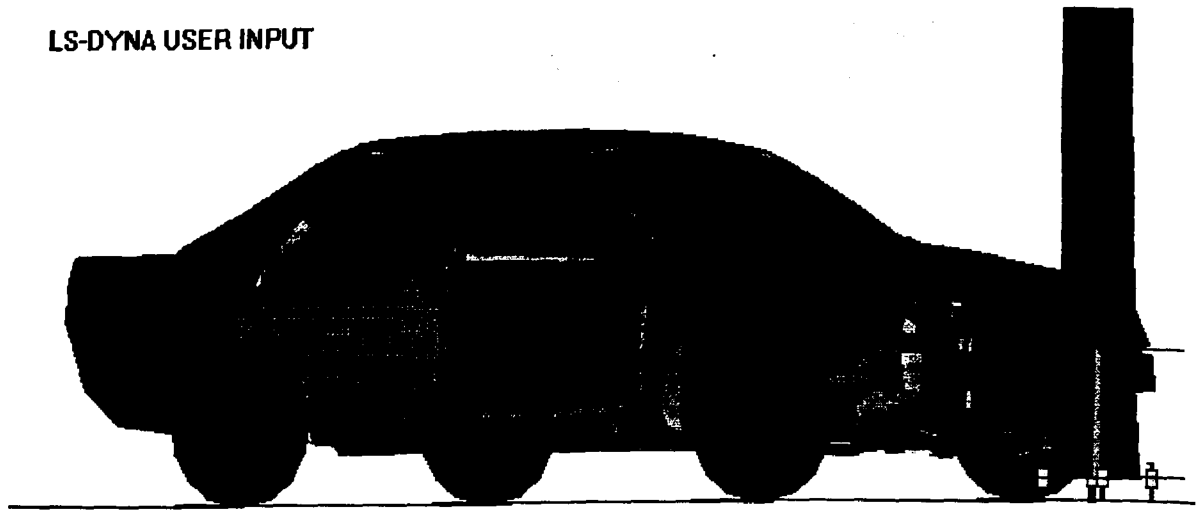

t = 0 ms

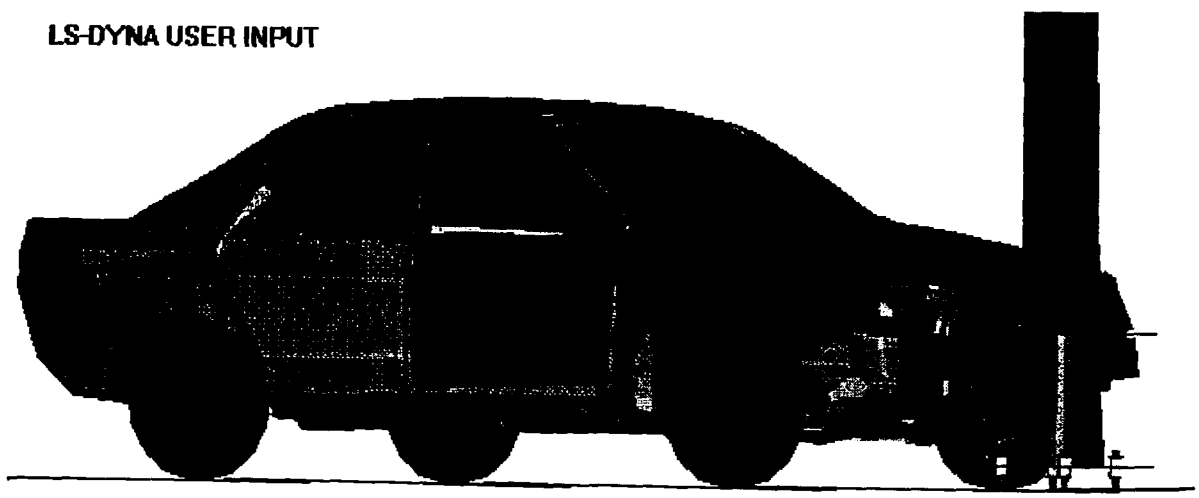

t = 25 ms

Figure 4.39 (a)

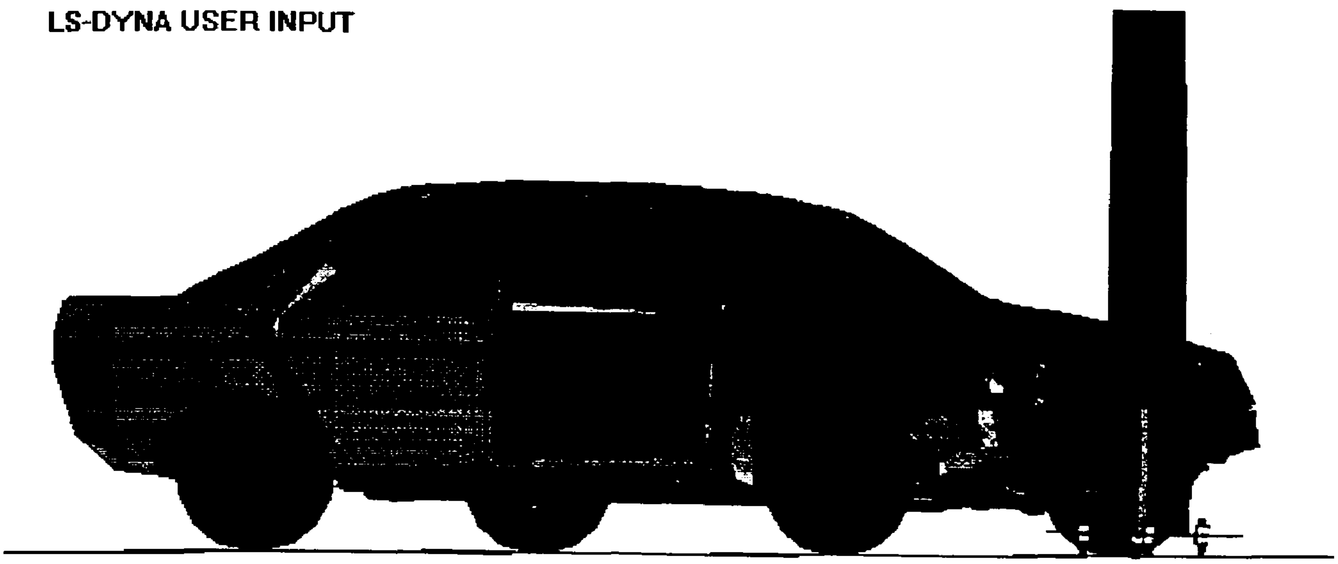

t = 50 ms

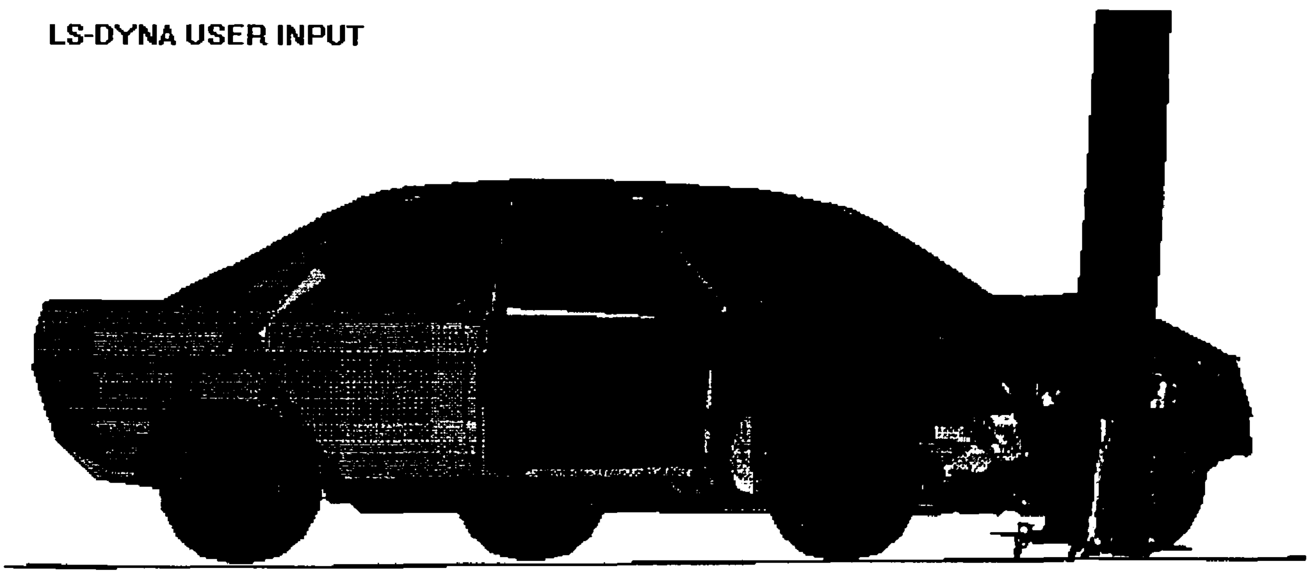

t = 100 ms

Figure 4.39 (b) Simulation results for steel pole supported on rubber base in frontal impact.

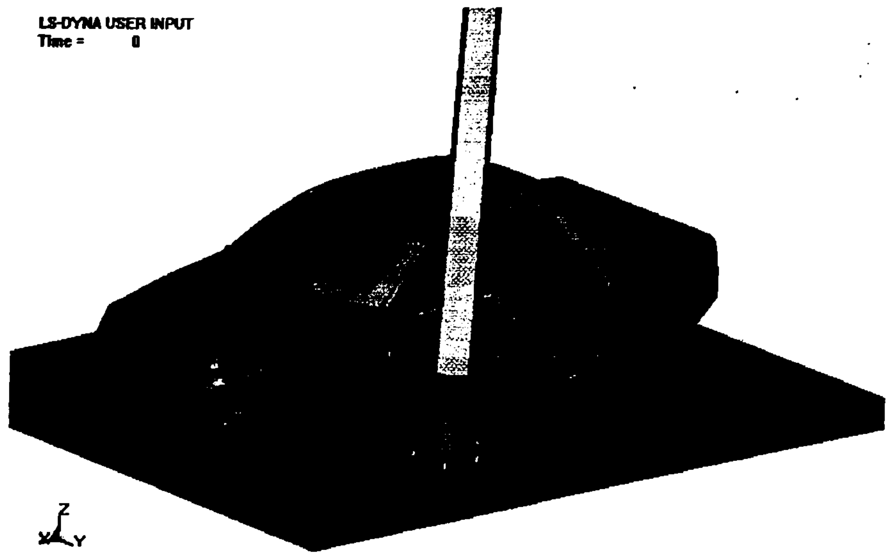

t = 0 ms

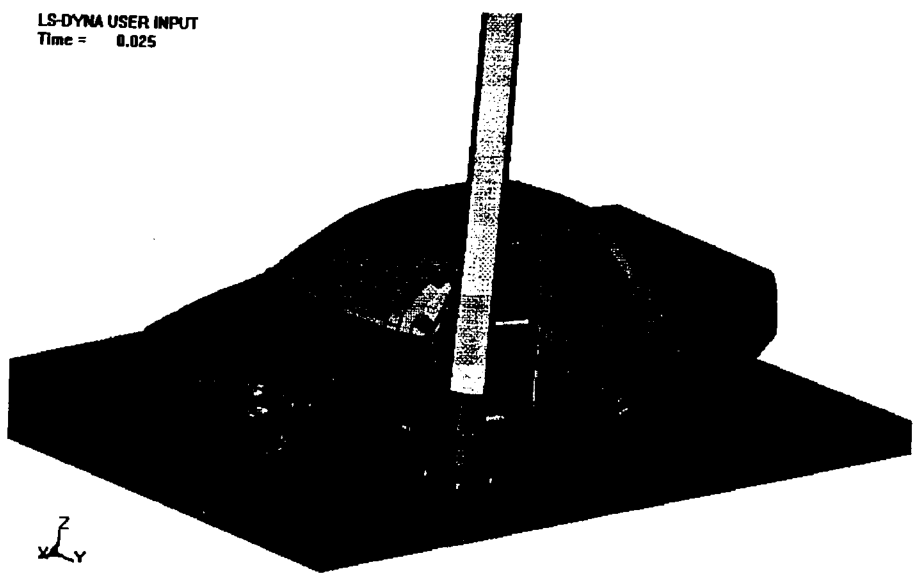

t = 25 ms

Figure: 4.40 (a) Simulation results of pole supported on rubber base for side impact.

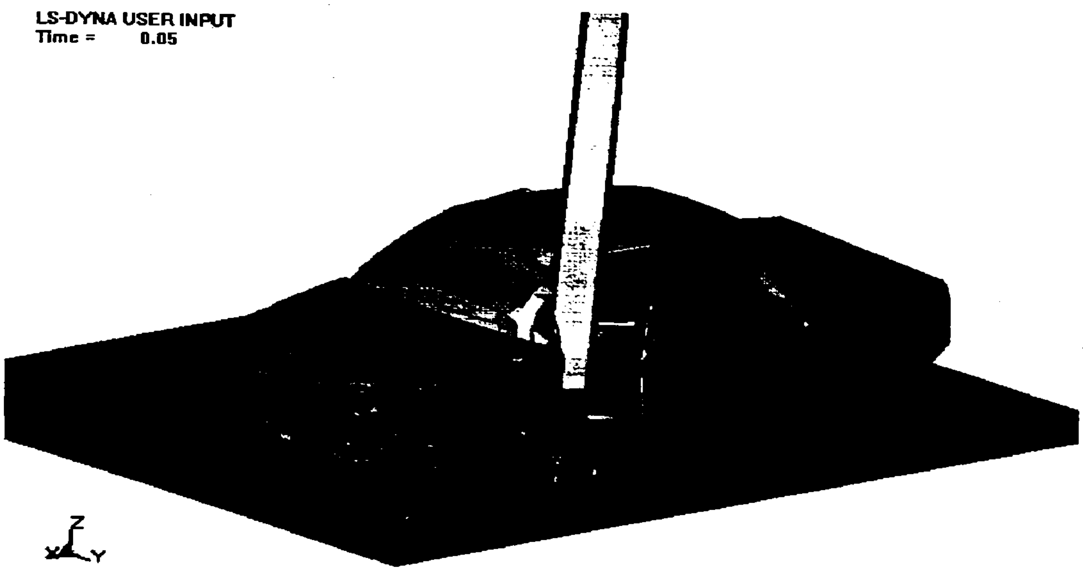

t = 50 ms

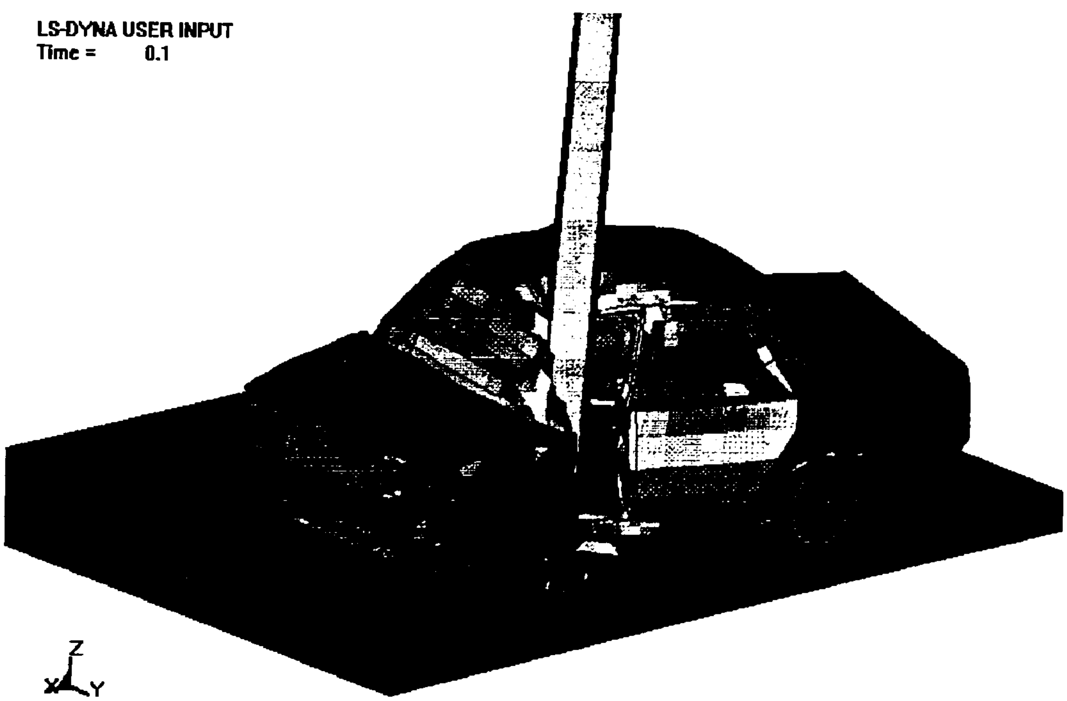

t = 100 ms

Figure: 4.40 (b) Simulation results of pole supported on rubber base for side impact.

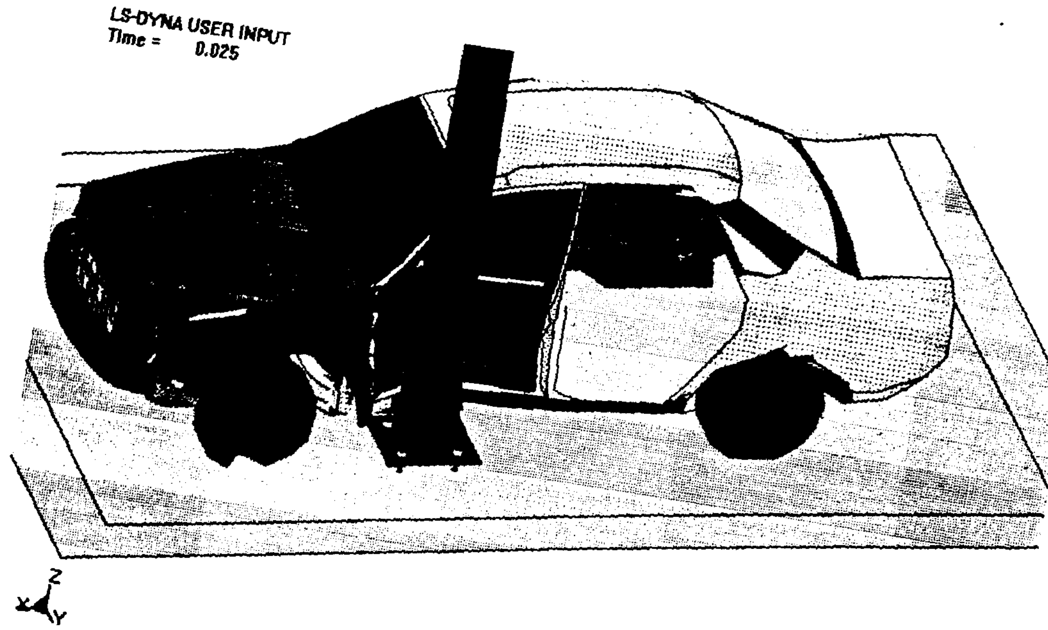

t = 25 ms

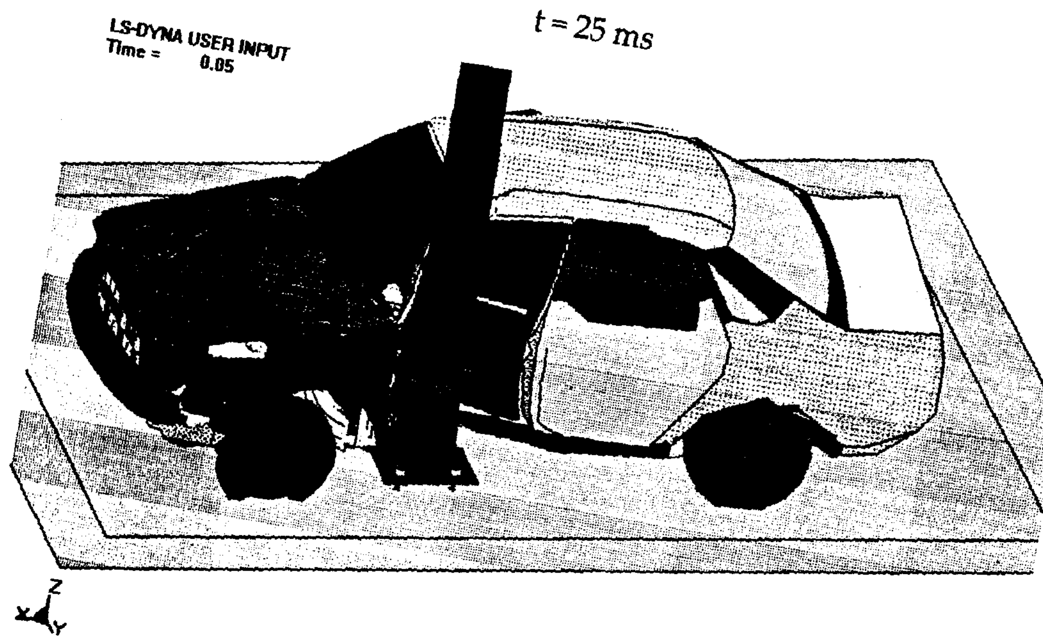

t = 50 ms

Figure: 4.41 (a) Simulation results of pole supported on rubber base for side impact.

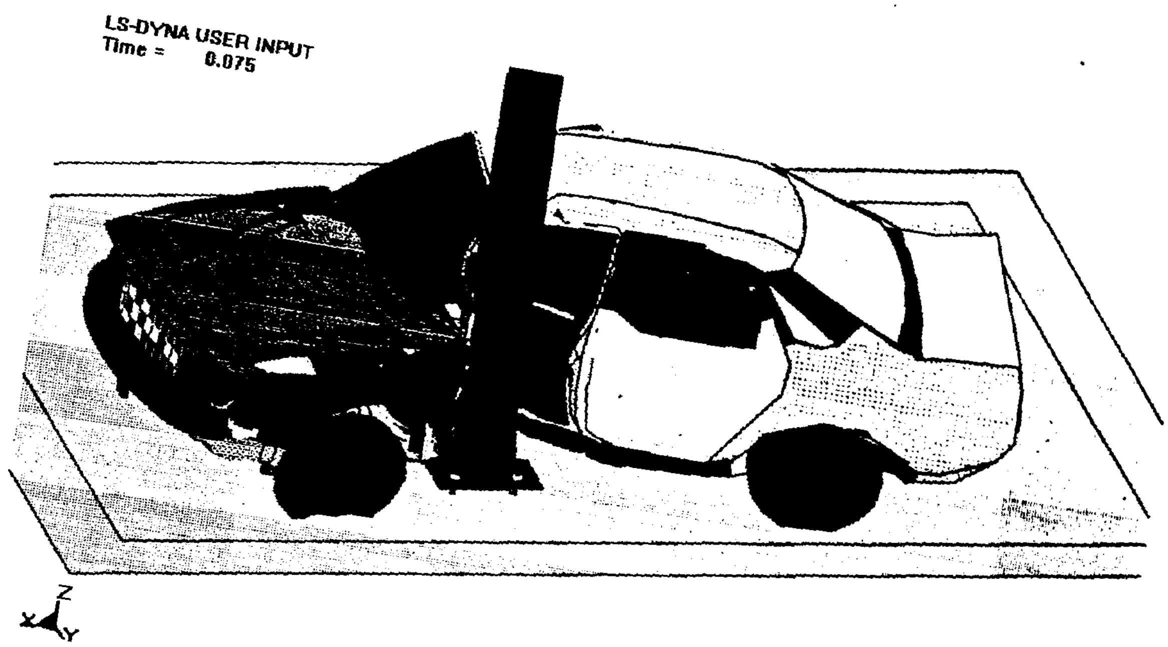

t = 75 ms

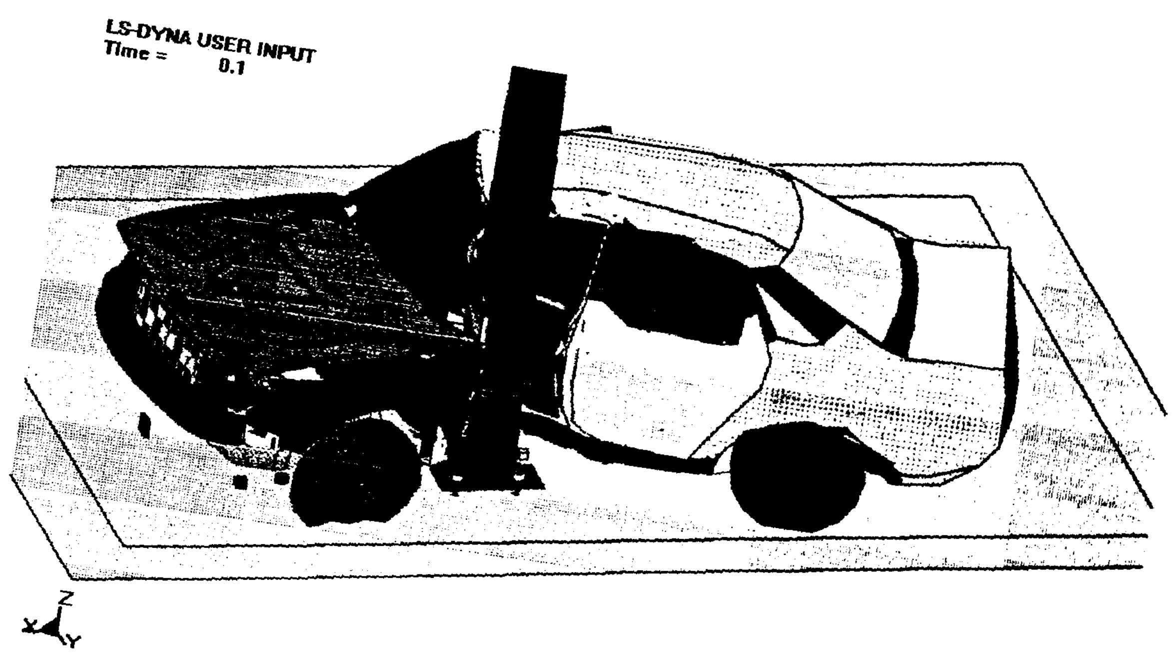

t = 100 ms

Figure: 4.41 (b) Simulation results of pole supported on conical rubber base in side impact.

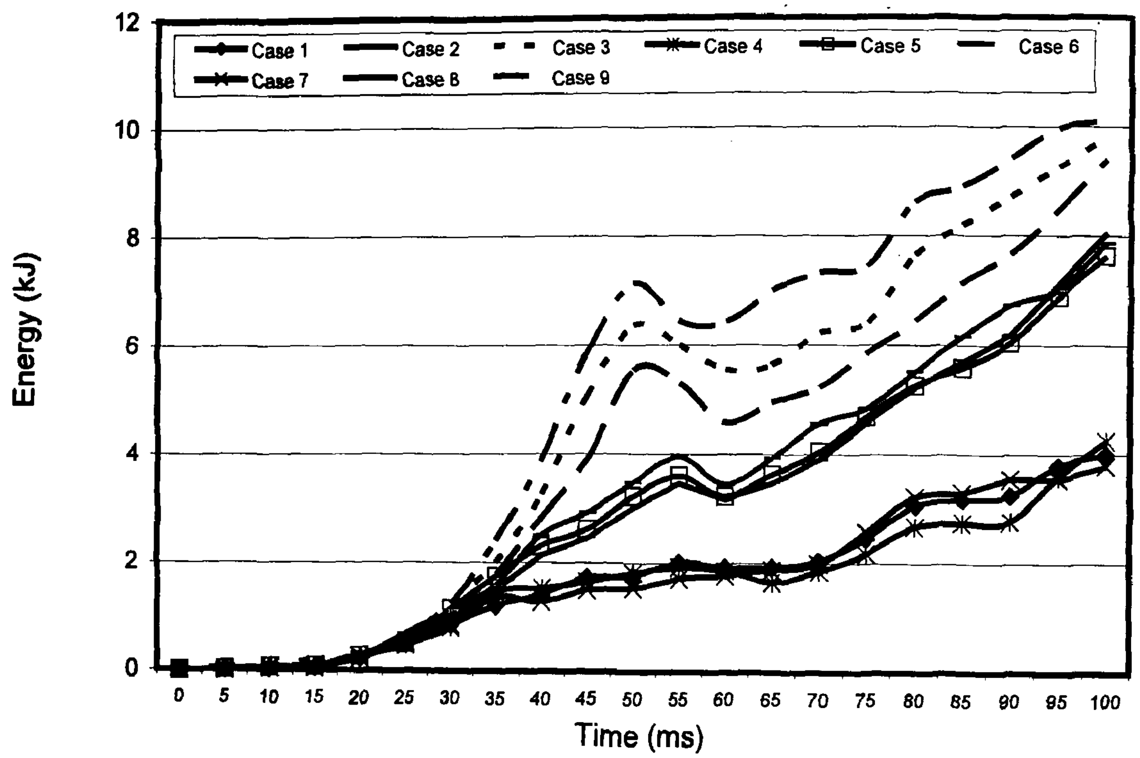

Figure 4.42 Energy absorbed by steel pole supported on different rubber bases in frontal impact.

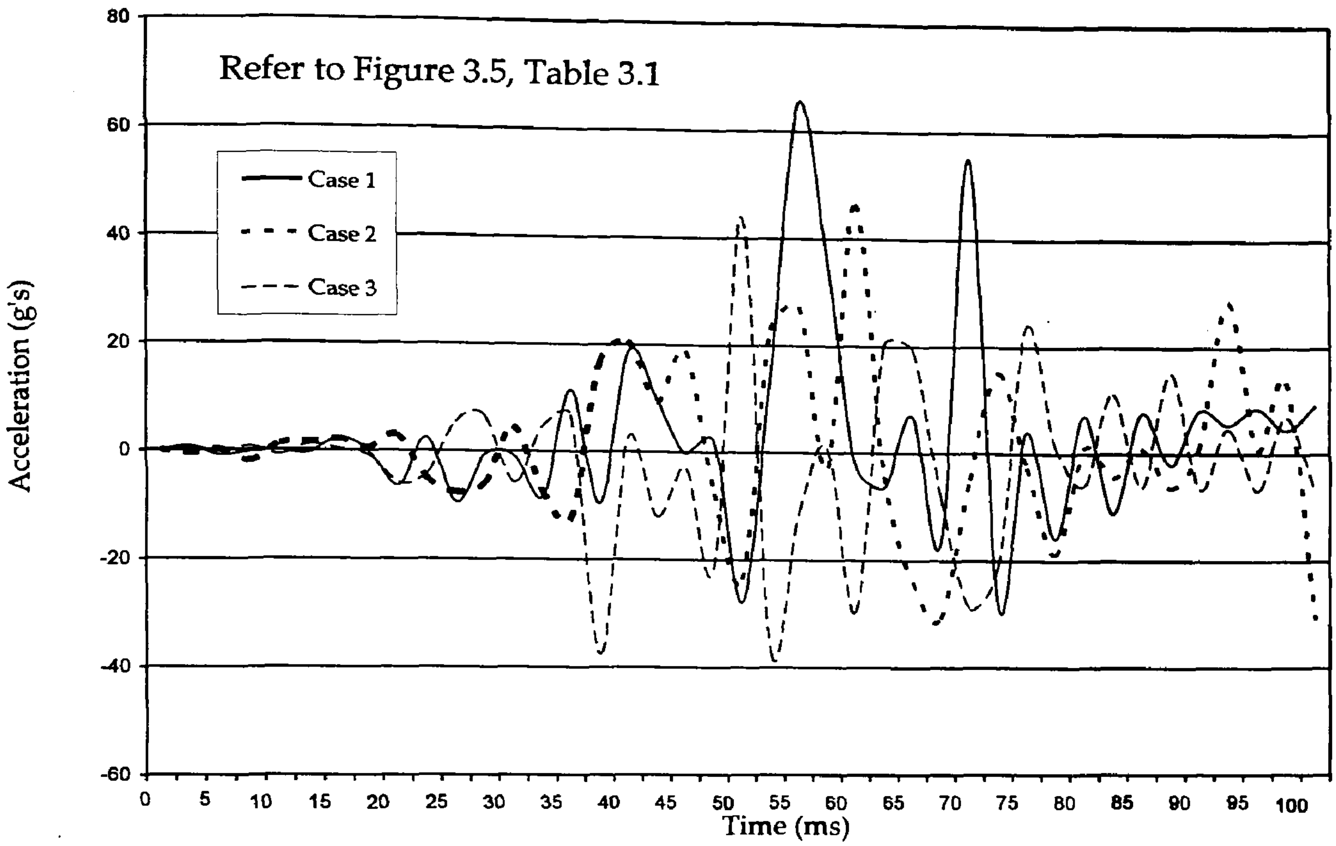
Refer to Figure 3.5, Table 3.1
Case 1
Case 2
Case 3
Acceleration (g's)
Time (ms)
80
60
40
20
0
-20
-40
-60
0 5 10 15 20 25 30 35 40 45 50 55 60 65 70 75 80 85 90 95 100

(a)

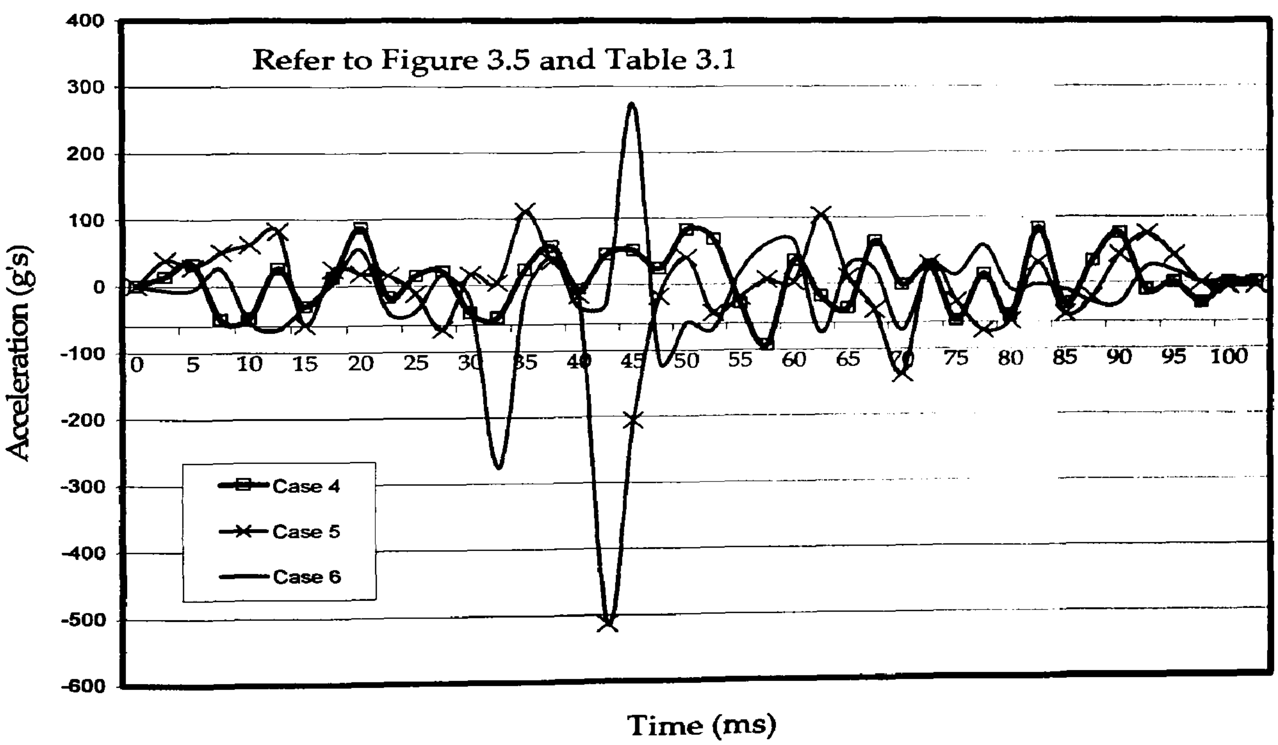
Refer to Figure 3.5 and Table 3.1
Case 4
Case 5
Case 6
Acceleration (g's)
Time (ms)
400
300
200
100
0
-100
-200
-300
-400
-500
-600
0 5 10 15 20 25 30 35 40 45 50 55 60 65 70 75 80 85 90 95 100

(b)

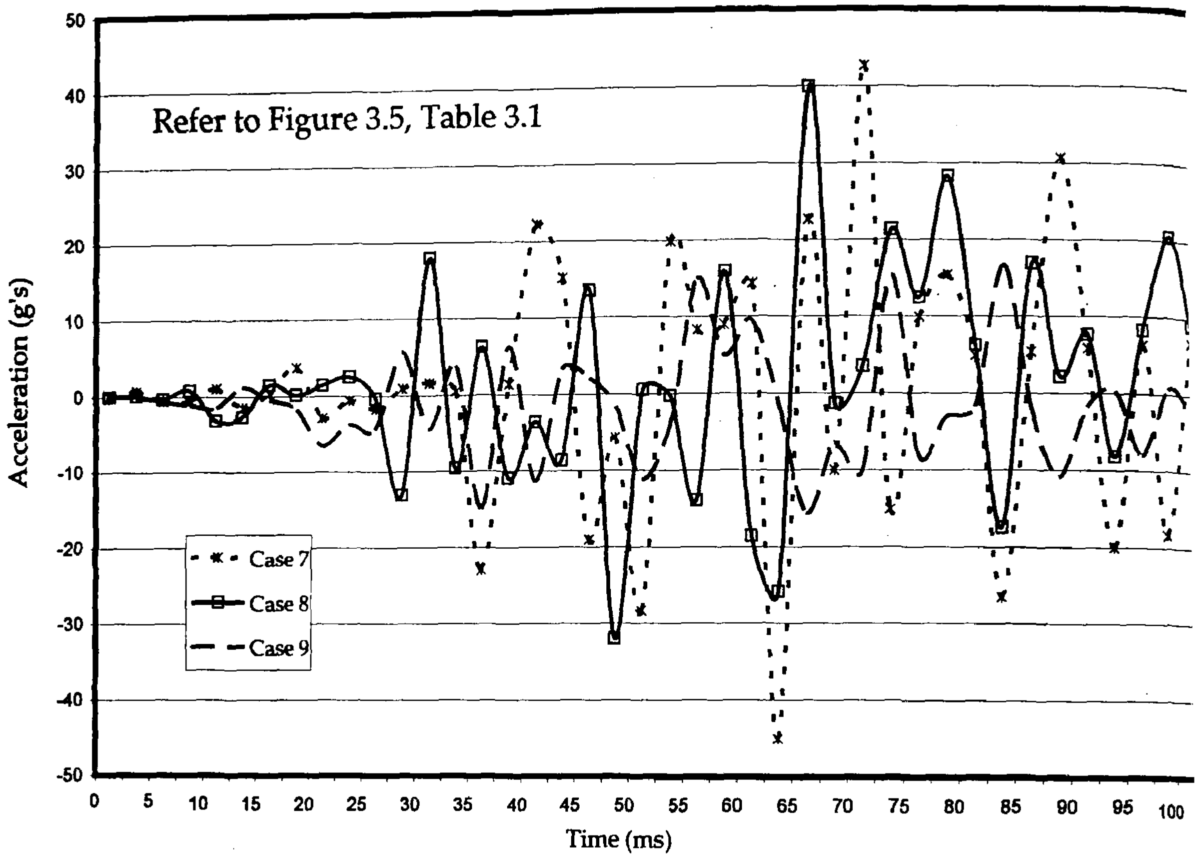

(c)

Figure 4.43 Acceleration time histories at a point on the steering wheel for frontal impact steel pole supported on rubber base.

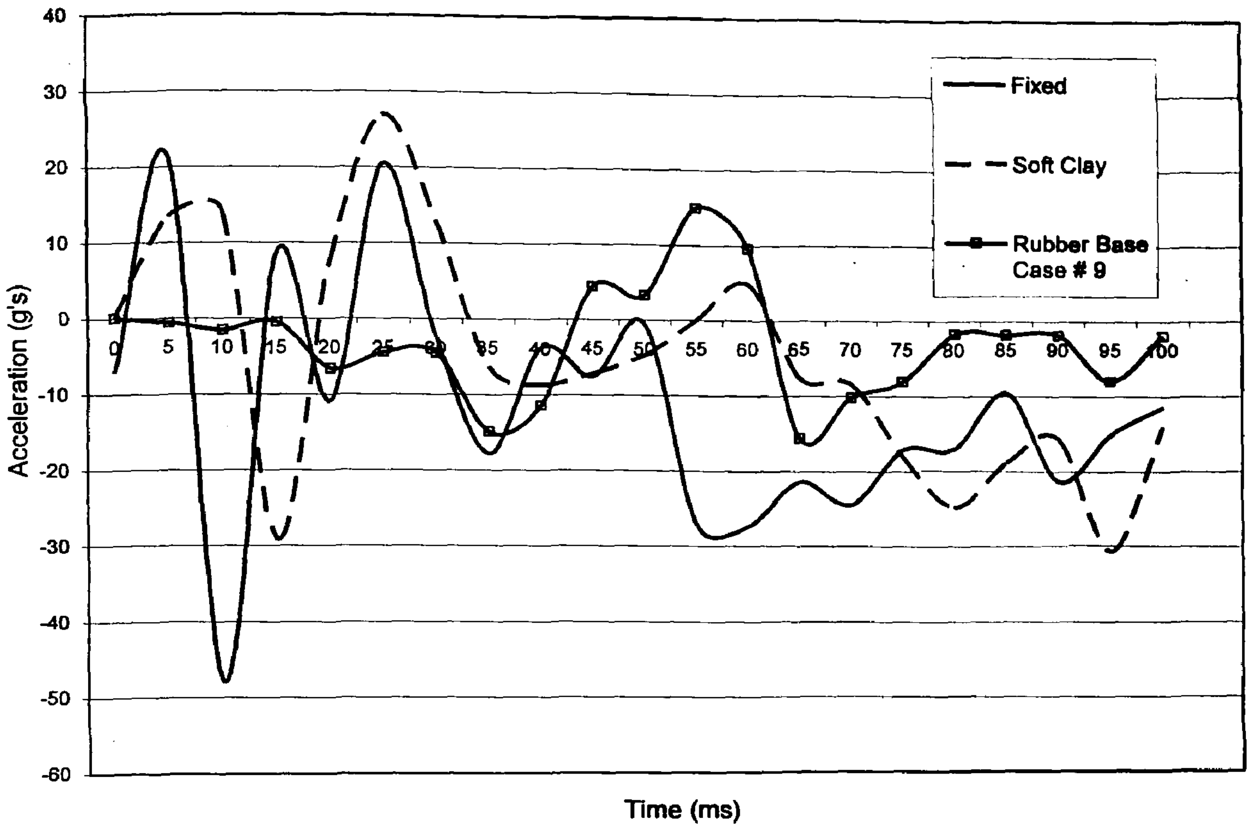

Figure 4.44 Comparative acceleration at the centre of the steering wheel for steel pole with three types of support conditions in frontal impact.

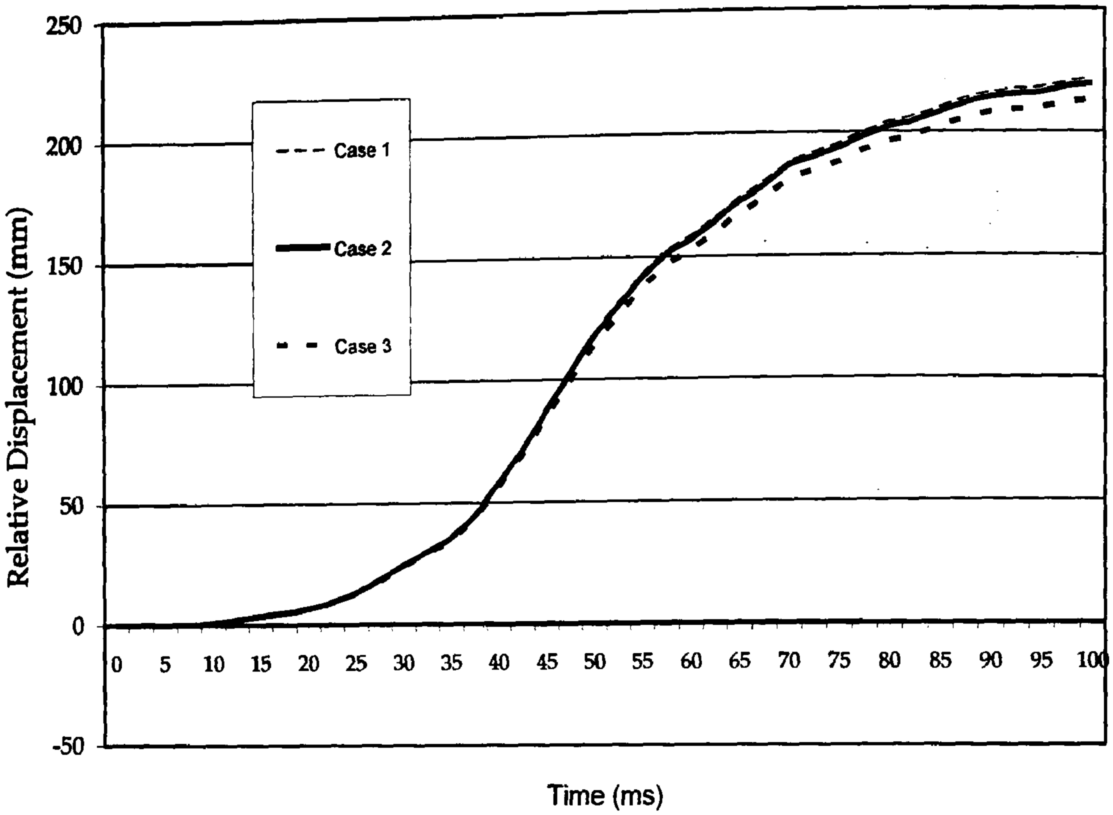
Relative Displacement (mm)
Time (ms)
Case 1
Case 2
Case 3
250
200
150
100
50
0
-50
0 5 10 15 20 25 30 35 40 45 50 55 60 65 70 75 80 85 90 95 100

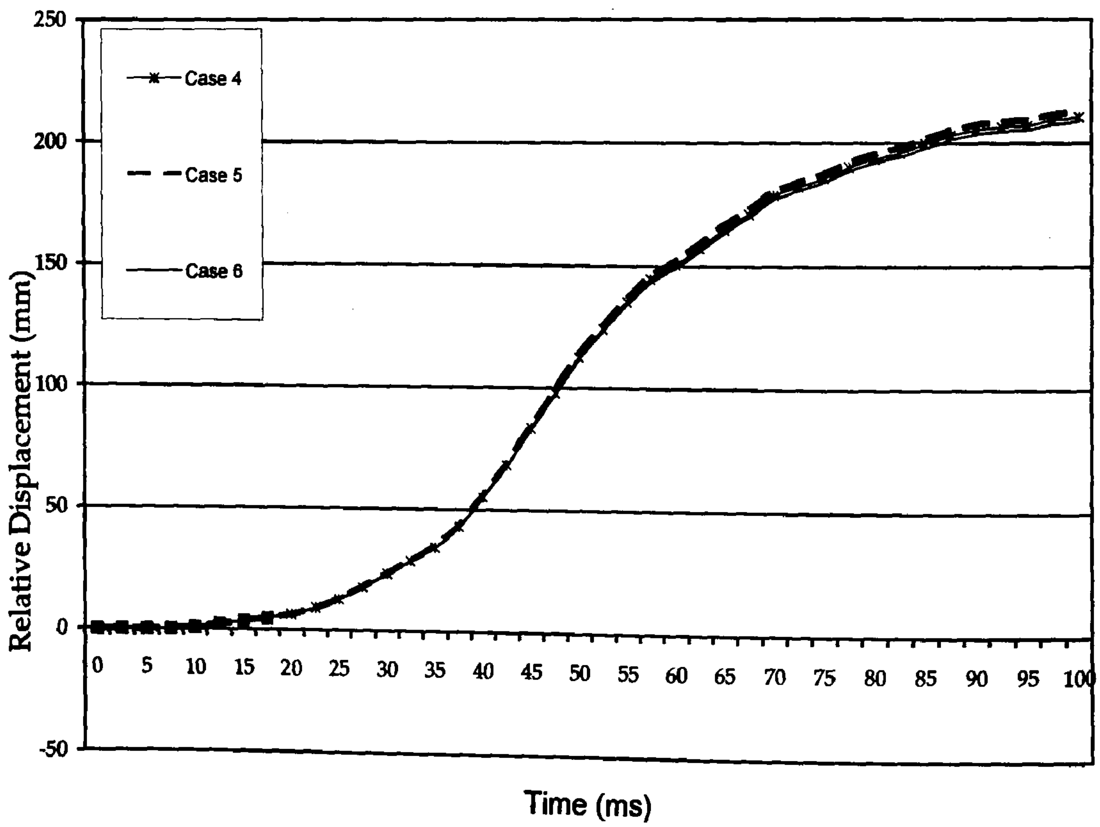
Relative Displacement (mm)
Time (ms)
Case 4
Case 5
Case 6
250
200
150
100
50
0
-50
0 5 10 15 20 25 30 35 40 45 50 55 60 65 70 75 80 85 90 95 100

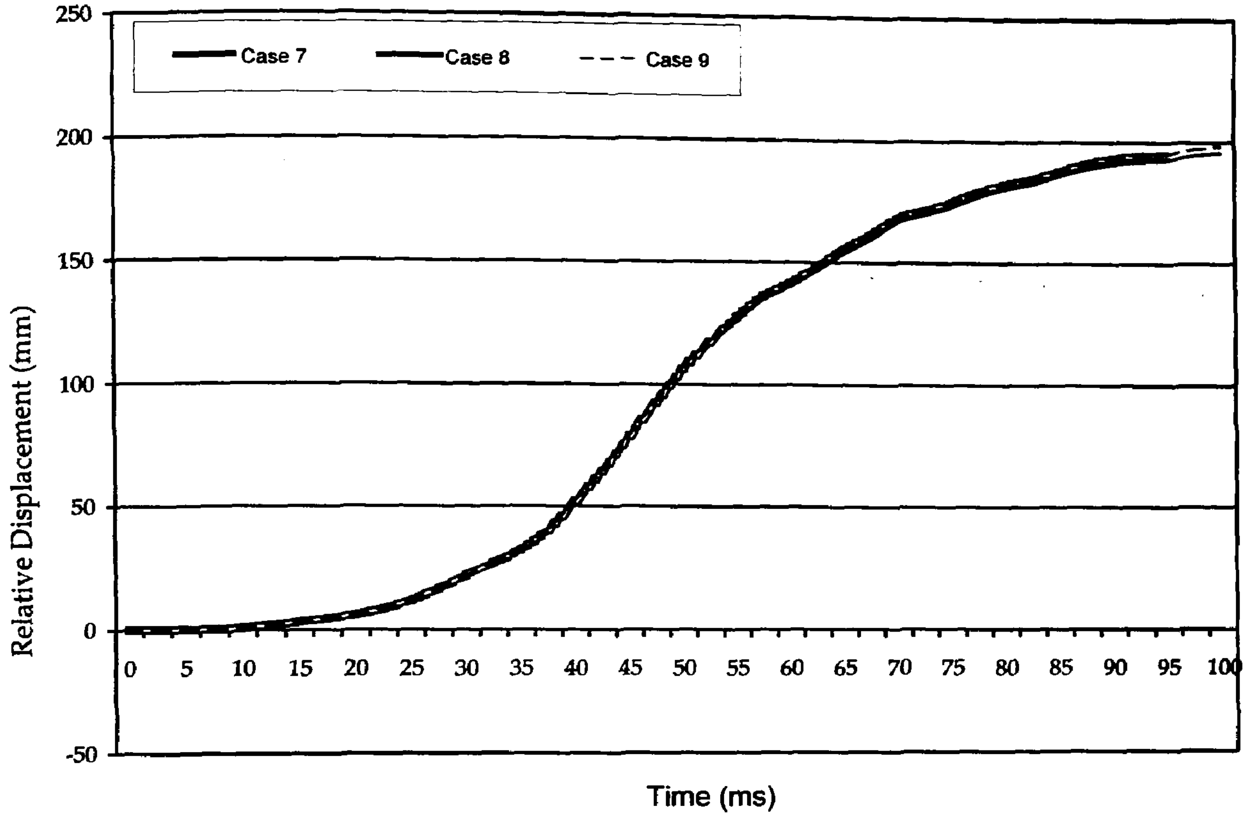

Figure 4.45 Relative distance between a point on the seat and the steering wheel for steel pole supported on rubber base in frontal impact.

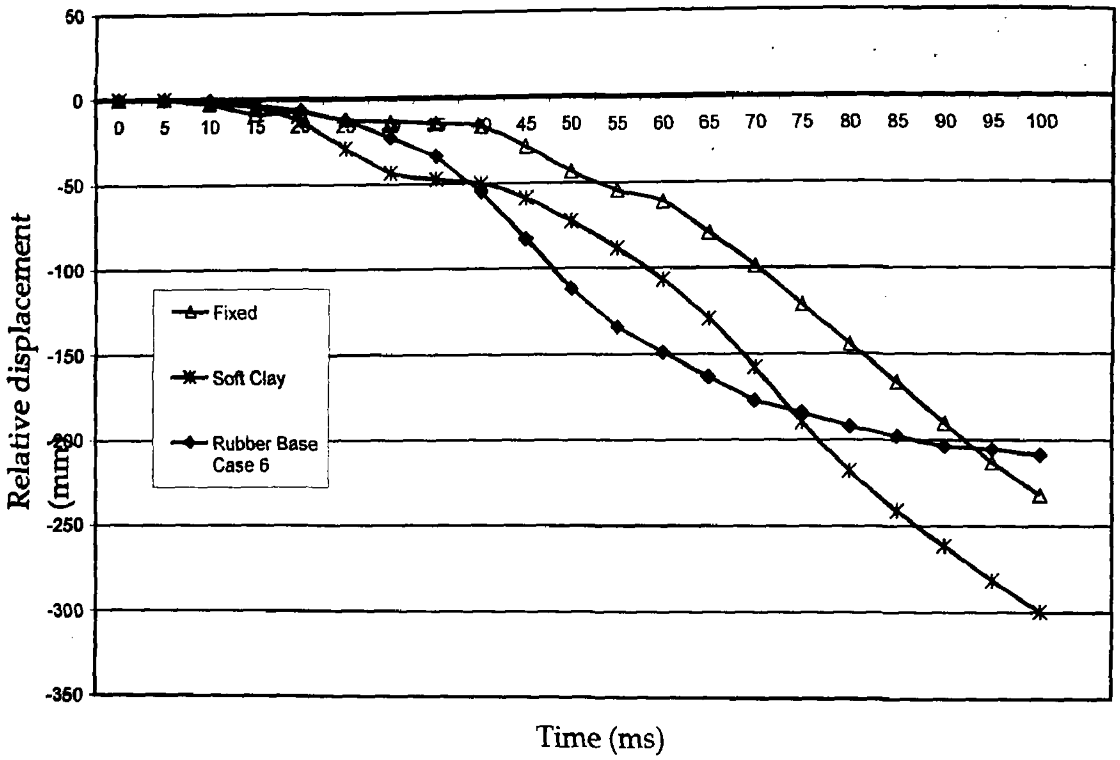

Figure 4.46: Relative distances between the centre of steering wheel and the corresponding point on the driver's seat in frontal impact.

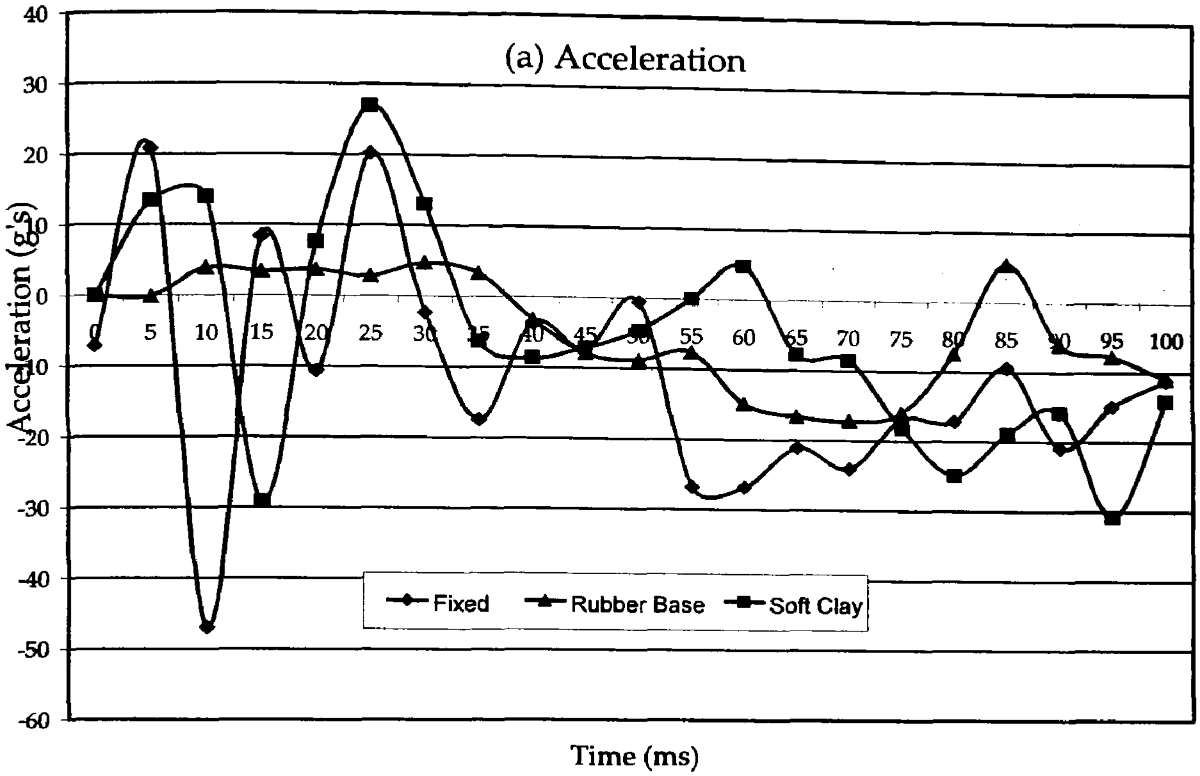

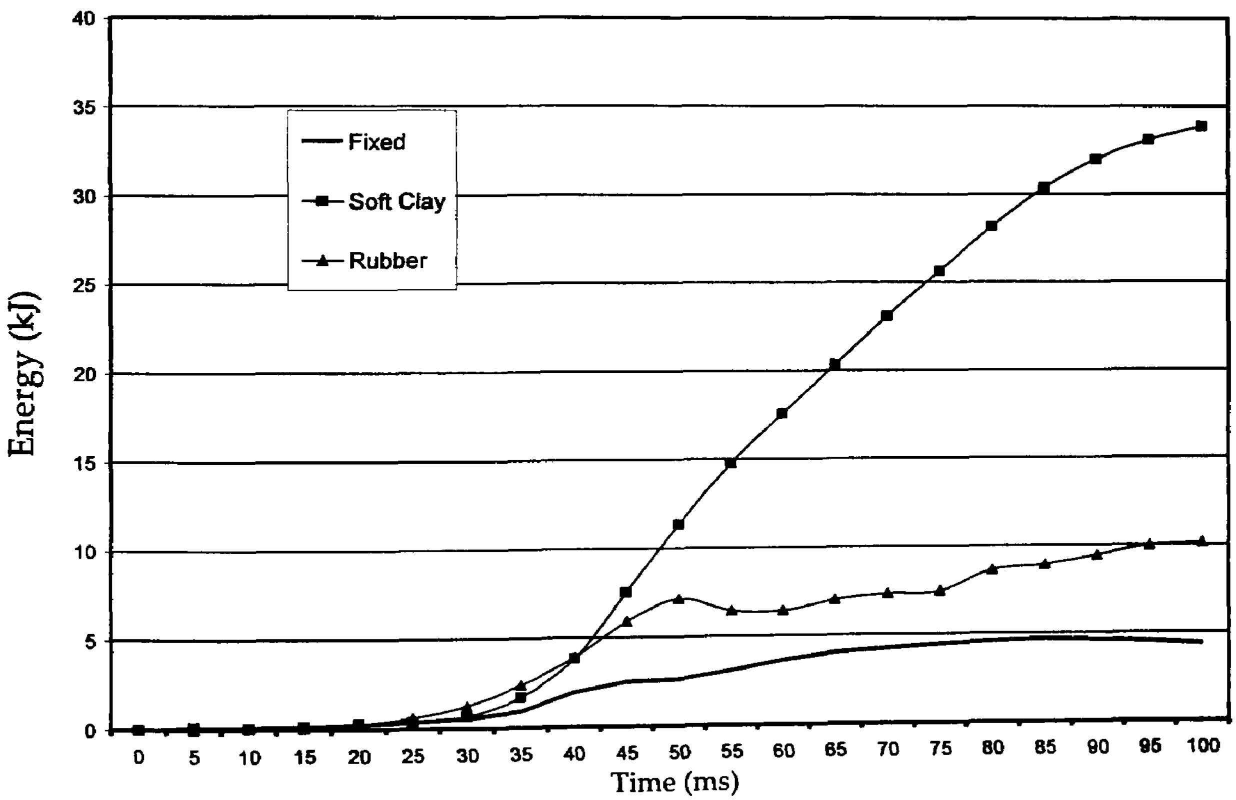

Figure 4.47: Comparative acceleration and energy absorption for different support conditions in frontal impact.

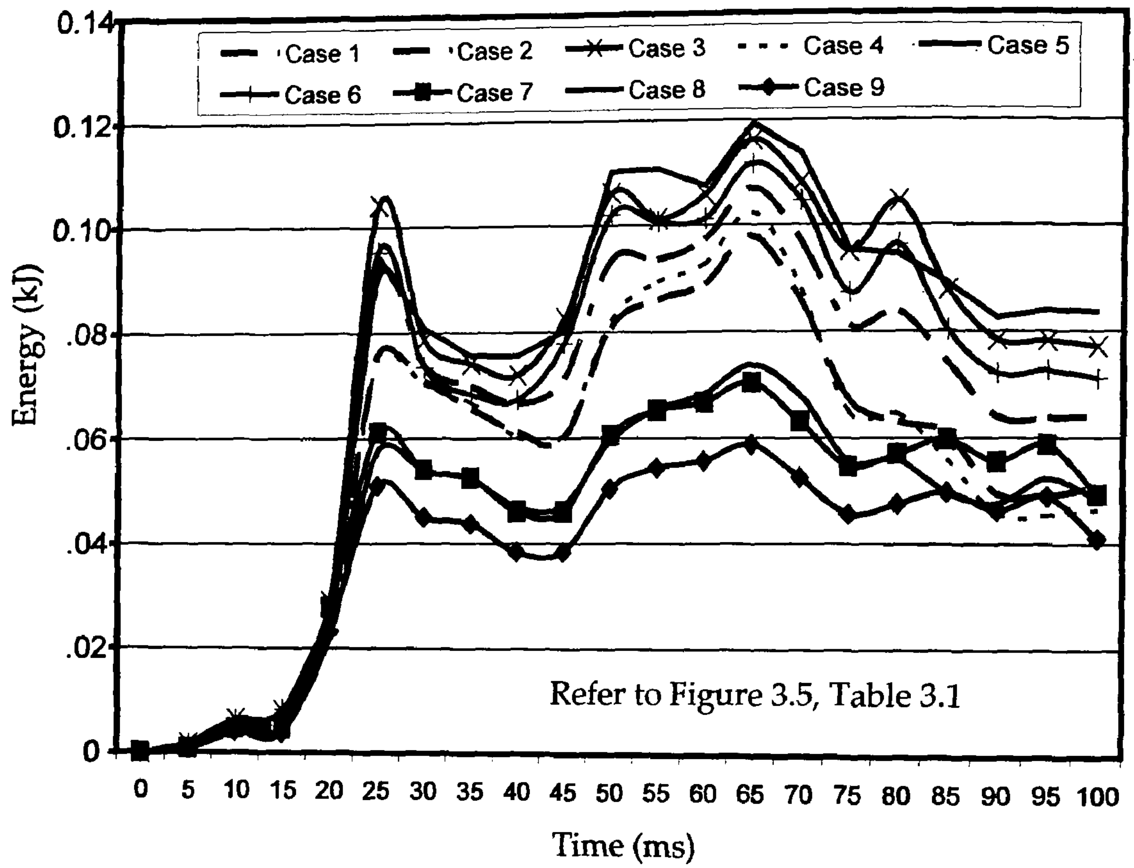

Figure 4.48 Energy absorbed by steel pole supported on different rubber bases in side impact.

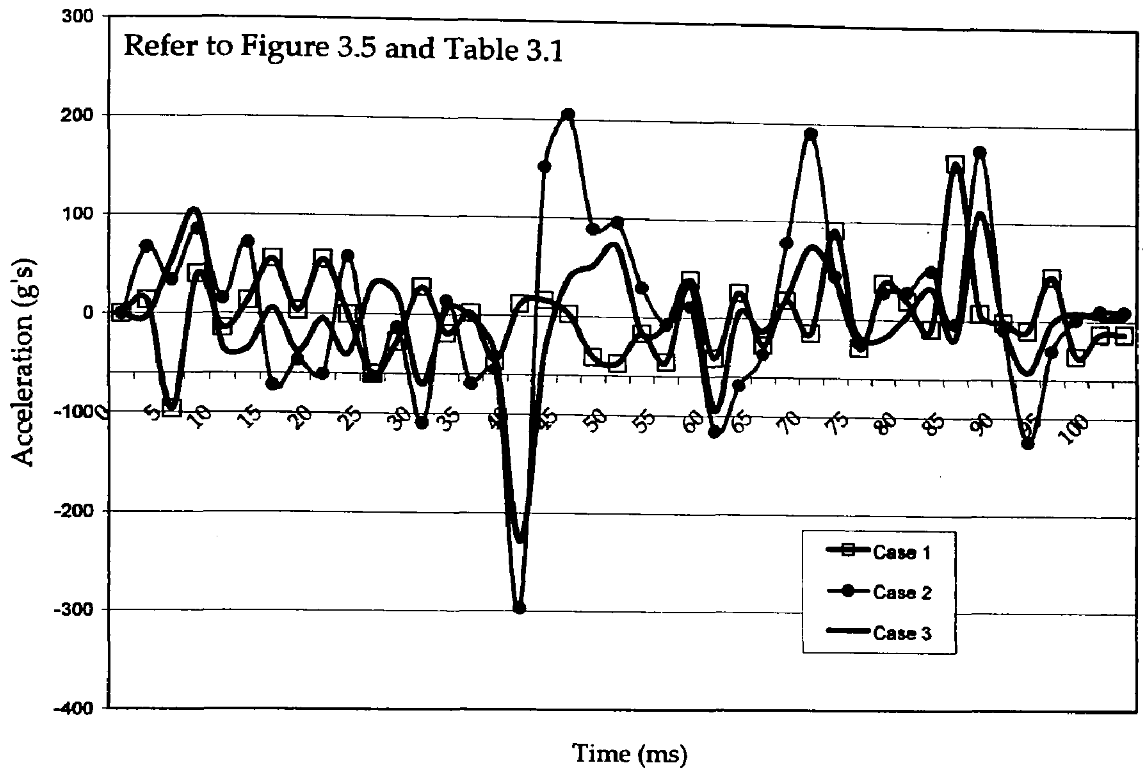

Refer to Figure 3.5 and Table 3.1
Acceleration (g's)
Time (ms)
Case 1
Case 2
Case 3
300
200
100
0
-100
-200
-300
-400

(a)

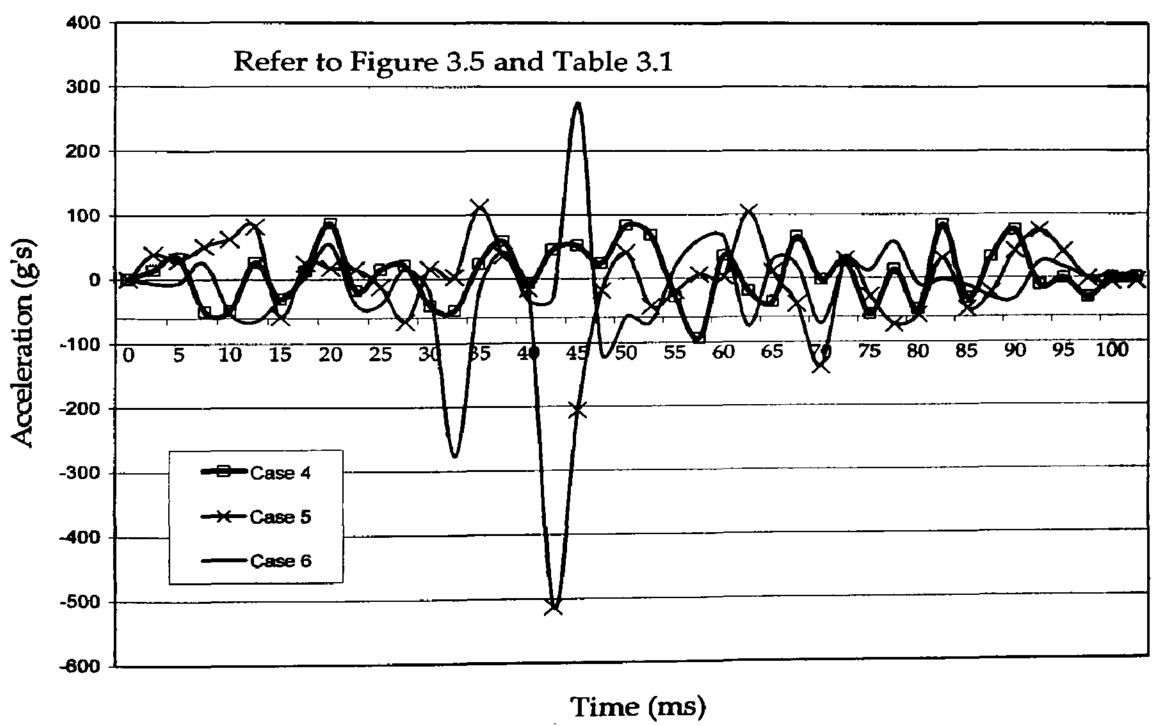

Refer to Figure 3.5 and Table 3.1
Acceleration (g's)
Time (ms)
Case 4
Case 5
Case 6
400
300
200
100
0
-100
-200
-300
-400
-500
-600
0 5 10 15 20 25 30 35 40 45 50 55 60 65 70 75 80 85 90 95 100

(b)

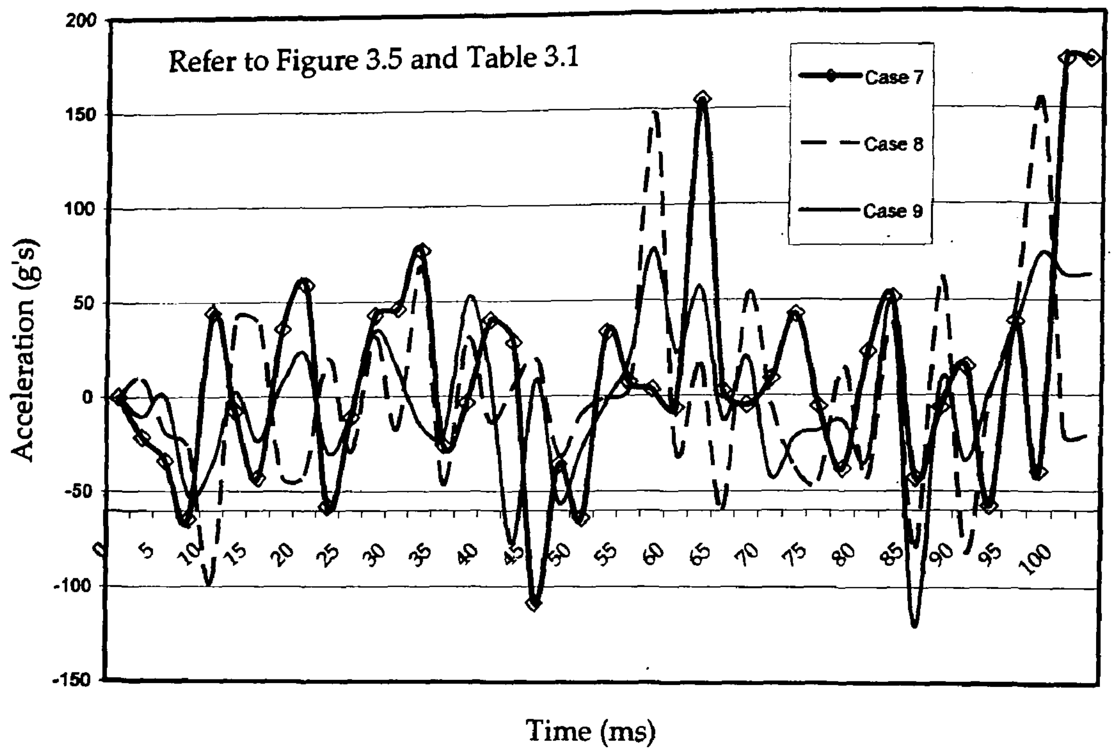

(c)

Figure 4.49: Acceleration at roof beam level for side impacted steel pole supported on rubber base.

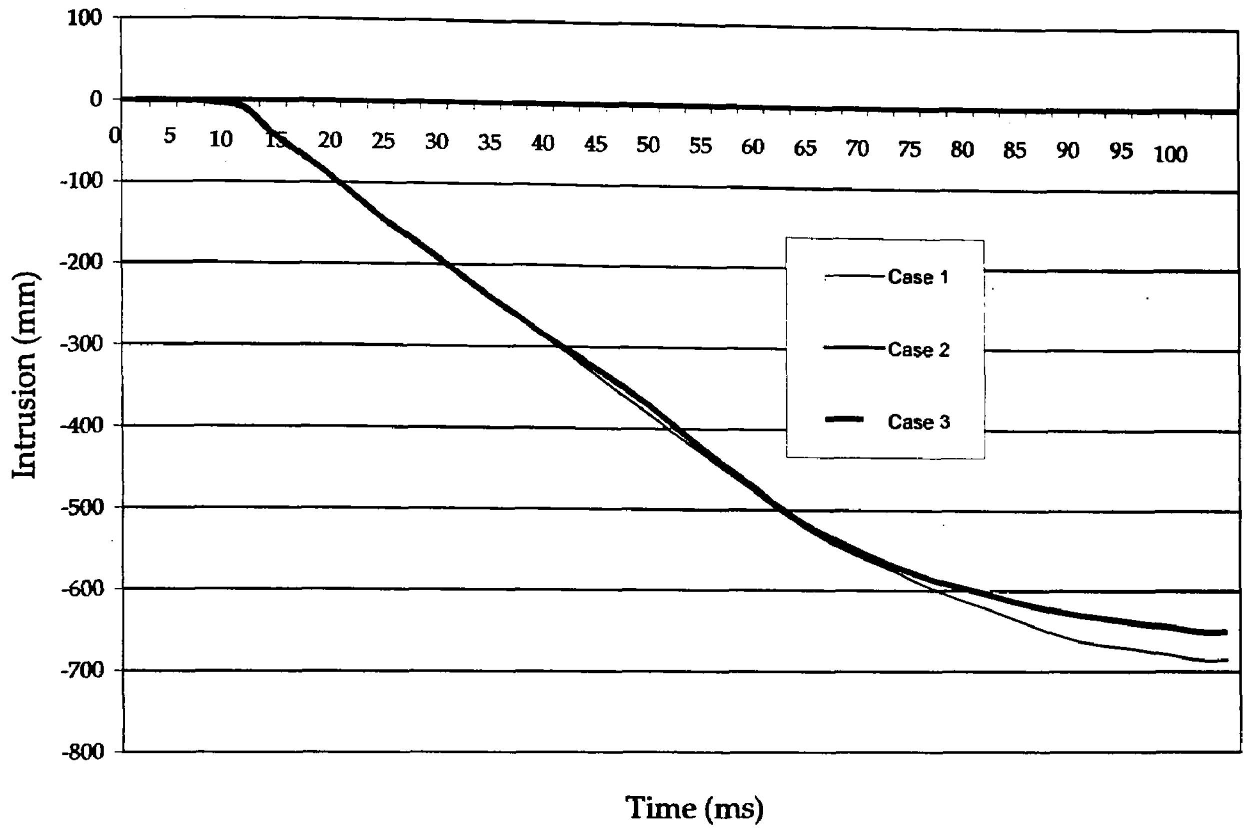
Intrusion (mm)
100
0
-100
-200
-300
-400
-500
-600
-700
-800
0
5
10
15
20
25
30
35
40
45
50
55
60
65
70
75
80
85
90
95
100
Case 1
Case 2
Case 3
Time (ms)

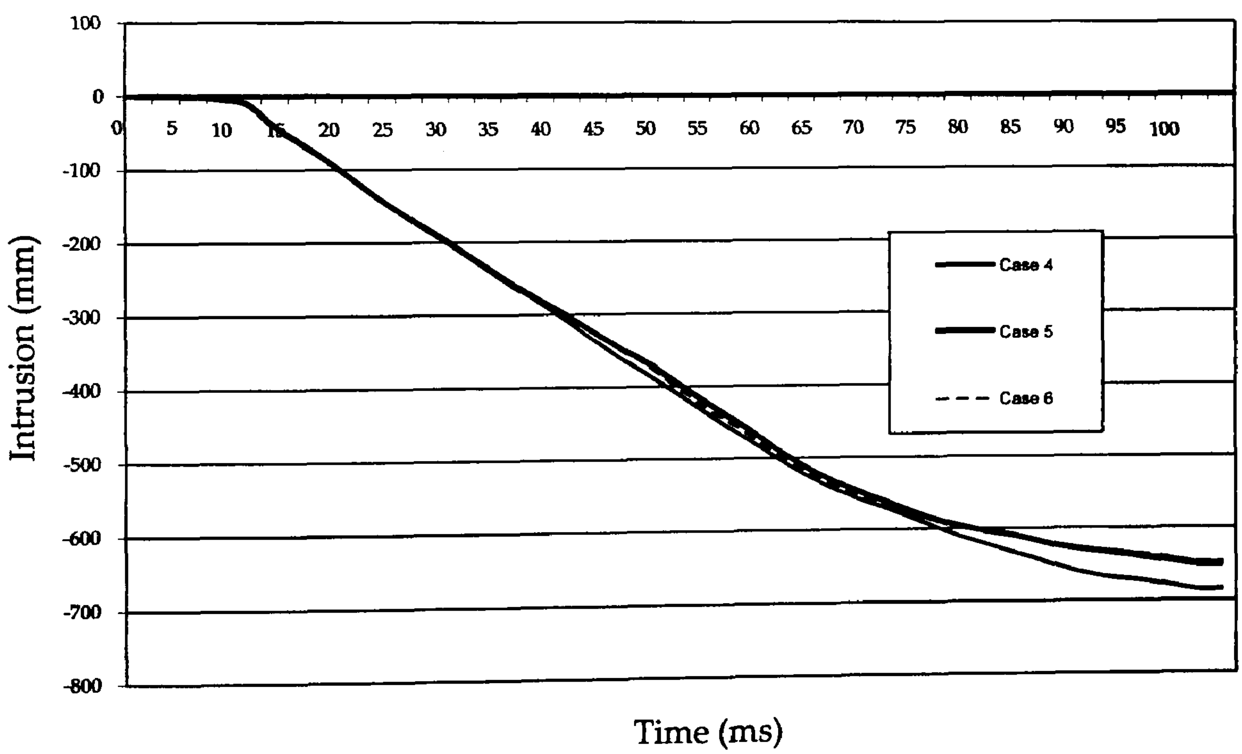
Intrusion (mm)
100
0
-100
-200
-300
-400
-500
-600
-700
-800
0
5
10
15
20
25
30
35
40
45
50
55
60
65
70
75
80
85
90
95
100
Case 4
Case 5
Case 6
Time (ms)

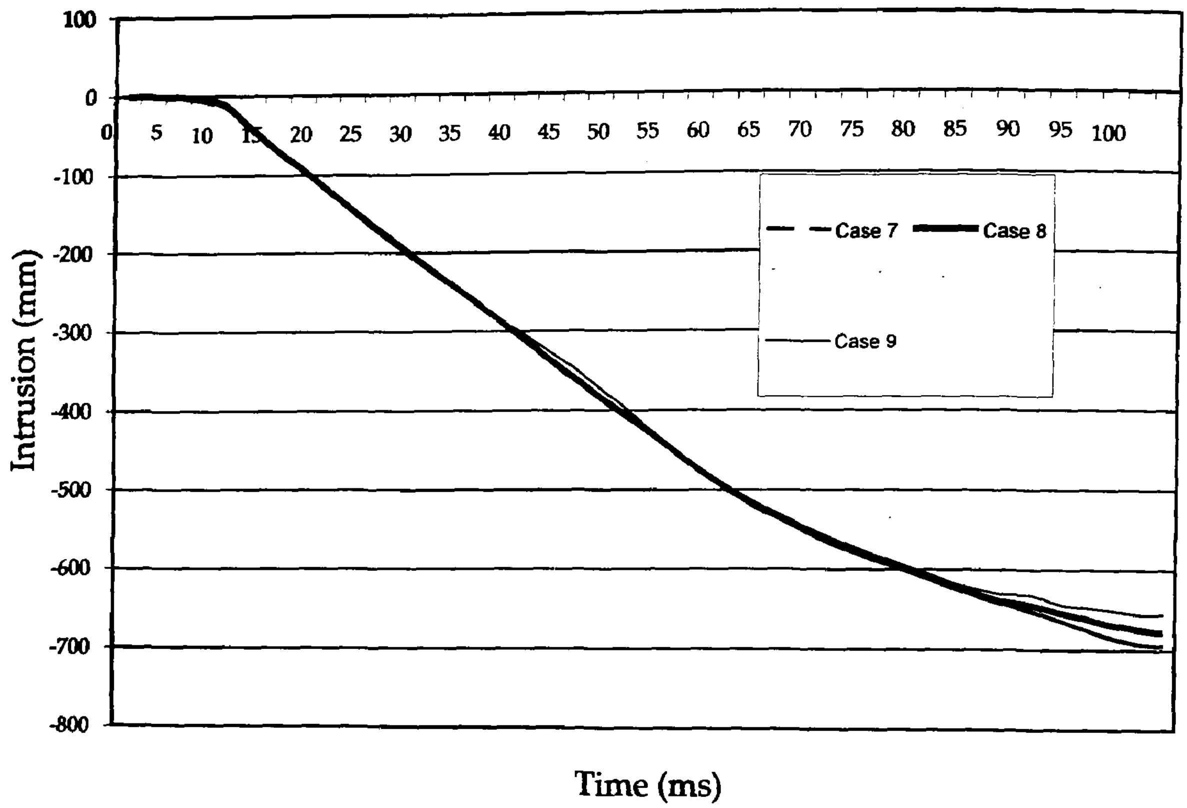

Figure 4.50 Intrusion of passenger compartment for steel pole supported on rubber base in side impact.

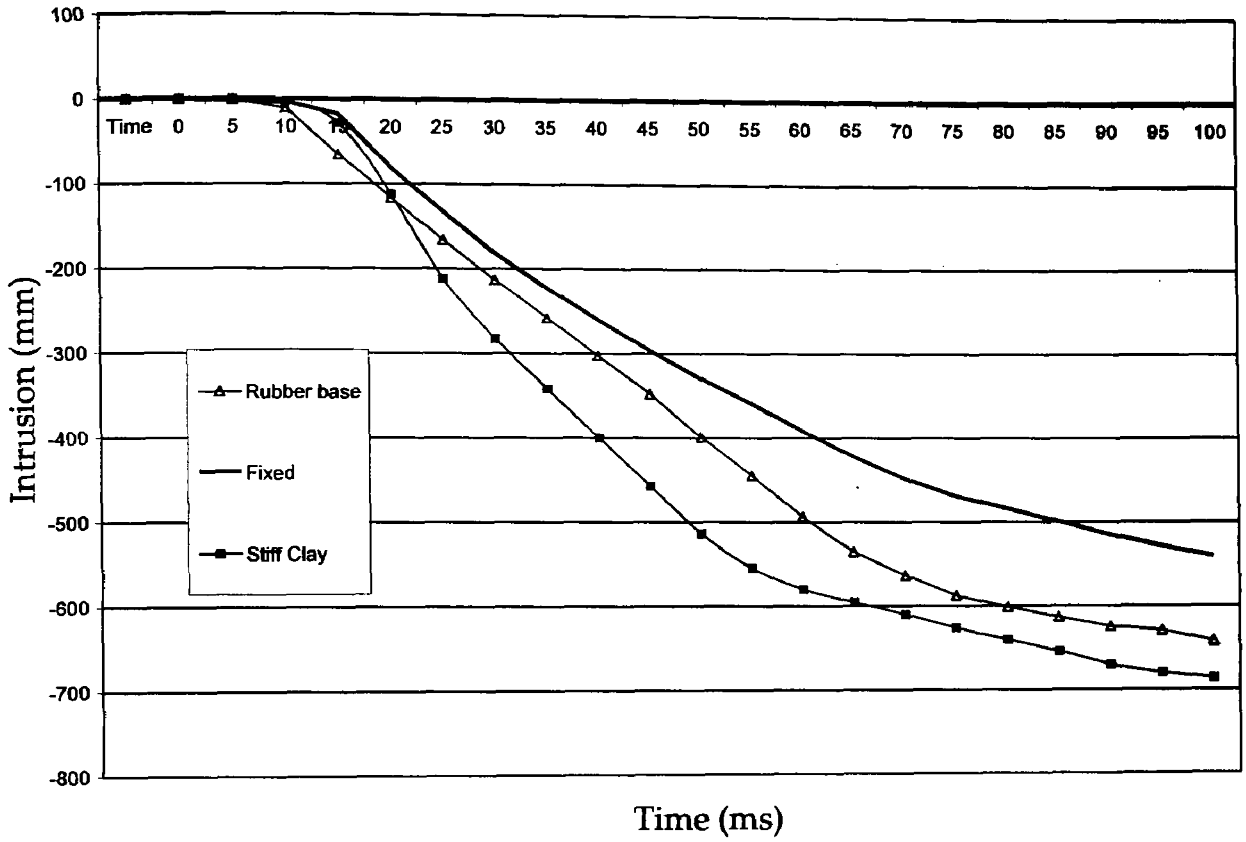

Figure 4.51 Comparison of passenger compartment intrusion for the cases of steel pole supported on base plate, embedded 1500 mm in soft clayey soil, and supported on a rubber base.

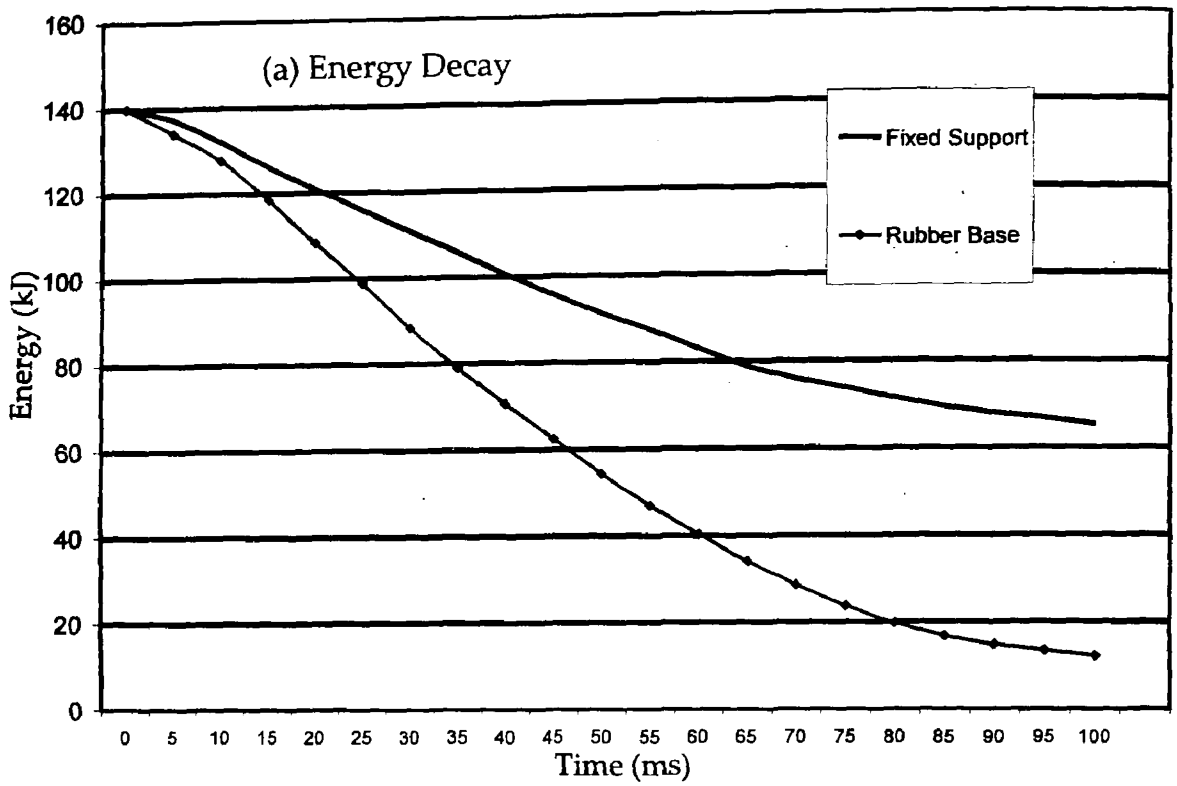

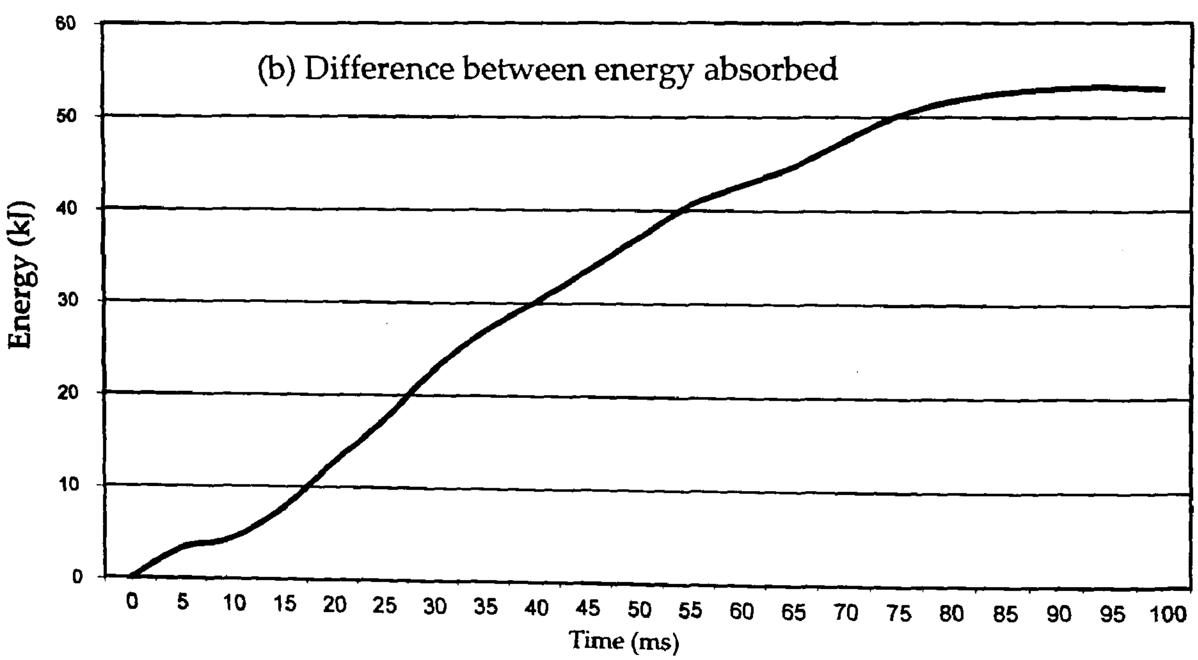

Figure 4.52 Decay of kinetic energy in case of side impact for steel pole supported on rubber base and Fixed support.

APPENDIX

Directory Structure of Input Files on CDROM

1. Front
    a. Steel Pole
        i. Fixed
            1. Input
        ii. Soil Embedded
            1. Soft Clay
                a. 1500 mm
    b. Rubber Base Supported Pole
        i. Case 1
        ii. Case 2
        iii. Case 3
        iv. Case 4
        v. Case 5
        vi. Case 6
        vii. Case 7
        viii. Case 8
        ix. Case 9
    c. Aluminium Pole
        i. Fixed
            1. Input
        ii. Soil Embedded
            1. Dense Sand
                a. 1500 mm
                b. 1300 mm
                c. 1100 mm
                d. 900 mm
            2. Loose Sand
                a. 1500 mm
                b. 1300 mm
                c. 1100 mm
                d. 900 mm
            3. Stiff Clay
                a. 1500 mm
                b. 1300 mm
                c. 1100 mm
                d. 900 mm

        4. Soft Clay
            a. 1500 mm
            b. 1300 mm
            c. 1100 mm
            d. 900 mm

2. **Side**
    a. Steel Pole
        i. Fixed
            1. Input
        ii. Soil Embedded
            1. Dense Sand
                a. 1500 mm
                b. 1300 mm
                c. 1100 mm
                d. 900 mm
            2. Loose Sand
                a. 1500 mm
                b. 1300 mm
                c. 1100 mm
                d. 900 mm
            3. Stiff Clay
                a. 1500 mm
                b. 1300 mm
                c. 1100 mm
                d. 900 mm
            4. Soft Clay
                a. 1500 mm
                b. 1300 mm
                c. 1100 mm
                d. 900 mm
    b. Rubber Base Supported Pole
        i. Case 1
        ii. Case 2
        iii. Case 3
        iv. Case 4
        v. Case 5
        vi. Case 6
        vii. Case 7
        viii. Case 8

ix. Case 9

c. Aluminium Pole
    i. Fixed
        1. Input
    ii. Soil Embedded
        1. Dense Sand
            a. 1500 mm
            b. 1300 mm
            c. 1100 mm
            d. 900 mm
        2. Loose Sand
            a. 1500 mm
            b. 1300 mm
            c. 1100 mm
            d. 900 mm
        3. Stiff Clay
            a. 1500 mm
            b. 1300 mm
            c. 1100 mm
            d. 900 mm
        4. Soft Clay
            a. 1500 mm
            b. 1300 mm
            c. 1100 mm
            d. 900 mm